

THÈSE

En vue de l'obtention du

DOCTORAT DE L'UNIVERSITÉ DE TOULOUSE

Délivré par :

Institut National Polytechnique de Toulouse (INP Toulouse)

Discipline ou spécialité :

Génie Electrique

Présentée et soutenue par :

M. ALVARO MORENTIN ETAYO

le vendredi 10 mars 2017

Titre :

Methods and tools for the optimization of modular electrical power distribution cabinets in aeronautical applications

---

Ecole doctorale :

Génie Electrique, Electronique, Télécommunications (GEET)

Unité de recherche :

Laboratoire Plasma et Conversion d'Energie (LAPLACE)

Directeurs de Thèse :

M. THIERRY MEYNARD

M. HUBERT PIQUET

Rapporteurs :

M. LAURENT GERBAUD, INP DE GRENOBLE

M. PHILIPPE VIAROUGE, UNIVERSITE LAVAL

Membres du jury :

M. PHILIPPE VIAROUGE, UNIVERSITE LAVAL, Président

M. HUBERT PIQUET, INP TOULOUSE, Membre

M. JEROME FAUCHER, AIRBUS FRANCE, Membre

M. MARC BUDINGER, INSA TOULOUSE, Membre

M. THIERRY MEYNARD, INP TOULOUSE, Membre

Resumé

Depuis des années, les avionneurs sont engagés pour la réduction de l'empreinte environnementale à travers le développement de nouveaux concepts**.** Ainsi**,** le remplacement des systèmes hydrauliques (*hydraulicless*) et pneumatiques (*bleedless*) de l'avion par des systèmes électriques sont envisagés d'où l'apparition du concept d'avion « plus électrique ». Toutefois, les gains espérés (diminution du coût, de la consommation de carburant ou de la masse) suite à cette substitution ne sont pas si faciles à obtenir, car les technologies précédentes ont bénéficié de plusieurs dizaines d'années de développement et d'optimisation. Les solutions électriques nouvellement proposées doivent donc elles aussi être très abouties pour être véritablement concurrentielles ; tous les degrés de liberté doivent être envisagés, qu'il s'agisse des technologies ou des architectures. En particulier, l'usage d'un nouveau réseau HVDC (540 V) semble être une solution prometteuse.

A partir de ce réseau HVDC, les différentes charges AC triphasées sont alimentées par une série d'onduleurs génériques. Compte tenu de la disparité des consommations pendant les différentes phases de vol, le même onduleur peut servir à alimenter plusieurs charges. La connexion entre les onduleurs et les charges est gérée par une matrice de contacteurs. Cette solution innovante considère également des cas de redondance pour augmenter la robustesse de la solution.

La conception de ce nouveau système est présentée dans ce rapport de thèse. Le compromis optimal entre le nombre d'onduleurs et la puissance nominale de chaque onduleur doit être obtenu. Ce choix déterminera fortement la taille de la matrice de contacteurs. Cependant, pour adresser cette problématique, il est nécessaire de connaître la masse des différents composants en fonction de la puissance requise.

Un environnement de conception est ainsi créé dans le but de réaliser le dimensionnement optimal de convertisseurs de puissance. Les différents composants sont décrits utilisant une approche « directe » et sont codés sous le formalisme « orienté-objet ». Ces modèles sont ensuite validés expérimentalement ou par simulation numérique. Les différents modèles sont couplés à un environnement d'optimisation et à un solveur fréquentiel qui permet une résolution rapide des formes d'ondes du régime permanent.

L'environnement d'optimisation réalise le dimensionnement précis des différentes parties de l'onduleur : dissipateur, module de puissance, filtre côté continu et inductance de couplage. Un onduleur est proposé pour différentes puissances nominales et fréquences de découpage. L'optimisation adresse également le choix des différentes technologies. Finalement, les résultats sont utilisés pour déterminer le meilleur compromis entre nombre d'onduleurs et puissance de l'onduleur à partir d'un algorithme heuristique.

Mots-clés

Avion plus électrique, Baie électronique, Conception automatique de convertisseurs, Optimisation, Conception d'éléments magnétiques, alimentations/convertisseurs mutualisés

Abstract

In recent years, aircraft manufacturers have been making progress in the design of more efficient aircrafts to reduce the environmental footprint. To attain this target, aircrafts manufactures work on the replacement of the hydraulic and bleed systems for electrical systems leading to a “More Electrical Aircraft”. However, the expected mass gain is a challenge, as previous technologies have been developed and optimized for decades. The new electrical solutions need to be look into detail to be competitive with previous technologies. All degrees of freedom must be considered, that is, new technologies and architectures. In particular, an HVDC network that reduces the number of rectifier stages seems a promising solution.

From the HVDC network, the different three phase AC loads will be supplied by a series of power generic inverters. As the power consumption of the different loads change during the flight mission, the same inverter is used to supply different loads. The connection between the inverters and the loads is managed by a matrix of contactors. The proposed solution also considers redundant configurations, thus increasing system robustness.

The design of the innovative system is presented in this document. That is, determining the optimal trade-off between the number of power inverters and the nominal power of each generic inverter that will also impact the size of the matrix of contactors. However, to assess the combinatory problem, the mass of the different components as a function of the nominal power needs to be calculated.

A design environment is therefore created to perform automatic and optimized design of power converters. The different components are described using a “direct modelling” approach and coded using “object-oriented” programming. The components are validated experimentally or by numerical simulations. The different models are coupled to an optimization environment and to a frequency solver allowing a fast calculation of the steady-state waveforms.

The optimization environment performs the precise design of the different parts of the power inverter: heatsink, power module, DC filter and coupling inductor. The power inverter is designed for different values of nominal power and switching frequency. The optimization assesses as well the usage of different technologies. Finally, the results are used to determine the optimal trade-off between the number of inverters and the nominal power of each inverter using a heuristic algorithm.

Key-words

More electric aircraft, Power electronics cabinet, Power electronics automatic design, Optimization, Power magnetics design, Shared power electronics

Acknowledgments

Ces travaux de thèse ont fait partie d'une convention CIFRE entre la société AIRBUS Operations SAS et le laboratoire LAPLACE à Toulouse.

Je tiens à remercier en premier lieu les différents membres du jury : Marc Budinger (examinateur), Laurent Gerbaud (rapporteur) et Philippe Viarouge (rapporteur). Merci d'avoir accepté de faire partie de mon jury de thèse. Merci également pour toutes vos remarques et suggestions, pertinentes et intéressantes. Le manque de temps ne nous a malheureusement pas permis d'approfondir tous les points mais j'espère dans le futur pouvoir rediscuter de ces sujets intéressants avec vous.

J'aimerais également remercier mes encadrants de thèse au sein du laboratoire. Je tiens à remercier à Thierry Meynard, pour m'avoir débloqué en quelques secondes sur des problèmes où j'ai pu passer des jours entiers à réfléchir et pour la recherche permanente de la perfection. Je tiens également à remercier Hubert Piquet, d'abord pour m'avoir proposé ce sujet thèse et ensuite pour tous tes conseils, tes informations, ta vision des choses et toutes les petites discussions qu'on a eu au long de la thèse, ce fut un réel plaisir.

D'AIRBUS je tiens à remercier dans l'ordre chronologique Jérome Mavier, Lucien Prisse et Jérôme Faucher. Mention spéciale pour ce dernier car tu as sacrifié une partie importante de ton temps quand ce n'était pas simple pour toi. Merci à tous de m'avoir apporté votre vision et votre expérience au cours de cette thèse.

Je remercie également les responsables du département systèmes électriques d'AIRBUS, Olivier Bouliou et Christophe Montret, pour m'avoir accueilli dans vos équipes. Merci également aux directeurs successifs du laboratoire LAPLACE, Christian Laurent et Thierry Lebey, pour m'avoir accueilli.

J'en profite aussi pour remercier tous mes collègues d'AIRBUS. D'abord, le responsable de l'équipe recherche systèmes électriques, Etienne Foch, pour m'avoir accueilli dans ton équipe ainsi que pour ton expertise de l'avion et ta croyance profonde en l'implantation de systèmes électriques à bord des aéronefs. Ensuite aux reste des collègues de mon équipe : Jean-François Allias, Gaëtan Bisson, Bernard Bonafos, Franck Chabot, Katell Delgado, Thierry Garcia, Hélies Guémar, Cedric Musotte, Olivier Rieux, Sebastien Vial ainsi qu'au reste des personnes du département. Merci pour la bonne ambiance et les bons moments. Mention spéciale à mon prédécesseur Xavier Giraud pour son accueil et ses explications ainsi qu'à Bernard Makhraz qui prend le relais dans le service et dans le bureau E523 du LAPLACE. Je tiens aussi à remercier Jeremy Bourdon qui a été mon collègue et qui a partagé les moments de joies, et de déprime pendant ces trois années, bonne chance pour la suite!

Au tours de mes collègues du laboratoire. Je vais commencer par remercier les différentes personnes qui sont passées par le bureau E523 : Xiao Zijian, Nicolas Videau, Thi Bang Doan, Xavier Bonnin, Julio Brandelero, Olivier Goualard, Anne Castelan, Clément Garreau, Alaa Hilal, Victor Dos Santos et Bouazza Taghia. Nous avons passé des très très bons moments

ensemble et même s'il y a eu beaucoup de départs et d'arrivées, la bonne ambiance a toujours régné. Merci pour toutes les blagues, croissants, « échanges culturels » et bons moments que nous avons passé ensemble.

A toutes les collègues doctorants du 5ème : Guillaume Delamare, Mame Andallah Diop, Mickael Faucher, Timothé Rossignol, Djamel Habdi, Houdhayfa Ounis, Andy Varais, Yan Ganthy, Najoua Erroui… pour les conversations (techniques ou pas) qu'on a pu avoir.

Enfin je remercie les autres personnes avec lesquels j'ai travaillé dans le laboratoire. Tout d'abord mon stagiaire Antoine El Hayek, tu trouveras une partie de tes travaux dans ce manuscrit. Ensuite Miguel Mannes Hillesheim et Leon Havez qui ont apporté leurs petites touches personnelles à mon travail. Ensuite je remercie les différents permanents. Tout d'abord Guillaume Fontes pour m'avoir introduit dans le fabuleux monde du GIT et MATLAB POO. Merci pour tes discussions, conseils, remarques et pour le temps que tu as dédié à ces travaux. Ensuite j'aimerais remercier Xavier Roboam, Bruno Sareni et Nicolas Roux avec lesquels j'ai pu avoir des discussions techniques qui ont contribué à ces travaux de thèse. Merci également aux différentes personnes des groupes CS et GENESYS ainsi qu'à leurs responsables, Fréderic Richardeau, Guillaume Gateau, Christophe Turpin, pour leur accueil et toutes les différentes réunions de groupe très intéressantes.

También me gustaría agradecer en estas líneas a todos mis amigos que vengan de Toulouse, Pamplona, Lodosa u otros lugares, por los momentos pasados y aquellos que quedan por venir.

Por ultimo me gustaría agradecerle también a familia que siempre ha estado a mi lado en los momentos buenos y no tan buenos incluso desde la distancia. Este trabajo también es parte vuestra, os quiero mucho.

Por supuesto los agradecimientos, no podrían acabar sin mencionar el mayor premio de esta tesis que fue conocer a Raquel. Muchas gracias por haber estado a mi lado y haberme dado fuerzas en estos últimos meses. Ahora me toca hacer lo mismo a mí en el futuro.

a mi familia

Resumé en français

Chapitre I – Contexte de l'avion plus électrique

Depuis des années, les avionneurs travaillent à la réduction de l'empreinte environnementale des avions. A cet effet, ils sont engagés sur l'axe du remplacement des systèmes hydrauliques (*hydraulicless*) et pneumatiques (*bleedless*) de l'avion par des systèmes électriques. Cette électrification permet de rationaliser les vecteurs de puissance pour les systèmes non propulsifs et apporte des avantages en termes de contrôle de puissance, maintenance, traçabilité et rendement.

Cependant, l'augmentation de la puissance électrique embarquée implique de revoir les solutions de distribution actuellement utilisées afin de réduire la masse au niveau avion. L'introduction d'un réseau de distribution à haute tension continue contribue à cet objectif, d'une part au niveau du câblage et d'autre part en supprimant les étages de redressement utilisés par une part significative des charges électriques sur les avions distribuant un réseau électrique de puissance alternatif.

Une étape d'intégration supplémentaire permettant de réduire la masse consiste à proposer des architectures avec mutualisation des convertisseurs alternatifs/continus (onduleurs de tension) alimentant les charges de forte puissance au moyen d'un ensemble d'onduleurs génériques. En effet, cette nouvelle architecture consiste à utiliser une baie électronique où se trouvent les onduleurs et une matrice de contacteurs qui gère les connexions entre les onduleurs et les charges. Cette solution s'avère plus avantageuse que la solution classique où un onduleur est dédié à chaque charge.

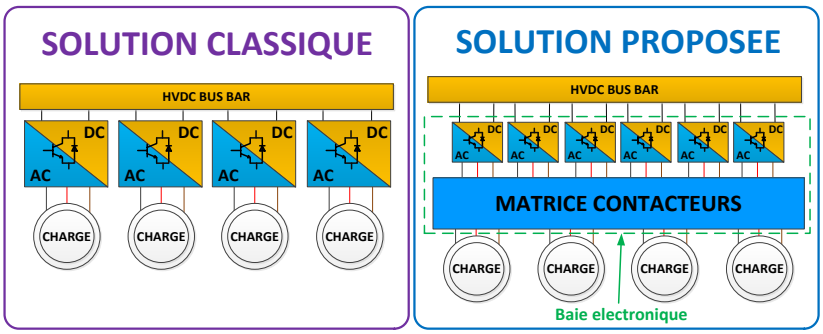


Figure I : Comparaison d'une architecture classique et l'architecture proposée

Les avantages de cette architecture sont :

- *Complémentarité des charges* : les consommations des différentes charges de l'avion varient selon les différentes phases de vol de l'avion et les conditions. Par conséquent, un module peut être utilisé pour alimenter des charges différentes pendant des phases de vol différentes.
- *Complémentarité des onduleurs* : De la même façon, des onduleurs peuvent être associés pour alimenter les charges de forte puissance. De ce fait, la puissance nominale des onduleurs peut être réduite.

- *Reconfiguration* : conséquence des deux premiers avantages, un onduleur peut être connecté à des charges différentes pour complémenter des demandes de puissance élevées.

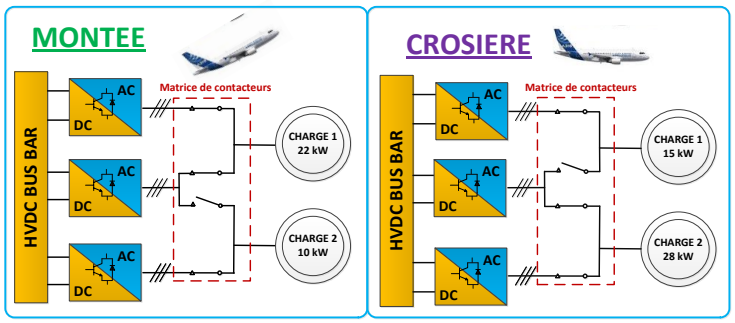


Figure II : Exemple de reconfiguration

- *Redondance* : quand un onduleur présente un disfonctionnement, les contacteurs peuvent être reconfigurés de façon à maintenir l'alimentation de la charge.

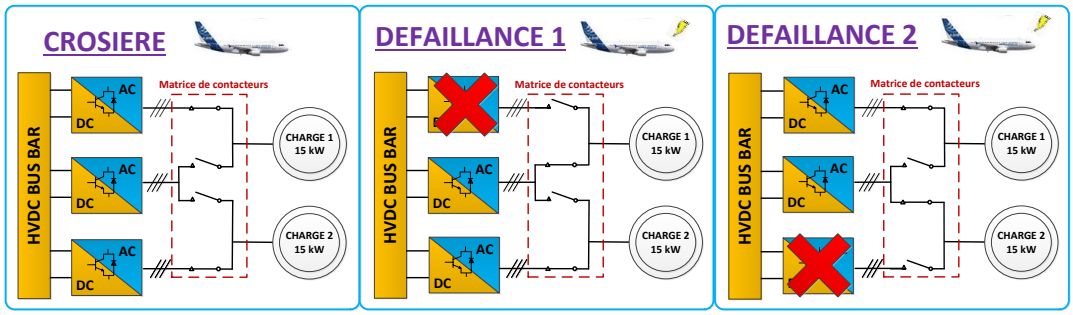


Figure III : Exemple de redondance

- *Coût* : les onduleurs sont génériques et standardisés, ce qui réduit le nombre de pièces différentes à concevoir, produire et stocker pour la maintenance des avions.

Six charges sont envisagées pour tirer profit du concept de mutualisation des onduleurs génériques :

- *deux compresseurs et une pompe du « Environmental Control System »* (ECS1, EC2 et ECS3) : ce système est chargé du conditionnement d'air pour assurer le confort des passagers dans la cabine. Les compresseurs sont en charge du contrôle de la pression et de la température des différentes zones pressurisées de l'avion,
- *une pompe du « Fuel Tank Inerting System »* (FTIS) : contrôle les niveaux d'oxygène des réservoirs de l'avion. Il s'agit de la seule charge de l'avion qui profite de ce concept et qui soit présente à bord en un seul exemplaire,
- *un transformateur AC* (TAC) : ensemble onduleur-transformateur, pour toutes les charges qui fonctionnent sous 115V/400Hz,
- *un moteur électrique pour assurer le démarrage des moteurs de l'avion* (STARTING).

L'utilisation du cœur électrique nécessite le dimensionnement des onduleurs et de la matrice de contacteurs. Deux sous-problèmes sont traités au cours de ce travail :

- Dimensionner les onduleurs pour répondre à divers cahiers des charges tout en satisfaisant les standards aéronautiques (chapitres II, III et IV)
- Déterminer le meilleur compromis entre le nombre d'onduleurs et leur puissance unitaire afin de minimiser la masse (chapitre V).

Chapitre II – Optimisation par association des composants

Lorsque la puissance nominale des onduleurs est une variable de dimensionnement de la baie électronique, la conception « classique » où l'ingénieur choisit les composants s'avère chronophage, compte tenu du nombre de cas à traiter. Un outil de « prototypage virtuel » semble la solution la plus pertinente pour résoudre ce problème. Les composants sont d'abord décrits mathématiquement et ensuite un algorithme d'optimisation prend en charge la conception. Utiliser des méthodes mathématiques permet non seulement de répondre au cahier des charges mais aussi de réduire la masse, l'encombrement, les pertes…

Les composants sont décrits par une approche dite « directe », c'est-à-dire qu'ils sont décrits par leur forme, leurs dimensions et les matériaux qui les constituent. A partir de ces données, certains paramètres (masse, volume,…) et les modèles équivalents de chaque composant (électrique, magnétique, thermique,…) sont extraits. Les avantages de cette approche sont :

- *L'unicité de la solution*. Les entrées décrivent un objet physique dont les paramètres sont connus et déterministes. Ce n'est pas le cas si par exemple, une inductance est initialement définie par sa valeur ; à partir de celle-ci, différentes géométries peuvent être considérée pour aboutir à la même valeur.
- *La précision* accrue sur le calcul de la masse et du volume, car toutes les définitions et paramètres physiques des composants sont bien connus.

Les modèles de simulation sont utilisés dans un logiciel de simulation afin de déterminer les formes d'ondes de chaque composant. Ces formes d'onde permettent d'estimer ainsi d'autres variables (pertes, températures) qui permettront de valider le dimensionnement des composants. Un solveur de type fréquentiel est utilisé dans le processus de conception : cette solution est particulièrement pertinente, car ce solveur permet de déterminer directement les formes d'ondes de régime permanent et donne donc un excellent compromis entre temps de calcul et précision. Ce type de simulateur s'avère aussi très intéressant pour le dimensionnement du filtre de mode commun ; en effet, les critères à satisfaire sont décrits par des gabarits fréquentiels auxquels peuvent être directement confrontés les résultats fournis par le solveur.

Une autre partie importante de l'outil de « prototypage virtuel » est constituée par l'algorithme d'optimisation. Des algorithmes de type gradient déjà intégrés dans MATLAB™ (*fmincon*) sont utilisés. Ces algorithmes sont caractérisés par une grande rapidité de convergence, mais la solution finale peut être très dépendante du point de départ et le risque de converger vers des minima locaux n'est pas négligeable.

La dernière étape du processus de conception consiste à valider la solution finale. Effectivement, il faut vérifier si les résultats du modèle analytique présentent une bonne corrélation avec le composant physique. Des logiciels de calcul par éléments finis (FEMM^{TM}, COMSOL^{TM}) sont utilisés pour valider la solution optimale. Dans le cas où les calculs analytiques s'éloignent des simulations numériques, le modèle analytique devra être révisé pour améliorer la précision dans ce point spécifique.

Le processus de dimensionnement est décrit dans la figure suivante :

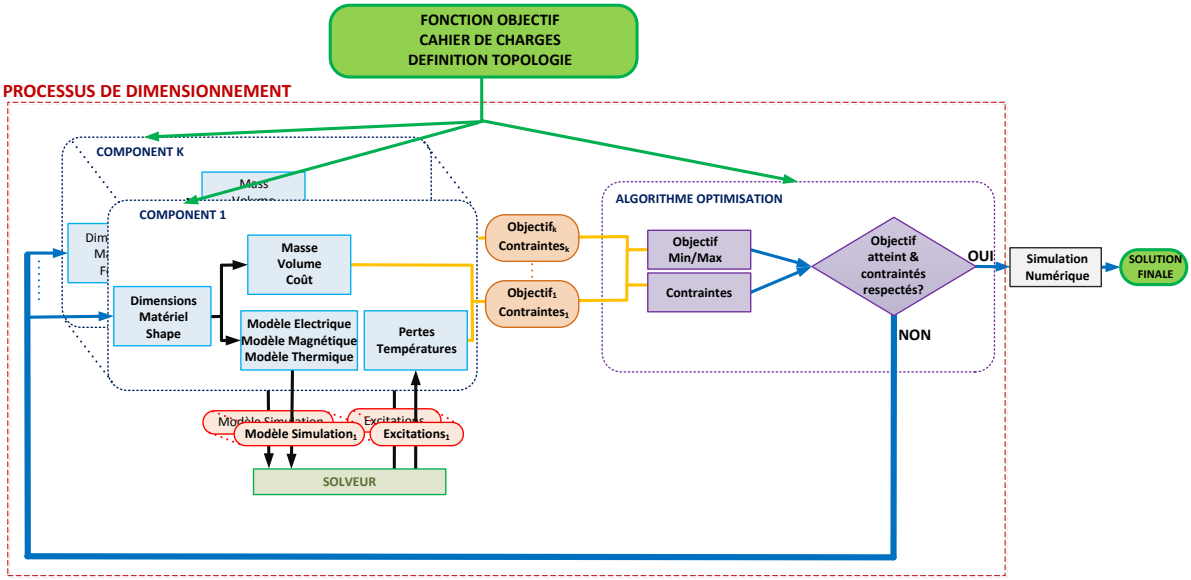


Figure IV : Description graphique du processus de dimensionnement

Chapitre III – Modélisation des composants physiques

Les différents composants qui servent à dimensionner les éléments d'un onduleur sont modélisés à partir de ces dimensions physiques. Ces éléments feront partie ensuite de l'outil de « conception automatisée » qui pourra traiter dans des travaux futurs des topologies de convertisseurs différentes. Les éléments sont classifiés selon les catégories suivantes :

- *composants actifs*,
- *composants passifs,*
- *éléments de refroidissement*,
- *éléments auxiliaires.*

Composants actifs

Le travail effectué sur les composants actifs concerne notamment le calcul des pertes dans les semi-conducteurs avec une attention particulière prêtée aux nouvelles technologies grand-gap (*SiC* et *GaN*). En effet, les composants basés sur ces technologies permettent d'une part une réduction des pertes par rapport aux composants élaborés à l'aide des technologies *Silicium (Si)* pour un même calibre en tension-courant et d'autre part un fonctionnement à des températures plus élevées. Ce gain sur les pertes pourrait être mis à profit pour choisir une

fréquence de découpage plus élevée (réduction de la taille d'éléments passifs) ou pour utiliser des solutions de refroidissement moins sophistiquées (convection forcée à air).

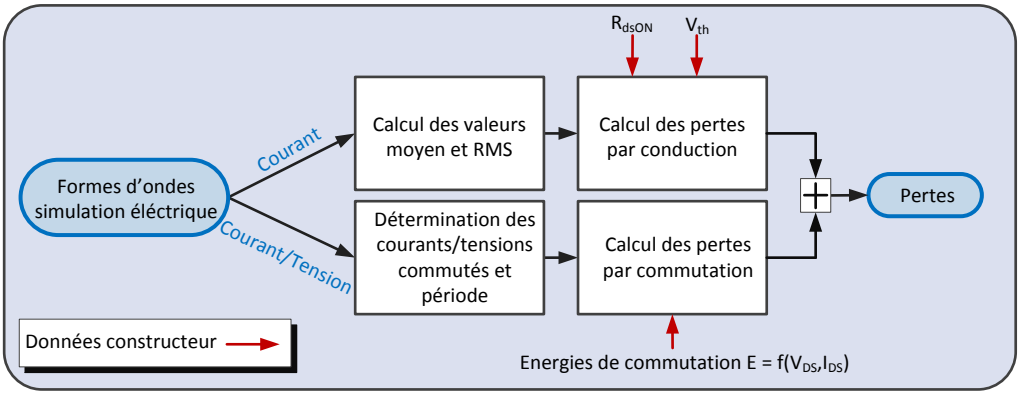


Figure V : Algorithme pour le calcul des pertes dans les semi-conducteurs

Le diagramme de calcul des pertes est présenté dans la Figure V. A partir d'une simulation électrique, les différentes formes d'ondes courant/tension que chaque semi-conducteur subit sont extraites. Avec les valeurs moyennes et RMS du courant et les données constructeurs pour les semi-conducteurs (R_{dsON}, V_{th}) nous calculons les pertes par conduction. Ensuite, à chaque commutation, nous calculons les tensions et courant commutés qui nous serviront à calculer les énergies à chaque commutation. Dans ces travaux, les énergies sont directement tirées des données fournies par les constructeurs et une interpolation est réalisée en fonction des grandeurs commutées. On fait donc implicitement l'hypothèse qu'on utilisera le même driver que dans la base de données. La somme de toutes ces énergies est divisée par la période pour calculer les pertes par commutation et les pertes totales permettent de dimensionner le système de refroidissement.

Composants passifs

Deux types des composants passifs sont modélisés dans ces travaux : les condensateurs et les composants magnétiques.

Les condensateurs, compte tenu de la difficulté de modélisation de tous les phénomènes physiques à partir des dimensions physiques, sont modélisés à partir des données constructeur. Différentes lois d'échelle sont dérivées des *datasheets* pour estimer la variation des propriétés importantes pour le dimensionnement du condensateur. La définition et la validation de ce modèle ont été réalisées dans le cadre d'autres travaux de thèse du laboratoire [75].

Les composants magnétiques représentent usuellement une partie relativement importante du poids global du convertisseur et leur optimisation est un point clé pour réduire la taille des convertisseurs. Les limites qui s'opposent à cette réduction du poids correspondent dans la plupart des cas, soit à des contraintes magnétiques, soit à des contraintes thermiques. Pour estimer les contraintes thermiques, les différents types de pertes doivent être calculés : les pertes fer et les pertes cuivre.

Pour estimer les pertes fer, les fabricants de matériaux donnent normalement la densité de pertes fer pour différents niveaux de champ magnétique, température et fréquence. Ces données sont souvent approximées par des formules comme la formule de Steinmetz [48] , qui n'est cependant valable que pour des excitations sinusoïdales. La méthode « Improved Generalized Steinmetz Equation » (iGSE) permet d'adapter ces formules à n'importe quelle forme d'onde en utilisant les mêmes coefficients de pertes [50]. Cependant, les coefficients de la formule de Steinmetz s'avèrent insuffisants pour avoir une haute précision dans un large domaine de fréquence et d'amplitude du champ. La formulation du modèle de Forest permet d'élargir le domaine de validité du modèle de Steinmetz et peut être combiné à l'iGSE pour donner le modèle de « Forest-Sullivan » qui permet de résoudre ces problèmes.

L'estimation des pertes cuivre dépend du courant traversant le conducteur et de la résistance électrique. Cette résistance dépend du matériau, de la longueur et de la section du conducteur et de la fréquence du courant. En effet, les différents courants créent des champs magnétiques qui génèrent des courants de Foucault à l'intérieur des conducteurs. La somme de ces courants de Foucault peut être vue comme une diminution effective de la section où circule le courant et donc une augmentation de la résistance et des pertes. Ce phénomène physique s'appelle « effet de peau » ou « effet de proximité » selon que le champ magnétique est généré par le conducteur lui-même ou les conducteurs voisins. Différentes formules [56] servent à estimer les pertes en tenant en compte de ces phénomènes mais elles sont souvent basées sur des hypothèses (facteurs de forme…) et s'avèrent donc peu intéressantes pour l'optimisation.

Une méthode basée sur l'utilisation d'une surface de réponse créée à partir des points issus des simulations numériques est proposée dans ces travaux. En utilisant l'interpolation linéaire sur différents points issus des simulations FEMM^{TM} une estimation plus pertinente des pertes cuivre est réalisée. Cette méthode est certes un peu lourde à mettre en place compte tenu du grand nombre des points à analyser, mais une fois les simulations effectuées, elle conduit à une implémentation rapide très bien adaptée à l'optimisation. La figure suivante montre la comparaison entre une formule classiquement utilisée (formule de Dowell) et le calcul à partir de la méthode basée sur la surface de réponse.

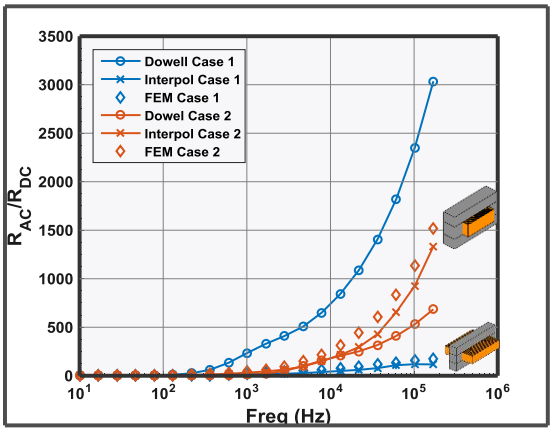


Figure VI : Comparaison entre la formule de Dowell, la méthode d'interpolation et les résultats issus d'une simulation numérique

Les résultats montrent une amélioration significative de la précision du modèle basé sur la surface de réponse, par rapport à des formules classiques.

Comme précédemment présenté au chapitre II, la simulation du couplage électromagnétique est aussi un point indispensable pour dimensionner les composants. Des approches classiques proposent la discrétisation du noyau en éléments caractérisés par leur « reluctances » qui sont décrites en simulation sous la forme de résistances. Cette approche nécessite un élément intégrateur ou dérivateur pour réaliser le couplage qui complexifie la simulation. Pour solutionner ce problème, d'autres approches proposent la substitution de ces résistances par des capacités aussi appelées « permeances ». La formulation utilisée dans ces travaux, utilise quant à elle des inductances et non des capacités. Cette approche simplifie l'élément de couplage électro-magnétique (transformateur à la place d'un gyrateur) et aide à la description des circuits magnétiques complexes et multiphasés (comme les inductances couplées).

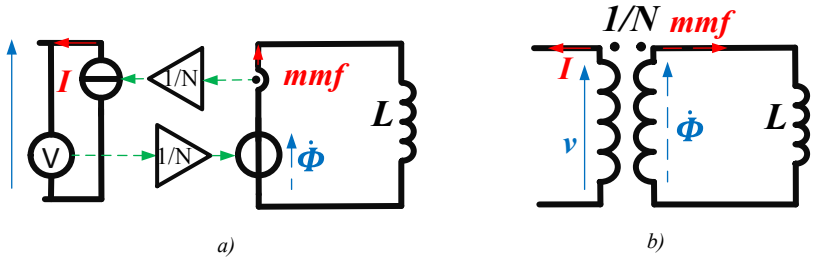


Figure VII : Description schématique du modèle à permeances - inductances

Une fois les excitations (courants, champs) et les pertes calculées, nous sommes en mesure d'estimer la température du composant. Les composants magnétiques sont discrétisés en différents nœuds où la température est calculée et un réseau de résistances est ainsi développé. Les différents mécanismes de transfert de chaleur (*conduction, convection, radiation*) sont pris en compte. Le calcul du coefficient de transfert convectif est basé sur des formules analytiques issues de la littérature et prend en compte la température de l'air qui entoure l'objet considéré. La détermination des températures aux différents nœuds du circuit thermique équivalent est réalisée à partir de la résolution d'un système matriciel d'équations.

$$[A][T]=[Q] \tag{1-1}$$

Où A est la matrice exprimant les différentes résistances thermiques, T est le vecteur de températures et Q le vecteur de sources de chaleur. Comme les résistances thermiques de la radiation et la convection dépendent de la température des différentes surfaces, plusieurs itérations sont réalisées pour déterminer la température finale des éléments magnétiques.

L'algorithme de résolution est présenté à la figure suivante :

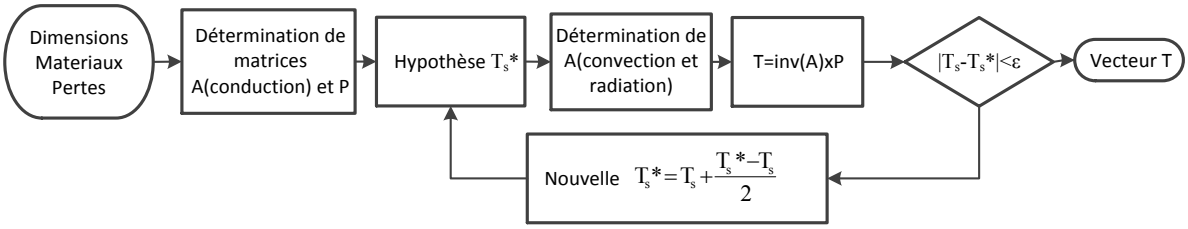


Figure VIII : Description de l'algorithme pour l'estimation des températures de surface (T_s)

Les différents modèles thermiques sont comparés avec des simulations numériques sous COMSOL^{TM} et montrent une bonne corrélation. Par exemple, pour le modèle thermique, les calculs analytiques sont comparés avec des simulations par éléments finis pour 4 cas différents.

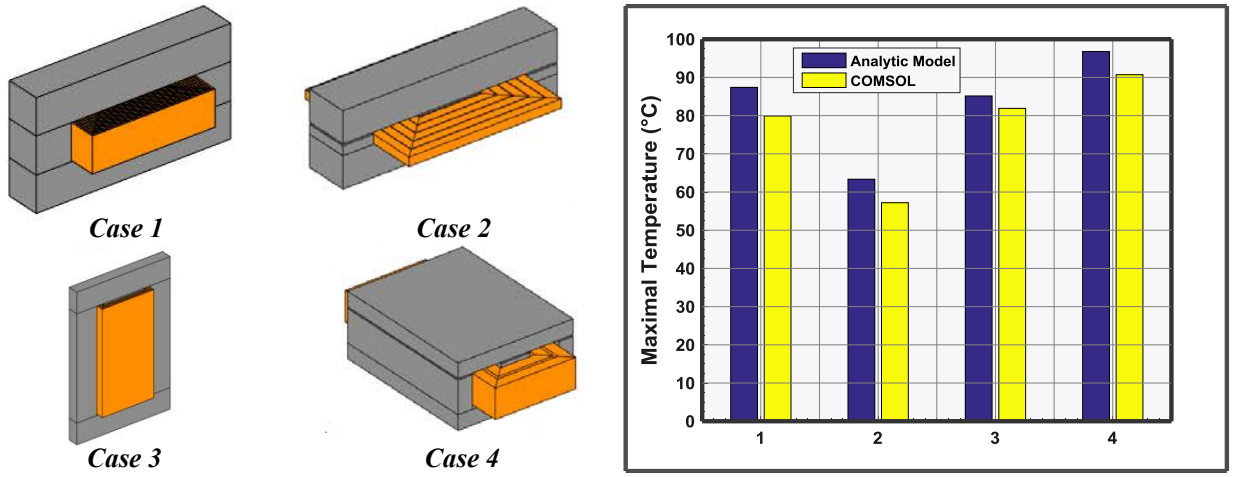


Figure IX : Comparaison entre les températures du modèle analytique et les simulations COMSOL pour 4 formes d'inductances différentes

Les inductances couplées sont aussi modélisées. Ces inductances sont caractérisées par l'utilisation d'un noyau magnétique commun à différents enroulements, parcourus par des courants différents. Les interactions entre phases de l'inductance couplée provoquent un comportement différent selon le sens des courants. De ce fait, dans le cas de coupleurs associés à des cellules connectées en parallèle, l'inductance vue par le courant de charge est inférieure à l'inductance vue par le courant circulant entre les cellules. La taille du noyau peut être réduite grâce à la réduction du champ magnétique dans le noyau. Cependant, ce comportement est seulement valable si toutes les phases de l'inductance sont utilisées ; sinon, le noyau de l'inductance est saturé (des entrefers doivent être ajoutés dans ces cas).

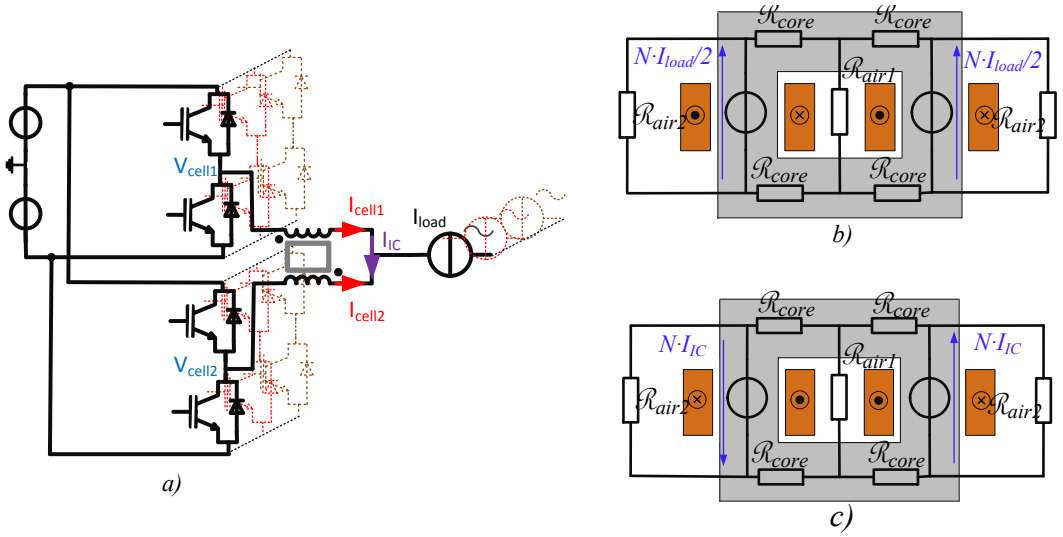


Figure X :a) Mise en place d'une inductance couplée entre deux bras d'onduleurs, b) Schéma équivalent à réluctances pour le courant de la charge et c) Schéma équivalent à réluctances pour le courant entre les bras.

Eléments de refroidissement

Les semi-conducteurs produisent des pertes dont une caractéristique est une densité surfacique élevée. Différents technologies (plaque froide, caloducs…) sont disponibles pour aider à l'évacuation de ces pertes dans les convertisseurs. Les avionneurs visent à utiliser des technologies de refroidissement basées sur l'utilisation de l'air pour se débarrasser de tous les systèmes hydrauliques de l'avion, y-compris le refroidissement liquide. Ce choix technologique est rendu possible grâce à la réduction de pertes obtenue par l'utilisation des composants grand-gap.

Dans ces travaux, un dissipateur à ailettes avec une évacuation de la chaleur par un flux d'air forcé en régime laminaire est décrit. Ce modèle est basé sur d'autres travaux [78][80] et a été validé expérimentalement au sein du laboratoire LAPLACE [79]. Les pertes de charge du dissipateur doivent être modélisées également pour dimensionner le système de refroidissement global (ventilateur, tuyauteries…). Afin de tenir compte de l'effet de propagation thermique quand la surface du dissipateur et du module sont différentes, une résistance de *spreading* est aussi calculée.

Eléments auxiliaires

Le câble (*feeder*) utilisé pour alimenter les différentes charges électriques doit être également modélisé. En effet, cet élément contribue à l'impédance de mode commun de la charge et va donc impacter le dimensionnement du filtre de mode commun. Pour tenir compte des phénomènes de propagation dans le câble, le modèle est discrétisé en différentes sous-parties. Des simulations par éléments finis sont réalisées afin de déterminer les différents paramètres (R,L,C) caractéristiques de chaque section.

Les contacteurs sont également des éléments très importants dans le dimensionnement de la baie électronique. Des contacteurs électromécaniques sont envisagés pour la matrice de

contacteurs qui gère les connections entre les charges et les modules. Pour estimer la masse de ces éléments, une surface de réponse a été créée à partir de données relatives à des contacteurs électromécaniques aéronautiques.

Les différents éléments qui vont servir à l'installation et à la protection mécanique des composants ne sont pas modélisés, ni optimisés dans les routines. Cependant, la masse de ces différents éléments est considérée en utilisant des facteurs d'installation basés sur des convertisseurs existants dans les avions actuels.

Chapitre IV – Dimensionnement de l'onduleur et cahier des charges

Dans ce chapitre, les différents éléments de l'onduleur générique sont dimensionnés en utilisant l'environnement d'optimisation. Le cahier des charges peut se décomposer selon la nature des contraintes associées. Trois types de spécifications sont identifiés lors de ces travaux : Fonctionnelles, Electriques et Thermiques

Spécifications fonctionnelles

Les onduleurs doivent non seulement être en capacité de transmettre aux charges alimentées la puissance requise pendant la phase de vol mais ils doivent aussi assurer le contrôle du point de fonctionnement dans le plan couple-vitesse. Trois types différents de charges sont identifiés selon leur caractéristique couple-vitesse : *quadratique*, *couple constant* et *tension constante*. La figure suivante présente selon le cas, l'allure des caractéristiques liant la puissance aux points de fonctionnement couple-vitesse ou courant-tension.

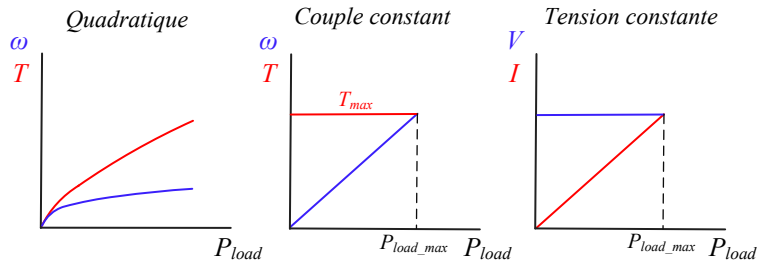


Figure XI : Caractéristiques des différents types de charge selon ses points de fonctionnement couple (rouge)-vitesse (bleu) ou courant (rouge)-tension (bleu)

La machine électrique qui constitue la charge de l'onduleur est simulée par un modèle R-L-E avec un point neutre flottant. De ce fait, différentes techniques d'injection du troisième harmonique peuvent être envisagées afin de réduire le niveau de courant et les pertes. Dans ces travaux, l'injection d'harmonique sinus d'ordre 3 est réalisée. Pour la détermination de la modulante nécessaire pour atteindre le point de fonctionnement (courant/tension), un passage du repère fixe triphasé *abc* dans le repère tournant *dq* est réalisé.

Spécifications électriques

Les équipements de conversion de puissance sont des sources de perturbations qui peuvent endommager d'autres équipements ou interférer dans leur fonctionnement. Afin d'éviter ce type de situations, les avionneurs imposent des standards aux équipementiers pour s'assurer du bon fonctionnement de l'ensemble du réseau et des appareils qui lui sont connectés. Deux standards impactent notamment le dimensionnement des solutions de filtrage pour les onduleurs dans ces travaux: les exigences Airbus pour les réseaux HVDC et le standard DO-160, à travers leur description des exigences concernant la qualité des grandeurs électriques. Ces spécifications prennent en compte la stabilité. Certaines charges ont en effet un comportement de charge à « puissance constante » (CPL), ce qui leur confère en dynamique un comportement d'impédance négative. Ce type de charge, associée au filtre qui permet de maîtriser la qualité de la tension qui l'alimente et du courant qu'elle prélève, peut constituer un ensemble instable. Dans ces travaux, seul le filtre du côté bus DC est considéré. La topologie du filtre retenue est présentée à la figure suivante :

Pour prendre en compte la contrainte concernant l'impédance totale d'entrée et le critère de stabilité, la fonction de transfert de l'admittance d'entrée équivalente de l'ensemble connecté au filtre (c'est-à-dire l'onduleur et la charge qu'il alimente) est indispensable. Dans cette perspective, l'admittance équivalente d'un onduleur connecté à une machine synchrone à aimants est déterminée autour d'un point de fonctionnement [19]. Ce calcul nécessite la prise en compte des boucles de régulation en courant et en vitesse. Sur cette base, les filtres sont pris en compte à travers une représentation quadripolaire.

Comme le courant nominal de l'onduleur n'est pas figé une surface de réponse est générée pour obtenir la masse des onduleurs à partir du courant nominal et la fréquence de découpage des onduleurs. Effectivement la fréquence de découpage des onduleurs est une variable de sensibilité de la surface étant donné qu'elle n'a pas encore été définie. De plus, le fait de fixer la fréquence pour chaque dimensionnement nous permet de découpler le problème en plusieurs sous-problèmes en prenant quelques hypothèses. Par exemple, le dimensionnement du dissipateur peut être dissocié du calcul du filtre en considérant que les variations de la tension DC sont faibles.

Le problème d'optimisation du filtre est résolu avec la fonction *fmincon* de MATLAB™ qui utilise une méthode de type gradient et une fonction de pénalité. Cependant cette approche s'avère parfois insuffisamment robuste pour optimiser dans de larges plages de variation des courants nominaux et des fréquences de commutation de l'onduleur. Les résultats finaux de la masse du filtre du côté continu en fonction du courant nominal de l'onduleur et de la fréquence de commutation sont présentés dans la figure suivante.

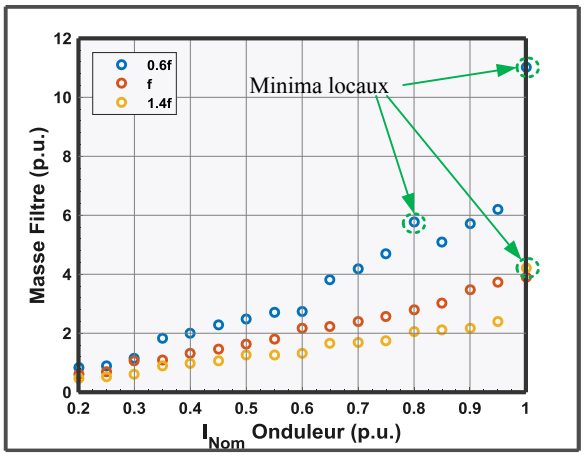


Figure XIII : Résultats pour la masse du filtre DC

Avec cette approche, certains résultats correspondent à des minima locaux (3 cas dans la figure) : ces résultats sont éliminés et sont approximés par interpolation/extrapolation linéaire à partir des résultats voisins, pour le design de la baie électronique. Cependant, si ces solutions s'avèrent effectivement être optimales, une reconsidération des résultats devra être réalisée. Une perspective de ces travaux est alors l'utilisation d'autres méthodes d'optimisation pour éviter le problème des minimaux locaux qui ensuite intégreront la plateforme d'optimisation.

Spécifications thermiques

Les différents composants doivent fonctionner dans un environnement à une température assez élevée compte tenu des différentes phases de vol de l'avion (altitude, pression, température). Deux types de solutions de refroidissement semblent pertinents: refroidissement liquide ou refroidissement par air. Ce choix adresse notamment le refroidissement des semi-conducteurs compte tenu de la haute densité des pertes surfaciques. Dans notre cas d'étude ces composants sont refroidis à l'aide de dissipateurs à ailettes dans lesquels l'air circule en convection forcée afin d'éviter d'intégrer une boucle de refroidissement liquide supplémentaire dans l'avion. Dans l'architecture de refroidissement envisagée, cet air est recyclé à partir de l'air de la cabine des passagers. Celui-ci provient du système ECS (Environmental Control System) qui compresse l'air provenant de l'extérieur de l'avion. De ce fait, l'air qui arrive pour refroidir les onduleurs dépend de l'altitude et des conditions extérieurs de l'avion mais reste à la fois assez stable pour assurer le confort de passagers. Des contraintes liées aux pertes de charge dans la baie et de contraintes soniques doivent être également prises en compte.

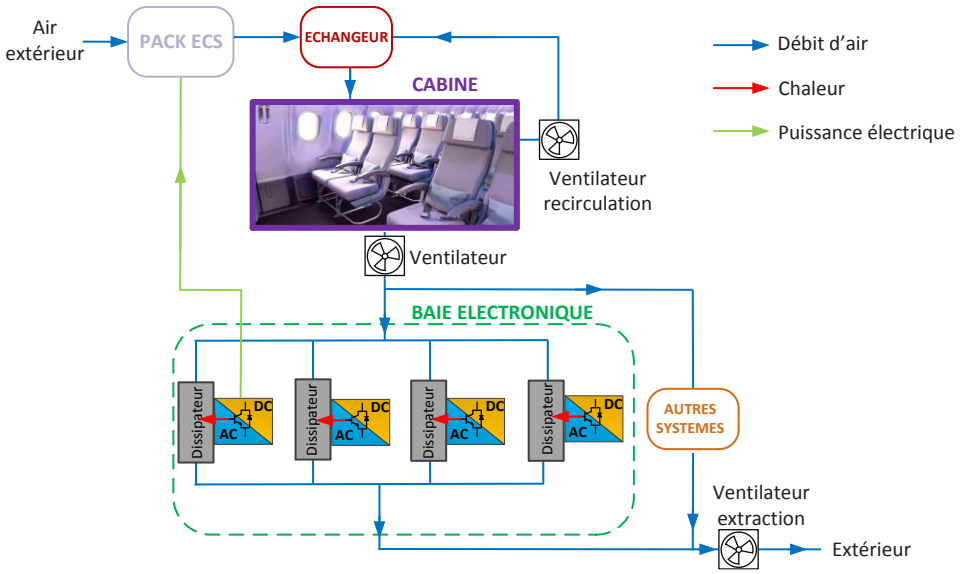


Figure XIV : Schéma du système de refroidissement des onduleurs

L'architecture de référence considère la mise en parallèle de vannes de refroidissement des onduleurs et par conséquent, le débit est équitablement réparti même s'ils ne sont pas utilisés. Les solutions avec des onduleurs à puissances nominales supérieures auront donc normalement plus de débit par onduleur mais à la fois plus des pertes. Dans nos travaux, les variables qui impactent le dimensionnement des ventilateurs sortent du périmètre d'étude de la baie électronique. Par conséquent, l'objectif pour le dimensionnement du dissipateur est de minimiser le débit d'air rentrant dans la baie.

Le dissipateur de chaque onduleur est dimensionné pour différents puissances nominales (0.2 p.u-1.p.u) et fréquences de découpage (*0.6f, f, 1.4f*). La somme de tous les modules des puissances plus dissipateurs dans la baie électronique est donnée dans la figure suivante:

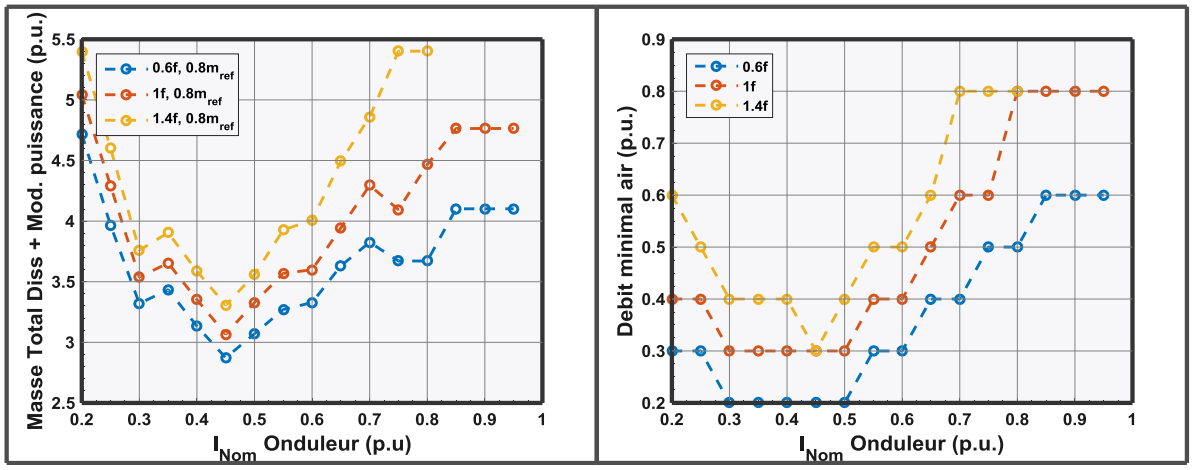


Figure XV : Masse totale de la baie correspondant aux modules de puissance+dissipateur (gauche) et débit minimal d'air nécessaire totale dans la baie (droite)

Dans la figure de gauche, on peut constater qu'il existe effectivement un meilleur compromis entre nombre d'onduleurs et le courant nominal de chaque onduleur. L'optimum se trouve à un courant nominal de 0.45 p.u. Les résultats montrent également qu'avec les conditions de refroidissement utilisées, les solutions avec de forts courants nominaux ne sont pas réalisables.

Ensuite, la figure de droite donne le débit minimal d'air total nécessaire en fonction de la puissance nominale des onduleurs. Les solutions avec des puissances nominales entre 0.3-0.55 p.u. montrent un besoin inférieur en termes de débit d'air total. Cela signifie que ces solutions auront besoin d'un système de refroidissement plus petit.

Elément de couplage

Pour limiter les effets des courts-circuits entre bras mises en parallèle et donc les courants générés, des inductances sont insérées à la sortie de chaque cellule. En effet, quand deux bras sont mis en parallèle pour alimenter la même phase de la machine, ils sont commandés aux mêmes instants et par conséquent la tension en sortie de chaque bras est idéalement la même. Cependant, les dispersions de valeurs au niveau du temps de propagation des composants de la boucle de commande et du temps de commutation des interrupteurs peuvent provoquer des court-circuits entre les bras homologues de deux onduleurs connectés en parallèle sur la même charge.

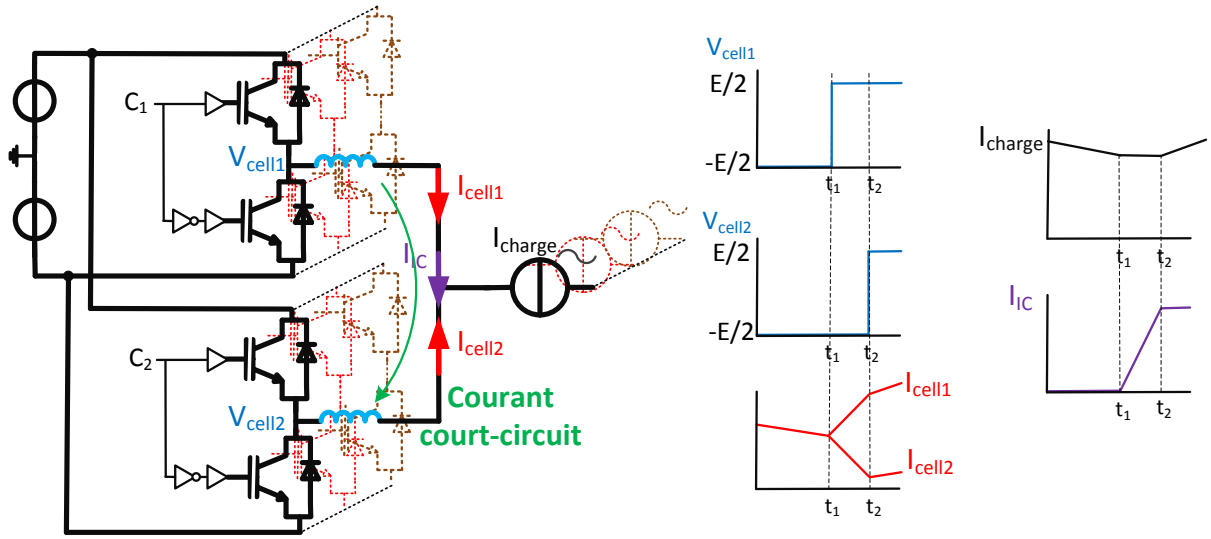


Figure XVI : Mise en parallèle des bras d'onduleurs : (gauche) architecture avec insertion d'inductances de couplage et (droite) chronogrammes des différentes variables

Les court-circuits éventuels vont avoir deux conséquences importantes dans le dimensionnement des onduleurs :

- *Augmentation des pertes* : l'augmentation de l'ondulation de courant de sortie de chaque bras provoquée par ces court-circuits augmente les pertes dans les semi-conducteurs et les éléments de couplage entre les bras.

- *Impact sur la régulation* : les ondulations des courants sont mesurées par les capteurs de courant en sortie de bras et donc sont transmises dans la boucle de régulation des onduleurs, pouvant ainsi perturber leur fonctionnement.

Les inductances sont dimensionnées pour limiter l'ondulation de ces courants de court-circuits à 10% du courant nominale de l'onduleur. Le dimensionnement doit également déterminer la meilleure solution de refroidissement : un refroidissement en convection forcée et un refroidissement en convection naturelle sont comparés. Ces deux calculs sont optimisés avec deux types de modèles: un modèle utilisant des lois de similitudes et un modèle où toutes les dimensions de l'inductance sont libres. L'algorithme d'optimisation utilisé est là encore *fmincon*; pour choisir le point de départ une fonction basée sur l'utilisation du critère du produit des aires est utilisée.

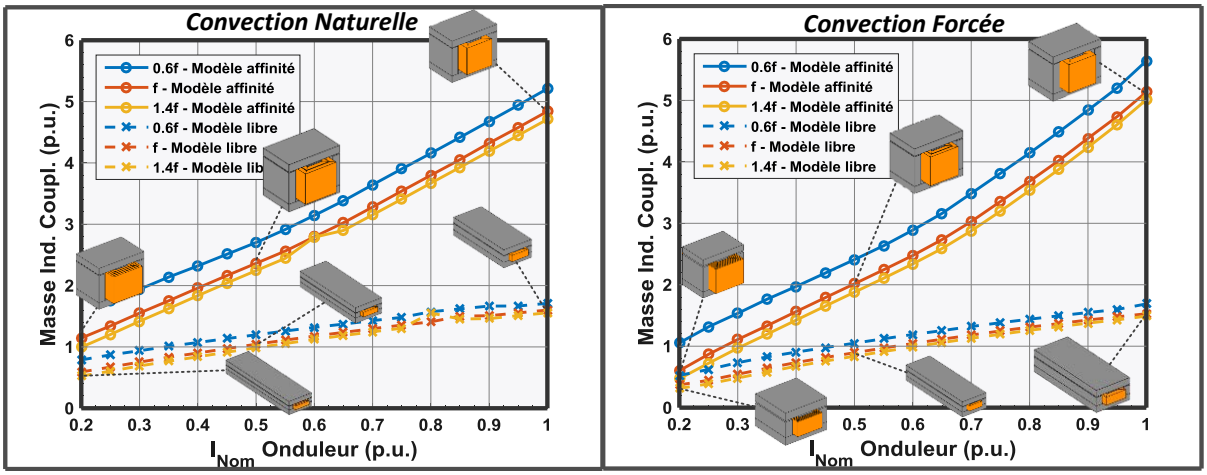


Figure XVII : Masse d'un groupe de 3 inductances de couplage en sortie d'un onduleur pour un refroidissement en a)Convection naturelle et b) Convection forcée

Les résultats montrent clairement que la thermique est un élément fortement déterminant de la masse totale des inductances. En modifiant le facteur de forme de l'inductance et donc ses performances thermiques, la masse de l'inductance peut être réduite d'un rapport 3. Pour le type de refroidissement (convection forcée ou convection naturelle), la convection forcée n'apporte pas un gain de masse significatif et compte tenu de sa complexité (systèmes auxiliaires), elle n'est pas retenue pour la suite.

Chapitre V – Dimensionnement de la baie électronique

Les masses des onduleurs, des inductances de couplage et des contacteurs en fonction de la puissance nominale de l'onduleur ont été calculées dans la partie précédente pour différentes fréquences de découpage. Le concepteur est maintenant en mesure de déterminer le meilleur compromis entre nombre de modules et puissance nominale des modules. Dans les travaux précédant réalisés au sein d'Airbus, un algorithme de type heuristique a déjà été utilisé pour concevoir la baie électronique [4]. Ces travaux ont été intégrés dans notre environnement de conception. L'algorithme qui résume le processus de conception est présenté dans la figure suivante.

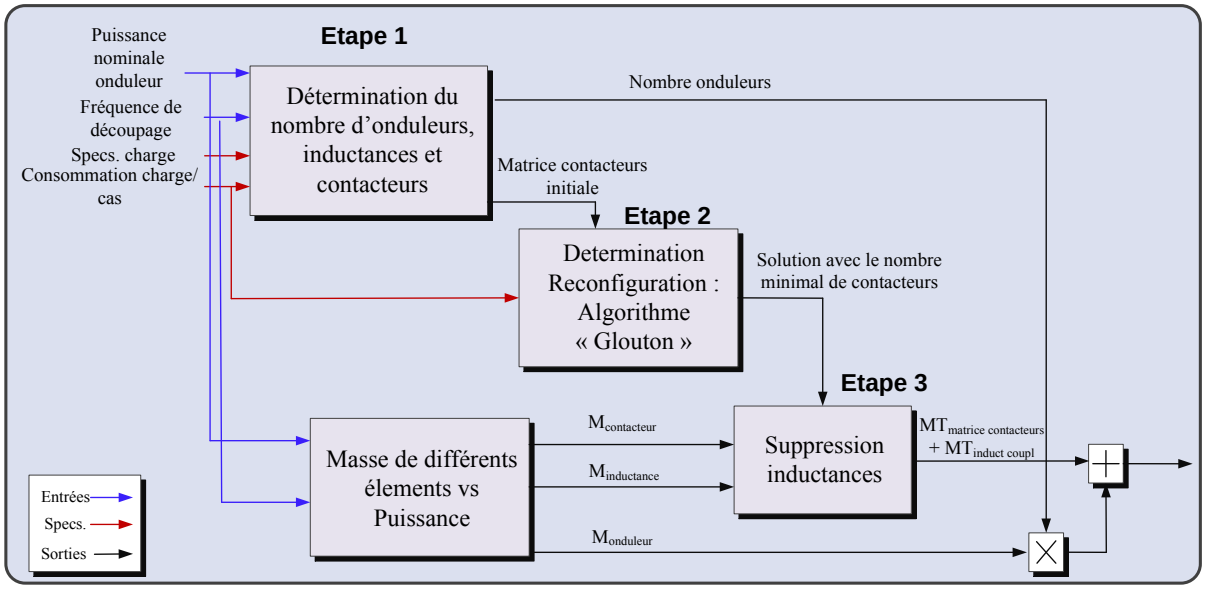


Figure XVIII : Algorithme de conception de la baie électronique

L'algorithme est divisé en trois étapes de conception

- *Première étape* : à partir des données concernant les charges et les consommations sur les différentes phases de vol, le nombre nécessaire d'onduleurs est déterminé. Le nombre minimal théorique d'inductances de couplage, de contacteurs ainsi qu'une matrice minimale de contacteurs sont définis.

- *Deuxième étape* : pour chaque phase de vol et à partir de la matrice minimale de contacteurs, les connexions entre onduleurs et charges sont déterminées. Des inductances sont placées aux endroits où elles s'avèrent indispensables. La solution se construit donc de façon itérative : une fois les connexions déterminées et les inductances insérées pour un cas de charge, cette solution n'est plus remise en question pour l'analyse des cas suivants. Le choix parmi les solutions de reconfiguration est déterminé en fonction de la nécessité de procéder à l'addition d'inductances par rapport à l'architecture de référence. A l'issue de ce processus d'optimisation, la solution comporte un nombre minimal de contacteurs; cependant le nombre d'inductances de couplage n'est pas nécessairement minimal.

- *Troisième étape* : cette étape consiste à essayer de supprimer certaines inductances de couplage. La suppression d'inductances entraîne alors l'insertion de contacteurs additionnels. C'est la comparaison des masses finales de chaque solution qui déterminera l'architecture choisie. La solution retenue in fine n'est pas obligatoirement minimale vis-à-vis du nombre de contacteurs ou d'inductances mais elle est optimale par rapport à l'ensemble des solutions évaluées et satisfaisante par rapport à un cahier des charges donné.

Les solutions obtenues en utilisant cet algorithme heuristique et les résultats concernant la masse des différents éléments sont présentés dans la figure suivante :

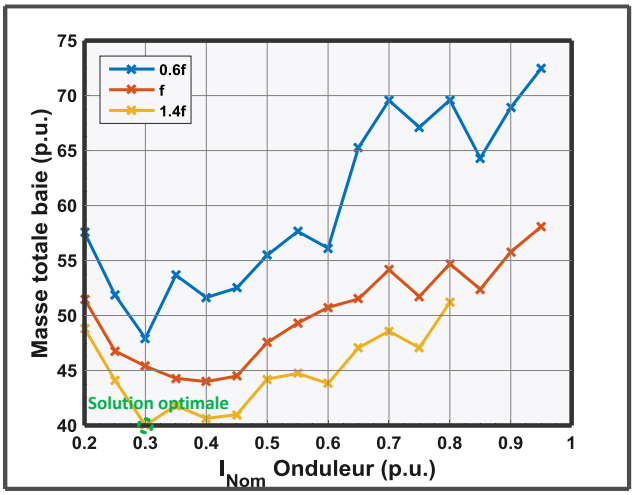


Figure XIX : Masse de la baie électronique en fonction du courant nominal des onduleurs pour différentes fréquences de découpages 0.6f, 1f et 1.4f

Les résultats montrent clairement l'intérêt de l'utilisation d'une fréquence de découpage élevée et du choix d'un courant nominal de 0.3 p.u. L'utilisation de fréquences de découpage plus élevées devrait être étudiée par la suite, bien que nous risquions alors d'être limités par les contraintes thermiques.

Pour la solution optimale, les caractéristiques des éléments magnétiques (obtenus par des expressions analytiques au cours du processus de conception) sont validées par des simulations par éléments finis. La comparaison entre les deux jeux de valeurs est présentée dans le tableau suivant (pour les inductances des filtres voir Figure XII).

	Pertes Joule			*Temperature*		
Inductance	*Analytique(W)*	*Simulation numérique (W)*	*Erreur rel. (%)*	*Analytique (°C)*	*Simulation numérique (°C)*	*Erreur rel. (%)*
Inductance Filtre DM_1	2.5626	2.5618	0.034	100.97	98.5	2.5
Inductance Filtre CM_1	2.015	2.043	-1.39	82.175	83.8	-1.94
Inductance Filtre DM_2	1.5679	1.5728	-0.314	114.26	114	0.23
Inductance couplage sortie	9.31	8.05	15.63	125	120	4.167

Tableau I : Comparaison entre les résultats des modèles analytiques et les simulations numériques

Les résultats montrent une bonne corrélation entre les calculs analytiques et les simulations (erreur inférieure à 15%). Des simulations sont aussi réalisées pour vérifier l'adéquation du filtre par rapport aux standards aéronautiques.

Conclusion et perspectives

Dans le contexte de l'avion « plus éléctrique » et donc de la réduction de la masse des systèmes électriques, une solution utilisant une baie électronique intégrant un ensemble d'onduleurs génériques associés à une matrice de contacteurs pour alimenter différentes charges électriques de l'avion a été envisagée. Cette solution s'avère avantageuse d'un point de vue masse, coût et redondance. Le dimensionnement de cette baie électronique a été étudié dans ce document.

Pour dimensionner l'onduleur générique, un environnement de « conception automatique » est développé dans ces travaux. Les différents modèles des composants sont décrits au moyen d'une « modélisation directe » et insérés dans une boucle d'optimisation. Les formes d'onde des grandeurs électriques que subit chaque composant sont calculées à l'aide d'un solveur fréquentiel ; cette solution de simulation offre un bon compromis entre précision et temps de calcul.

Le chapitre 3 présente les différents modèles de composants utilisés dans ces travaux (éléments magnétiques, dissipateurs…). Des validations ont été réalisées pour estimer la pertinence des modèles. Ces modèles sont utilisés dans le chapitre 4 pour dimensionner les différentes parties de l'onduleur (filtre en entrée, dissipateur et inductance de couplage).

Dans le chapitre 5 les résultats concernant le dimensionnement de l'onduleur sont utilisés au sein d'un algorithme heuristique pour déterminer la masse optimale totale de la baie électronique.

Au niveau des perspectives, certaines hypothèses et validations concernant les modèles devront être améliorés dans des travaux futurs. Toutefois, les travaux présentés ici ont construit les bases d'un environnement de conception optimale qui pourra être exploité dans différents problèmes de conception dans le domaine de l'électronique de puissance - les opportunités d'évolution et d'exploitation de ce nouvel outil sont donc infinies.

Contents

Resumé V
Abstract VII
Acknowledgments IX
Resumé en français XIII
Contents XXXIII
List of Figures XXXVII
List of Tables XLIII

General Introduction 1

Chapter 1 : More Electrical Aircraft context 3

1.1 Introduction 3
1.2 Energy vectors on aircraft 3
1.3 Increment of aircraft efficiency, towards a more electrical aircraft 6
1.3.1 Bleedless and hydraulicless concepts 6
1.3.2 New electrical architecture development 8
1.4 New electronic power cabinet for the More Electrical Aircraft 9
1.4.1 Mission profile for the design of the electrical network 9
1.4.2 A set of power converters to supply the main loads 10
1.5 Power cabinet design problem 13
1.5.1 Architectural design of the power cabinet 14
1.5.2 Inverter design 14
1.6 Conclusion 15
1.6.1 Component modelling 16
1.6.2 Inverter design 16
1.6.3 Architectural power cabinet design problem 16

Chapter 2 : Optimization by component association 19

2.1 Introduction 19
2.2 Direct modelling approach 20
2.3 Object-oriented programming 21

2.4 Excitations calculation 23
2.4.1 Simulation software 23
2.4.2 Frequency solver 25
2.5 Design process 30
2.6 Optimization Algorithms 31
2.7 Conclusion 32
Chapter 3 : Physical components modelling 35
3.1 Introduction 35
3.2 Active devices 35
3.2.1 Converter cell 35
3.2.2 Wide band-gap semiconductors 37
3.2.3 Nominal current increment of power semiconductors 39
3.3 Passive components 39
3.3.1 Magnetic components 39
3.3.1.1 Magnetic materials 41
3.3.1.2 Core Losses 42
3.3.1.3 Winding 44
3.3.1.4 Skin effect 45
3.3.1.5 Proximity effect 48
3.3.1.6 Circuit modelling 50
3.3.1.7 Permeance-inductor calculation 51
3.3.1.8 Core losses equivalent resistance 52
3.3.1.9 Thermal behavior 53
3.3.1.10 E-I Inductor Model 55
3.3.1.11 Coupled Inductor Model 62
3.3.1.12 Common Mode Inductor 66
3.3.2 Capacitor 69
3.3.2.1 Introduction 69
3.3.2.2 Capacitor model 69
3.4 Cooling devices 71
3.4.1 Heat Sink 72

3.4.1.1 Pressure drop model 72
3.4.1.2 Spreading resistance 73
3.5 Connexion elements 75
3.5.1 Power cables 75
3.5.2 Contactors 78
3.6 Assembly elements 79
3.7 Conclusion 79
Chapter 4 : Inverter specifications & design 81
4.1 Introduction 81
4.2 Specifications 81
4.3 Functional specifications 82
4.4 Electric specifications 85
4.4.1 Differential mode 85
4.4.1.1 Current harmonics absorbed by the inverters 85
4.4.1.2 RMS DC-bus Current caused by harmonics of DC bus voltage 86
4.4.1.3 Transient specifications 87
4.4.2 Common mode 89
4.4.3 Stability specifications 91
4.4.4 Filter design 93
4.4.4.1 Material selection 95
4.4.4.2 Optimization results (filter design) 97
4.5 Thermal specifications 101
4.5.1 Cabin air flow recycling 101
4.5.2 Power module and heat sink 102
4.6 Parallel inverter operation 107
4.6.1 Paralleling cells problematic 107
4.7 Final inverter results 111
4.8 Conclusions 112
Chapter 5 : Cabinet design 113
5.1 Introduction 113

5.2 Functional requirements 113
5.3 Determination of minimal theoretical elements 115
5.4 Contactor matrix design 115
5.4.1 Problem description 115
5.4.2 Minimal contactor matrix 116
5.4.3 Reconfiguration of the contactor matrix 116
5.4.4 Inductance suppression 118
5.5 Results 119
5.6 Coupling inductor technology 122
5.7 Conclusion 126
Conclusions & Perspectives 127
Appendix 131
Appendix A: Magnetic validation results 132
Appendix B: Heat Sink Thermal Model 134
Appendix C: Heat-sink aeraulic model 136
Appendix D: DQ model of the machine 138
Appendix E: Equivalent linearized transfer function of the inverter + PMSM machine 142
References 144

List of Figures

Figure 1.1 : Double-flux turbofan description (Pratt & Whitney) [3] 4

Figure 1.2 : Location of the different flight controls on the classical civil aircraft 5

Figure 1.3 : Efficiency of the different energy vectors during flight phases for an Airbus A330 [5] 6

Figure 1.4 : a) EHA (left) & Hydraulic actuator (right), b) EMA actuator 7

Figure 1.5 : Hydraulicless and Bleedless axes representation [11] 8

Figure 1.6 : Considered flight mission phases [4] 10

Figure 1.7 : Classical one inverter per load solution (left) and new solution using an electrical power cabinet (right) 11

Figure 1.8 : Utilization of the same module for different loads during different flight phases 11

Figure 1.9 : Example of inverter paralleling for high peak demand 12

Figure 1.10 : Contactor matrix reconfiguration depending on flight phase for three 15 kW inverters 12

Figure 1.11 : Contactor matrix reconfiguration in case of inverter failure 12

Figure 1.12 : Architecture of future MEA with location of the power electronic cabinets [4] 13

Figure 1.13: Solution example of high nominal inverter power (left) and low nominal inverter power (right) 14

Figure 1.14 : Inverter design specifications and choices illustration 15

Figure 1.15 : Schematic of the work presented in this document 17

Figure 2.1 : Classical Design Process (left) & Proposed Design Process (right) 20

Figure 2.2 : Direct modelling approach (left) & inverse modelling approach (right) 21

Figure 2.3 : Working flow principle of object with addition of external excitations 22

Figure 2.4 : Tree class diagram 23

Figure 2.5 : Communication schematic between components and the solver to design a LV filter in a buck converter. 24

Figure 2.6 : Average model of the switching cell 25

Figure 2.7 : Differential model of the commutation cell 26

Figure 2.8 : Parasitic capacitances: (left), origin ; (right), equivalent common mode of the commutation cell) 27

Figure 2.9 : Representation of the trapezoidal waveform 27

Figure 2.10 : Simulated common mode architecture 28

Figure 2.11 : Comparison between experimental (blue) and simulation data (red) for the common mode simulation 29

Figure 2.12 : Comparison between temporal simulation (black) and experimental (blue) data for the input common mode current without filter [37] 29

Figure 2.13 : Schematic of the design process with the optimization loop 30

Figure 2.14 : Graphic description of gradient descent algorithm, a) a simple case b) Example of local optimum vs global optimum 32

Figure 3.1 : Switching energies vs Drain to source current (Ref. CAS325M12HM2) 36

Figure 3.2 : Loss calculation algorithm 37

Figure 3.3 : Figure of merit Qg vs RdsON for different reference data a) Si based b) GaN & SiC devices compared to Si-based[25] 38

Figure 3.4 : Inductor, a) Physical device, b) Equivalent reluctance model 40

Figure 3.5 : Comparison between experimental and theoretical losses 44

Figure 3.6 : Skin effect in a round conductor a) 3D representation of currents, b) Current density at different frequencies 45

Figure 3.7 : Skin effect in windings left) grid representation of main parameters& right) Interpolation surface 47

Figure 3.8 : Comparison between analytic, interpolation model and FEMM^{TM} simulation of skin effect (Left) for round conductor (Case 1: d=5mm, Case 2: d=10mm) (Right) for rectangular conductor (Case 1: h=100mm, t=4mm, Case 2: h=20mm, t=20mm) 48

Figure 3.9 : a) Representation of skin effect, b) Current density representation at different frequencies 48

Figure 3.10 : Comparison between interpolation model and FEMM calculations taking into account proximity and skin effect 50

Figure 3.11 : Inductor a) Physical component, b) Permeance-capacitor model, c) Gyrator-based representation 51

Figure 3.12 : Permeance-inductor model ; a) with controlled sources, b) with a transformer. 51

Figure 3.13 : Permeance-inductor representation and analytic formulas 52

Figure 3.14 : 2D thermal modelling of magnetic components , a) General view, b) local zoom 53

Figure 3.15 : Temperatures calculation algorithm 55

Figure 3.16 : Inductor description and dimensions used to describe the object 56

Figure 3.17 : Permeance-inductor modelling of the E-I chosen inductor 58

Figure 3.18 : left) Equivalent resistance network of the E-I represented inductor, right) notation of the areas for the different thermal exchange coefficient 58

Figure 3.19 : distance used for semi empirical formulas for a) inductor cross section b) vertical surfaces c) top surfaces d) botoom surface 60

Figure 3.20 : Validation of the hot point thermal model of inductor for 4 different geometries 61

Figure 3.21: Inductor a) node numbering, b) analytic distribution of temperatures & c) temperature distribution in COMSOL^{TM} simulation 61

Figure 3.22 : Inter-cell transformer for two output cell; a) circuit, b) reluctance model for equal currents, c) reluctance model for opposite currents 62

Figure 3.23 : left) 3D view of a two-phase coupled inductor & right) dimensions used to describe the object 64

Figure 3.24 : Permeance-inductor equivalent simulation model representation of the two-phase coupled inductor 64

Figure 3.25 : Thermal network model of the coupled inductor 65

Figure 3.26 : Validation of the hot point model for four different geometries of 2-cells Inter Cell Transformers 66

Figure 3.27 : Common mode inductor; left) 3D image & right) dimensions used to define the component 66

Figure 3.28 : Electro-magnetic lumped equivalent simulation model of the common mode inductor 67

Figure 3.29 : Thermal network representation of the common mode inductor 68

Figure 3.30 : Validation of the hot point thermal model of common mode choke for 3 different components 68

Figure 3.31 : Energy density vs Capacitance for ceramic (left) and film (right) capacitors 69

Figure 3.32 : Equivalent capacitor simulation model and impedance Bode plot of the model 70

Figure 3.33 : Relative error between the calculated model parameters (C, ESR, mass…) and manufacturer data for rectangular capacitors(AVX) [75] 70

Figure 3.34 : Relative error between calculated model parameters (C, ESR, mass…) and manufacturer data for cylindrical capacitors(AVX) [75] 71

Figure 3.35 : Overall heat exchange coefficient for different fluids in different forms 71

Figure 3.36 : Heat sink: (left) 3D representation (right) definition of dimensions 72

Figure 3.37 : Comparison between calculated & experimental pressure drops in four different heat sinks 73

Figure 3.38 : Heat sink base plate1) Dimensions and heat source 2) Thermal resistance evolution for different dimensions ratio (a = 20cm, b= 10cm) 74

Figure 3.39 : Comparison between analytic model and COMSOL simulations 75

Figure 3.40 : Division of power cable into smaller subsections 75

Figure 3.41 : Electrical model of each cable section 76

Figure 3.42 : Common mode impedance of the considered power cable 78

Figure 3.43 : Contactor: (left) Schematic & (right) comparison between contactor mass model and reference data 78

Figure 4.1 : Speed/ Torque points as a function of the load power demand for different types of loads 83

Figure 4.2 : Equivalent electric model of PMSM (left) and Fresnel diagram of one phase (right) 83

Figure 4.3 : Graphical description of the differential current envelope standard test 85

Figure 4.4 : Graphic description of the differential current rms test 86

Figure 4.5 : Graphic description of the differential current transient test 87

Figure 4.6 : Regulation schematic of the Inverter+PMSM at maximal torque 88

Figure 4.7 : LISN circuit representation and values 90

Figure 4.8 : DO160 common mode current measurement setup 90

Figure 4.9 : Common mode impedance of the load used in the present work (Hypothesis) ... 91

Figure 4.10 : Constant power load characteristic curve representation 91

Figure 4.11 : a) Quadrupole representation b) Cascading quadrupoles association 92

Figure 4.12 : Modified input admittance by insertion of filter 93

Figure 4.13 : Solution with common mode filter at beginning of the load (left) and chosen solution (right) 94

Figure 4.14 : Maximal allowed magnetic field vs frequency for different losses densities left) 250 W/m^3, right) 750W/m^3 96

Figure 4.15 : Filter optimization. left) Evolution of the objective function and the maximal value of the constrain vector for 45% of the nominal current & switching frequency equal to 1f right) comparison of results between the optimization results with and without a penalty function 99

Figure 4.16 : Algorithm to eliminate undesired local minima 100

Figure 4.17 : Filter results vs nominal inverter current for different power: (left) optimized results using the penalty function & (right) re-optimization using the methodology described in Figure 4.16 100

Figure 4.18 : Cooling architecture of the power cabinet 101

Figure 4.19 : Input temperature variation depending on the altitude and flight phase (See Figure 1.6) 102

Figure 4.20 : Heat Sink design algorithm graphical description 103

Figure 4.21 : N° of necessary inverters vs the nominal current of each inverter 104

Figure 4.22 : Heat Sink & Power module per inverter mass vs I_{Nom} : (left) for different power modules references and switching frequencies and fixed $m=m_{ref}$, (right) Heat Sink & Power module per inverter mass vs I_{Nom} for different mass flow and fixed switching frequency f_2 and Ref. 3. 106

Figure 4.23 : (left) Minimal required total mass flow versuss nominal current for power module Ref. 3 and different switching frequencies & (right) Total mass of the power modules + heat sinks for $0.8m_{ref}$ and power module Ref. 3 107

Figure 4.24 : Propagation time dispersion problem example 108

Figure 4.25 : Insertion of the coupling inductors and the chronogram of the different waveforms 108

Figure 4.26 : Synchronous (left) and Phase-Shifted (right) command waveforms 109

Figure 4.27 : Trapezoidal waveform for the inter-cell current 110

Figure 4.28 : Coupling mass results for: (left) natural convection and (right) forced convection. (Note: Components are not on the same scale) 111

Figure 4.29 : Mass of the different elements as function of the switching frequency and nominal current for: (left) Inverter + installation, (center) coupling inductor + installation & (right) contactor + installation 112

Figure 5.1 : Failure example of one module 114

Figure 5.2 : Problem description (left) & example of matrix for a given architecture (right) 116

Figure 5.3 : Example of compliant and not compliant configuration for the same case 117

Figure 5.4 : Step example of “ Greedy Algorithm” for the case k 117

Figure 5.5 : Example of inductor deletion algorithm 118

Figure 5.6 : Architectural cabinet design algorithm 119

Figure 5.7 : total mass results for the electrical cabinet vs nominal current of the inverter: (left) for f switching frequency & right) for all the different switching frequencies 119

Figure 5.8 : comparison of simulation data with differential HVDC standard: (left) current envelope test & (right) RMS current test 121

Figure 5.9 : comparison of simulation data with HVDC standard: (left) common mode current envelope test & (right) differential current transient test 121

Figure 5.10 : left) Separate inductor structure & right) Coupled Inductor structure 122

Figure 5.11 : Coupled inductors technology: (left) monolithic and (right) cyclic cascade.... 123

Figure 5.12 : Number of coupling elements versus nominal power of the inverters 124

Figure 5.13 : (left) Magnetic field in the core when only one phase of the inductor is connected & (right) mass results of the group of 3 coupled inductors + installation versus nominal current of the inverter and compared to the results of separate inductors..... 125

Figure 5.14 : redundant solution using : (left) separate inductors & (right) coupled inductors 125

Figure 5.15 : Magnetic coupling elements mass difference between the solution using coupled inductors and the solution using separate inductors in terms of contactor number 126

Figure 0.1 : Network representation of two fins 134

Figure 0.2 : Pressure drop- mass flow chart for operating point of the system 136

Figure 0.3 : dq reference frame representation 138

List of Tables

Table 2-1 : Advantages and drawbacks of each kind of solver 25
Table 4-1 : Parameters of the machine and its supply 84
Table 4-2 : Subscript table 84
Table 5-1 : Validation of optimal inductors in the DC filter 120
Table 5-2 : Validation of coupling inductor 122

General Introduction

Electrical energy has been present in the aircrafts since the beginning of the 20th century. In the past decades, electric systems have progressively replaced the non-propulsive hydraulics and the bleed systems of the aircraft thus evolving towards a “more electrical aircraft”. A recent example is the Airbus A380 on which the actuators of the aircraft have been made electric, thus reducing the number of hydraulic networks.

The progressive increase of electrical systems in the aircraft requires a consequent reconsideration of the electrical distribution network. The present work takes place in the field of HVDC network for electrical energy distribution. In this framework, a solution using a set of generic power inverters to supply a set of essential electrical loads offers very promising perspectives: previous studies have shown that it seems to reduce the mass and the costs and to improve load availability. The connections between the loads and the inverters change depending on the flight phase and are managed by a contactor matrix. As the consumption of the loads changes between different flight phases, the same power inverter can be used for different loads.

The design of this new concept is not trivial. On the one hand, the designer must find the optimal trade-off between the number of inverters and the nominal power of each inverter, taking into account the impact on the contactor matrix. On the other hand, the design of the power inverter requires fulfilling a set of specifications (thermal, electromagnetic compatibility…) with a lot of possible solutions (topologies, materials, circuit layout…) and finding the optimal solution becomes very difficult. As a consequence, in the present work a set of methods and tools is created to assist the designer in the definition of the final product. The tools are defined in a general way so they can be used to solve a large number of different problems in electrical power distribution.

In chapter I, the “more electrical aircraft” concept is presented. The non-propulsive systems of the aircraft and the recent achievements of this concept are described. In addition, the perspectives for the new generations of aircrafts are briefly detailed. The inclusion of an HVDC network seems an interesting solution as it reduces the number of rectifier stages. The new network leads as well to the aforementioned concept of mutualizing a set of generic power inverters. The loads that could use this solution are presented in this chapter and a general overview of the work is shown.

In chapter II, the principles and bases of the environment used for the automatic design of power electronics devices are presented. In this environment, all the different components of the power converters are described using a “direct modelling” approach, that is, by their physical dimensions, materials and shape. From these inputs, the equivalent electric, magnetic or thermal models of the component are extracted and simulated by a very fast frequency solver to calculate the interaction between different components and therefore the compliance

of the solution can be checked. The models and the solver are inserted in an optimization loop to find out the optimal solution in terms of mass.

In chapter III, the modelling of the different components used in this work is described. Power modules, magnetic elements, capacitors and heat-sinks models are presented in detail and validated using numerical simulation or experimental data. These models constitute a root library for other future works using the automatic design environment.

In chapter IV, the different component models and the optimization environment are used to design in detail some parts of the generic power inverters. The inverter design is divided into three major blocks: the power module with their heat sinks, the DC filter, and the magnetic element to couple the power inverters. The different aeronautic specifications involved in each optimization problem are presented. At the end, the power inverter mass is given as a function of the nominal current and switching frequency. These results are necessary to assess the global optimization problem developed in chapter V.

In chapter V, the trade-off between the number of power inverters and the nominal current of each power inverter is determined. This design takes into account the contactor matrix and the necessary coupling inductors. The problem is solved using a “heuristic” algorithm developed in a previous work. The solution determines as well the optimal switching frequency. The optimal components are validated using numerical simulations. Finally, this chapter assembles all the developed tools to design the optimal electric power cabinet, which is the main problematic solved in this work.

Chapter 1 : More Electrical Aircraft context

1.1 Introduction

Human activity is responsible of the global warming over the past half century. The temperature increment is caused by the higher concentrations of CO_2, CH_4 and N_2O on atmosphere produced by the human activities. Aviation currently accounts for 2% of CO_2 emissions [1], but its impact is expected to increase. Only during the last decade, the air world annual traffic has grown by 62%. Previsions expect an average annual air traffic growth of 4.6 % for the next 20 years [2]. To anticipate the future impact of aviation, authorities impose new regulations on aircraft CO_2 emissions. By 2020, the existing environmental goals are to reduce CO_2 emissions by 50% [1]. As a result, a key priority for aircraft manufacturers is to design more efficient aircrafts that drastically reduce fuel aircraft consumption and as a consequence CO_2 emissions. For example, a 1% structural weight saving reduces aircraft fuel consumption by 0.5%-1.5% depending on the aircraft [1].

A better rationalization of the aircraft energy usage for the systems will help to achieve these results. Indeed, in the first part of this chapter the four energy vectors used on current state-of-the-art aircraft are described (pneumatic, hydraulic, mechanical and electrical). We will show how the replacement of the hydraulic and pneumatic systems by electrical systems is a promising development axis for aircraft manufacturers. The potential advantages of this new “More Electric Aircraft” will be introduced. The “electrification” of the aircraft opens new solutions in terms of electrical architecture. In the present work, a new electrical distribution concept is studied and will be presented at the end of this chapter. The development of this concept is the main goal of the present work.

1.2 Energy vectors on aircraft

To reduce aircraft CO_2 emissions the energy consumption needs to decrease. The engines/turbines are the principal source of power for aircrafts. The engines are in charge of aircraft propulsion and provide all the necessary energy for the different loads on the aircraft. On current civil aircrafts, the engines are double-flux turbofans due to the good trade-off between efficiency and noise. A simple schematic is presented in Figure 1.1.

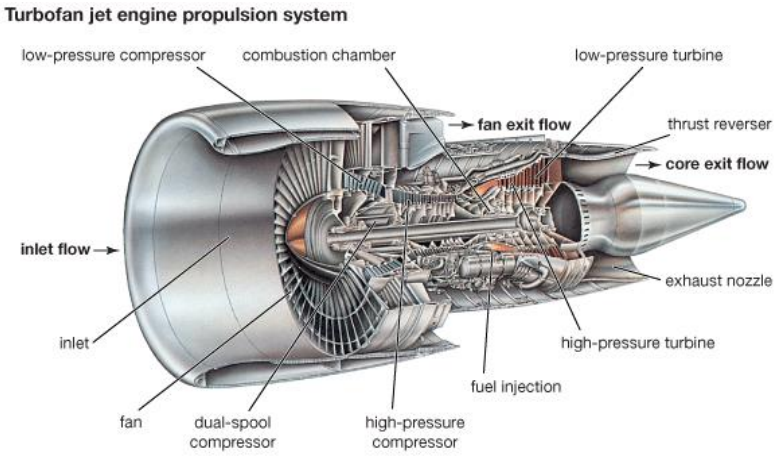


Figure 1.1 : Double-flux turbofan description (Pratt & Whitney) [3]

The energy not used for the aircraft thrust is called "non-propulsive energy" and it represents 3% of the total power produced by the engines [4]. Aircraft non-propulsive energy must be reduced and used more efficiently. The four kinds of non-propulsive energy installed on a current state-of-the-art aircraft are:

- **Pneumatic**: represents the energy transported as compressed air into the aircraft and distributed through the aircraft by the pneumatic network (*Bleed Network*). For the bleed network, hot air is taken from the compressor stages of the engine before the fuel is added. The main loads consuming pneumatic energy are:
    - *Environmental Control System (ECS)*: responsible of keeping the interior air of the cabin at pressure and temperature levels for people to travel comfortably at high altitudes. The ECS system possesses compressors motioned by the compressed air of the bleed network,
    - *Wing Ice Protection System (WIPS)*: prevents the formation of ice (*anti-ice*) on the wings or engines nacelle. The ice-formation on wings is a critical issue as it modifies the wing profile,
    - *Motor Starting*: motor start–up is performed by a turbine working with hot air injection from the Auxiliary Power Unit (APU).
- **Hydraulic**: represents the energy transported as a pressurized liquid fluid to motion other systems. The pressurization of the liquid is done by a pump driven by the engine. The loads using hydraulic energy are:
    - *Flight Controls*: they are divided in primary flight controls and secondary flight controls. The primary flight controls change the orientation of the aircraft around its center of gravity. Primary flight controls include the rudder, the ailerons and the elevator. The secondary flight controls help modifying the lifting and drag forces acting on the aircraft. The secondary flight controls include the slats, the flaps, the Trimmable Horizontal Stabilizer and the spoilers. A detailed schematic of the localization of the different flight controls is presented in the Figure 1.2:

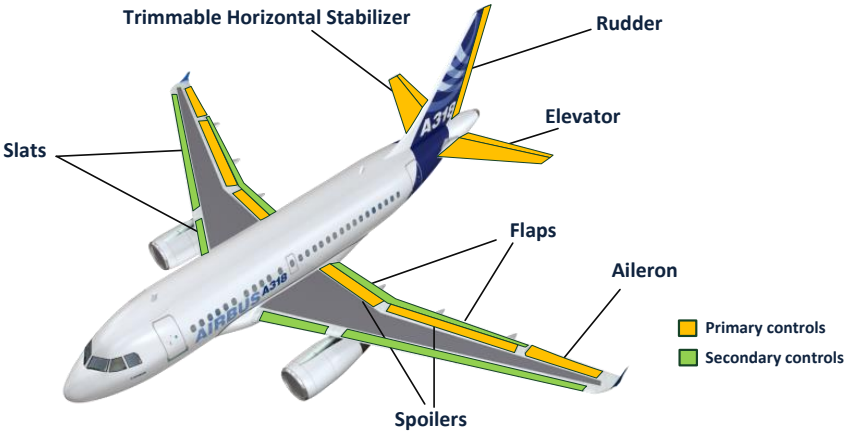


Figure 1.2 : Location of the different flight controls on the classical civil aircraft

- *Landing Gear System*: ensures the aircraft taxi and braking operation of the aircraft when aircraft is on the ground. The Nose Landing Gear ensures the direction of the aircraft and the Main Landing Gear supports the major aircraft weight on ground. The brakes are located on the Main Landing Gear.

- **Electric**: the electric energy of the aircraft is obtained by transformation of the non-propulsive mechanical energy into electricity by an electric generator. The main electrical loads on current state-of-the-art civil aircrafts are:
  - *Fuel pumps*: transport the fuel from the tanks to the engines,
  - *Anti-icing system for the cockpit*: to ensure a good visibility for the pilots (Windshield system),
  - *Ventilation system of the ECS*: includes all fans for hot air extraction and ventilation (Avionics Extract Fans and Avionics Blowing Fans),
  - *Avionics systems*: calculators installed on the aircraft. The consumed power for the avionics systems increases with each new generation of aircrafts,
  - *Cabin systems*: includes all the necessary electrical systems for the aircraft cabin such as galleys, lighting, "In Flight Entertainment" systems… The cabin systems vary depending on the aircraft configuration chosen by the flight company.
- **Mechanical**: One part of the non-propulsive energy is used for the engine's own systems. Pumps (Fuel and oil) are motioned by the engine itself.

1.3 Increment of aircraft efficiency, towards a more electrical aircraft

1.3.1 Bleedless and hydraulicless concepts

As stated in previous section, aircrafts use four kinds of energy. A better use of aircraft energy implies reducing the number of energy networks. In Figure 1.3, the efficiency of the different energy vectors and for different flight phases is presented.

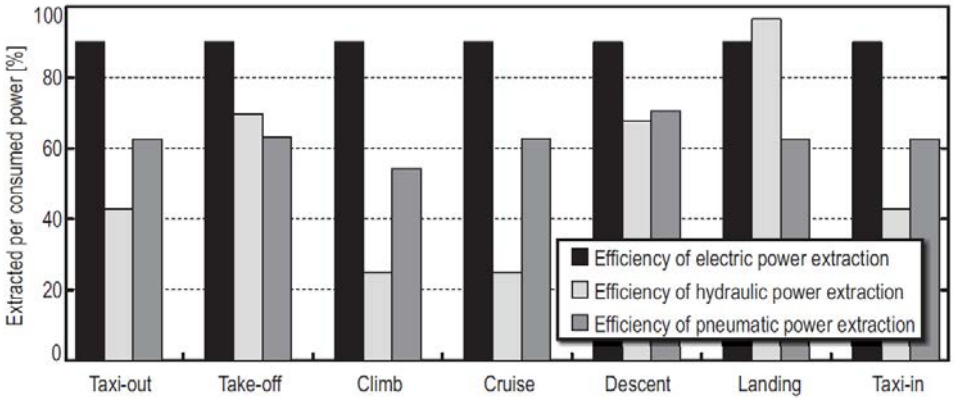
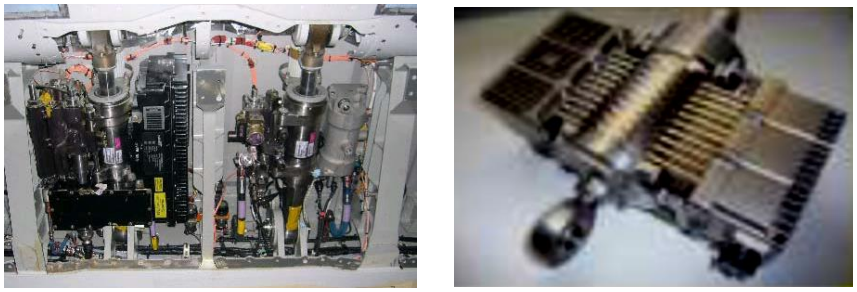


Figure 1.3 : Efficiency of the different energy vectors during flight phases for an Airbus A330 [5]

Electrical systems are the most efficient systems on aircraft, which means that less energy is needed from the source (engines) and therefore fuel consumption. As a result, aircraft manufacturers are looking forward to perform all the aircraft functions using electrical devices. The progressive aircraft electrification is performed in two different axes:

- *Hydraulicless axis*: consists of the replacement of hydraulic systems by electric systems as shown in Figure 1.5. The A380 was the first to replace one of the three hydraulic circuits by an electric actuator [6]. In addition, a part of the flight control actuators is electrified. On the hydraulicless axis, the hydraulic actuators are replaced by two kind of devices:
  - Electro-Hydrostatic Actuators (EHA): hydraulic actuator supplied by a local hydraulic circuit driven by an electric pump. The Airbus A380 was the first aircraft where the hydraulic actuators where replaced by electro-hydrostatic actuators [7].
  - Electro-Mechanical Actuators (EMA): is an electro-mechanichal actuator driven by an inverter. EMAs are more efficient than EHAs. Their major drawback is the potential of mechanical jamming [8]. On the B787, EMAs are used for braking operation and for a pair of spoilers [9].



a) b)

Figure 1.4 : a) EHA (left) & Hydraulic actuator (right), b) EMA actuator

- *Bleedless axis*: consists of the replacement of bleed systems by electric systems (See Figure 1.5):
  - Electrical Environmental Control System (ECS): instead of obtaining bleed air from the main engine, the air is taken from the outside and compressed using electric power. In the Boeing B787, the air-conditioning system includes this kind of architecture thus eliminating the bleed system and air ducts from the engine [9].
  - Electrical Wing Ice Protection System (WIPS): two approaches appear to prevent or eliminate ice creation. The first one consists of placing electric wires on the wing surface. By Joule effect, the dissipated heat will evaporate the ice on the wing. The second solution consists on using electromagnetic actuators to produce mechanical vibrations to get rid of the created ice. [10]
  - Main Engine Start: traditionally, engines are started by a turbine driven by compressed air provided by the Auxiliary Power Unit (APU). Boeing 787 was the first large aircraft to use the main engine generators as electrical motors to perform the starting function.

The Figure 1.5 summarizes the two development axes discussed before. The addition of these two axes leads to the convergence towards a full electric aircraft. The full electric aircraft refers to an aircraft where all non-propulsive systems will be electric.

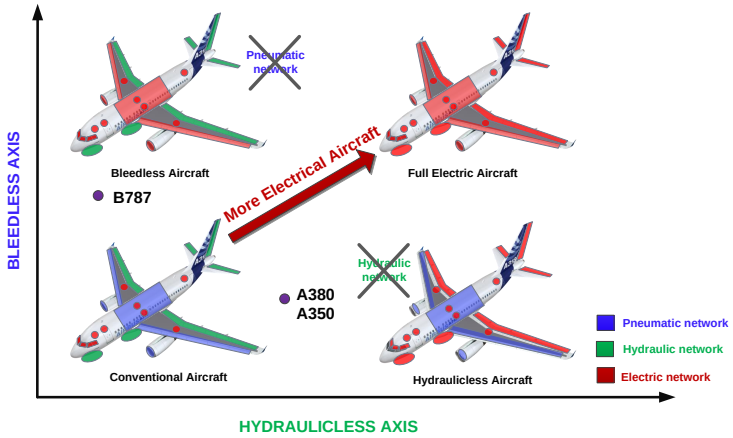


Figure 1.5 : Hydraulicless and Bleedless axes representation [11]

In the path to the Full Electric aircraft, the More Electric Aircraft is an intermediate step to increase aircraft profitability and respond to environmental constraints. These gains are a sum of the advantages that electric systems provide:

- *Power rationalizing*: an efficient management of the energy taken from the engines is easier when there is only one energy vector on the aircraft [12].
- *Mass saving*: suppressing the heavy pneumatic and hydraulic networks reduces volume and mass. Electric technology development predicts a reduction on the state-of-the-art electric systems mass.
- *Protection*: the segregation and isolation of an electric failure is simple and fast-performed. Failure isolation is hard to solve in other systems. E.g. a fluid leakage on an aircraft pipe.
- *Maintenance*: the systems are monitored. As a consequence, a failure is easily detected, thus reducing maintenance time. This is already a reality in the car industry. Maintenance times result in high costs to flight operators.
- *Synergies*: lots of industrial sectors, especially energy and automotive sectors are pushing towards the development of cheaper, more efficient, more integrated and robust electric equipment. As a consequence, the associated costs of electric systems could be reduced thanks to a greater mass market [13].

1.3.2 New electrical architecture development

As electric systems become a more relevant part of the aircraft, they become a major player on aircraft total weight and therefore fuel-consumption. Aircraft manufacturers look forward to find new ways of reducing the total weight of electric systems [13]:

- *More integrated power systems*: apparition of wide bandgap semiconductors (GaN, SiC) opens a complete new era in power converters design. Wide bandgap devices allow operation at higher temperatures and a reduction of switching and conduction losses opening a window to new cooling strategies and integration. Furthermore, the switching

frequency of power converters could be increased, reducing the size of passive components [14].

- *New HVDC architecture*: increasing the number of electric loads in a classical AC network would mean larger number of AC-DC rectifier stages & filters. A solution consisting of DC bus bars, to which all the loads are connected, was demonstrated to save weight on the aircraft [15].

  The use of HVAC 230 V generators (A350, B787) and classical diode rectifier stages will potentially lead to a DC network level of 540V which is called HVDC. Current state of the art aircrafts already include some local HVDC bus bars [16]. The new level of high DC voltage will lead to a reduction of the mass of electrical systems. For example, cable weight is reduced by the use of higher voltages. First, wire section is reduced for given power loads. Second, the voltage drop on wires is reduced, which is the key factor in the design of power cables [17]. In [18], a significant weight potential saving is expected on a modern aircraft with +/-270V DC network. The addition of this HVDC network imposes other new challenges such as the quality and stability of the DC network [19][20].

- *Energy management optimization*: as a consequence of increasing the total electrical power on the aircraft, disruptive architectures start to appear. One solution involves using the same power inverter to supply different loads during different flight phases of the aircraft. This solution is used on the Boeing B787 bleedless aircraft [16]. The same power inverter is used for the compressor of the cabin air conditioning system and the engine starter. The design approach in the context of power converter sharing will be the main problematic treated of this work and it will be further developed in section 1.4.

1.4 New electronic power cabinet for the More Electrical Aircraft

1.4.1 Mission profile for the design of the electrical network

Any electrical designed equipment on aircraft must provide full operability for all the different mission profiles it may encounter during its full operational life. The operation point of each aircraft load depends on four main factors:

- *Mission phases of the aircraft operation*: the mission of the aircraft is decomposed in different phases depending on the operational state of the aircraft. Altitude, ambient pressure, temperature and pressure conditions vary depending on the flight phase. In addition, the loads demand changes through the aircraft mission. Ex. the pressurization of the cabin will not require the same amount of power on ground (0 ft.) than at cruise (40000 ft.). In the current work the mission profile is decomposed into 11 phases. The sequence of phases is presented in Figure 1.6.

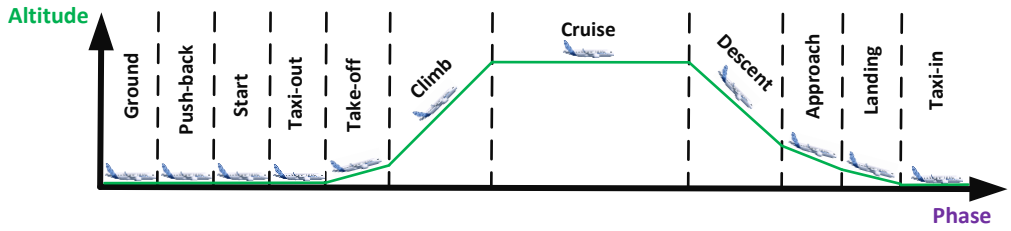


Figure 1.6 : Considered flight mission phases [4]

- *Network state*: depending on the available sources and the required consumption of each load, the network reconfigures itself to ensure connections between sources and loads. To avoid over-sizing of the electrical generators, some loads adapt their consumption to the source availability. For example, the commercial loads (Galleys, IFE…) could be disconnected in case of generator failure to keep the remaining power on the essential loads.
- *Load availability*: when a failure occurs in one load, the consumption of other loads might be impacted. For example, in the More Electrical Aircraft, two ECS packs are in charge of supplying the necessary pressurized hot air. In case one ECS pack is disconnected, all the necessary air is provided by the remaining pack.
- *External conditions*: the external temperature and pressure conditions have an impact on the power consumption. These conditions depend on the altitude and the weather during the mission. For example, the de-icing system is operated depending on the external temperature and humidity levels. The "International Standard Atmosphere" (ISA) normalizes the values for the external conditions to be taken as reference on the design.

1.4.2 A set of power converters to supply the main loads

The variation of consumption during the flight mission and the inclusion of an HVDC network to supply some of the loads led to new electrical architectural solutions. For future aircraft generations, manufacturers are developing a new concept, consisting of a power electronic cabinet connected to the HVDC network to supply the whole set of main electrical loads. The new electronic cabinet is composed of:

- *A set of power electronics modules*: to supply several loads for any flight phase, any failure mode… All the considered loads are three-phase AC loads. Therefore the power modules are three- phase DC-AC inverters
- *A contactor matrix*: to manage the connections between the power electronics modules and the loads. The contactor matrix must ensure all the connections between the modules and the loads in order to ensure safe operation of the aircraft.

The following figure shows the difference between a classical architecture and the new proposed architecture using a power cabinet.

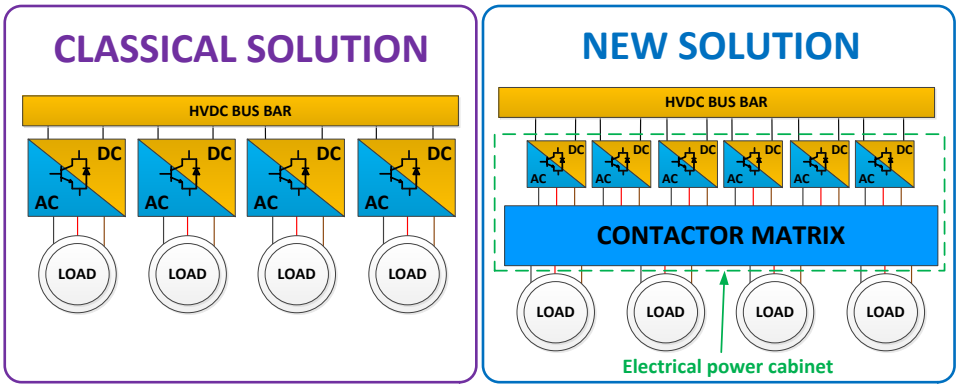


Figure 1.7 : Classical one inverter per load solution (left) and new solution using an electrical power cabinet (right)

Six different loads are identified as candidates to benefit from the electrical power cabinet:

- *Three compressors from the "Environmental Control System"* (ECS1, ECS2 and ECS3): The compressors control the pressure and the temperature of the pressurized zones in the aircraft.
- *One pump of the "Fuel Tank Inerting System"* (FTIS): controls the oxygen levels on the tanks of the plane. This is the only non-redundant load.
- *One AC transformer* (TAC): for all the AC electrical loads operating at 115 V 400Hz.
- *One electrical motor for the starting of the aircraft engines* (STARTING)

The advantages of the proposed architecture are:

- *Load complementarity*: the same power inverter that supplies power load 1 during a certain flight phase could be re-used to supply load 2 when load 1 is not needed.

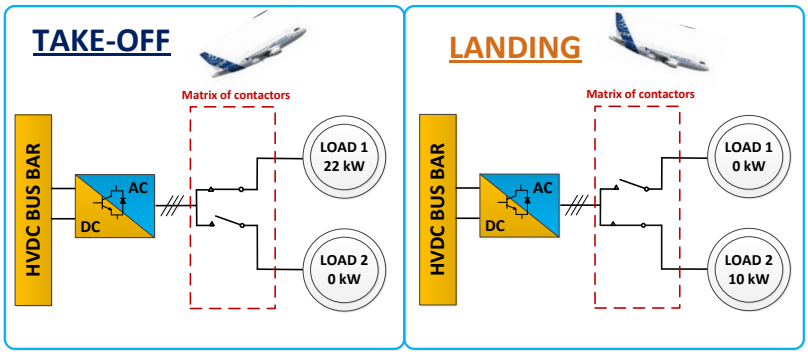


Figure 1.8 : Utilization of the same module for different loads during different flight phases

This is for example done on the Boeing B787: the same power inverter used for the ECS compressor being used for motor starting [16].

- *Power complementarity*: during a load high power demand, additional inverters are connected to the load. As a result, the power inverters nominal power is downsized. In the Figure 1.8, an example for three power inverters of 15 kW nominal power is represented.

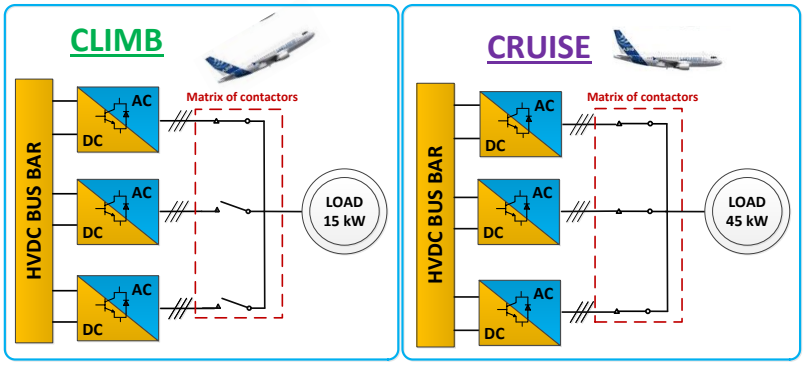


Figure 1.9 : Example of inverter paralleling for high peak demand

- *Reconfiguration*: As a consequence of the two first advantages. The same inverter is connected to different loads to complement the high power demand of the loads. The number of required inverters is therefore reduced. Reconfiguration of an electrical power cabinet was already validated in a test bench [21]. In Figure 1.10 the contactors matrix is reconfigured and the second inverter supplies both loads during high demand.

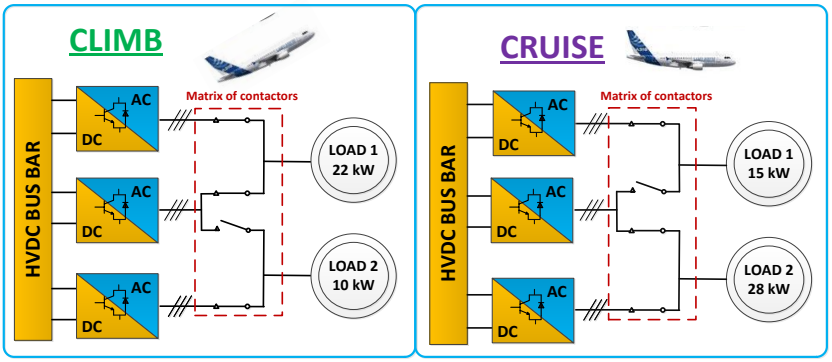


Figure 1.10 : Contactor matrix reconfiguration depending on flight phase for three 15 kW inverters

- *Redundancy*: when a failure occurs in one of the power inverters, other available power inverter modules takes over, continuing the mission of the aircraft.

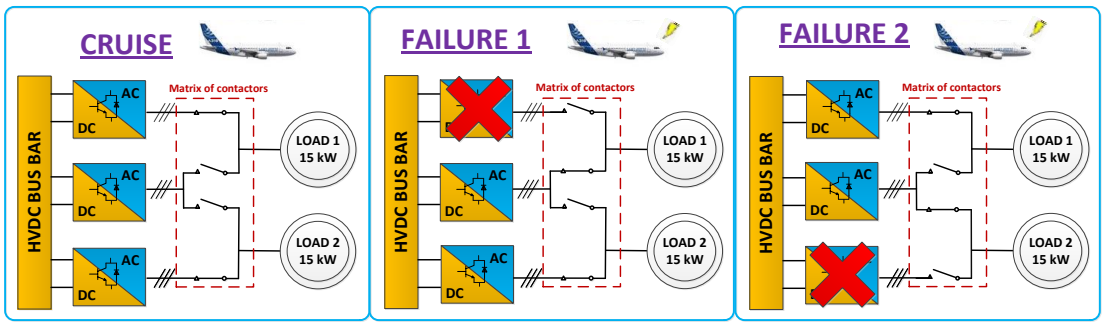


Figure 1.11 : Contactor matrix reconfiguration in case of inverter failure

- *Standardization*: using generic power converters leads to the reduction of part numbers on an aircraft. As a result, the number of manufactured parts and the number of stocked parts for aircraft manufacturers and airline companies decreases. The concept of standardizing and mutualizing embedded electronics in aircraft is already performed. On

the Airbus A380, the concept of Integrated Modular Avionics (IMA) was already inserted. This concept uses standardized calculators with a communication network (AFDX). A simple calculator stores applications coming from different systems [22].

On the future architecture of a more electrical aircraft, two power electronic cabinets are connected to the HVDC network and the loads as shown in Figure 1.12.

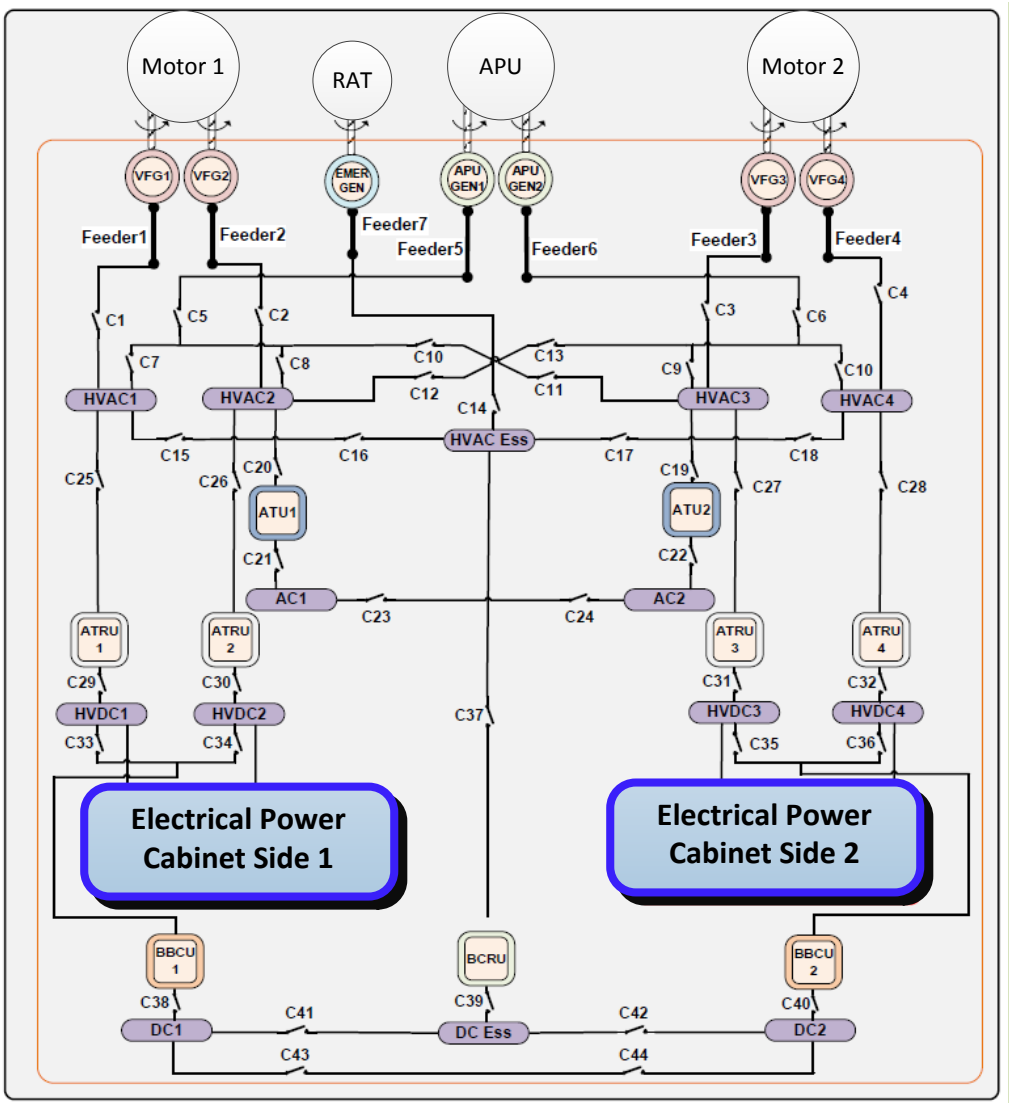


Figure 1.12 : Architecture of future MEA with location of the power electronic cabinets [4]

1.5 Power cabinet design problem

The concept and the advantages of using a power electronic cabinet have been presented in the previous section. The power electronic cabinet seems a promising solution for future generation aircrafts but is it an attractive solution from an aircraft point of view?

The present work aims at answering this question. The design of the power electronic cabinet is presented on this document. The design problem is decomposed into two sub-problems: the architectural design of the power cabinet and the design of the inverters.

1.5.1 Architectural design of the power cabinet

Designing the electronic power cabinet requires determining the power inverters and contactors necessary to fulfil the different mission profiles. The final design strongly depends on the nominal power of each inverter. For instance, designs using inverters with high nominal power will require a smaller number of inverters and less contactors between loads and inverters. However, the unitary mass of inverters and contactors will be higher. This dilemma leads to a first optimization problem aimed at determining the optimal trade-off between the number of inverters and the nominal power of each inverter, as shown in the Figure 1.13.

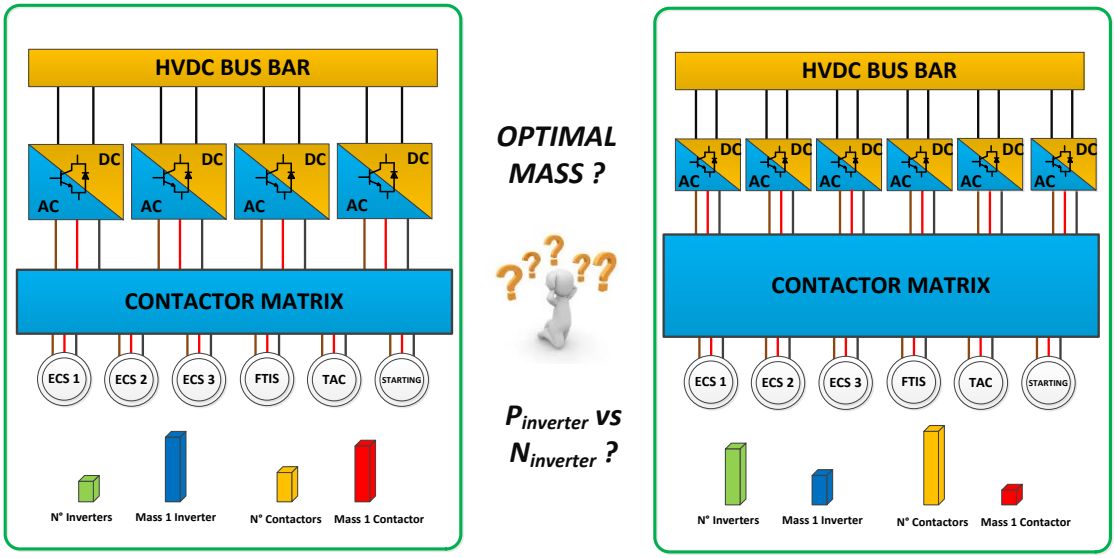


Figure 1.13: Solution example of high nominal inverter power (left) and low nominal inverter power (right)

1.5.2 Inverter design

To solve the architectural optimization problem the mass of an inverter for a certain nominal power is required. The design of a power inverter is a complex task involving many possible combinations between components to fulfill the specifications. The different specifications a power electronics engineer must comply within a design process are described in Figure 1.14.

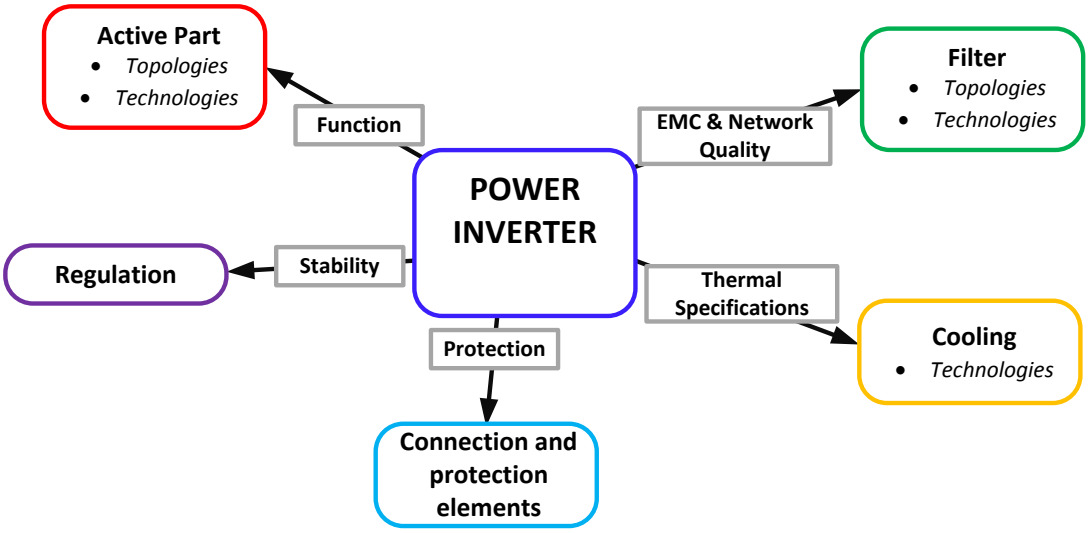


Figure 1.14 : Inverter design specifications and choices illustration

As shown, the design must be compliant with all the different specifications of the aircraft:

- *Function*: the power inverter must perform the DC /AC conversion at all the required operation points of the loads. It must provide the necessary voltage, current and frequency levels to satisfy the proper operation.
- *EMC & Quality*: electric systems must not cause other equipment's malfunctioning. To avoid this situation, standards that every system must comply are defined. The standards are used to design the filters.
- *Thermal Specifications*: electrical systems generate losses that need to be evacuated to avoid temperature rise and equipment failure. Specifications define a thermal environment within which the electric equipment must operate without degradation.
- *Stability*: electrical equipment must not destabilize the electrical network and interaction effects between equipment must be reduced. This specification will have an impact on filter and controller design [19].
- *Connection & protection*: the protection specification is performed in two different ways. First, the equipment operation should not be impacted by any external aggression (mechanical, electrical, thermal…). Second, if a failure occurs on the electrical system, the failure must be rapidly segregated to avoid impacting other equipment.

1.6 Conclusion

Through this introductory chapter, the different energy networks on the current state-of-the –art aircraft have been presented. It has become clear that reduction in the number of energy networks would lead to a better management of the energy on board. The More Electrical Aircraft aims at replacing the pneumatic and hydraulic systems by electric systems.

In this context, a solution consisting on using a set of power modules to supply different power loads was identified. The modules are connected using a contactor matrix to ensure the power demand of the loads during all flight phases. The modules and the contactor matrix are inserted into an electrical power electronic cabinet that ensures electric distribution of the different loads. Design of the electronic power cabinet was found as a complex task. On the one hand, the power inverters must be designed for different loads and for different nominal power. On the other hand, the optimal trade-off between nominal module power and number of modules must be found. The present works aims at solving both design problems. The design algorithm is decomposed into three different steps presented in this document.

1.6.1 Component modelling

The methodology to design the power inverter is presented in chapter II. The main elements of the converter impact are modeled using a “direct modelling” approach. The components are described by their shape, dimensions and materials becoming the design variables. The different component models used on the design of the power inverters are presented and validated in chapter III.

1.6.2 Inverter design

The components are associated to create the inverter. To test the compliance of the different specifications, the inverter is simulated using different solvers. Chapter IV addresses several optimization problems related to power inverter design. At the end of this part, a response surface is given to determine the unitary mass of a power inverter depending on the nominal power. The response surface is used to feed the architectural power design problem.

1.6.3 Architectural power cabinet design problem

In chapter V, the architectural cabinet problem is addressed. The architectural design problem is solved using a “heuristic algorithm” which is based on the work of [4]. The power electronic cabinet is designed for different nominal power of the generic inverters. The optimal trade-off between number of inverters and nominal power is therefore found.

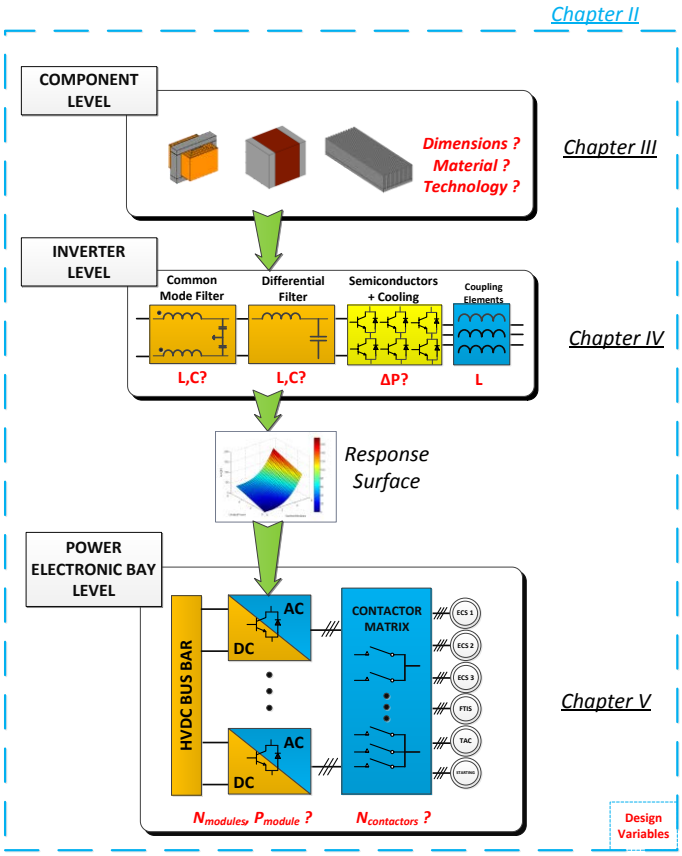


Figure 1.15 : Schematic of the work presented in this document

The context of the More Electrical Aircraft has been introduced and design problematic of the power cabinet has been presented. It becomes important now to describe the environment that has been developed in the current work and that will be the base to design the power inverters.

Chapter 2 : Optimization by component association

2.1 Introduction

To design the power electronic cabinet we must first design the generic inverters. A power converter is a complex system. Designers choose between a series of different components, topologies, control laws… to create a product fulfilling the expected performance and the specifications. In addition, the characteristics of the electrical equipment (lower mass, volume, cost and higher efficiency and reliability) must be improved.

To perform such task, designers make use of more and more calculation capacity of computers to assist the design process. Nowadays, software is used to check the system behavior (electrical, thermal, mechanical…) before building the prototype. For example, numerical simulation software solves complex physics problems under certain hypothesis. Other common applications are circuit solvers to validate the behavior of different elements at functional level. Moreover, software is as well a key enabler in the manufacturing process. Computer Aided Design (CAD) software specifies in a schematic the different physical dimensions of the components. Modifications, copies are easily performed and the schematics are interpreted by numerical control machines … to manufacture precise components.

Nevertheless, device design still remains a task performed by the designer/engineer. The final device is strongly dependent on designer's skills and experience. Furthermore, there are many compliant solutions that the designer cannot consider because of time limitations. To overcome this limitation, companies and universities are investigating new ways to use "virtual prototyping" in the design of power electronics devices.

In the present work, our contribution involves using specific software to replace the designer in the design process looking at all the possible combinations between components and finding an optimal solution. As a result, the time-to-market of the product is reduced. A schematic of the proposed new design process is presented in Figure 2.1. The "Device design" in a classical approach (left) performed by the engineer is replaced by a machine (right). The rest of the process remains the same but the number of physical prototypes is reduced and therefore the associated costs and time-to-market. Moreover, since the number of looked solutions has increased the solution should be closer to the "optimal" (lower mass, lower losses…).

Virtual prototyping is considered as the new challenge in the domain of power converter integration. Predictions estimate that in 2020, 80% of the design process will be performed by virtual prototyping [23].

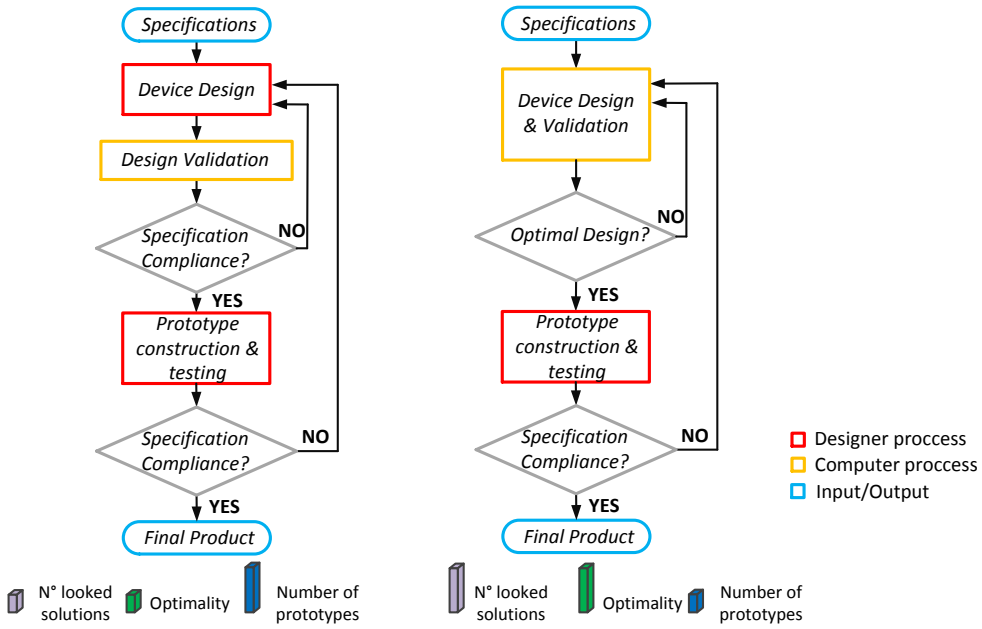


Figure 2.1 : Classical Design Process (left) & Proposed Design Process (right)

"Virtual prototyping" in the domain of power electronics has already been used in numerous works. In [24], a design environment is presented to conceive a single-phase PFC converter. In [25], a tool is proposed to design a DC-DC converter. Other works involve the design of a permanent magnet synchronous machine [26]. In [27], an optimization framework called CADES (Component Architecture for Design of Engineering Systems) is presented to perform optimized system design. In the present work, a "design environment" to perform the design process will be also created, mainly focused on electrical power cabinet inverters.

In this chapter, our proposal for this "design environment", principles and structure, are presented. First, the approach used for modelling the elementary components of power converters is described. Second, the models are implemented under an object-oriented approach. A whole library set of components is created under the same pattern. Finally, the models and the simulation software are inserted in an optimization loop to find optimal solutions. The optimization is performed using several different optimization algorithms.

2.2 Direct modelling approach

All the elements of the power converter (inductors, heat sinks…) are represented using a "direct modelling" approach [28][29]. Under this approach, the components are described by their physical dimensions, materials and shape. Different parameters (mass,…) are calculated from these inputs.

The "direct modelling" approach has many advantages:

- *Injective solution*: as the objects are described by their physical dimensions, the calculated parameters are deterministic. For example, let us consider the design of an inductor core as presented in Figure 2.2: the only criterion considered here is that the core needs to

operate below a certain saturation flux. If the dimensions and the material are defined, the saturation flux is straightforward calculated (direct modelling approach in Figure 2.2). On the contrary (inverse modelling approach), for a given saturation flux, several combinations of materials and dimensions achieve the required saturation flux: that means the final values are not unique and will be determined by specific choices (form factors, materials…) of the calculation model.

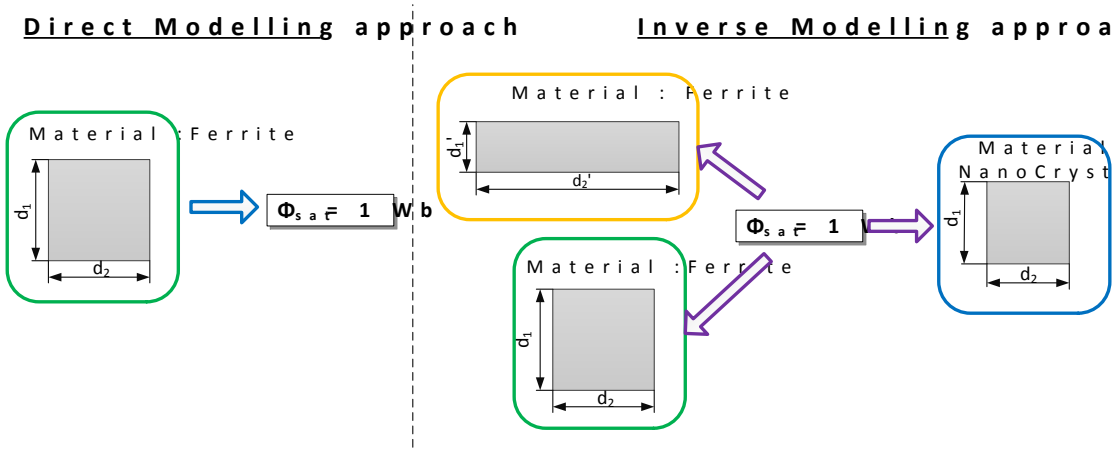


Figure 2.2 : Direct modelling approach (left) & inverse modelling approach (right)

- *Precision on physical parameters*: the objects are described using their physical dimensions and materials. As a result, the calculation of the volume and mass of the component is accurate. This advantage is particularly interesting in the present work since aircraft equipment weight is a primordial design parameter.

However, the "direct modelling" approach has some limitations. In some electrical components (capacitors and semiconductors), due to the difficulty of creating a customized design and the complex physics, the "direct modelling" is not adapted. To overcome this limitation, these components are represented using:

- databases containing information given by the manufacturer,
- regression laws obtained from data provided in manufacturer's datasheet.

Further information about the model description is given in Chapter III.

2.3 Object-oriented programming

In the present work, power converter components are represented using an object-oriented programming approach. Each component is coded as an *object* with some characteristics or *properties* and some mathematical functions or *methods* to calculate the different data of the component. The calculation process behind every object of the design environment is presented in Figure 2.3.

From the inputs (physical dimensions, material and shape) the parameters (mass, volume, cost) and the equivalent simulation models are extracted. The insertion of external excitations

(electrical, thermal, magnetic…) helps extracting more data (losses, temperatures, magnetic field…) to ensure proper design of the components.

The objects are grouped together in different categories or families depending on their function, materials... A tree class is created to group the elements that share certain properties or methods. For example, all magnetic components (inductors, transformers…) share the material *properties* or the *methods* to calculate the core losses.

In addition, in the tree class, abstract classes are inserted to define a standard or skeleton for all components to be inserted in the library. The standard is important for incremental development. It helps understanding other users' developed models and eases utilization.

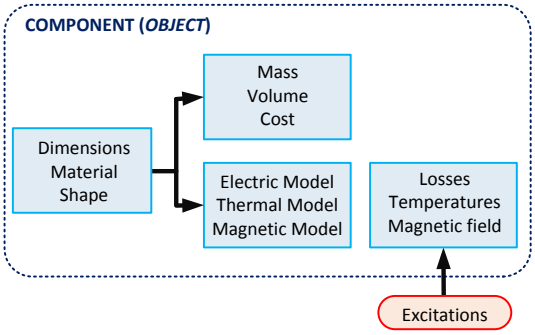


Figure 2.3 : Working flow principle of object with addition of external excitations

At the top of the tree class (See Figure 2.4) is situated the abstract class *Component* that contains the skeleton properties (geometric data, electric data for example) and abstract methods (display methods, parameter computation).

From this class, two abstract classes are derived:

- *Element:* is the mother class for every physical device and contains all shared properties (shape, dimensions and material) specific to the "direct modelling" approach. Deriving from this class we can find devices such as inductors, capacitors, heat sinks…
- *Composite:* is the mother class for any device which is formed by the association of *Elements*. For example, an LC filter is formed by the association of an inductor *Element* and a capacitor *Element*.

Below these two main classes, additional abstract classes are derived as well. For example, a magnetic class to regroup the different magnetic components. The main objective is to define the different functions only one time in the environment. Code implementation repetition is avoided and bug fixing becomes less tedious. The completed tree class used and developed is presented in the Figure 2.4. The tree class was also intended to anticipate future developments. For example, a transformer model can be derived from the magnetic abstract class that profits from the core loss density method of the magnetic class.

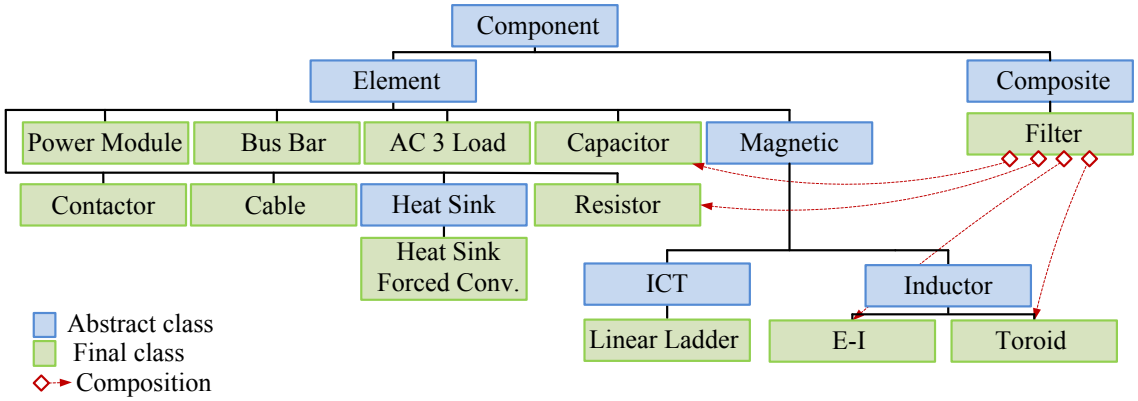


Figure 2.4 : Tree class diagram

Another important advantage of object-programming is the encapsulation. Once an object has been created and tested, its code might be hidden to users to prevent future "customized" modifications. In addition, the object controls how the user will interact, preventing usage errors (For example the objectives include specific methods to reject any negative dimension that would be defined by the user).

2.4 Excitations calculation

2.4.1 Simulation software

Once all the dimensions of each component are defined, the designer needs to verify if the association of components satisfies the required operation conditions. The operation conditions refer to the different waveforms each component must withstand. These waveforms are stored in the property "excitations". The excitations are determined by the interaction between all components. In the design environment, the excitations can be defined by the user (for example, design a transformer when the current/voltages are known) or they can be calculated by a circuit solver. The solver gets the equivalent simulation model of each component, builds the equivalent simulation model of the system, runs a system simulation, extracts the excitations and dispatches the waveforms to the different components to design. From the excitations, the rest of the other necessary output data (temperature, losses,…) is calculated. The working algorithm is described for an example of an LV-side LC filter in a buck converter (Figure 2.5).

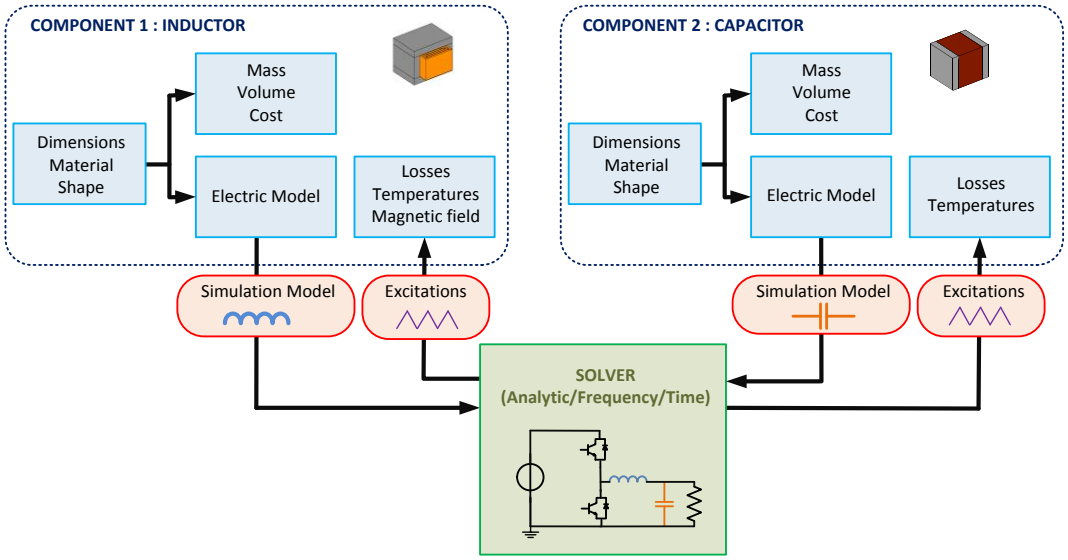


Figure 2.5 : Communication schematic between components and the solver to design a LV filter in a buck converter.

Three different kinds of solvers can be used for circuit solving:

- *Analytic*: the different excitations are calculated using analytic expressions. These equations are often based on hypothesis and simplifications; the validity domain is usually restrained. This is the fastest method to compute the waveforms. The major drawback is that equations must be defined for all the different topologies reducing the flexibility of the approach. In the present work, it is not used but it may become the only solution in future developments for specific topologies where other solvers are limited.

- *Time domain*: time solvers comprehend the majority of commercial simulation software (SABER™, PLECS™, PSIM™…). The equivalent simulation models of each component are assembled in a circuit representation and the partial differential equations are solved using different numerical methods. This type of solver achieves an accurate resolution of the circuit and can take into account the different regulation strategies. Their major drawback is the high computation time required.

- *Frequency*: the equivalent simulation models are assembled in a circuit representation. and simulated at specific frequencies. The time signal is obtained by the inverse Fast-Fourier Transform and corresponds to the steady-state operation of the circuit.

  The frequency solving method offers a good trade-off between precision and computation time. For example, to calculate the steady state of a three-phase inverter, our frequency solver provided a computation time of 0.15 seconds compared to a PLECS™ simulation time of 1.24 seconds. A frequency solver is also particularly interesting when only specific frequencies need to be calculated (Ex. common-mode simulation). The major drawback of frequency solvers is that transient states or

spontaneous events (diode behavior) are not simulated. As a result, only some topologies are compatible with this kind of solver.

The following table summarizes the advantages and drawbacks of each solver type:

Solver Type	*Advantages (+)*	*Drawbacks (-)*
Analytic	- Short computation time	- Low topology flexibility - Based on hypothesis
Time Domain	- Precision - High topology flexibility	- Long computation time
Frequency	- Intermediate computation time - Simulate specific frequencies (interesting for common mode) - Medium topology flexibility - Direct determination of steady-state waveforms	- Does not simulate spontaneous switching - Does not calculate transient state

Table 2-1 : Advantages and drawbacks of each kind of solver

2.4.2 Frequency solver

Frequency solver is used in the present work as it combines a good trade-off between computation time and flexibility. The spontaneous conduction limitation is not an issue for the design of the inverter topology required in the present study. For the transient specifications, a mix of analytic and time solvers is used. Analytic approximation is used in the optimization process and once the solution is found, the approximation is verified with a time solver (SABER^{TM} in the present work for reasons of availability). The frequency solver used in the design environment has been developed in the Laplace laboratory [30]. It performs three different types of simulations. For each type of simulation, the equivalent model of the switching cell is different. The different simulations are:

- *Average simulation*: the switching cell is represented by its average equivalent mode, which is presented in the following figure.

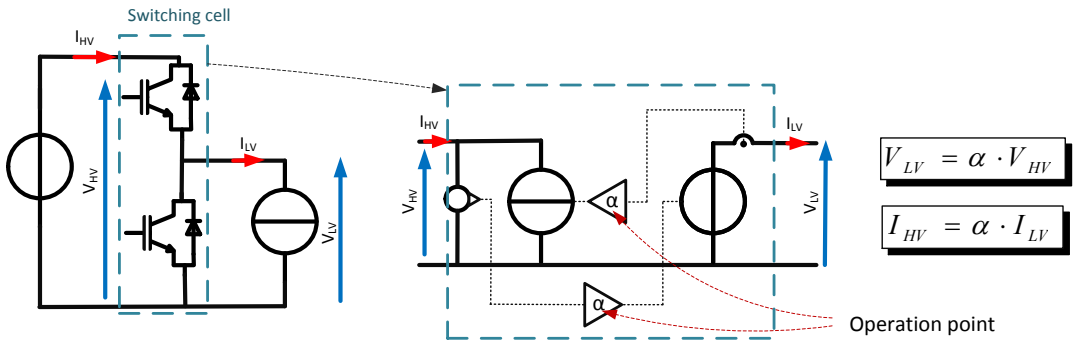


Figure 2.6 : Average model of the switching cell

In the average model, the current and voltages in the low voltage side and high voltage side of the switching cell are coupled: the LV-side voltage depends on the HV voltage and the HV current depends on the LV current. The purpose of this simulation is to extract the necessary waveform amplitudes for the differential simulation ($V_{HVavg.}$ and I_{LVavg}). The discontinuous high frequency behavior of the converter is not considered and therefore only low frequencies can be simulated.

- *Differential simulation*: the high frequency differential-mode behavior of the power converter is considered in this simulation. The equations describing the behavior of a switching cell, using the equations in Figure 2.6 are:

$$V_{LV}(t) = \alpha(t) \cdot V_{HV}(t) \tag{2-1}$$

$$I_{HV}(t) = \alpha(t) \cdot I_{LV}(t) \tag{2-2}$$

When these two expressions are defined in the frequency domain, the following equations can be obtained using the Convolution Theorem [31].

$$V_{LV}(f) = \alpha(f) * V_{HV}(f) \tag{2-3}$$

$$I_{HV}(f) = \alpha(f) * I_{LV}(f) \tag{2-4}$$

The symbol * represents the circular convolution of the two frequency signals. The calculation of the circular convolution of two signals increases enormously the computation time and the memory requirements. In our tests, memory override problems appear when trying to apply convolution for a large number of frequencies. To overcome this problem, the switching cell is represented by an equivalent pair of independent current/voltage sources as shown in Figure 2.7. To calculate the waveforms of each source, the carrier and the reference signals are compared to determine the pulsed-width modulated (PWM) signal. The PWM signal is multiplied by the average values calculated in the previous step ($V_{HVavg.}$ and I_{LVavg}).

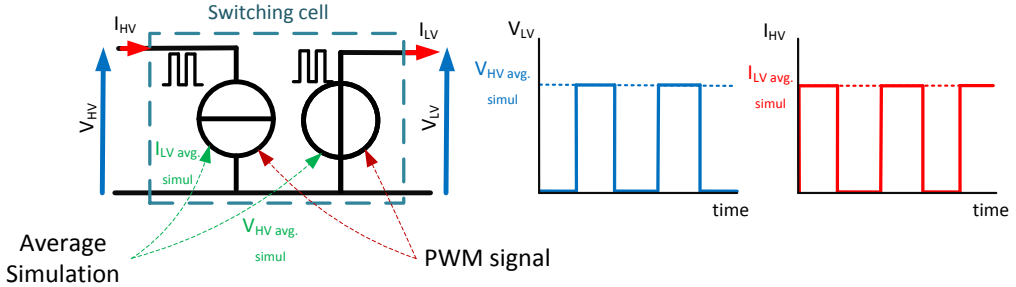


Figure 2.7 : Differential model of the commutation cell

The simplification slightly reduces the precision but it drastically reduces the computation time and memory needs compared to a simulation using signals convolution.

- *Common mode simulation*: in the present work, specifications include limitations on the conducted common-mode currents. Common-mode modelling and design of common mode filters has been treated in numerous works [32][33][34][35]. Most of them employ frequency solvers. Common-mode and differential-mode are coupled phenomena. Voltage variations originated by the differential currents will impact the common-mode currents and vice versa. The simulation of the coupling between both modes has been treated in [36] using frequency solvers, however the trade-off between added precision and computation time is not found interesting for our application. Common mode is separately simulated from the differential mode. In addition, if common mode is separately simulated, the number of frequencies to be calculate is reduced since common mode currents appears normally at high frequencies.

  In power converters, the main conducted common currents are generated by the fast voltage variations created by the switching cell (*dV/dt*) and circulate through the parasitic system capacitances (Heat sink parasitic capacitance…). The resulting common mode simulation model for a single switching cell is presented in Figure 2.8.

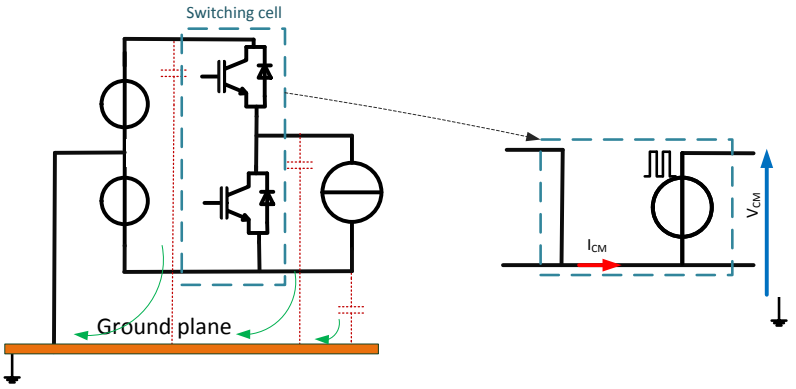


Figure 2.8 : Parasitic capacitances:
(left), origin ; (right), equivalent common mode of the commutation cell)

The common mode voltage at the mid-point of the switching cell is approximated as a trapezoidal waveform. It takes into account the rise (t_r) and fall times (t_{rf}) of the power semiconductors which depends on the technology (IGBT, MOSFET…).

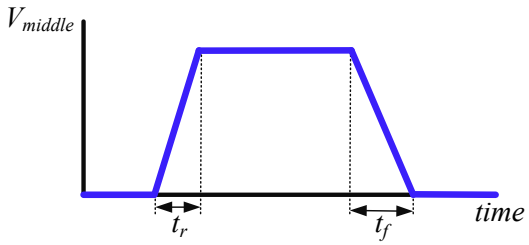


Figure 2.9 : Representation of the trapezoidal waveform

Obviously, trapezoidal behavior is only a vague approximation of experimental waveforms of common mode voltage. A series of phenomena (stray inductance, driver

operations, semiconductor technology….) will generate high frequency harmonics. These high frequency phenomena are not considered in our simulations. The validity of the simulations will be considered fair until a certain frequency F_{val}.

$$F_{val} = \min\left(\frac{1}{t_r}, \frac{1}{t_f}\right) \tag{2-5}$$

The common mode simulation model is validated with the experimental data from [37]. The simulated model is presented in the following figure, more information about common mode impedances values is given in the aforementioned document.

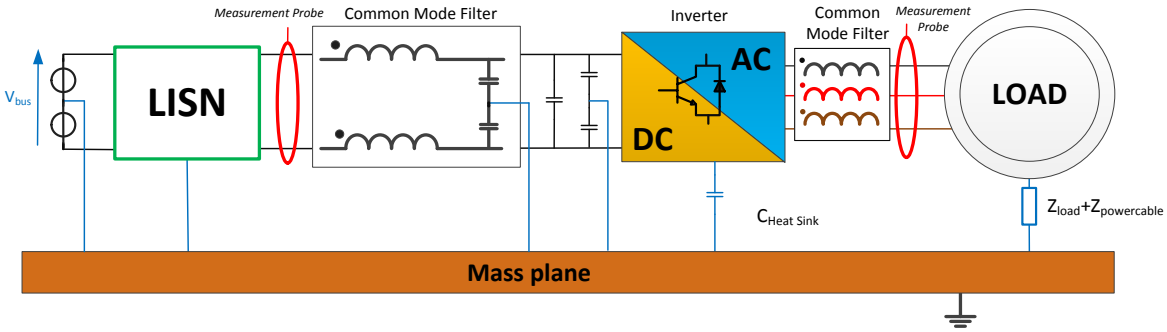


Figure 2.10 : Simulated common mode architecture

In the same document, three experimental tests are performed and compared to a temporal simulation: one without input filters, one with the input filter only and the third one using both common mode filters. The envelope of the experimental data is compared to the simulation data obtained with our common-mode solver. The rise and fall times of the trapeze are fixed at 800ns. The comparison is shown in Figure 2.11, the dashed line defines the limit frequency of validity F_{val}.

At some frequencies the error between the envelope and simulation reaches a few tens of dB. This is the same order of magnitude for the errors in the source document between simulation and experimental data (See example Figure 2.12). As a result, the major source of error may come from common mode paths not taken into account, experimental errors…

The simulation shows the implemented common mode simulation model of the cell is enough to estimate the common mode envelope up to a certain frequency F_{val}=*1/800ns=1.25MHz* (Dashed orange line).

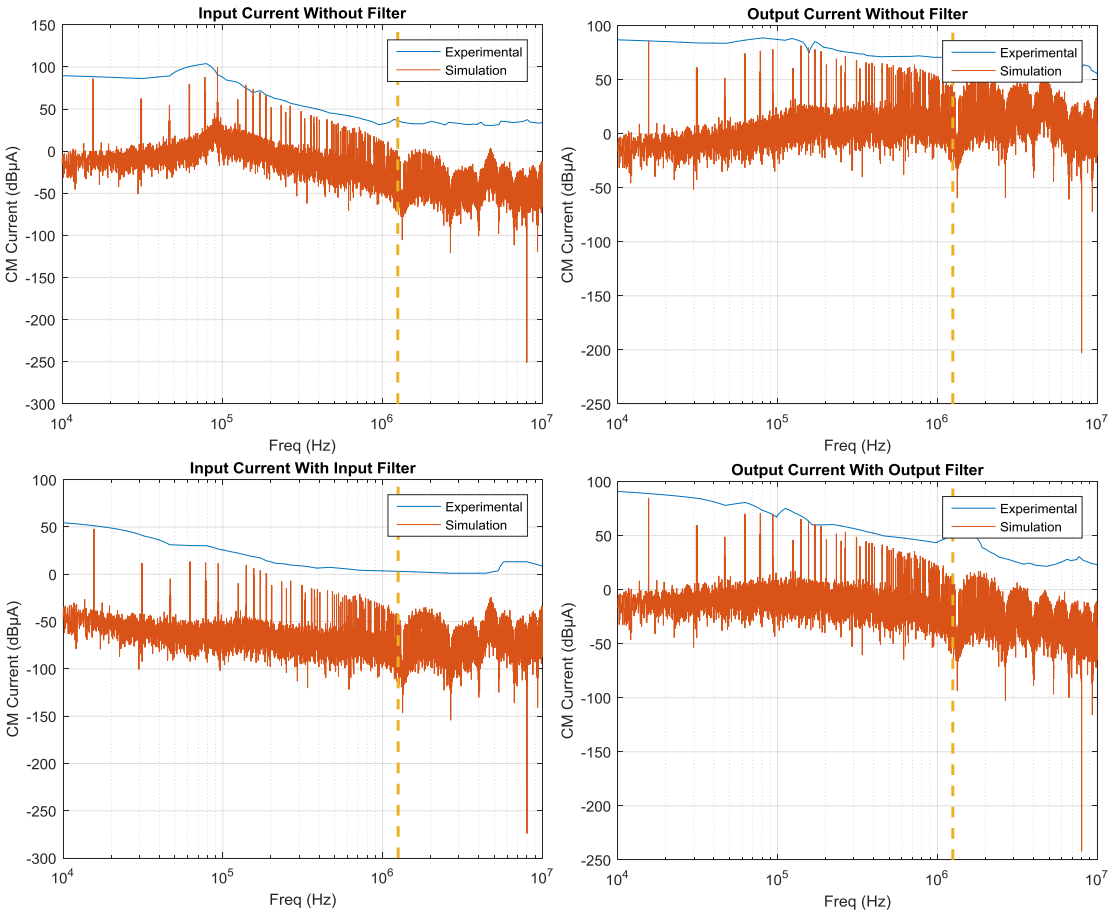


Figure 2.11 : Comparison between experimental (blue) and simulation data (red) for the common mode simulation

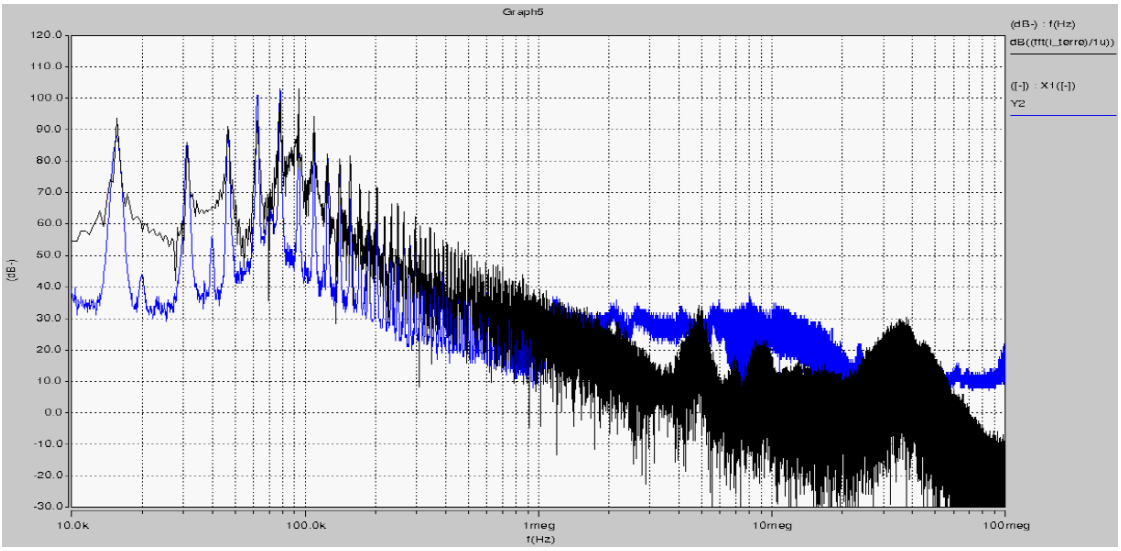


Figure 2.12 : Comparison between temporal simulation (black) and experimental (blue) data for the input common mode current without filter [37]

2.5 Design process

The component models are inserted in an optimization loop to find the best power converter. The whole process algorithm is described in Figure 2.13.

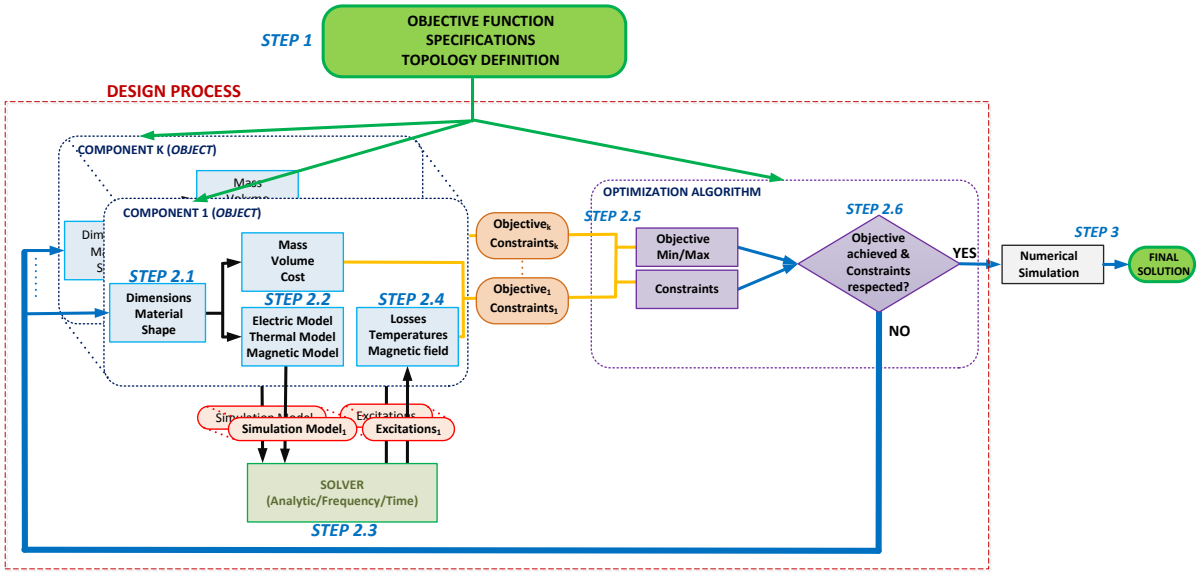


Figure 2.13 : Schematic of the design process with the optimization loop

At the very beginning (step 1), the designer defines the objective function to be optimized (in our case the objective to be minimized is the mass but this objective can be easily changed to losses, volume or cost), the topology (inverter with differential filter) and the particular specifications of our design (maximal temperatures, electrical standards… further details are given in Chapter IV). From the chosen topology, the components to be designed are created and inserted in the design process (step 2). Materials do not change during the optimization process (they are selected at the beginning). The user has two options: he can define the material or use different implemented methods to anticipate the materials that lead to the best result (further specific information are given in Chapter IV). Depending on the optimization algorithm, the initial point determination is critical (step 2.1). The user has again two options: define all the dimensions of the components or use classical implemented methods (area product, ….) to estimate a good starting point.

In any case, some component parameters are directly extracted from the dimensions (“Direct modelling approach”) and the equivalent simulation models are sent to the frequency solver (step 2.2). The solver realizes the assembly into a model of the system; then it performs the simulation and dispatches the waveforms to the component model (excitations of each component, step 2). These excitation waveforms are used to calculate locally (at the component level) some additional information (losses, temperatures…,step 2.4). The contribution of each component to the objective function and constraints are sent to the optimization algorithm (step 2.5). If the point is found to be optimal (in terms of mass for our case) and the constraints are respected, the point will be kept as the final optimal design

solution. Otherwise, the optimization algorithm will change the values of the optimization variables (physical dimensions) to find a possible optimal point (step 2.6).

The final step is to validate the optimal solution with numerical simulation to test if calculations made by the analytical component models for the optimal point are below a certain threshold of relative error. If the comparison is found unsatisfactory, the model needs to be redefined to be more accurate in this specific point. The optimization process finishes once the numerical simulation of the optimized point is in accordance with the values calculated in the optimization process.

2.6 Optimization Algorithms

In the design process, the optimization algorithm is a key element to find the global optimum of the solution. The design problem involves a large number of variables and constraints which increases the chances of finding a local minimum (for example, for the design of the filter, presented in Chapter IV the optimization problem considers 30 optimization variables and 25 constraints). In the present work, all the classes are implemented in the MATLAB™ environment.

First motivation was that the frequency solver was developed under MATLAB™ software and it eases communication between models and solver. Secondly, MATLAB™ already implements a lot of functions, in particular optimization functions. The base line algorithm for all the optimizations is the *fmincon* function (in particular with interior-point method). The *fmincon* function uses mainly gradient-type optimization algorithms to solve nonlinear constrained optimization problems. Gradient-type algorithms are particularly interesting for two reasons: fast convergence time (which is important as in our problems one iteration requires about one second for calculations) and they are deterministic. However, all design variables of the problem and all constraints need to be treated as continuous variables. The discrete variables (number of turns, number of fins…) are treated as continuous during the optimization and in the final result the value is rounded.

Basically, gradient-type optimization algorithms are characterized for using the opposite direction of the objective function gradient to determine their improvement direction (See Figure 2.14). Due to the complexity of the relationships on the objective functions, in our case, the gradient is estimated by finite-differences. There are two main stopping criteria to end the optimization process: when the change in the objective function falls below a certain threshold (Eq. (2-6)) or when the change in the optimization variables to perform the next iteration falls below a certain threshold.

$$\left|f_{i+1} - f_i\right| \leq \varepsilon_{fun} \tag{2-6}$$

$$\left|x_{i+1} - x_i\right| \leq \varepsilon_{var} \tag{2-7}$$

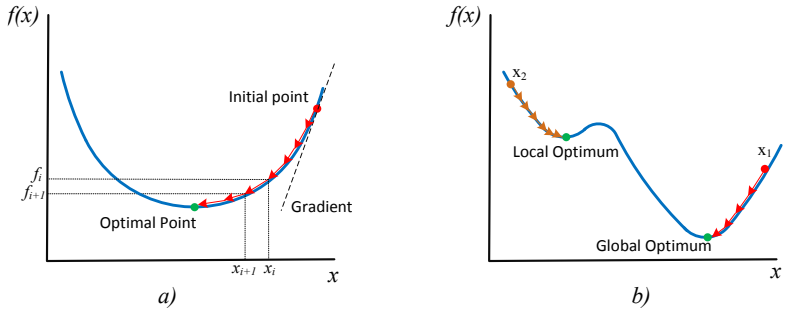


Figure 2.14 : Graphic description of gradient descent algorithm, a) a simple case b) Example of local optimum vs global optimum

Gradient descent algorithm has one major drawback. When the function has various local minima the final result is strongly dependent on the initial point (See Figure 2.14). To overcome this limitation other optimization algorithms can be used to compare the optimum point obtained with gradient descent.

In the design environment, the Genetic Algorithms developed by the Laplace Laboratory are included as well [38][39]. However, they have not been fully tested and therefore they are not treated in this work. Genetic algorithms are an improved version of classical niching genetic algorithms. Niching algorithms keep several local minimums during the optimization process which makes them attractive for multi-objective optimization and Pareto front determination. However, genetic algorithms are stochastic algorithms. The final results may vary from one optimization to another. The Hook & Jeeves optimization algorithm is as well implemented in our design environment [40]. The Hook & Jeeves algorithm is dependent upon the initial start point but in this case it has a capability to avoid convergence towards local minimum. The optimization algorithm developed in the environment is based on the work developed in [41].

2.7 Conclusion

In this chapter, the design approach used to design the generic power inverters of the electric cabinet is presented. To that effect, a library of component models using an object-oriented approach has been created. The components are described under a “direct modelling approach” or response surfaces built from databases. The component behavior is simulated using a solver to ensure proper operation of the power converter and the components. In the present work, a frequency solver is used because of the good trade-off between precision and computation time. To sum up, the solver and the component models are inserted in an optimization loop to ensure a good design of the power converter. The different optimization algorithms used in the present work are as well presented.

In the next chapter, the different mathematical models used for the design of the power inverter are detailed. The different models are validated using experimental data or numerical simulation. These models will build the basis of the model library.

Chapter 3 : Physical components modelling

3.1 Introduction

In this chapter, the main components of the power converter are mathematically represented to perform the optimal design. Even if the components could potentially be used in a large number of different power converter topologies, the present work focuses on designing power inverters. Some of these models come from other works performed at the Laplace laboratory and as a consequence they will be just briefly introduced in the present document.

3.2 Active devices

3.2.1 Converter cell

Loss reduction is a critical parameter in the selection of a semiconductor device as they impact the converter efficiency. In addition, semiconductors have small surfaces from which the heat must be evacuated to avoid temperature rise of the component and device failure. The losses in power semi-conductors are divided into two categories.

- *Conduction losses*: when the device is controlled to be conducting, the I(V) characteristic involves complicated phenomena related to semiconductor physics, but it can be approximated as a piecewise linear characteristic with an ON resistance (R_{dson}) and a threshold voltage V_{th}(the conduction losses in the OFF state are generally negligible). Consequently, the conduction losses for an IGBT are approximated using the following equation.

$$P_{cond} = V_{th} \cdot < I > + R_{dson} \cdot I_{rms}^{\ 2} \tag{3-1}$$

  with $<I>$ the average current and I_{rms} the RMS current circulating in the semiconductor when the semiconductor is in the ON state.

- *Switching losses*: when changing from the ON state to the OFF state or vice-versa some energy is lost. Losses resulting from these switching transition can be classified and related to some physical phenomena as follows:
  - Switching losses independent of current driven by the semiconductor device: e.g. losses associated to the charges stored in the parallel capacitor of the semiconductor,

- Switching losses proportional to the current: e.g. losses due to the voltage.current product during current rise, assuming a constant voltage level,
- Switching losses proportional to the square of the current: losses related to the energy stored in the stray inductance of the switching cell.

Manufacturers sometimes provide the switching energies of power semiconductors for a given operating junction temperature, driver and commutation cell layout. Normally, the switching energies are provided for a certain constant switched voltage (V_{ds}) and a range of switched current (I_{ds}).

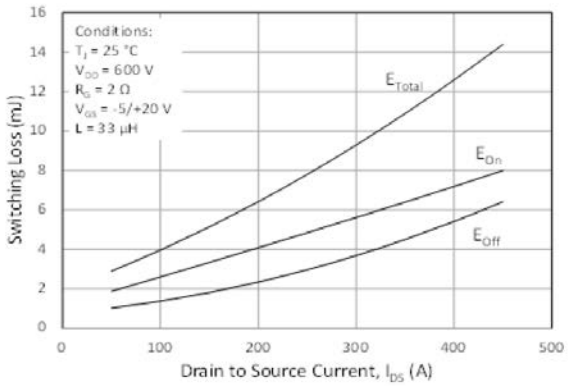


Figure 3.1 : Switching energies vs Drain to source current (Ref. CAS325M12HM2)

In the present work, the data coming from manufacturer datasheets are directly used to estimate the losses of the power converter. It means that we implicitly assume the operating conditions found in the final product are similar to the ones encountered on the experimental bench by the manufacturers: driver, stray inductance, decoupling capacitor, etc… To estimate how energies vary with the switched current, linear interpolation is used and, in order to take into account the actual value of the switched voltage, a linearization around the defined switched voltage is used.

$$E_V = E_{V_{def}} \cdot \left(\frac{V}{V_{def}} \right) \tag{3-2}$$

With E_V the switching energy at a certain voltage V and $E_{V_{def}}$ the switching energy defined by the manufacturer at a specific voltage V_{def}. For example, for the component in Figure 3.1, V_{def} is 600 V.

From the simulation, the waveforms of the circulating current and the differential voltage of the semiconductor are extracted. From the current waveform, the mean and RMS values are calculated and used to estimate the conduction losses as shown in equation (3-1).

The voltage and current waveforms are also used to determine, for each switching event, the voltage and current values and which semiconductor is switching (the transistor or the anti-parallel diode). The switching energies are then calculated as described in the previous part. All switching energies encountered during a T period time interval are summed; the

obtained result is divided by the period T of the waveforms to calculate the switching losses P_{sw}.

$$P_{sw} = \frac{\sum E_{ON} + \sum E_{OFF} + \sum E_{rec}}{T} \tag{3-3}$$

With:

- E_{ON} the switching energy to close the transistor,
- E_{OFF} the switching energy to open the transistor,
- E_{rec} the recovery energy of the diode.

The implemented algorithm is presented in the Figure 3.2.

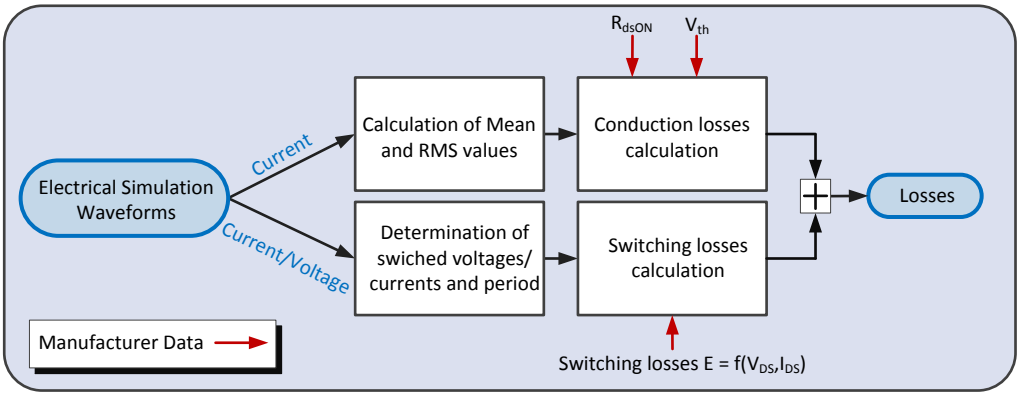


Figure 3.2 : Loss calculation algorithm

3.2.2 Wide band-gap semiconductors

Over the last decades, all the semiconductor devices have used Si-based technologies. However, these devices are now reaching their technological limits. In recent years, the wide-band gap materials (*SiC* et *GaN*) have been introduced in the field of power conversion. *SiC* components are mainly MOSFETs while *GaN* devices use a quite specific High-Electron-Mobility Transistor (HEMT) structure [42]. It has been theoretically shown in the 80s that wide band-gap devices were able to reach better performances; however, such devices became commercially available only recently. As a result, they are not available at high scales of production and they have a limited maturity in industrial applications. The wide band-gap components have several advantages compared to classical *Si* devices:

- lower R_{dson} resistance for the same semiconductor surface and voltage threshold,

- higher operating temperature limit,

- faster commutation, thus reduction of the switching losses.

The reduction of switching energies is a gain in itself, indeed the losses of the power converter are reduced. As a result, we can increase the switching frequency thus reducing the

size and weight of passive components in the filters [14]. However, there are still some drawbacks to overcome:

- the higher *dV/dt* and *dI/dt* generated by the switching cell impacts EMC disturbances and the consequence on common mode filters needs to be considered [43], these high voltage transitions are a source of overvoltage in long cables [44],
- fast commutations imply a control circuit capable of creating fast transitions. Special attention must be paid to the minimization of loop inductance and to the design of semiconductor packaging [42].

Nevertheless, wide band-gap devices seem to be a promising technology for power conversion in civil aircraft domains. Indeed, loss reduction could lead to air-cooling solutions [45] thus avoiding the heavy today's hydraulic cooling. MOSFET SiC is the only semiconductor technology used for loss calculation in the present work as it has been found more appropriate to work with the new HVDC voltage level (more than 540 V).

To illustrate the advantages of wide band-gap semiconductors, the figure of merit of all semiconductors available in our database is displayed in the $Q_g(R_{dson})$ plane (gate charge, ON resistance). These quantities are somehow related to respectively the switching and the conduction losses. Devices closer to the (1,1) coordinate produce therefore less losses for the same operating conditions.

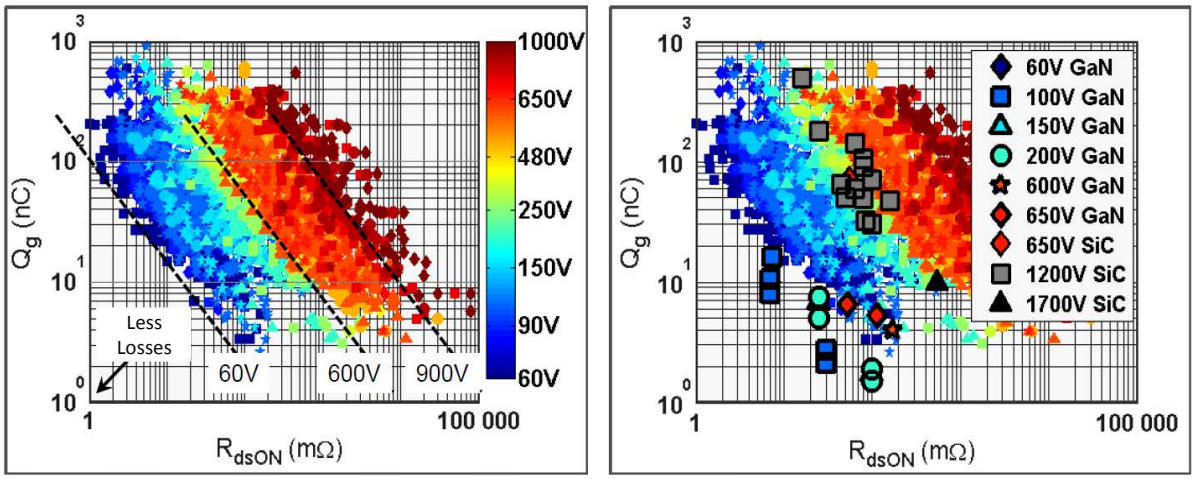


Figure 3.3 : Figure of merit Qg vs RdsON for different reference data a) Si based b) GaN & SiC devices compared to Si-based[25]

As shown in this figure, for the same nominal voltage, wide-band gap semiconductors provide better performances. For example, if the 600V GaN is taken at reference it is shown how this component is closer to the origin (1mΩ, 1nC) than the 600 V Si-based (dashed line), meaning it will have lower losses for the same operation condition.

3.2.3 Nominal current increment of power semiconductors

To reduce the conduction losses and the thermal resistance the dies are connected in parallel. However, paralleling power semiconductors implies ensuring current balance in all the dies and a synchronous command of all devices in parallel. In fast switching *SiC* or *GaN* devices, stray inductance on the control loop becomes a major concern and efficient strategies need to be assessed [46].

There are two different ways of paralleling power semiconductors:

- *Discrete paralleling*: discrete devices in standard packages (TO-247, TO-220…) are used in parallel in the converter. The design of the control loop and the thermal isolation becomes a crucial design parameter. This approach is convenient when a reduced number of semiconductors need to be parallelized. The advantage is the high degree of freedom on the design.
- *Power module*: the dies are integrated by the manufacturer in a larger package (module) to form a single switching device. The stray inductance of the control loop can be optimized and the thermal resistance of the module can be reduced. In addition, the dies can be electrically insulated in the module. The main advantage of this solution is the high degree of integration, the ease of assembly and the reduced cost of the design. However, flexibility is reduced.

In the present work, the high currents on each cell make semiconductors paralleling necessary. A bare MOSFET SiC die can provide tens of amperes but in our applications we need currents above one hundred amperes. Power modules are therefore chosen to build the switching cell. Power modules reduce design costs and at the same time, they offer better performances in terms of control and thermal constraints balance (which is a very important concerning the thermal management).

3.3 Passive components

Passive components are divided into two groups: magnetic devices and capacitors. Modelling and optimization of these components, especially magnetic devices, is a key factor to improve the power density of power converters.

3.3.1 Magnetic components

All magnetic components are created by the assembly of three elements: the winding, the magnetic core and the insulation (Not treated in detail in this work). From Faraday's law, the inductance L of a given coil arranged around a given magnetic core is related to the electro motive force (*emf*) generated to counter a certain current variation.

$$emf = -N\frac{d\phi}{dt} = -L\frac{dI}{dt} \tag{3-4}$$

Where:

- N represents the number of turns of the coil
- ϕ is the magnetic flux in the core
- I is the current

The magnetic behavior of an inductor is often described by its analog magnetic circuit model. The Gauss's and Ampere's laws are assimilated as the Kirchoff's current and voltage laws. As a result, the magnetomotive force (*mmf*) and the magnetic flux are expressed as the "effort" and "flux" variables of the model of the magnetic circuit. By analogy with the "electrical resistance", the "reluctance" variable expresses the relationship between the effort and flux variables.

$$R = \frac{mmf}{\phi} \tag{3-5}$$

These definitions lead to the reluctance equivalent model of the inductor. A representation of this model is presented in Figure 3.4. This model takes into account the electro-magnetical coupling between variables which is expressed according to Lenz's law and the definition of the magnetomotive force.

$$mmf = N \cdot I \tag{3-6}$$

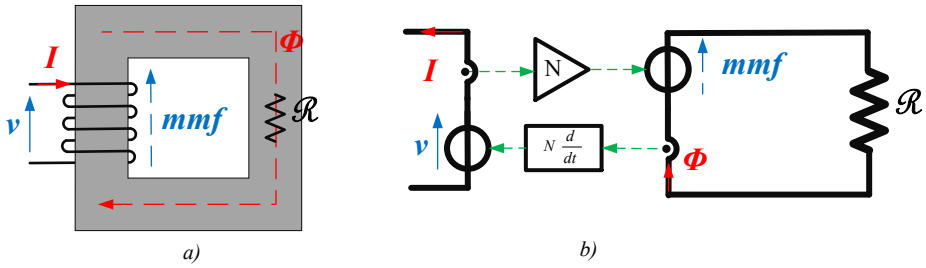


Figure 3.4 : Inductor, a) Physical device, b) Equivalent reluctance model

The reluctance of the circuit is also in relation with the core dimensions and properties with the following expression:

$$R = \frac{l}{\mu_r \cdot \mu_0 \cdot A} \tag{3-7}$$

in which :

- l represents the length of the magnetic path,
- A the effective magnetic area of the core,
- μ_0 is the air magnetic permeability,
- μ_r is the relative permeability of the core material.

Magnetic cores are available in different shapes *Toroid, E, U, I* ,… and for different magnetic materials.

3.3.1.1 Magnetic materials

Using the definitions of the previous sections, the inductance is directly related to the reluctance value:

$$L = \frac{N^2}{R} = \frac{N^2 \cdot \mu_r \cdot \mu_0 \cdot A}{l} \tag{3-8}$$

As a result, magnetic core made of materials with a high permeability μ_r allow reducing the volume of the component (which is proportional to the product $A \cdot l$). However, the choice of the magnetic core is not a simple task and is highly dependent on several parameters:

- operating frequency,
- permeability,
- shape,
- maximal saturation induction,
- losses,
- Curie temperature,
- density,
- variation of the aforementioned properties with frequency, temperature and magnetic field.

Magnetic materials are mainly divided into two sub-categories: soft materials and hard materials. Soft materials are characterized for a low coercitive field and are used in power electronics applications because of their reduced hysteresis losses. Soft materials are classified in different groups:

- *Soft iron* is used mainly in magnetic assemblies that withstand high magnetic fields (up to 2,16 T) or in large components because of its low cost. However, due to the high conductivity, eddy current losses make them inappropriate for high efficiency converters. To overcome this drawback, iron is laminated or mixed with Silicon (Fe-Si alloys) to increase resistivity. These materials have a high Curie temperature.
- *Iron alloys* are a combination of iron and other components (Fe-Ni, Fe-Co): their main characteristic is their high permeability. However, they have a high cost, especially when cobalt alloys are concerned.
- *Ferrites* are ceramic materials with high resistivity. They are used for high-frequency applications because of their low core losses (Prevention of eddy currents). Another advantages is their lower cost. Their main limitation is their low

saturation field. Also, ferrites are hard and brittle at the same time and it makes them difficult to machine. They are manufactured in different shapes by compression of powders before sintering and can be mechanically assembled to generate bigger cores.

- *Amorphous and nanocrystalline alloys* provide a combination of reduced core losses and high saturation levels (more than 1.5T). They are used at high frequency (> 1MHz) and their properties are stable with temperature and DC magnetic fields. Their major drawbacks are a high cost and the limited number of core shapes (mainly toroids and U cores).
- *Iron powders* are composed of an insulation material matrix in which the metal powder is inserted. The objective is to create a distributed air gap within the core. Iron powders are characterized by a low permeability and high magnetic saturation field, thus having a large energy storage capacity. Their main drawback is a relatively high level of core losses at high frequencies.

As it can be shown, there is a wide range of different magnetic soft materials with different properties that have a large impact in the design of magnetic components.

3.3.1.2 Core Losses

On magnetic materials there are two main sources of losses: winding losses in the conductor material and core losses in the magnetic material. Core losses are divided in three phenomena:

- hysteresis losses, caused by rapid jumps of the domain walls that are responsible for the non-reversibility of the magnetizing curve [47],
- eddy current losses caused by the currents generated inside the core due to the variable magnetic field,
- extra losses due to ferromagnetic resonance and inter-granular barrier losses.

Core losses depend on frequency, magnetic field and temperature. Manufacturers provide datasheets with the loss density as a function of the three parameters considering a sinusoidal excitation. The data provided by manufacturers is classically fitted with an analytic expression. The most generalized expression to calculate core losses (P_c) is the Steinmetz equation [48]:

$$P_c = Vol \cdot k \cdot f^{\alpha} \cdot B^{\beta} \tag{3-9}$$

in which k, α, β are coefficients dependent on the material and obtained from the manufacturer, Vol is the volume, and f and B being are respectively the frequency and amplitude of the magnetic field density. However, core losses vary with temperature. This dependence if often assumed in a quadratic form:

$$P_c = (K_2 \cdot T^2 - K_1 T + K_0) \cdot Vol \cdot k \cdot f^{\alpha} \cdot B^{\beta} \tag{3-10}$$

In this equation, T represents the core temperature. Temperature dependence is a parabola and its shape is important because its minimum determines the limit temperature of the material before thermal runaway temperature. Steinmetz coefficients are valid only for a certain range of frequency and magnetic fields. In [49], the authors propose a new model (referred as the "Forest model") to take into account a slight variation of the Steinmetz coefficients with the frequency and widen the validity domain:

$$P_c = Vol \cdot k \cdot (s \cdot f^{\alpha_s} + u \cdot f^{\alpha_u}) \cdot B^{(\beta + z \cdot f)} \tag{3-11}$$

with s, u, α_s, α_u, β and z empirical coefficients determined by fitting of experimental datasheet characteristics.

However, these two formulas still have a major limitation: they are only valid for sinusoidal excitations, and in power electronics, this is almost never the case. PWM imposes square or quasi-square voltage waveforms across the windings that impose asymmetrical triangular induction in most magnetic components. The non-linearity of the physical phenomena ruling losses does not allow using the superposition method to evaluate losses in such conditions. Further works tried to improve the Steinmetz formula to take into account minor hysteresis loops. This led to the *Improved Generalized Steinmetz Equation (IGSE)* (referred to as the "Sullivan model") [50]:

$$P_c = Vol \cdot \frac{1}{T} \int_0^T k_i \left| \frac{dB}{dt} \right|^{\alpha} (\Delta B)^{\beta - \alpha} dt \tag{3-12}$$

$$k_i = \frac{k}{(2\pi)^{\alpha - 1} \int_0^{2\pi} |\cos\theta|^{\alpha} \cdot 2^{\beta - \alpha} d\theta} \tag{3-13}$$

where k, α, β are the Steinmetz parameters and ΔB is the peak-to-peak flux density.

In [50], an algorithm is explained to extract the minor loops of any waveform. This approach can be combined to the previous, thus giving the "Forest & Sullivan model", that is implemented in the present work:

$$P_c = Vol \cdot \frac{1}{T} \int_0^T k_1 \left| \frac{dB}{dt} \right|^{\alpha_s} (\Delta B)^{\beta - \alpha_s + \frac{z}{dt}} dt + Vol \cdot \frac{1}{T} \int_0^T k_2 \left| \frac{dB}{dt} \right|^{\alpha_u} (\Delta B)^{\beta - \alpha_u + \frac{z}{dt}} dt \tag{3-14}$$

$$k_1 = \frac{k \cdot s}{(2\pi)^{\alpha_s - 1} \int_0^{2\pi} |\cos\theta|^{\alpha_s} \cdot 2^{\beta - \alpha_s} d\theta} \tag{3-15}$$

$$k_2 = \frac{k \cdot u}{(2\pi)^{\alpha_u - 1} \int_0^{2\pi} |\cos\theta|^{\alpha_u} \cdot 2^{\beta - \alpha_u} d\theta} \tag{3-16}$$

Calculating exactly the core losses is complex and it is still a subject under investigation. The main drawback of the iGSE and "Forest & Sullivan" models is that they do not consider the relaxation effects and the DC bias. Other methods, i^{2}GSE [51], mapping losses [52]…

solve some of these drawbacks, however they require parameters that must be obtained through experimentation. A large amount of time and experimental setups is necessary. This major drawback makes them not suitable for the present work as in our design we want to compare a large number of materials.

The implemented iGSE model is compared to experimental data. The source of the data and the experimental setup is described in [53]. Two materials, 2065SA1 and Megaflux, are used to create 3 different inductors used in a DC-DC boost converter. The comparison between experimental data and losses obtained with the iGSE model implemented in the present work is shown in Figure 3.5.

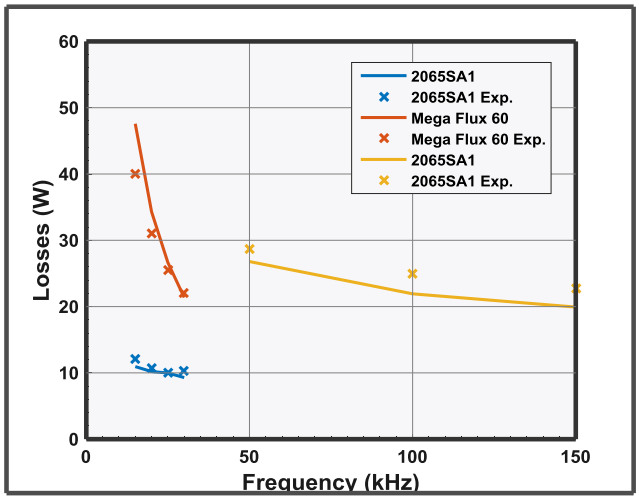


Figure 3.5 : Comparison between experimental and theoretical losses

As shown, there is a difference between the theoretical and experimental data. The first cause that we are certain of is the approximation made by the Steinmetz coefficients. The Steinmetz formula does not fit 100% to the manufacturer data. In the present work the average error between the manufacturer data and the approximation formulas (Steinmetz, Forest model) was estimated at 11,3%. Second, as previously said the "Forest & Sullivan" model does not take into account all phenomena like for example the DC bias in the boost converter. However, in this second point no further assessment was performed. The conclusion is that the "Forest & Sullivan" model offers good performances for the present case of study. Further work could be made to enhance the model, but it is already considered good enough to start working.

3.3.1.3 Winding

The main winding shapes used in current state of the art are foil conductors and round wires. Foils are normally better adapted to high switching frequencies and allow a better use of available space. However, they are not adapted to toroidal shapes and special attention must be paid to parasitic capacitances. When enclosed by a magnetic material and properly disposed, round conductors have higher frequency losses for the same winding section compared to thin foil windings [47]. Litz round wires are composed of multiple twisted

smaller wires and they allow reducing high frequency losses. However this is only valid up to a certain frequency where Litz wire resistance surpasses solid round wire again.

The geometric disposition of the winding influences as well the winding losses. In magnetic components with more than one phase, optimized interleaving of windings reduces enormously high frequency losses in the winding; this is applied particularly in high frequency transformers and coupled inductors [54].

The most employed winding materials are copper and aluminum. Copper is thermally and electrically more interesting (37% lower resistivity and 69% higher thermal conductivity than aluminum). However, when the mass or cost becomes critical parameters, it is often replaced by aluminium. As shown, selection of the optimal combination of conductor and magnetic materials is an important subject that determines the final design of the magnetic component and a separate discussion is given on this topic in Chapter IV.

Winding losses are proportional to the square of the *rms* current and the magnitude relating both variables is called resistance of the material *R*. Winding losses are expressed as follows.

$$P_{winding} = P_{joule} = R \cdot I_{rms}^2 \tag{3-17}$$

The resistance of a certain winding increases with the frequency as a consequence of the skin and proximity effects.

3.3.1.4 Skin effect

Skin effect is the redistribution of the current density in a conductor section caused by the magnetic field from the circulating current in the conductor itself. A representation of the phenomena is shown in Figure 3.6.

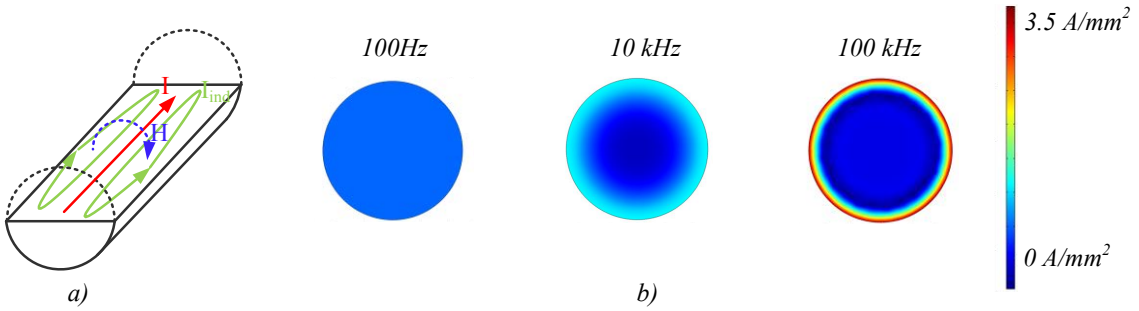


Figure 3.6 : Skin effect in a round conductor
a) 3D representation of currents, b) Current density at different frequencies

As shown, the current circulating in the conductor (red) creates a magnetic field (blue) generating currents (green) in the conductor itself. These currents are called “eddy currents”. The sum of all the generated eddy currents increases the current density near the surface and decreases the current density in the section center. It can be represented as a reduction of the effective area, thus increasing wire resistance and losses. To take into account skin effect, the losses are multiplied by a correction factor as shown in the following formula.

$$P_{skin} = F \cdot R_{DC} \cdot I_{rms}^2 \tag{3-18}$$

with F a function depending of the frequency to consider resistance variation due to skin effect losses, I_{rms} the RMS value current and R_{DC} the DC resistance.

In the present work, for the calculation of function F the winding is considered as infinite and only 2D effects are considered. Error due to the 2D hypothesis compared to 3D calculation has not been treated in the present work. In the case of solid round conductor, the following equations give the exact resistance value for a conductor of infinite length (L>>d)[55].

$$\delta = \frac{1}{\sqrt{\pi \sigma \mu f}} \tag{3-19}$$

$$\xi = \frac{d}{\sqrt{2} \cdot \delta} \tag{3-20}$$

$$F = \frac{\xi}{4\sqrt{2}} \left(\frac{ber_0(\xi) bei_1(\xi) - ber_0(\xi) ber_1(\xi)}{ber_1(\xi)^2 + bei_1(\xi)^2} - \frac{bei_0(\xi) ber_1(\xi) + bei_0(\xi) bei_1(\xi)}{ber_1(\xi)^2 + bei_1(\xi)^2} \right) \tag{3-21}$$

with f the frequency, d the diameter of the conductor, ber_n and bei_n the real and imaginary parts of the Kelvin function of order n ($n=0,1$), σ the electrical conductivity and μ the magnetic permeability.

For the foil conductors, normally the Dowell formula is used [56] to calculate the F function value:

$$\delta = \frac{1}{\sqrt{\pi \sigma \mu f}} \tag{3-22}$$

$$X = \frac{t}{\delta} \tag{3-23}$$

$$F = X \frac{\sinh 2X + \sin 2X}{\cosh 2X - \cos 2X} \tag{3-24}$$

However, this formula makes the assumption that the width of the winding t is smaller than the height h ($t<<h$). In Figure 3.8, the Dowell formula is compared to Finite Element results for both round and rectangular conductors. It can be seen that the analytic formula is inaccurate in case 2 when the hypotheses are not respected (in case 1 $t=0.04h$ while in case 2 $t=h$). As a result, these hypotheses limit the exploration area where the formula will be valid, which makes the formula unsuitable for optimization processes because a large variety of cases are going to be explored.

To overcome the limitations of the Dowell formula, a map of discrete points is calculated using finite element analysis. Magnetostatic calculations are performed on 2D geometries using FEMM^{TM} software for a whole set of different points. A similar approach using a parameter reduction was performed in [57]. From the resulting points, a response surface is created using linear interpolation between nearest points. In addition, the calculated data

points are used in a grid form to reduce computation time. The surface has three inputs which are:

- frequency,
- height of the foil,
- width of the foil.

The interpolation calculation is performed by the *griddedInterpolant* class developed by MATLAB™. Gridded interpolation computation time is shorter than any other interpolation method provided in MATLAB™ [58] and it is well adapted for a large number of variables.

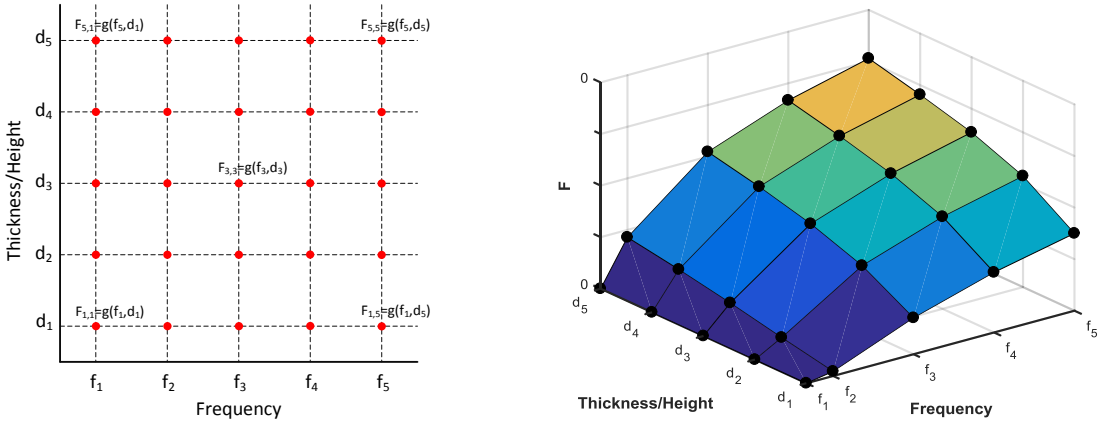


Figure 3.7 : Skin effect in windings
left) grid representation of main parameters& right) Interpolation surface

Grid points must be equally distributed between their maximal and minimal value. However, the data base is iteratively fed. That is, when the optimal design is obtained, a numerical simulation is performed. If the numerical simulation is not within a certain error range compared to the interpolation surface, the point is inserted in the surface. This approach is interesting from a multiple-user point of the view. As more points are inserted in the surface a higher precision of the surface will be obtained.

In Figure 3.8, analytic results, interpolation method results and FEMM simulations are compared.

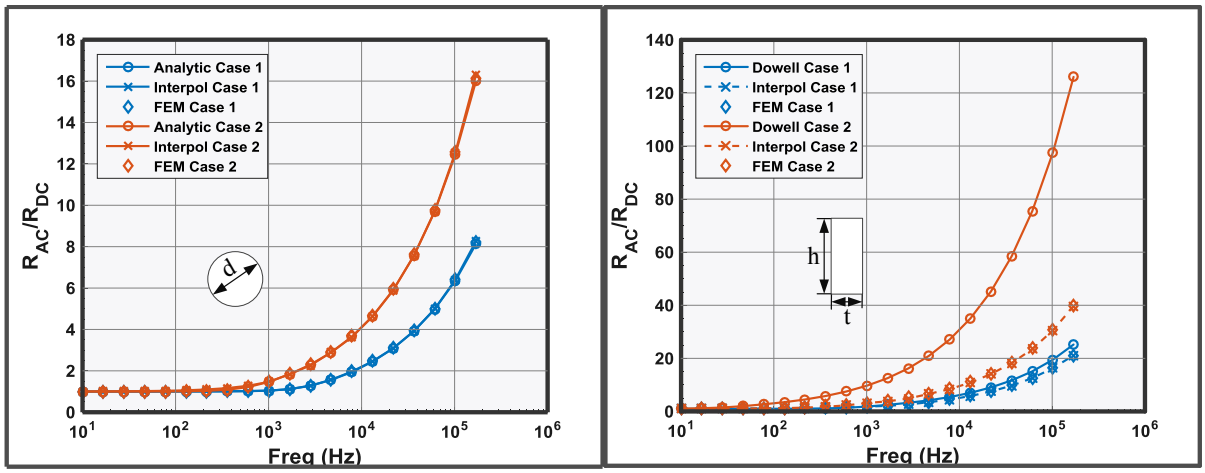


Figure 3.8 : Comparison between analytic, interpolation model and FEMM^{TM} simulation of skin effect (Left) for round conductor (Case 1: d=5mm, Case 2: d=10mm) (Right) for rectangular conductor (Case 1: h=100mm, t=4mm, Case 2: h=20mm, t=20mm)

As shown, the analytic formula for round conductors fits perfectly to the FEMM simulations and the interpolation. As a consequence, the analytic formula is kept to model the skin effect. For foil conductors the analytic formula does not provide enough precision and is discarded. The interpolation surface method on the other hand shows a 2% relative error, which is accepted in the present study; it can be used for f in [1Hz, 150 kHz], h in [0.5mm, 100mm], t in [0.5mm, 100mm]. The points outside the grid are estimated as well with linear extrapolation. In any case, the method allows the inclusion of further points, thus increasing the precision.

3.3.1.5 Proximity effect

Proximity effect is the redistribution of the current density in a conductor section caused by an external magnetic field. A schematic representation of the phenomena is shown in Figure 3.9.

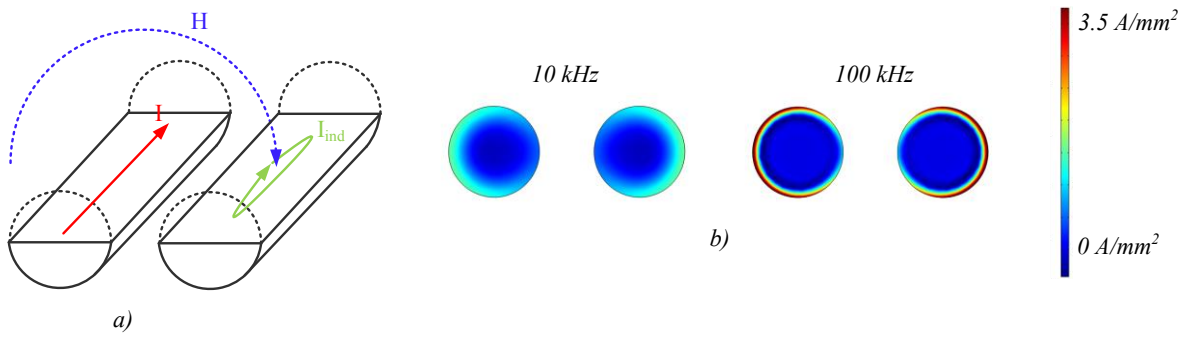


Figure 3.9 : a) Representation of skin effect, b) Current density representation at different frequencies

The phenomena explanation is similar to the skin effect except that the magnetic field originating the currents is external to the conductor. Proximity effect is another effect that can be seen as reducing the effective area where the current circulates, or increasing the apparent resistance. Disposition of the conductors is an important parameter to be taken into account. Innovative interleaving techniques can lead to the reduction of current losses [54]. Special attention must be paid when including the air gap. Fringing effect originated by the air gap leads to an increase of the losses in the neighboring windings. The expression to estimate proximity effect losses is analogous to the skin effect losses except that this time the external magnetic field is used.

$$P_{prox} = G \cdot R_{DC} \cdot H^2 \tag{3-25}$$

with G the proximity factor to take into account the proximity effect losses and H the RMS value of the external magnetic.

Calculation of the magnetic field in the conductors can be approximately calculated for the window of transformer [56] or ICT [59] where the magnetic field is considered one dimensional (1D). Considering this strong hypothesis and making some assumptions, Dowell established a relationship to calculate the magnetic field in a transformer with foil conductors [56]. From this calculation the proximity effect losses are calculated as follows:

$$P_{prox} = R_{DC} \cdot 2 \cdot X \cdot \frac{m^2 - 1}{3} \frac{\sinh X - \sin X}{\cosh X + \cos X} {I_{rms}}^2 \tag{3-26}$$

with m the number of layers, X is calculated with the equations (3-22)(3-23) and I_{rms} is the RMS current.

In round conductors, the analytical expression was published in [60]. The Dowell formula (3-26) is traditionally used as well to estimate proximity effect losses in power inductors. Indeed, due to the lack of any other analytic expression, Dowell's formula is used to calculate the proximity effect in inductors. However, as shown in Figure 3.10, the formula is found inaccurate, especially when air-gaps are involved (Case 1) (For the two formulas, the skin effect based on the surface response was used). An approach similar to the one employed for the skin effect in foil conductors is used. As results, a grid using finite element calculations is deployed to extract an interpolation surface. However, this time the number of variables to consider increases, up to 8 in our interpolation approach. These variables are:

- frequency,
- height of the foil,
- width of the foil,
- number of turns,
- distance between turns,

- air gap,
- width of the core leg,
- magnetic permeability of the core.

In Figure 3.10, the comparison between the interpolation surface and the numerical simulations are shown. Even if this approach seems extremely interesting, (error below 26% for the two cases), it is not adapted to be used with grid data. Indeed, including iteratively new points means recalculating a lot of combinations because of the high number of interpolation variables. In future works, variable reduction techniques and other interpolation methods should be studied to correct this drawback.

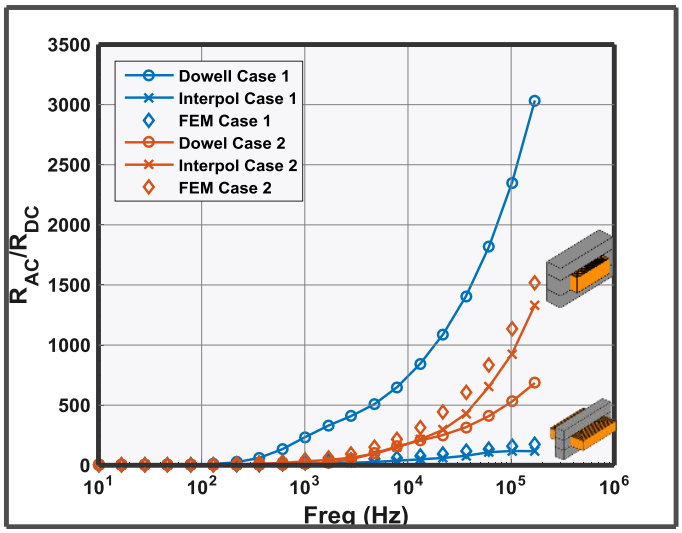


Figure 3.10 : Comparison between interpolation model and FEMM calculations taking into account proximity and skin effect

3.3.1.6 Circuit modelling

As stated in chapter II, a simulation model is needed for each component. In the case of magnetic components, the magnetic behavior must be simulated. A classic approach to simulate magnetic behavior involves using the reluctance model presented in section 3.3.1.

The main disadvantage of this modelling is the derivate/integral term to simulate the electrical-magnetic coupling (See equation (3-4)). An approach to avoid derivate/integral operation is to consider on the magnetic part, not the flux but the derivative of the flux. The induction tube is represented as a capacitor and it represents the permeance of the magnetic material [61]. The electro-magnetic coupling is substituted by a gyrator element.

$$mmf = N \cdot I \tag{3-27}$$

$$v = N \cdot \dot{\phi} \tag{3-28}$$

$$C = \frac{d(mmf)/dt}{\dot{\phi}} \tag{3-29}$$

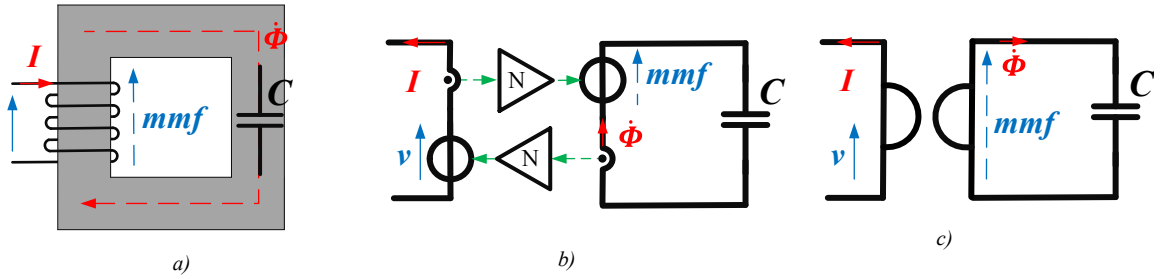


Figure 3.11 : Inductor a) Physical component, b) Permeance-capacitor model, c) Gyrator-based representation

Instead of using the gyrator element, another similar approach is to use a simulation transformer element. This approach was first introduced in [62]. The derivative of the magnetic flux is analogous to an "effort" and the electromotive force to a "flux". The permeance is represented by an inductor.

$$L = \frac{d(mmf)/dt}{\dot{\phi}} \tag{3-30}$$

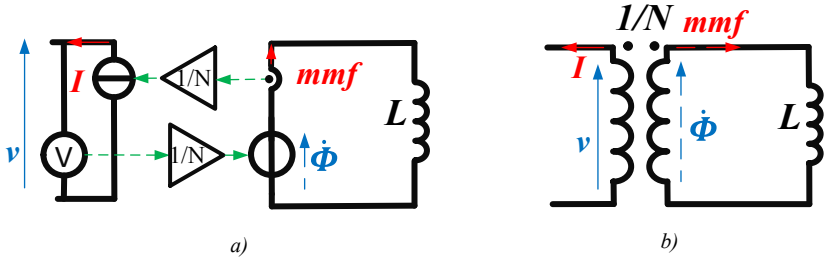


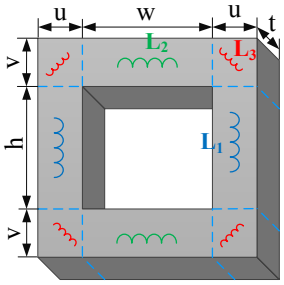
Figure 3.12 : Permeance-inductor model ; a) with controlled sources, b) with a transformer

The permeance-inductor modelling keeps all the advantages of the permeance-capacitance modelling and is better adapted to complex magnetic shapes when interleaving the conductors of the different phases [25].

3.3.1.7 Permeance-inductor calculation

To estimate the permeance-inductor values, the following formulas are used for the magnetic length and area of each section of the magnetic core. These formulas are based on

the reluctance calculation from [47]. A special attention must be paid to the core corners where the flux lines concentrate closer to the window. A simple "quarter radius" approximation is used in this section. The magnetic permeability is supposed constant. Future works should overcome this hypothesis and take into account the variation with temperature, magnetic field and frequency.



Parameter	*l*	*A*	Permeance
L_1	h	$u \cdot t$	$\frac{\mu \cdot u \cdot t}{h}$
L_2	w	$v \cdot t$	$\frac{\mu \cdot v \cdot t}{h}$
L_3	$\frac{\pi}{8} \cdot (u+v)$	$\frac{(u+v) \cdot t}{2}$	$\frac{4 \cdot \mu \cdot t}{\pi}$

Figure 3.13 : Permeance-inductor representation and analytic formulas

3.3.1.8 Core losses equivalent resistance

Core losses are also represented in the permeance-inductor modelling with an equivalent resistor. For a given *rms* flux derivative $\dot{\Phi}_{rms}$ in a core volume, core losses are calculated with the following expression:

$$P_{core} = \frac{\dot{\Phi}_{rms}^2}{R_{core}} \tag{3-31}$$

The core losses for a sinusoidal waveform are also calculated with the Steinmetz formula Eq. (3-9). Thus the core losses equivalent resistance is expressed as follows:

$$R_{core} = \frac{\dot{\Phi}_{rms}^2}{Vol \cdot k \cdot f^{\alpha} \cdot B^{\beta}} = \frac{\dot{B}_{rms}^2}{A^2 \cdot Vol \cdot k \cdot f^{\alpha} \cdot B^{\beta}} \tag{3-32}$$

In addition, as the resolution is performed with a frequency solver, the core resistance frequency behavior is easy represented. Another simplification is performed in the previous expression; coefficient β is approximated to 2 (For example, in our core data bases for the Steinmetz formula β varies between 1.8 and 2.8 meaning our approximation is reasonable). The core losses equivalent resistor is then:

$$R_{core} = \frac{f^{2-\alpha} \cdot 2\pi^2}{A^2 \cdot Vol \cdot k} \tag{3-33}$$

In this work, R_{core}, the resistance representing core loss is only an approximation. It allows taking the core losses into account in the simulation but is not intended to calculate them exactly (Indeed, the physical total core loss is not the sum of the loss for each harmonic and the β coefficient has been approximated to 2 for the simulations).

3.3.1.9 Thermal behavior

Winding and core losses are transformed into heat that needs to be evacuated to remain at a safe temperature. In magnetic devices, the three heat transfer phenomena (conduction, convection and radiation) are involved and need to be represented. The thermal model is simulated by a network of thermal resistances as shown in the following figures.

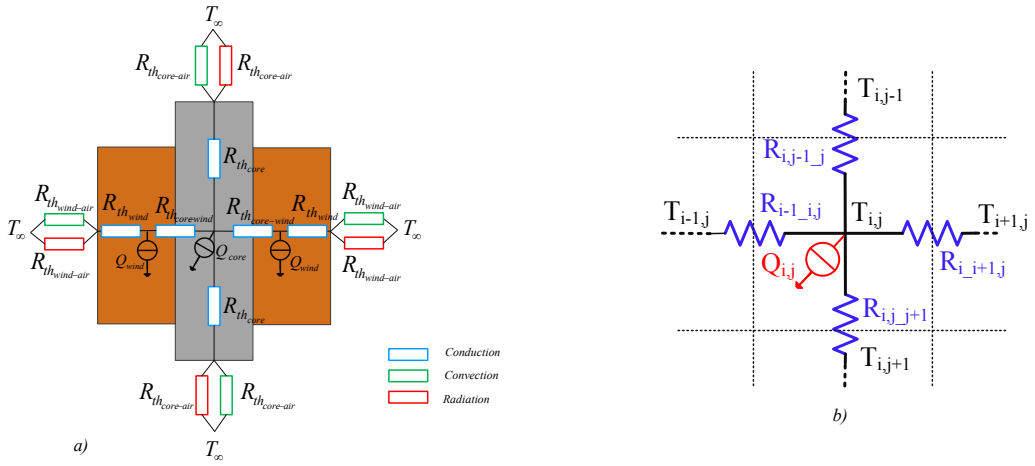


Figure 3.14 : 2D thermal modelling of magnetic components ,
a) General view, b) local zoom

For all the considered magnetic components, the calculation of the temperatures is made using a linear system of equations that can be represented in a matrix form as follows:

$$[A][T]=[Q] \tag{3-34}$$

For a thermal network of *m* nodes or temperature values, A is a *mxm* matrix describing the thermal resistor network, *T* is the vector *mx1* of temperatures and *Q* is a vector mx1 describing the heat fluxes at each node. To present a limited example of how the matrix is calculated let us consider the small network example of Figure 3.14b). If the Kirchhoff's node law is applied to node I, the following expression is obtained:

$$\frac{T_{i,j}-T_{i-1,j}}{R_{i-1_i,j}}+\frac{T_{i,j}-T_{i+1,j}}{R_{i_i+1,j}}+\frac{T_{i,j}-T_{i,j-1}}{R_{i,j-1_j}}+\frac{T_{i,j}-T_{i,j+1}}{R_{i,j_j+1}}=Q_{i,j} \tag{3-35}$$

If the terms are grouped, the expression is derived as follows where the different values that need to be inserted in matrix *A* are displayed.

$$\underbrace{\left(\frac{1}{R_{i-1_i,j}}+\frac{1}{R_{i_i+1,j}}+\frac{1}{R_{i,j-1_j}}+\frac{1}{R_{i,j_j+1}}\right)}_{A_{ii}}T_{i,j} - \underbrace{\frac{1}{R_{i-1_i,j}}}_{A_{i,i-1}}T_{i-1,j} - \underbrace{\frac{1}{R_{i_i+1,j}}}_{A_{i,i+1}}T_{i+1,j} - \underbrace{\frac{1}{R_{i,j-1_j}}}_{A_{i,x}}T_{i,j-1} - \underbrace{\frac{1}{R_{i,j_j+1}}}_{A_{i,y}}T_{i,j+1} = \underbrace{Q_{i,j}}_{Q_{ij}} \tag{3-36}$$

The calculation of the different thermal resistances depends on the heat transfer mechanism: conduction, convection or radiation. The general expression for the thermal conduction resistances is:

$$R_{th_{cond}} = \frac{L}{k \cdot S} \tag{3-37}$$

with L and S the length and transversal surface of the wall where the heat is circulating and k the thermal conductivity of the material.

The radiation phenomenon is approximated with the following thermal resistance expression.

$$R_{th_{rad}} \approx \frac{1}{\varepsilon \cdot \sigma \cdot S \cdot (T_s^2 + T_\infty^2) \cdot (T_s + T_\infty)} \tag{3-38}$$

with ε the emissivity of the material, σ the Stefan-Boltzmann constant ($5.67073 \cdot 10^{-8}$ $W \cdot m^{-2} \cdot K^{-4}$), S the external surface, T_s the surface temperature and T_∞ the temperature of the external cooling fluid.

The emissivities of the different materials are 0.8 for copper and 0.9 for the core material. However, when radiation is taken into account the surrounding environment must be considered as well. Other components emit heat or reflect some of the radiation. As a consequence, a de-rating factor of 50% is taken on the emissivity values. This factor is estimated in our present work to be a fair compromise between neglecting radiation phenomena and considering that the other elements have no influence on the radiation cooling. Future works should address the validity of this de-rating coefficient.

Convection thermal resistance is calculated as follows:

$$R_{th_{conv}} = \frac{1}{h \cdot S} \tag{3-39}$$

where h is the heat transfer coefficient and S is the external surface (formulas to calculate h are normally obtained through semi-empirical formulation; more information is given in section 3.3.1.10).

For the local heat fluxes $Q_{i,j}$ a constant loss density q is considered and it is multiplied by the node volume $Vol_{i,j}$.

$$Q_{i,j} = Vol_{i,j} \cdot q \tag{3-40}$$

As shown in the previous equations, the equivalent thermal resistances of convection and radiation depend on the temperature surfaces and vice-versa. In our case, to solve this problem, the solution is found iteratively. A hypothetic surface temperature T_s* is determined at the beginning of the calculation and in the end the calculated temperature T_s is compared to the hypothesis. If the error between hypotheses is below a certain threshold ε the mean of both temperatures is taken as the new initial hypothesis. The whole process is described in Figure 3.15.

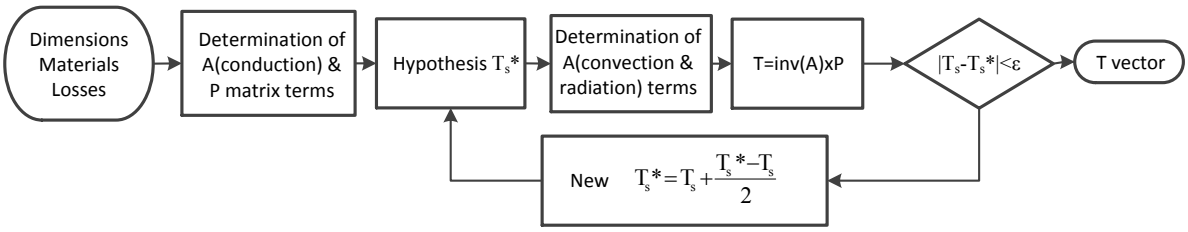


Figure 3.15 : Temperatures calculation algorithm

Losses temperature dependence is not included in the thermal calculation. Indeed influence of the temperature in all the design will imply re-simulating the system which will increase rapidly the computation time. Other works however have addressed this subject [63] and therefore it remains a perspective for future works.

3.3.1.10 E-I Inductor Model

The inductors represented in the present works, consist of a union of an E-I core and foil conductor used for the winding. The choice of this kind of core is motivated by considering an air gap in the inductor which becomes necessary to avoid core saturation for high currents. Foil conductors are chosen because they provide a higher integration and lower high frequency winding losses than round conductors, if properly designed [47]. The inductor model used in the present work and in the optimization process is described in Figure 3.16.

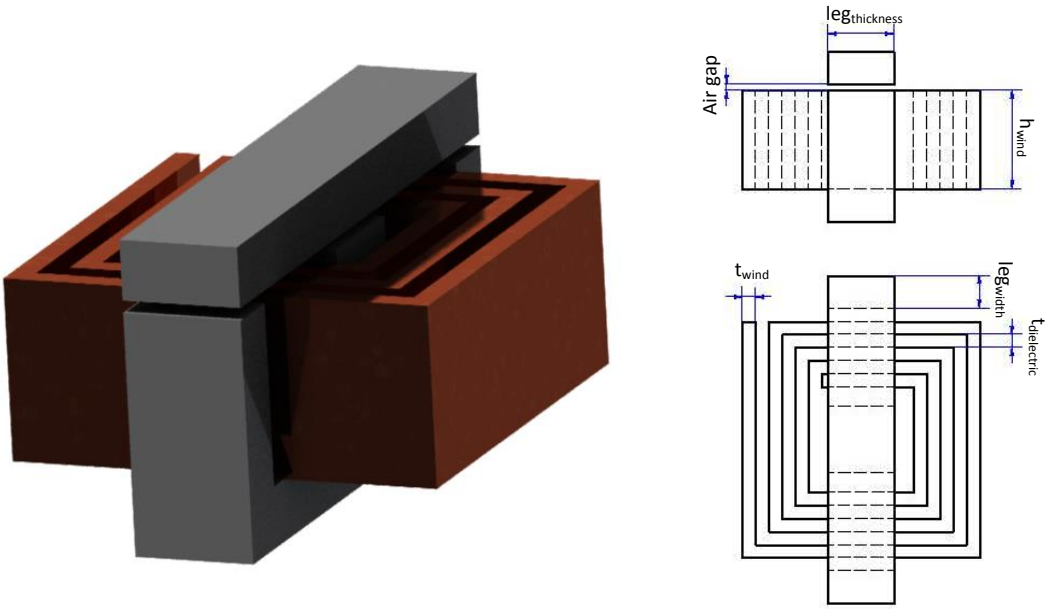


Figure 3.16 : Inductor description and dimensions used to describe the object

The inductor is described by two different approaches that are presented below: affinity laws and free model.

Description by affinity laws

Description by affinity laws considers there is a relationship between the different dimensions of the physical object. As a result, the number of necessary variables to describe the inductor is reduced. This approach is particularly interesting in optimization processes since the number of optimization variables is reduced; as a consequence the optimization time is also reduced. In addition, affinity laws are often used by core manufacturers, which makes optimal inductor feasible with standard on-the-shelf magnetic cores.

The affinity model used on the present thesis is based on [64]. The input variables to describe the inductor are:

- product area of winding section and core section ($A_w A_c$),
- number of turns (N),
- air gap (*Air gap*),
- core material,
- winding material.

The first three dimensions constitute the optimization variables of this model. In the mentioned work, relationships are extracted to minimize the weight for a specific application case. The description establishes that for a given product area, the optimal winding transversal section A_w^{opt} is:

$$A_w^{opt} = 0.83 \cdot \sqrt{A_w A_c} \cdot \left(\frac{\rho_c}{kW \cdot \rho_w} \right)^{0.46} \tag{3-41}$$

In this expression ρ_c, ρ_w represent the density of the core and winding material and kW is the filling factor which is set at 0.9 in the present work. The rest of the inductor dimensions are derived as follows:

$$leg_{width} = 0.3497 \cdot \sqrt[4]{A_w A_c} \left(\frac{\rho_c}{kW \cdot \rho_w} \right)^{-0.2539} \tag{3-42}$$

$$leg_{thickness} = 1.7204 \cdot \sqrt[4]{A_w A_c} \cdot \left(\frac{\rho_c}{kW \cdot \rho_w} \right)^{-0.20339} \tag{3-43}$$

$$h_{wind} = 1.41 \cdot \sqrt[4]{A_w A_c} \cdot \left(\frac{\rho_c}{kW \cdot \rho_w} \right)^{0.20388} \tag{3-44}$$

$$t_{wind} = \frac{A_w \cdot kW}{N \cdot h_{wind}} \tag{3-45}$$

$$t_{dielec} = \frac{A_w \cdot (1 - kW)}{(N+1) \cdot h_{wind}} \tag{3-46}$$

Free model

In the free modelling description, all dimensions of the inductors are optimization variables and no mathematical relation exists between them. The inductor is described using the following dimensions as shown in Figure 3.16:

- leg thickness ($leg_{thickness}$),
- leg width (leg_{width}),
- height winding (h_{wind}),
- thickness winding (t_{wind}),
- thickness dielectric ($t_{dielectric}$),
- air gap (*Air gap*),
- number of turns (N),
- core material,
- winding material.

This modelling presents the advantage of being completely free (considering all the physical characteristics of the device under design), thus the optimal solution should have optimal form factors. However, manufacturing these power inductors may become difficult. The equivalent permeance simulation model is presented on Figure 3.17.

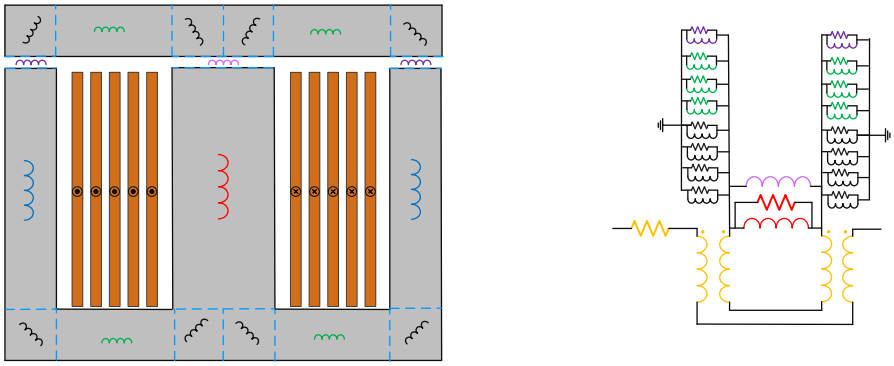


Figure 3.17 : Permeance-inductor modelling of the E-I chosen inductor

The leakage inductor is not considered. In any case, leakage inductance increases the total inductance value of the inductor, while respecting the saturation magnetic constraint and therefore it just improves the magnetic properties.

From the simulation, the magnetic fields in each part of the core and the circulating current are obtained. These excitations will allow calculating the winding and core losses as previously described in sections 3.3.1.2, 3.3.1.4 and 3.3.1.5. In the next step, the temperature of the core and winding are calculated. To represent the thermal behavior of the inductor a quarter of the inductor is discretized using an equivalent resistance network of 21 nodes. The disposition of the nodes and the thermal resistance network considered are presented in Figure 3.18.

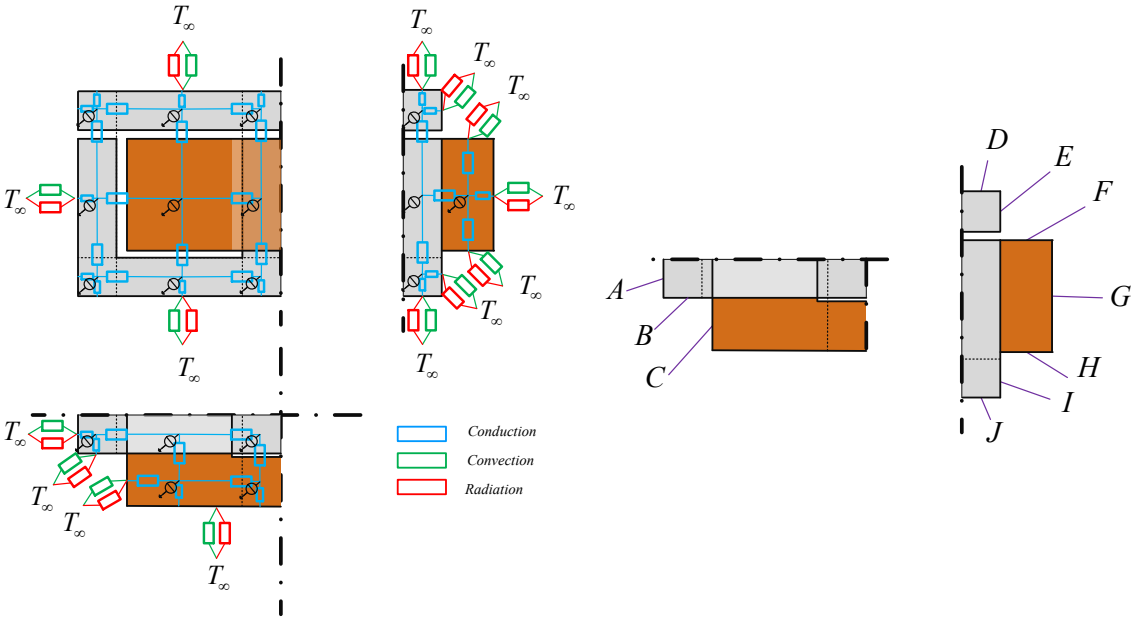


Figure 3.18 : left) Equivalent resistance network of the E-I represented inductor, right) notation of the areas for the different thermal exchange coefficient

To consider the equivalent heat exchange coefficient *h*, semi-empirical formulas from literature are used for natural convection [65][66]. For the surfaces E, F, G, H, I it makes common sense to use a formula that takes into account the length of the boundary layer associated to the particular shape. In [65], a semi-empirical model was extracted from experimental data of a transformer. The equation for the equivalent transfer coefficient was:

$$h_{natural} = 1.58 \cdot \left(\frac{p}{p_{ref}}\right)^{0.477} \cdot \left(\frac{T_a}{T_{a,ref}}\right)^{-0.218} \cdot \frac{(T_s - T_a)^{0.225}}{L^{0.285}} \tag{3-47}$$

In this expression, p_{ref} is the pressure at sea altitude (Pa) and $T_{a,ref}$ is 25°C, T_a and T_s are the ambient and surface temperatures and *L* is total distance where the air circulates, which is calculated using expressions in Figure 3.19 a). For the vertical surfaces (A, B, C) the classical forms for vertical surfaces are employed [66].

$$h_{natural} = \frac{k}{L}\left(0.68 + \frac{\left(0.67 Ra^{1/4}\right)}{\left(1 + \left(\frac{0.492}{\mathrm{Pr}}\right)^{9/16}\right)^{4/9}}\right) \quad Ra \le 10^9 \tag{3-48}$$

$$h_{natural} = \frac{k}{L}\left(0.825 + \left(\frac{\left(0.387 Ra^{1/6}\right)}{\left(1 + \left(\frac{0.492}{\mathrm{Pr}}\right)^{9/16}\right)^{8/27}}\right)^2\right) \quad Ra > 10^9 \tag{3-49}$$

with *Pr* the adimensional Prandtl number, *k* the thermal conductivity of the fluid, L the characteristic length calculated with the equation in Figure 3.19b) *Ra* the Rayleigh number calculated with the following formula:

$$Ra = \frac{C_p g \beta \,\mathrm{Pr}(T_s - T_\infty) L^3}{\nu^2} \tag{3-50}$$

with C_p the specific heat at constant pressure, *g* the gravity constant, β the thermal expansion coefficient, T_s the surface temperature, T_∞ the external air temperature, ν the kinematic viscosity and *L* the characteristic length for vertical surfaces as shown in . For the horizontal surface at the top part of the core (surface D) the following expression is used.

$$h_{natural} = \frac{k}{L}\left(0.54 Ra^{1/4}\right) \quad Ra < 10^7 \tag{3-51}$$

$$h_{natural} = \frac{k}{L}\left(0.15 Ra^{1/3}\right) \quad Ra \ge 10^7 \tag{3-52}$$

with *L* the ratio between the surface area and the perimeter. For the bottom part of the core (surface *J*) the following expression is used.

$$h_{natural} = \frac{k}{L}\left(0.27 Ra^{1/4}\right) \tag{3-53}$$

with L again the ratio between the surface and the perimeter.

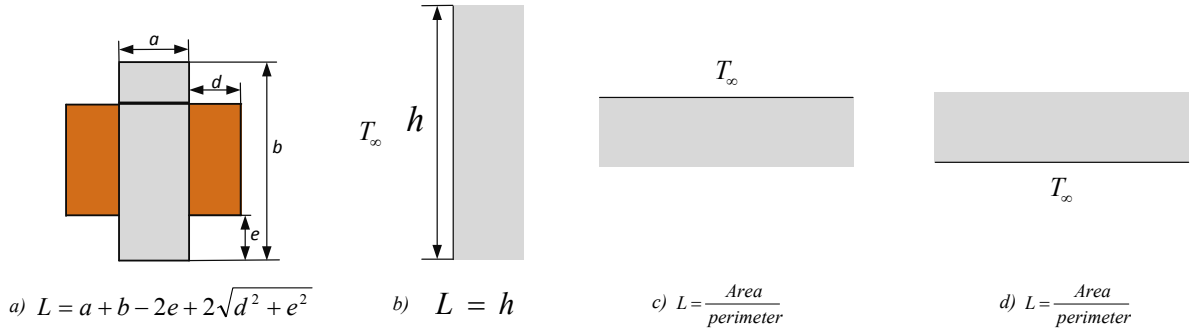


Figure 3.19 : distance used for semi empirical formulas for
a) inductor cross section b) vertical surfaces c) top surfaces d) botoom surface

In the case of an inductor cooled by forced convection the following expressions are used for all the surfaces [67]:

$$h_{forced} = \left(3.33 + 4.8 \cdot u_\infty^{0.8}\right) \cdot L^{-0.288} \tag{3-54}$$

In this expression u_∞ represents the forced air speed in the vertical direction and L is calculated using the expressions in Figure 3.19 a). Validation of this coefficient should be performed in future works.

The thermal network was validated using 3D numerical simulation with COMSOL™ software. The validation only takes into account conduction effects and the heat exchange coefficients are fixed with the previous detailed analytic formulas (the same h from the analytic models). Indeed, the equivalent thermal coefficient is highly dependent on the environment and for each application the coefficients should be modified. An improvement of this work would be to determine an equivalent global exchange coefficient depending on the definition of the different elements. The error between the models comes from an insufficient number of nodes, particularly in the core where the thermal conductivity is lower and from the hypothesis of isothermal temperature at the surfaces which is not respected in the simulation. Indeed, future works should address the trade-off between nodes number and computation time. The model is validated on four different geometries; the objective is to validate the thermal network for all the different optimization forms. The different results are presented on Figure 3.20. More information on the inductors can be found in Appendix A.

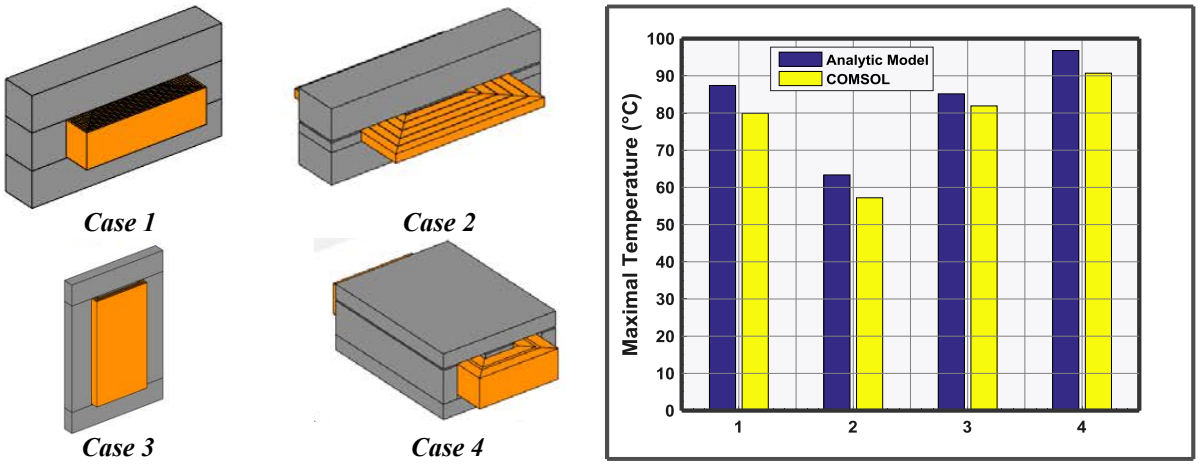


Figure 3.20 : Validation of the hot point thermal model of inductor for 4 different geometries

The validation shows a good estimation for the maximal temperatures (relative error below 12%). Causes of the relative differences have not been studied deeply in this work; however, the fact of discretizing the losses in the nodes is certainly a conservative hypothesis and a hint for future works. In any tested case, the maximal temperature is overestimated, compared to thermal simulations, which provides confidence that final design is feasible.

This model has the main advantage to calculate the temperature distribution in the inductor. Temperature dispersion in the component may become critical. For example, if the simulation of the case 3 in Figure 3.20 is presented, it is shown how the difference between the "hottest" and "coldest" point reaches more than 10°C (See Figure 3.21). Indeed as shown in the numerical simulation the temperature gradient in the core is significant; the central leg is at higher temperature than the external surfaces. It means that temperature distribution calculation needs to be taken into account in the design, especially when the proportion between dimensions is highly variable.

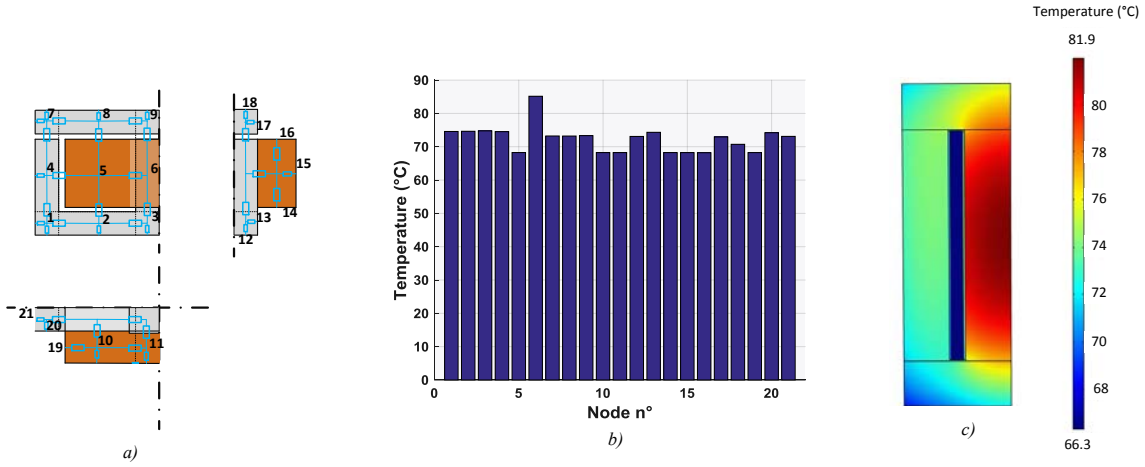


Figure 3.21: Inductor a) node numbering, b) analytic distribution of temperatures & c) temperature distribution in COMSOL™ simulation

3.3.1.11 Coupled Inductor Model

One of the main advantages of the power cabinet is to use several inverters to supply the same load. In these cases, using a coupled inductor was found as a more performant solution in terms of mass and efficiency in a series of studies [54][59][68][69][70]. A coupled inductor "couples" magnetically the fields produced by the current of each output cell. As a result, the coupled inductor behaves differently for the current flowing to the load and the inter-cell current. Let us consider the parallel operation of two switching cells as shown in Figure 3.22: the current of a cell k (I_{cell_k}) is decomposed in two terms: the current going to the load (I_{loadk}) and the current between cells or inter-cell current (I_{IC}). The load current (I_{load}) is the sum of all the cell currents and the inter-cell current is derived as follows:

$$I_{load} = \sum_{i=1}^{N} I_{cell_i} \tag{3-55}$$

$$I_{cell_k} = I_{load_k} + I_{IC_k} \tag{3-56}$$

For the particular case of two cells in parallel, equivalent reluctance model of the coupled inductor is represented in Figure 3.22.

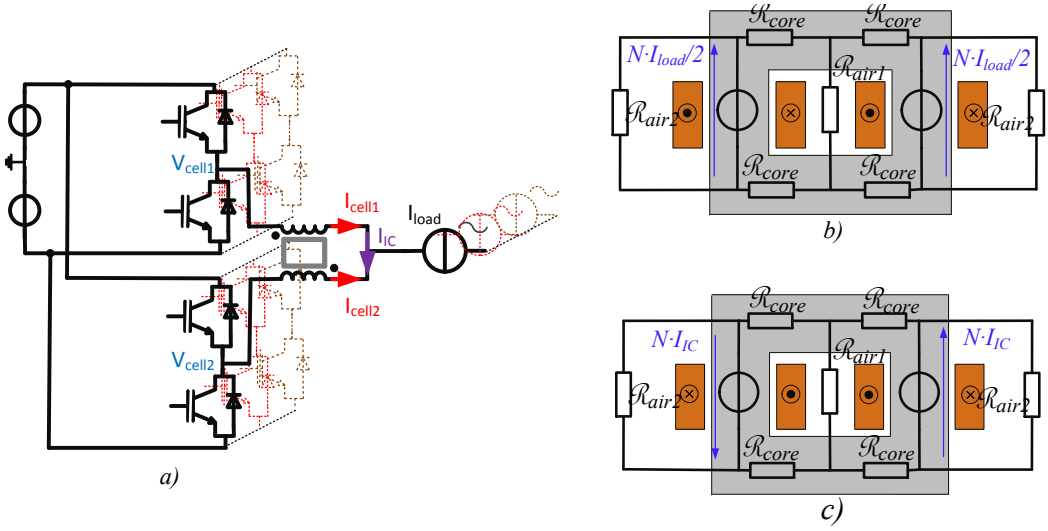


Figure 3.22 : Inter-cell transformer for two output cell;
a) circuit, b) reluctance model for equal currents, c) reluctance model for opposite currents

In this particular case, the following expressions of the inductance value for each current component are extracted. The inductance value seen by the load is:

$$L_{load}^{CI} \cong \frac{N^2}{(R_{air2} \,//\, (R_{air1} + 2 \cdot R_{core}))} \tag{3-57}$$

with N the number of turns for each phase.

If the core reluctance is assumed to be much smaller than the air reluctance (normally $\mu_{core}>>\mu_{air}$), the following equation is extracted.

$$L_{load}^{CI} \cong \frac{N^2}{(R_{air2} // R_{air1})} \tag{3-58}$$

The inductance value for inter-cell current is :

$$L_{IC}^{CI} \cong \frac{N^2}{R_{core}} \tag{3-59}$$

The reluctance of the core is normally much smaller than the reluctance of the air and as a consequence, the inductance seen by the inter-cell current is higher than the inductance seen by the load current. This is particularly interesting in the design of magnetic components where the magnetic field *B* must be always below the saturation limit B_{sat}.

$$B = \frac{L \cdot I}{N \cdot A_{core}} < B_{sat} \tag{3-60}$$

For a given current *I* and inductance value *L*, in order to fulfill the magnetic constraint, the number of turns N or the section of the core A_{core} must be increased to satisfy the previous inequality. In both cases the mass of the magnetic component increases (more winding or more core volume respectively). Normally, the load current is higher than the inter-cell current, which means that reduction of L_{load}^{CI} is found hereby interesting. Indeed, inter-cell transformer may result in low “load” inductance and “high” inter cell inductances reducing the size of the final core.

A major limitation of this solution is that it only works when all the different phases are connected. If one phase is disconnected, the core might saturate. Unfortunately, such a disconnection is possible in our application: as presented in Chapter I, the inverters are connected and disconnected, depending on the load consumption. A proven solution is to increase the airgap in each leg of the coupled inductor [68]. However, the inter-cell inductance value is reduced and the solution becomes less attractive.

The coupled inductors are categorized in two different groups, depending on the construction and implementation: monolithic and cascaded. In [68], the monolithic solution appears as a lighter option and it is the one chosen in the present work. The construction and the design input dimensions of the model are presented in the following figure. The number of turns (N_{turns}) is also an input dimension. As a reminder, the dimensions are the optimization variables in the design problems.

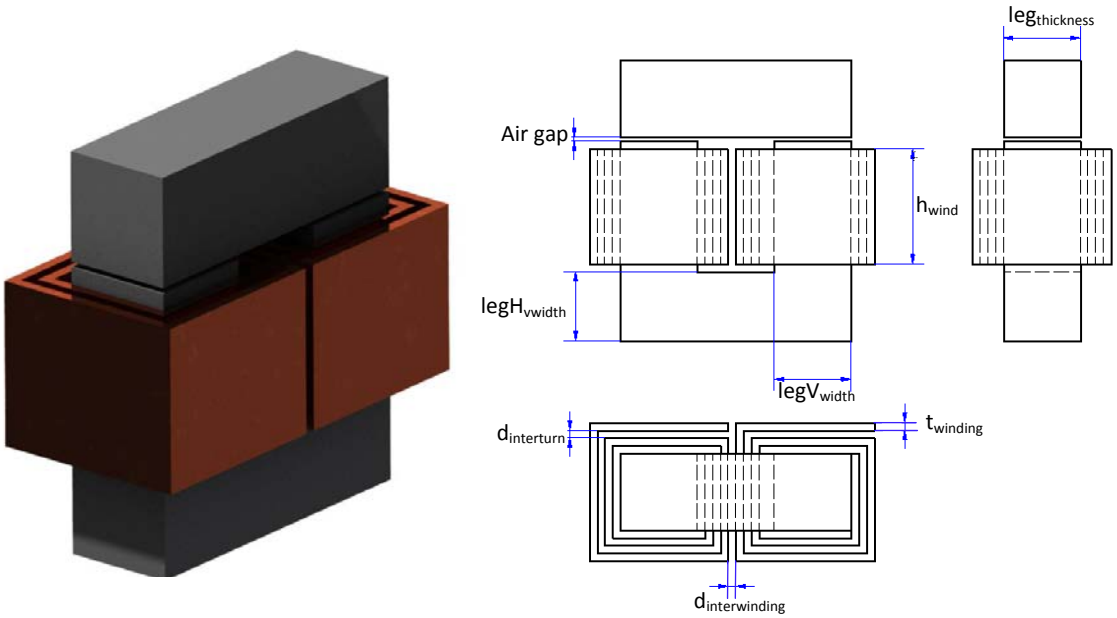


Figure 3.23 : left) 3D view of a two-phase coupled inductor & right) dimensions used to describe the object

The coupled inductor, as well as all the represented objects in the library, needs also an equivalent electro-magnetic simulation model, in order to extract the different waveforms. The lumped electro-magnetic model using the permeance-inductor approach is presented in the following figure. The permeances are calculated using the permeance formulas presented in section 3.3.1.7.

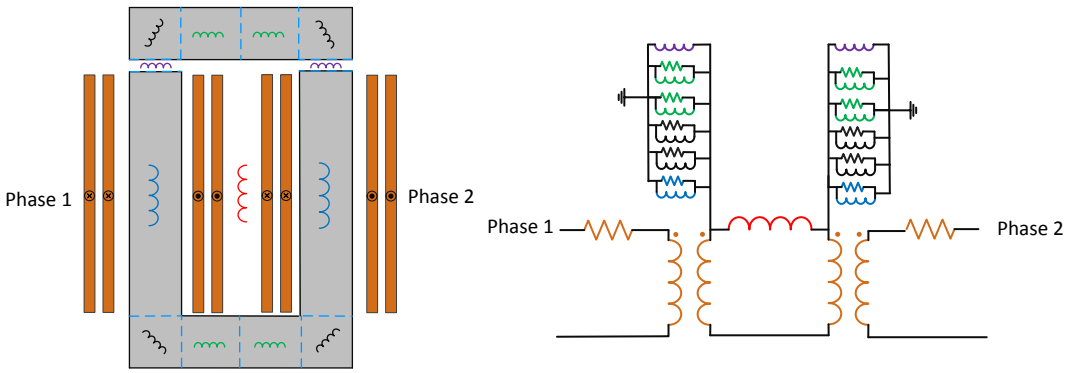


Figure 3.24 : Permeance-inductor equivalent simulation model representation of the two-phase coupled inductor

The calculation of the core and winding losses follow a similar approach as the one described in sections 3.3.1.2 and 3.3.1.4. For the interpolation surface, minimal distance between the phases is added as an additional input parameter. In addition, the magnetic field depends on the way the different phases currents interact. As a result, winding losses are decomposed into losses generated by the common part of winding currents (half the load

current for two-cell configuration) and losses generated by opposite currents (circulating current). For each calculation an independent response surface is created.

For the thermal model, an equivalent resistance network of 18 nodes is used. The shape of the coupled inductor is similar to the E-I inductor described in previous section and the same heat exchange convection coefficient formulas are used. The description of the thermal model for the coupled inductor is shown in the Figure 3.25.

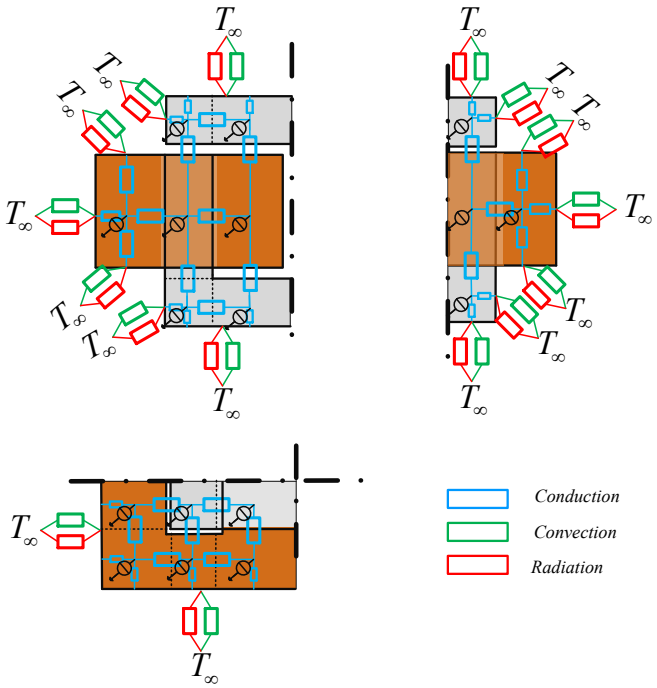


Figure 3.25 : Thermal network model of the coupled inductor

The shape of the coupled inductor is analog to the one presented for the E-I inductor in section 3.3.1.10. The formula (3-47) is used for the convection thermal exchange coefficients of all the external surfaces.A 3D thermal validation is also performed on different geometries for two-phase coupled inductors. Like for inductors, only conduction is considered, the exchange coefficients calculated in the model are imposed in the COMSOL simulation and only the hottest points of the model and the COMSOL simulation are compared. More details on the calculations are given in Appendix A.

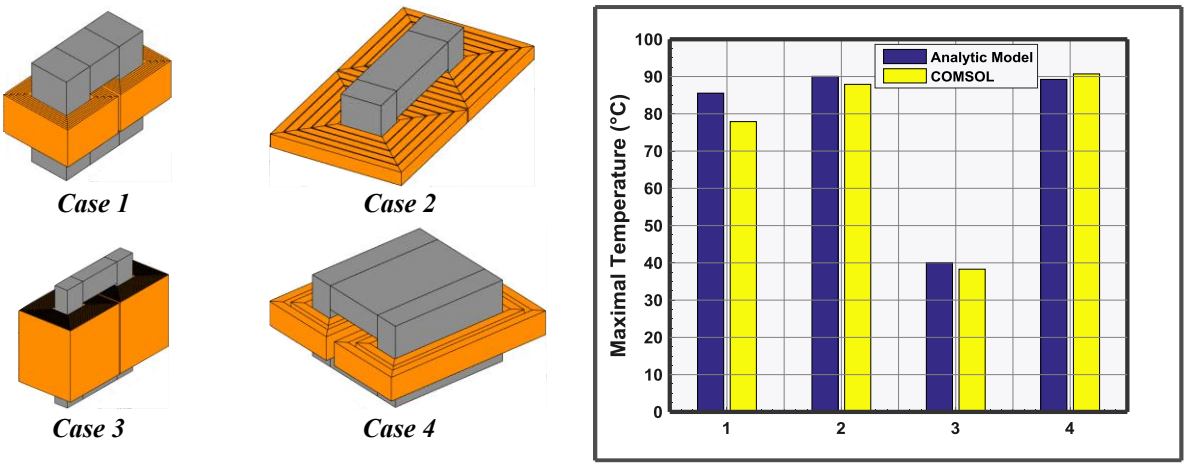


Figure 3.26 : Validation of the hot point model for four different geometries of 2-cells Inter Cell Transformers

The results show good agreement between the analytical values and the numerical simulations (error below 10%). Moreover, in the worst case the temperature is overestimated. No further study was performed to assess the cause of this difference.

3.3.1.12 Common Mode Inductor

To respect the common mode aeronautic standards, a common mode inductor is necessary. The common mode inductor is constructed using a toroidal core and solid round winding. Common mode inductors are often made of one layer to avoid increasing the parasitic capacitance and to decrease the proximity effect. Moreover, solid round wire is preferred to Litz wire to increase the impedance at higher frequencies [71]. In the present work the common mode inductor is described using the dimensions presented in Figure 3.27.

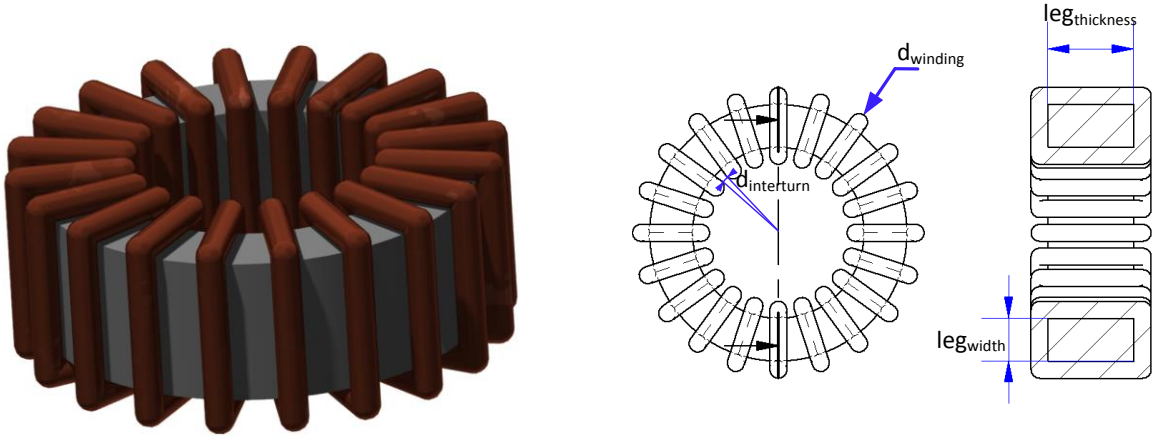


Figure 3.27 : Common mode inductor;
left) 3D image & right) dimensions used to define the component

The equivalent permeance-inductor simulation model is presented in

.

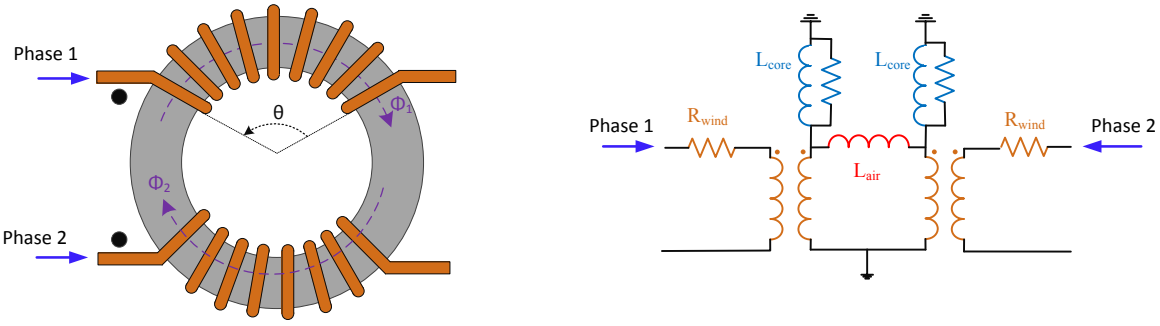


Figure 3.28 : Electro-magnetic lumped equivalent simulation model of the common mode inductor

To calculate the permeances of the core the following formula often described in the manufacturers datasheet is used [72].

$$L_{core} = \frac{\mu_r \mu_0 A_c}{l_e} = \frac{\mu_r \mu_0 A_c}{\frac{\pi (D_{ext} - D_{int})}{\ln \frac{D_{ext}}{D_{int}}}} \tag{3-61}$$

With A_c the core area, μ_r,μ_0 the relative and air permeability and D_{ext} and D_{int} the external and internal core diameters. For the permeance of the air, the analytic formula employed in [73] is used. Leakage inductance is highly dependent on the manufacturing process so accurate estimation is difficult in pre-design steps. As a consequence, the proposed formula is accepted to give an "approximate" value of the leakage inductance.

$$L_{air} = \frac{\mu_0 A_c \mu_{eff}}{l_{eff}} \tag{3-62}$$

l_{eff} is the effective magnetic path length that depends on the angle covered by the each of the windings θ as described in Figure 3.28.

$$l_{eff} = l_e \sqrt{\frac{\theta}{2\pi} + \frac{1}{\pi} \sin \frac{\theta}{2}} \tag{3-63}$$

The effective permeability is obtained from the chart provided in [73]. The chart provides the effective permeability as a function of the core relative magnetic permeability and another parameter Γ calculated with the following formula.

$$\Gamma = \sqrt{\frac{\pi}{A_c}} \cdot \frac{l_e}{2} \tag{3-64}$$

For the winding resistance R_{wind}, the dc value is calculated using the classical dc winding resistance and the analytic formula (3-21) to take into account the skin effect. The proximity effect is not considered in the calculations. Instead, a safety margin of 25°C is taken for the maximal operating temperature. Again, a response surface could be used to estimate the proximity effect and this is clearly a point to address in future works.

The equivalent thermal model is presented in Figure 3.29. For the equivalent heat exchange convection coefficients, classical analytical formulas for external natural convection with rectangular and circular ducts from literature are employed [74].

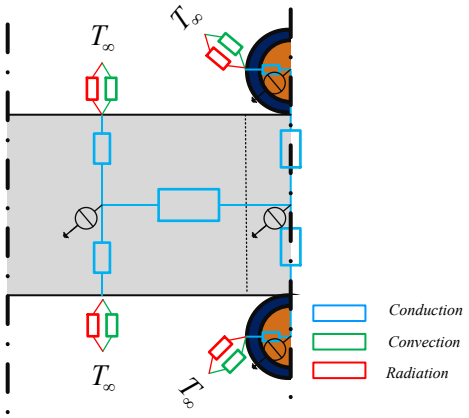


Figure 3.29 : Thermal network representation of the common mode inductor

The model is validated with numerical simulation calculations. Further information on the calculations is given in appendix A.

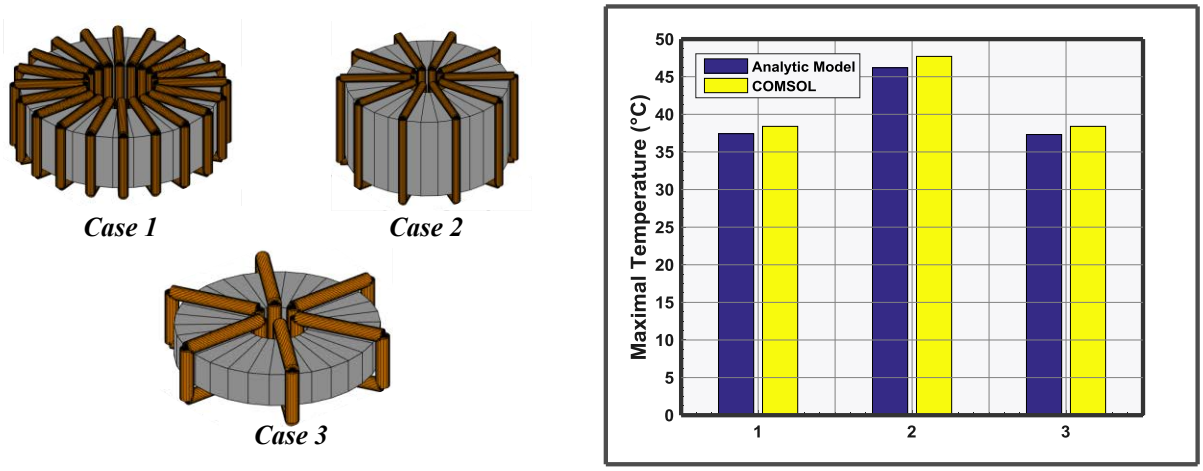


Figure 3.30 : Validation of the hot point thermal model of common mode choke for 3 different components

The model calculations are in accordance with the numerical values (below 4%). However, the analytical expressions for the heat exchange coefficients are extracted for semi-empirical models which have strong hypothesis (Length>> transversal section). Future works, should work this problem more in detail to increase the accuracy of the heat exchange coefficients.

3.3.2 Capacitor

3.3.2.1 Introduction

In the present work, only two types of power capacitors are considered: ceramic and film capacitors. A good performance factor to classify the power capacitors is the energy density:

$$Energy\ density = \frac{C \cdot V^2}{2 \cdot weight} \tag{3-65}$$

C represents the capacitance value and V the maximal allowed voltage. Figure 3.31 represents the energy density for the two chosen technologies.

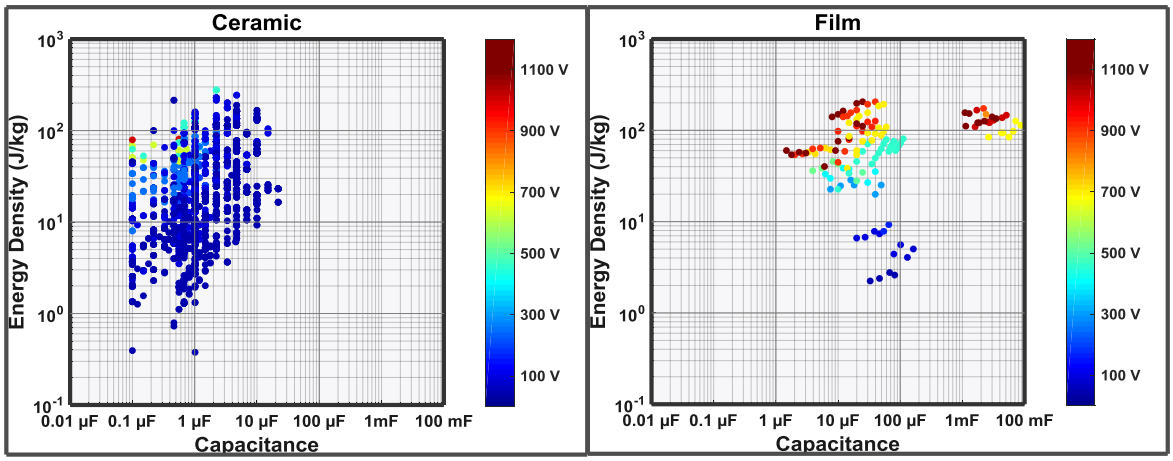


Figure 3.31 : Energy density vs Capacitance for ceramic (left) and film (right) capacitors

As shown, ceramic capacitors exhibit better energy densities than film capacitors for low voltages (100-500 V) while at higher voltages (500-1000 V) film capacitors are preferred.

3.3.2.2 Capacitor model

The capacitor model used in the present work is based on the work described in [75]. The calculations are based on regression models using manufacturer's data. The electric equivalent simulation model used is presented in Figure 3.32.

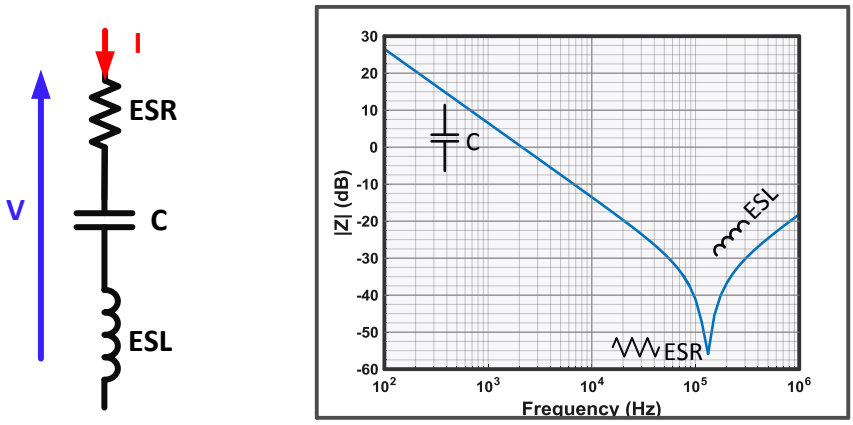


Figure 3.32 : Equivalent capacitor simulation model and impedance Bode plot of the model

The model represents the capacitor behavior C and two parasitic effects of the capacitor: the Equivalent Series Resistance (ESR) and the Equivalent Series Inductance (ESL). The equivalent series resistance simulates all the losses on the capacitor. The ESR is important as it gives the minimal impedance of the capacitor, which occurs at the self-natural frequency. At higher frequencies, the behavior of the capacitor is inductive as shown in Figure 3.32.

The model from [75] calculations were compared to some manufacturer data obtaining the following relative errors.

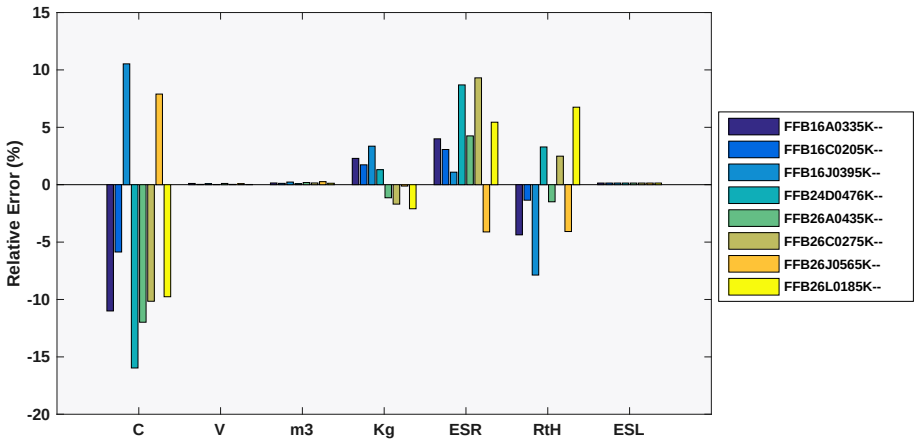


Figure 3.33 : Relative error between the calculated model parameters (C, ESR, mass…) and manufacturer data for rectangular capacitors(AVX) [75]

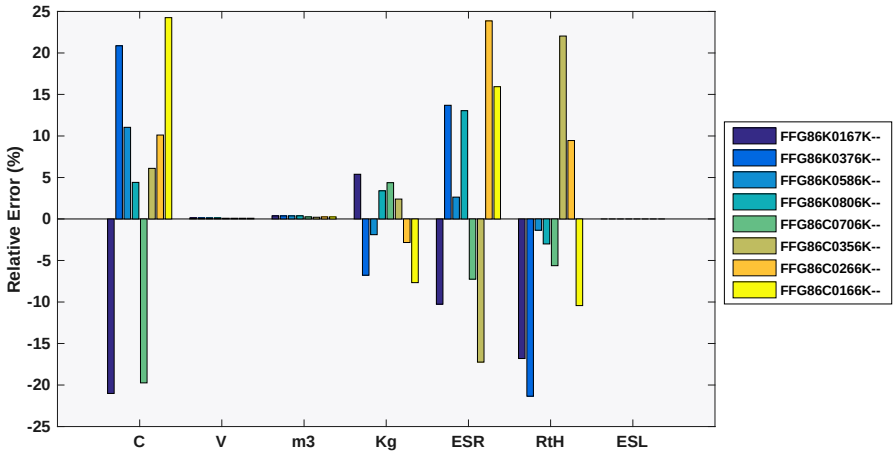


Figure 3.34 : Relative error between calculated model parameters (C, ESR, mass…) and manufacturer data for cylindrical capacitors(AVX) [75]

As shown in Figure 3.33 and Figure 3.34 the maximal relative error between the model and the manufacturer data is around 25% (for the capacitance value) and the mean error remains within acceptable margins. Concerning the volume and the weight, the error is small (< 5%), which is important as it will be the main parameter of the objective function and it will help us finding the optimal mass.

3.4 Cooling devices

To ensure operation below a certain temperature, additional cooling devices are inserted in the power converter. In some cases, cooling devices insertion is mandatory (ex. evacuation of semiconductor losses) due to the poor cooling performances of the component. In other cases, cooling devices are interesting from a system point-of-view (for example, in [76] reduction of passive element mass by addition of heat sink)

There are different kinds of cooling technologies having different advantages and drawbacks [77]: liquid cooling, forced air cooling, heat pipes…. The typical heat transfer exchange coefficient values for the different technologies are shown in Figure 3.35.

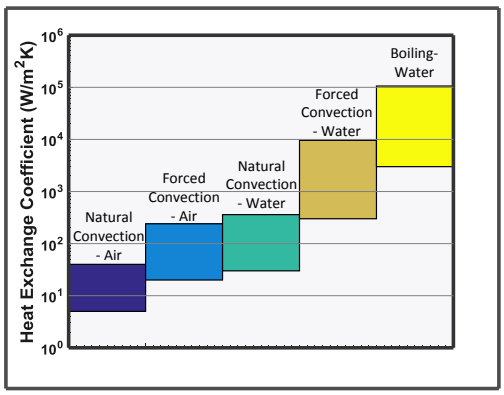


Figure 3.35 : Overall heat exchange coefficient for different fluids in different forms

As stated in chapter I, the apparition of wide band gap semiconductors has pushed the limits of forced air cooling [45]: it is the only one technology studied in the present document.

3.4.1 Heat Sink

Heat sink is the most common method to improve the cooling performances of a device. The principle is simple: by adding extra fins to a cooled surface, the contact area between air and the cooled surface increases. However, their impact is limited. Fins add a thermal conduction resistance that limits the usefulness of the fin up to a certain fin height. In addition, heat sink increases weight and cost of the power converter.

In the present work, a straight-fin heat sink is represented as presented in Appendix B. The model assumes laminar flow between the different fins. The model is mainly based on analytic equations from bibliography [25][78][79]. The different dimensions to define the heat sink are shown in Figure 3.36.

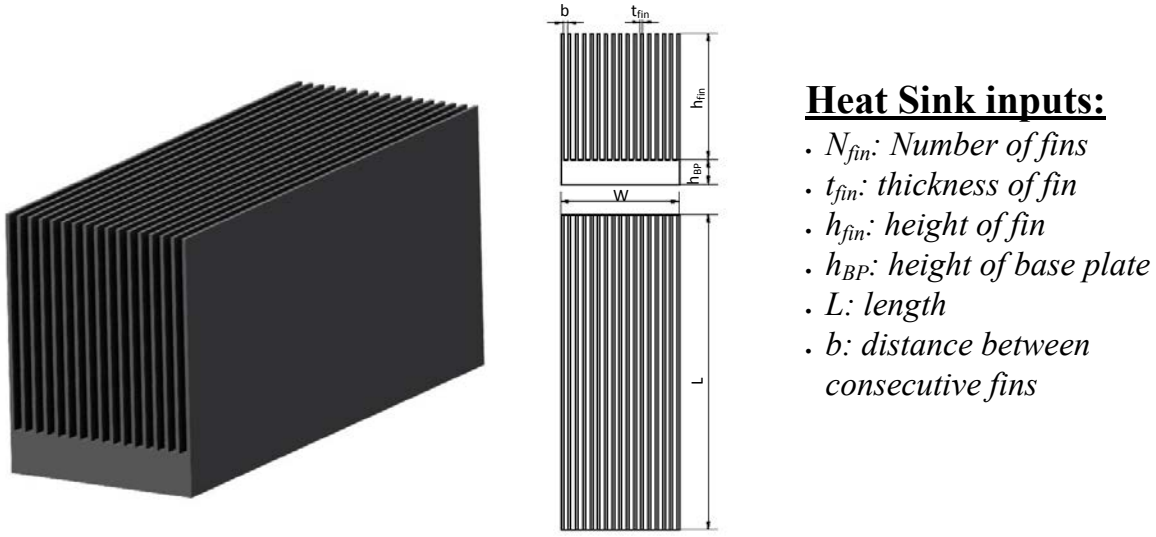


Figure 3.36 : Heat sink: (left) 3D representation (right) definition of dimensions

The most common heat sink materials are aluminum alloys because of the good trade-off between cost, mechanical and thermal properties that they offer; as a consequence it is the only material we will use in our designs. The thermal model was validated using experimental data in [79][75] and relative errors were found below 5% which is an acceptable value for the calculations. The model is directly used from the bibliography and no study has been performed to assess the origin of the differences.

3.4.1.1 Pressure drop model

Air has a certain viscosity causing friction losses when the air circulates on a determined surface. To overcome the friction losses and ensure the necessary mass flow, a fan is required. The aeraulic behavior of a fan is characterized by a curve giving the evolution of the pressure drop versus flow rate. To take into account the impact of the heat sink on the whole cooling

system, an aeraulic model of the heatsink is also required. In Appendix B such a model is presented and experimentally validated on four different heat sinks for different air speed points [80]. The comparison between the experimental data and the model is presented in Figure 3.37.

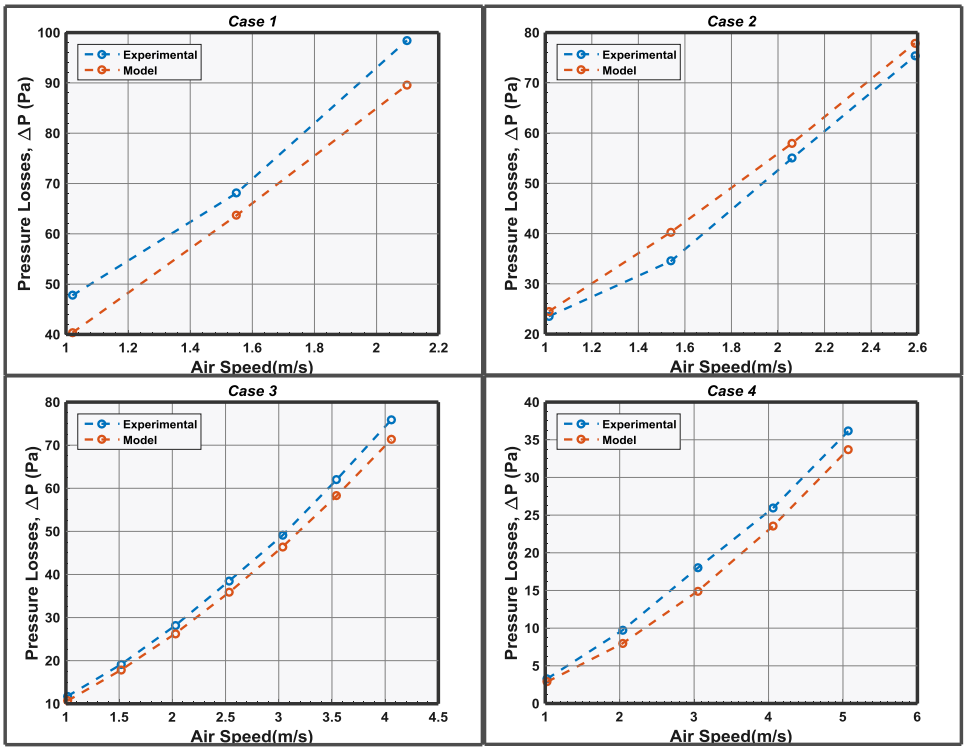


Figure 3.37 : Comparison between calculated & experimental pressure drops in four different heat sinks

As shown in Figure 3.37, there is a good agreement between the model and experimental data. The maximal calculated relative error is 13%, which is found acceptable for the present work. No further study has been performed to assess the causes of the error.

3.4.1.2 Spreading resistance

The spreading resistance considers the spreading/constriction effect of the heat flow when a change on the cross-section area happens. As shown in Figure 3.39, the temperature of the baseplate is not always homogeneous. As a result, the edges of the heatsink are not at the same temperature as the cooled surface and fin addition may become unattractive in those points. Several authors propose analytic expressions to take into account the heat dissipation effect [81] but their range of application is limited. In the present work, the formulas to estimate the spreading resistances are based on [82][83], where a unique heat source is considered at the center of the surface (Figure 3.38).

$$R_s = \frac{1}{2a^2cdk}\sum_{m=1}^{\infty}\frac{\sin^2(a\delta_m)}{\delta_m^3}\cdot\varphi(\delta_m) + \frac{1}{2b^2cdk}\sum_{n=1}^{\infty}\frac{\sin^2(b\lambda_n)}{\lambda_n^3}\cdot\varphi(\lambda_n) + \frac{1}{a^2b^2cdk}\sum_{m=1}^{\infty}\frac{\sin^2(a\delta_m)\sin^2(b\lambda_n)}{\delta_m^2\lambda_n^2\beta_{m,n}}\cdot\varphi(\beta_{m,n}) \quad (3\text{-}66)$$

with a,b,c,d the geometric dimensions of the cooled surface and the base plate, as shown in Figure 3.38 and k the thermal conductivity of the base plate.

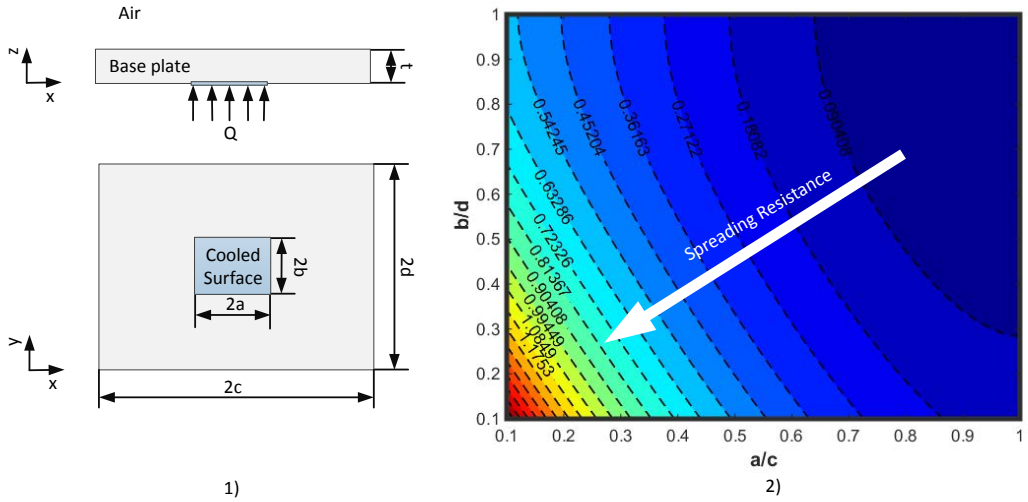


Figure 3.38 : Heat sink base plate1) Dimensions and heat source 2) Thermal resistance evolution for different dimensions ratio (a = 20cm, b= 10cm)

The coefficients δ_m, λ_n, $\beta_{m,n}$ and the function φ are derived from the following formulas.

$$\varphi(x) = \frac{(e^{2xt}+1)x - (1-e^{2xt})\frac{h}{k}}{(e^{2xt}-1)x + (1+e^{2xt})\frac{h}{k}} \quad (3\text{-}67)$$

$$\delta_m = \frac{m\pi}{c} \quad (3\text{-}68)$$

$$\lambda_n = \frac{n\pi}{d} \quad (3\text{-}69)$$

$$\beta_{m,n} = \sqrt{\delta_m^2 + \lambda_n^2} \quad (3\text{-}70)$$

The terms h,t correspond to the heat exchange coefficient at the surface of the baseplate and the thickness of the baseplate. As shown in Figure 3.38, keeping the dimension ratio close to 1 is important to avoid spreading effects. The spreading resistance model was validated using Finite Element Method calculation with COMSOL™ (See Figure 3.39).

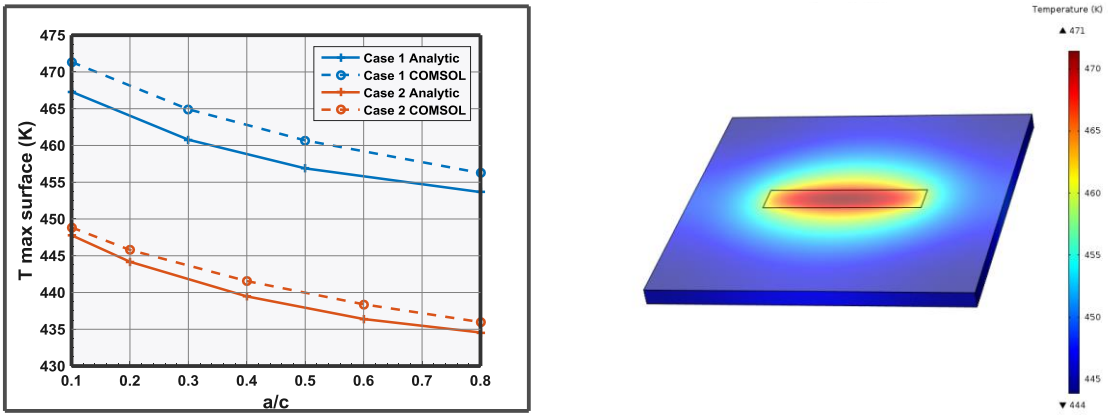


Figure 3.39 : Comparison between analytic model and COMSOL simulations

As shown in Figure 3.39, the difference between the numerical simulations and the analytic expressions is of some degrees. The formula was not further studied to find the origin of the error.

3.5 Connexion elements

In the present work, the modelling of power cables and contactors has also been detailed.

3.5.1 Power cables

In future "more electrical aircraft", cable length can sometimes reach tens of meters. When long cables are used, propagation effects can cause important overvoltage on power lines, thus degrading the lifetime of supplied equipment. This effect is more critical for aircraft equipment located in low pressure zones. The use of higher voltages (inclusion of HVDC) and the fast switching of wide band-gap semiconductors are certainly a point to be addressed in future works to avoid apparition of partial discharges phenomena [44]. In the present work, to take propagation phenomena into account, the cable electric model is divided into smaller subsections where the waveform is approximately considered position-invariant. A reasonable approximation to divide the cable is to divide the cable into sections with length L, with L less than one tenth of the signal wavelength λ ($L < \lambda/10$) [35].

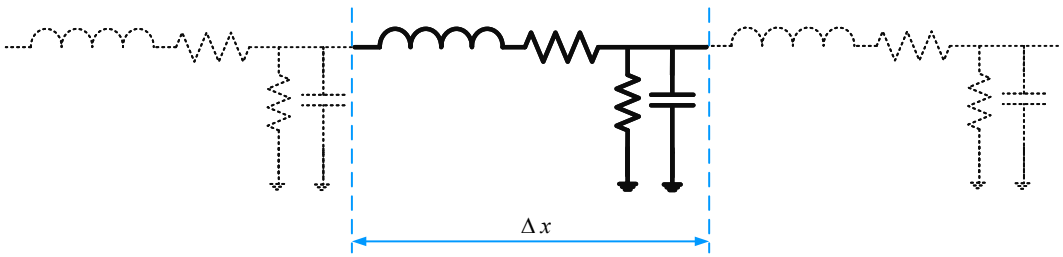


Figure 3.40 : Division of power cable into smaller subsections

Partial discharges phenomena impact should be treated in future works. However, in this work, the cable is represented to take into account the common impedance. DO160 standard

(Chapter II) imposes common mode conducted current to respect a given envelope. As a result, an estimation of the common mode paths is needed.

In the present work, the power cable is considered as a shielded three conductor power cable. Different power cable disposition and shapes will be included in future works. Here, the disposition of the cable is a mere hypothesis and the only purpose of this study is to determine a rough representative simulation model of the power cable (particularly the common mode impedance). To calculate the conductor section, the hypothesis of a flowing current density of 5A/mm^2 is taken. For the dielectric thickness, using current aircraft power cable manufacturer data [84], a oversizing ratio of 40% of the conductor radius was estimated. Materials employed are aluminum for the conductor and Kapton^{TM} for the insulation.

The modelling of the power cable must be as representative as possible of the physical behavior at high frequencies. All parasitic inductances and capacitances shall be represented and the variation with frequency must be included (which is a particular advantage of using a frequency solver). The skin effect of the power cables is considered as well, but proximity effect is neglected. The chosen electrical simulation model of each unitary section is represented in Figure 3.41.

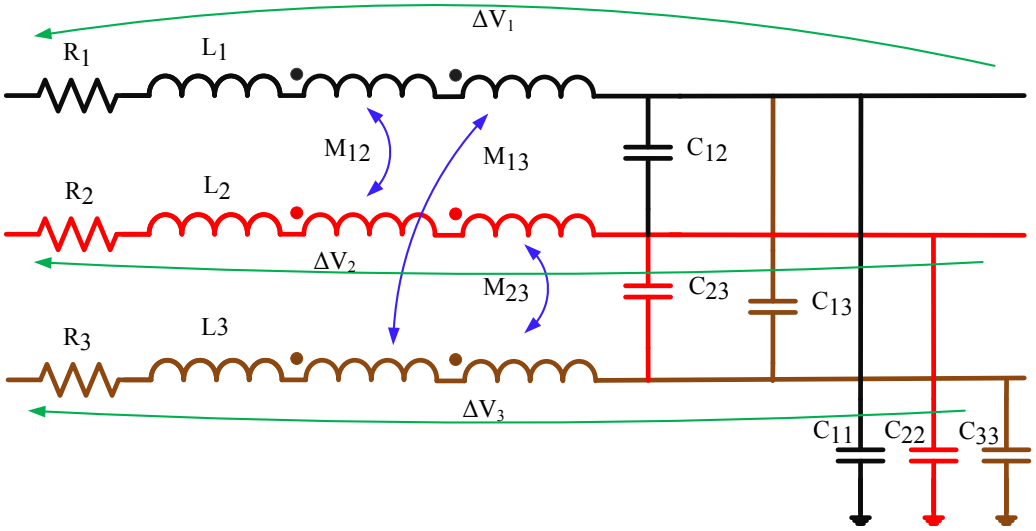


Figure 3.41 : Electrical model of each cable section

The voltage across each phase ΔV is described using the following equation:

$$[\Delta V] = [R][I] + j\omega[L][I] - j\omega[C][I] \tag{3-71}$$

with R, L, C the resistor, inductor and capacitor matrix ($3x3$ matrix), I the current vector and ω the pulsation of the excitation.

$$[R]=\begin{bmatrix} R_1 & 0 & 0 \\ 0 & R_2 & 0 \\ 0 & 0 & R_3 \end{bmatrix} \tag{3-72}$$

$$[L]=\begin{bmatrix} L_1 & M_{12} & M_{13} \\ M_{21} & L_2 & M_{23} \\ M_{31} & M_{32} & L_3 \end{bmatrix} \quad M_{ij}=M_{ji} \ \ \forall i,j=1,2,3 \tag{3-73}$$

$$[C]=\begin{bmatrix} C_{11} & C_{12} & C_{13} \\ C_{21} & C_{22} & C_{23} \\ C_{31} & C_{32} & C_{33} \end{bmatrix} \quad C_{ij}=C_{ji} \ \ \forall i,j=1,2,3 \tag{3-74}$$

To calculate the different parameters several authors [85][86] propose different analytic expressions to calculate the common mode impedance of power cables. These expressions are based on transmission line theory and consider some hypothesis unsuited for aeronautical environment. Other authors extract directly the simulation model parameters using experimental data [37][33]. Normally, 3D effects are neglected assuming the length of the power cable is much higher than the diameter of the cable (L>>d). Moreover, in our case the power cable is an input of the problem and not a design variable. Heavy computations are not a limitation to calculate the different parameters. As a result, 2D FEM simulations are performed with FEMM^{TM} software at several frequencies.

To estimate the inductance and the resistance of the power cable, a magneto-static simulation is performed where the current disposition is known. From the resulting real and imaginary voltage drops in the different cable sections the values are extracted. This is an approach similar to the one employed in the calculation of ICT matrix [87]. The capacitance values are also calculated with an electrostatic simulation where the potential of the different conductors is fixed. In our design approach a shielded cable with shielding connected to the ground of 5m is considered for the load.

The common mode impedance in open-circuit (end terminals of the cable disconnect) and short-circuit (end terminals connected to ground) of the considered cable is represented in the Figure 3.42.

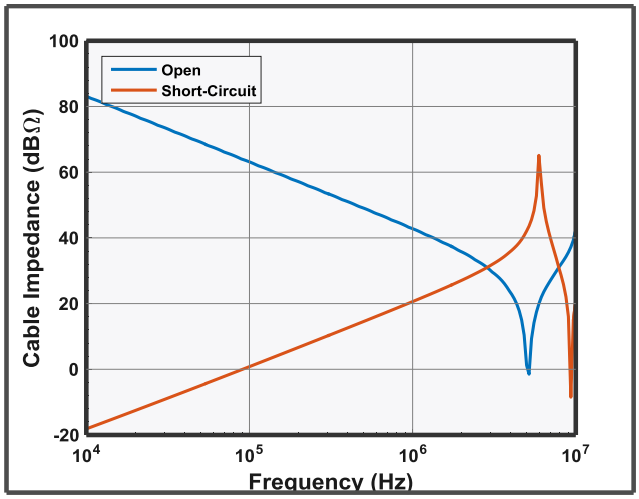


Figure 3.42 : Common mode impedance of the considered power cable

As shown, at frequencies below several MHz the behavior is assimilated to a capacitor of approximately 1.11nF. So far, no data was found to correlate our estimation. As an order of magnitude to compare our value, in [37] a common mode impedance of 800pF was found (however no information was given about the disposition of the cable). As a result, as a first order approach, the estimation of the common mode impedance is accepted for the design.

3.5.2 Contactors

A contactor is an electromechanical switch controlled by an electrical signal. In the power cabinet, the contactors are generic and designed for the worst-case scenario. A possible improvement for the total mass of the power cabinet could be the use of solid-state contactors like they are used nowadays on aircrafts for the protection function [88]. To estimate the unitary contactor mass, a surface response is created as a function of the nominal current and voltage using reference data from aircraft manufacturers. The equivalent response surface is presented in the Figure 3.43 where the regression model and the data used for the model are displayed.



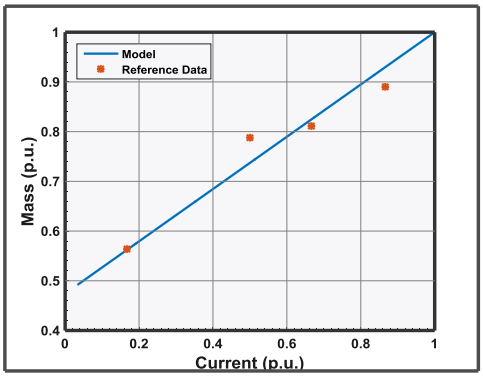


Figure 3.43 : Contactor: (left) Schematic & (right) comparison between contactor mass model and reference data

3.6 Assembly elements

In this category, all components that ensure the integration, mechanical protection and installation of the power converters are considered. That is, all the casing and assembly elements of the power converter. As a result, in the present work, the mass of these elements is considered as a ratio of the mass of the other elements.

$$M_{assembly} = K_1 \cdot N_{converters} \cdot M_{converter} + K_2 \cdot N_{contactors} \cdot M_{contactor} \tag{3-75}$$

These ratios are extracted from reference data on current existing power converters on current aircrafts.

3.7 Conclusion

In this chapter the mathematical models of the different components used in the design of the power electronic cabinet have been presented. Some models like the capacitor, the power modules and the contactors are directly extracted using regression laws. The regression models are compared to the given manufacturer data to determine a validity region.

For the heat sink and magnetic components the direct modelling approach is used. In the magnetic modelling, two important modelling steps have been made. First, increment of resistance with frequency is calculated by a response surface using FEM calculation data. Second, a thermal network has been deployed to take into account temperature distribution depending on the geometry of the inductor. All these models have been validated using manufacturer, experimental or simulation data. Results show an acceptable correlation between the models and the data to be employed in the optimization design.

Chapter 4 : Inverter specifications & design

4.1 Introduction

The different models presented in Chapter III, will be used in this chapter for the design of the power inverter which is a key element of the electrical power cabinet. The power inverter is designed to fulfill all its functions under a certain environment, which defines a set of operating constraints. To ensure compatibility of all the systems, aircraft manufacturers define a series of specifications that each device must comply with.

In this chapter, the different specifications used for the design of the power inverter are presented. These specifications are the basis for the definition of the architecture of the power inverter. Using these specifications each part of the inverter is optimized using the optimization environment described in Chapter II and the component models presented in Chapter III. At the end, a response surface of the different elements that will be used to design the power bay is extracted.

4.2 Specifications

The power inverter specifications can be divided into six different categories:

- *functional*: the power inverter must provide all the different operation points required by the loads, taking into account the environmental conditions: altitude, temperature, humidity …,
- *electrical*: to ensure interoperability between electrical power sources and loads, quality and stability standards are defined and must be fulfilled by each electrical system,
- *thermal*: to ensure working below limit temperatures, aircraft manufacturers specify the cooling conditions (temperature, pressure, air speed…) of the different elements,
- *mechanical*: aircraft equipment must be designed to support different forces and vibrations during its lifetime,
- *reliability*: every system in the aircraft must ensure a certain reliability. Indeed, equipment robustness is a crucial design parameter in aircraft systems,
- *protection*: if a failure occurs in one system, it must be rapidly segregated and isolated to prevent failure in other system.

In the present work, only the functional, electrical and thermal specifications are considered for the design of the power inverter and treated in more detail in the optimization process.

4.3 Functional specifications

The electrical power cabinet must supply six different 3-phase AC loads (ref. Chapter I). Except for the 3-phase transformer, the rest of the loads are smooth-pole permanent magnet synchronous machines in the present work. As stated in Chapter I, load power demand varies depending on the flight phase. The power consumed by each load, P_{load}, is calculated with the following formula:

$$P_{load} = 3 \cdot V_{ph} \cdot I_{ph} \cdot \cos\varphi = T \cdot \omega \tag{4-1}$$

with V_{ph}, I_{ph} the RMS value of the phase voltage and current respectively (electrical quantities controlled by the inverters) and $\cos\varphi$ the power factor of the load. The voltage and the current are related to the mechanical speed ω and torque T of the load respectively. The required operation points (voltage, current) of the electric motor depend on the specific needs of the mechanical load. Three different kinds of mechanical loads are found in the reference case of study:

- *Quadratic*: the mechanical torque is proportional to the square of the machine speed ($T = k \cdot \omega^2$). As a consequence the necessary speed is expressed as follows:

$$P_{load} = T \cdot \omega = k \cdot \omega^3 \rightarrow \omega = \frac{(P_{load})^{1/3}}{k} \tag{4-2}$$

$$P_{load} = T \cdot \omega = T \cdot \frac{(P_{load})^{1/3}}{k} \rightarrow T = k \cdot (P_{load})^{2/3} \tag{4-3}$$

To extract the proportional term k we use a reference point where speed, torque and power ($\omega_{ref}, I_{ref}, P_{load_ref}$) are known.

$$\frac{\omega}{\omega_{ref}} = \left(\frac{P_{load}}{P_{load_ref}} \right)^{1/3} \tag{4-4}$$

$$\frac{T}{T_{ref}} = \left(\frac{P_{load}}{P_{load_ref}} \right)^{2/3} \tag{4-5}$$

The loads behaving as quadratic loads, supplied by the electrical power cabinet are the three rotational machines (two compressors and one pump) of the ECS system (ECS1, ECS2, ECS3) and the FTIS system.

- *Maximal torque:* in the More Electrical Aircraft, engine starting is performed by an electrical machine. Indeed, electrical machines can provide high torques even at low speed. Higher torque means higher angular acceleration of the machine which means

less time required to perform engine starting operation. The torque is always at the maximum allowed value:

$$T = T_{\max} \tag{4-6}$$

$$\omega = \frac{P_{load}}{T} \tag{4-7}$$

- *Constant voltage*: the electrical power cabinet feds a three-phase transformer (TAC) linked to a 115V 400Hz electrical network where different AC loads are connected. As a result, regardless of the consumed power, the supplied voltage and frequency needs to remain constant. The voltage and current operation points are calculated with the following equations.

$$\omega = \omega_{ref} = 2 \cdot \pi \cdot 400 \tag{4-8}$$

$$I_{ph} = \frac{P_{load}}{3V_{ph} \cos\varphi} \tag{4-9}$$

The Figure 4.1 displays the variation of the torque and speed operating points depending on the load power demand.

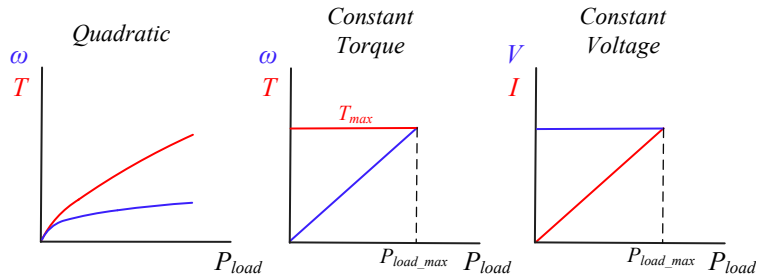


Figure 4.1 : Speed/ Torque points as a function of the load power demand for different types of loads

For electric simulations in the design environment, an equivalent R-L-E model is used for the load (See Figure 4.2). The hypothesis of perfectly sinusoidal *emf* waveforms is considered and the neutral point of the load is floating. Different modulation strategies could be applied to reduce the phase current for the same consumed power (Third harmonic injection)[89] or to reduce the switching losses of the inverter (SVPWM…)[90][91]. In the present study, only third harmonic sinus injection is considered. Studying the impact of the other modulation strategies is certainly a perspective for this work.

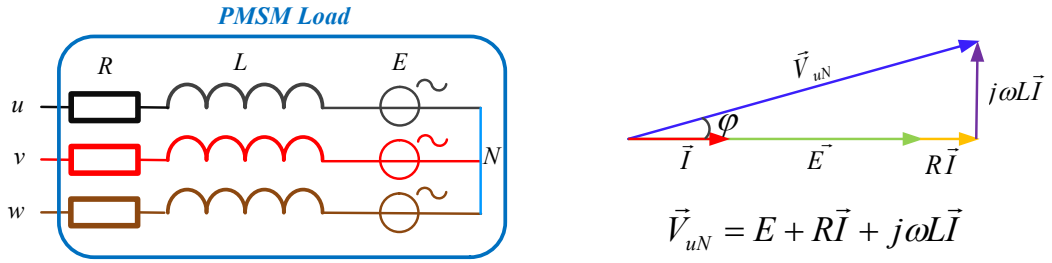


Figure 4.2 : Equivalent electric model of PMSM (left) and Fresnel diagram of one phase (right)

Knowing the different parameters of the machine and the desired speed/torque, the electrical operating point at which the machine must operate is extracted. To determine the electric point, the Fresnel diagram is transformed from the *abc* reference frame into the *dq* reference frame using the power invariant transformation [92]. The transformation and the used equations to calculate the electrical point are given in Appendix D. The different parameters used to describe the different parameters of the electrical machine are given in the following tables.

Symbol	Meaning
$R_{d,q}$	Stator phase resistance of the machine in the *dq* frame
$L_{d,q}$	Cyclic phase inductance of the machine in the *dq* frame
N_p	Number of poles pairs of the machine
Φ_{rd}	Magnet flux of the machine in the *dq* frame
J	Moment of Inertia of the machine
f	Friction coefficient of the machine
Kem	Motor torque constant
V_{DC}	Bus bar voltage
I_{DC}	Bus bar current
$I_{d,q}$	Machine phase current in the *dq* frame
$I_{a,b,c}$	Machine phase current in the *abc* frame
$V_{d,q}$	Machine phase voltage in the *dq* frame
$V_{a,b,c}$	Machine phase voltage in the *abc* frame
ω	Mechanical speed of the machine
C_{res}	Resistive torque of the machine
K_p	Proportional coefficient for the Proportional-Integral corrector
τ_i	Time constant for the Proportional-Integral corrector
G	Ratio of the modulator (Assumed $1/V_{DC}$ at the nominal operation point)

Table 4-1 : Parameters of the machine and its supply

Subscript	Meaning
0	Initial value of the magnitude at a certain operation point of the machine
ref	Reference value of the magnitude desired in the control loop
i	Variable associated to the current control loop
ω	Variable associated to the speed control loop

Table 4-2 : Subscript table

4.4 Electric specifications

High frequency current harmonics created by the inverters in the DC bus can cause other equipment malfunctioning. To prevent this situation, power equipment must satisfy electric standards defined by aircraft manufacturers. In this study, the standards are the HVDC standard [93] defined by Airbus and the DO-160 [94] defined by EUROCAE & RTCA. The electric specifications are as well divided into three subcategories depending on their range of application: *differential mode*, *common mode* and *stability*.

4.4.1 Differential mode

To avoid propagation of current harmonics through the network, a filter is inserted between the bus and the inverter. However, other systems generate voltage harmonics in the dc bus that are absorbed by the filter and thus generate extra current harmonics in the dc bus.

4.4.1.1 Current harmonics absorbed by the inverters

The current harmonics absorbed by the inverter are the sum of two contributions: the harmonics generated by the switching cells themselves and the current harmonics originated by DC bus voltage variations. The differential HVDC standard takes into account both phenomena and imposes a certain current envelope (magnitude of the current harmonics) in the dc bus to be satisfied when the inverter is supplied by a voltage fulfilling a certain voltage envelope (magnitude of the voltage harmonics), as shown in Figure 4.3.

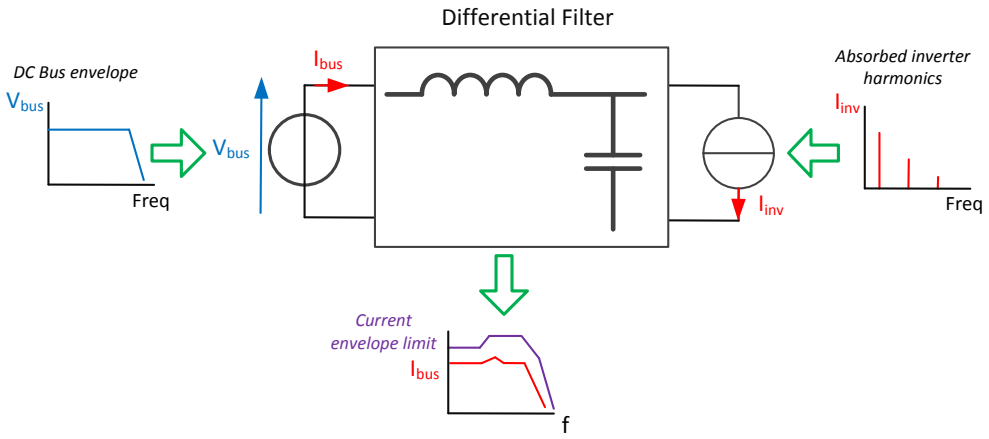


Figure 4.3 : Graphical description of the differential current envelope standard test

If the current envelope is respected, the impedance of the load is ensured to be above a certain limit which is a key element to ensure system stability, using Midlebrook's theorem [96]. Mathematically, the absorbed bus current I_{bus} at each specific frequency f is the sum of two contributions, that are calculated with the transfer functions TF_1 and TF_2:

$$I_{bus}(f) = TF_1 \cdot V_{bus}(f) + TF_2 \cdot I_{inv}(f) \tag{4-10}$$

with V_{bus} the voltage harmonics defined in the HVDC standard test and I_{inv} the absorbed power inverter current harmonics. To design the filter, specifications are treated to create an optimization constraint that is the maximal difference between the standard limit, I_{NORM}, and the estimated magnitude of the bus current harmonic at a specific frequency, $|I_{bus}(f)|$.

$$\max_f(|I_{bus}(f)| - I_{NORM}(f) \leq 0 \tag{4-11}$$

The mathematical expression of this constraint is not well adapted for a continuous optimization, because it is not derivable at all points respect to the optimization variables (dimensions of the filters). However, despite this drawback, this solution was chosen as it highly penalizes resonant solutions when the optimization is running.

4.4.1.2 RMS DC-bus Current caused by harmonics of DC bus voltage

In the second HVDC standard specification, for each voltage harmonic injected by the dc bus, the RMS value of the differential dc bus current must remain below a certain limit. The threshold is determined as a function of the load nominal power using a function defined in the HVDC standard.

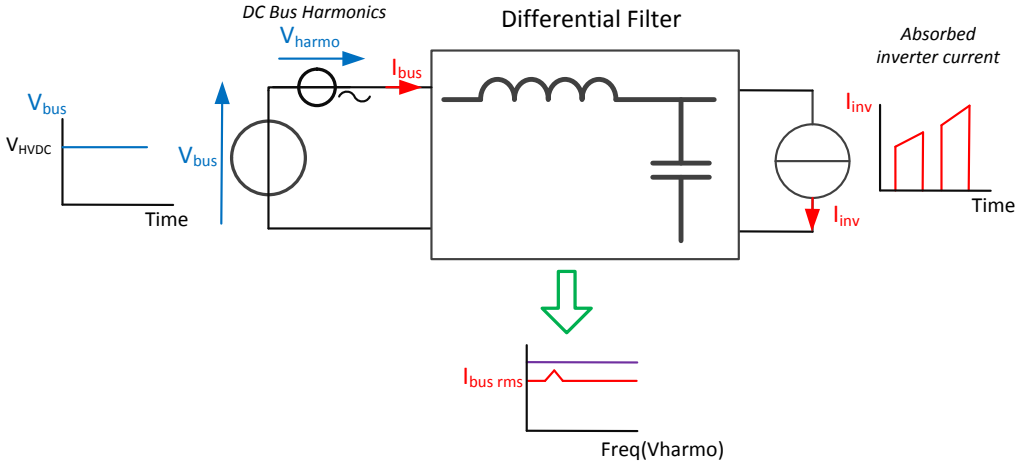


Figure 4.4 : Graphic description of the differential current rms test

The RMS value of the absorbed bus current when an additional injected bus voltage frequency at frequency f_n is inserted $I_{busrms}(f_n)$; is calculated with the current harmonic contribution caused by the injected bus harmonic voltage and sum all of the inverter absorbed current harmonics taking.

$$I_{busrms}(f_n)=\frac{1}{\sqrt{2}}\sqrt{(TF_1\cdot V_{HVDCbus}(f_n)+TF_2\cdot I_{inv_i}(f_n))^2+(\sum TF_2\cdot I_{inv_i}(f_k))^2+2I^2{}_0};\forall k\neq n \quad (4\text{-}12)$$

with I_0 the absorbed DC current. To define the RMS specification as an optimization constraint in our design problem, the RMS value at each injected harmonic is compared with the threshold value limit of the HVDC standard $I_{NORM\,rms}(f)$.

$$max(|I_{busrms}(f)|-I_{NORM\,rms}(f))\leq 0 \quad (4\text{-}13)$$

4.4.1.3 Transient specifications

The HVDC standard takes into account transient states of the DC bus. Even in case of variation of the DC bus voltage, the current response must remain below a certain limit, as presented in Figure 4.5.

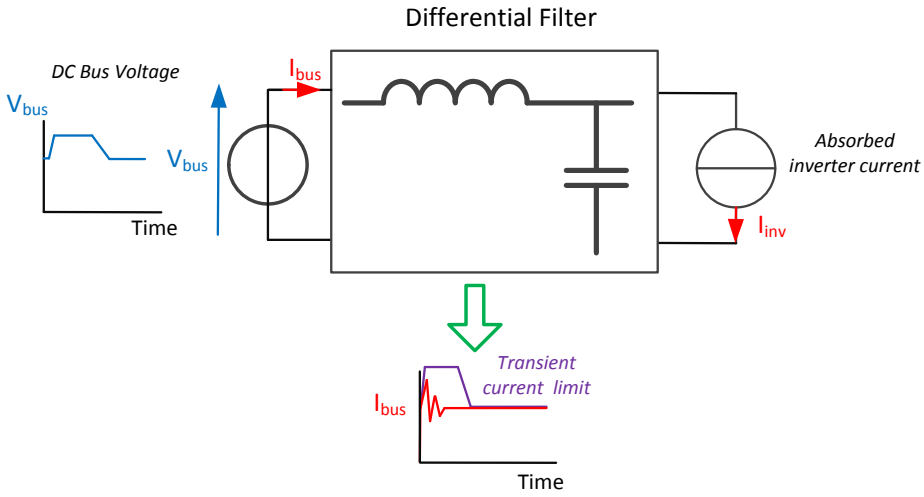


Figure 4.5 : Graphic description of the differential current transient test

However, to compute this specification, the regulation loop must be also defined. In the present work, design of the regulation strategy is out of the scope, but control issues must be considered for the transient design. A simple classical cascaded regulation strategy is used as a reference because it is one of the most used regulation strategies in industry for this kind of load. The outer slow speed control loop drives the inner faster current loop; *(d, q)* frame is selected for this purpose and the maximal torque by amps strategy is implemented (i_{dref}=0). Figure 4.6 presents the schematic of the regulation loops.

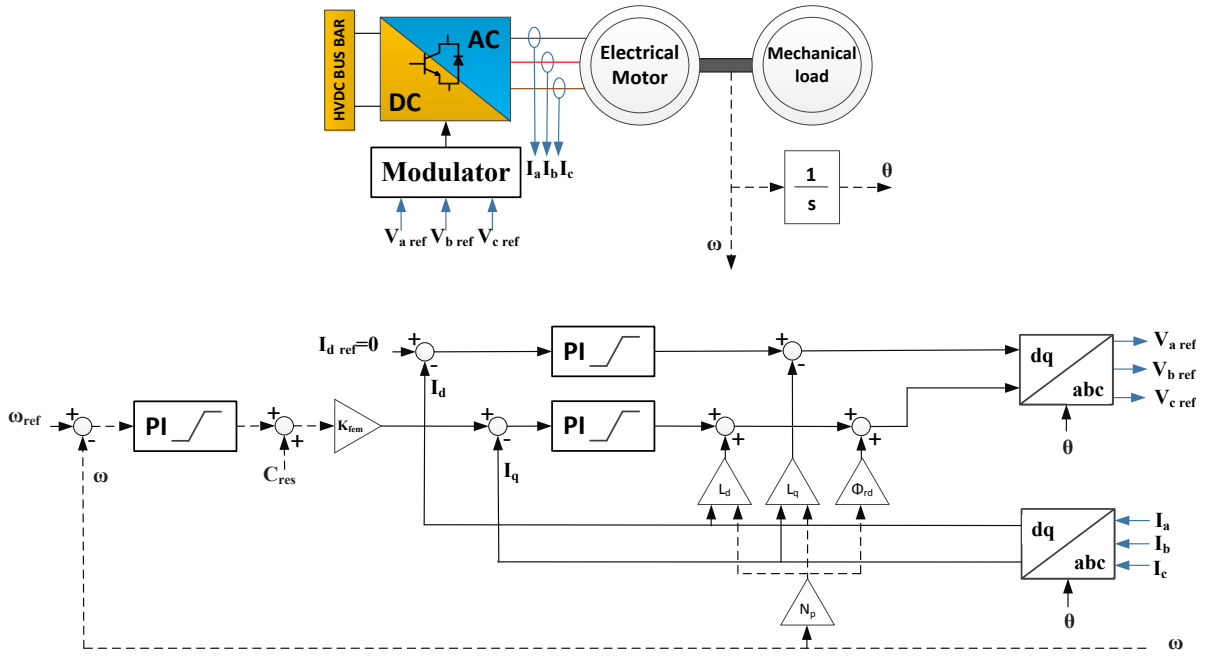


Figure 4.6 : Regulation schematic of the Inverter+PMSM at maximal torque

Both regulators are of Proportional-Integral (PI) type. The transfer functions for both regulation loops are expressed as follows:

$$\frac{I_{d,q}}{I_{d,q_{ref}}} = \frac{1+\tau_{i_i} s}{1+\tau_{i_i}\left(1+\frac{R_{d,q}}{K_{p_i}}\right)s+\frac{\tau_{i_i} L_{d,q}}{K_{p_i}}s^2} \tag{4-14}$$

$$\frac{\omega}{\omega_{ref}} = \frac{\left(1+\tau_{i_\omega} s\right)}{1+\tau_{i_\omega}\left(1+\frac{f}{K_{p_\omega} Kem}\right)s+\frac{\tau_{i_\omega} J}{K_{p_\omega} Kem}s^2} \tag{4-15}$$

with K_p and τ_i the proportional and time constant of the current and speed regulators. If these expressions are associated to a canonic second order function, the proportional and integral terms can be expressed as a function of the band-pass pulsation ω_n and the damping coefficient ξ.

$$K_{p_i} = 2\xi_i L_{d,q}\omega_{n_i} - R_{d,q} \tag{4-16}$$

$$\tau_{i_i} = \frac{2\xi_i}{\omega_{n_i}} - \frac{R_{d,q}}{L_{d,q}\omega_{n_i}^2} \tag{4-17}$$

$$K_{p_\omega} = \frac{2\xi_i J\omega_{n_i} - f}{Kem} \tag{4-18}$$

$$\tau_{i_\omega} = \frac{2\xi_\omega}{\omega_{n_\omega}} - \frac{f}{J\omega_{n_\omega}^2} \tag{4-19}$$

To ensure a proper regulation, the band-pass of both regulations must be below the switching frequency. In addition, the band-pass frequency of the current control loop must be above the band-pass frequency of the speed control loop. For the damping coefficient, from the abacus of a second order system the coefficient is chosen to reduce the transient time (which is 0.707). The different chosen values of the regulators are selected as follows:

$$\xi_i = \xi_\omega = 0.707 \tag{4-20}$$

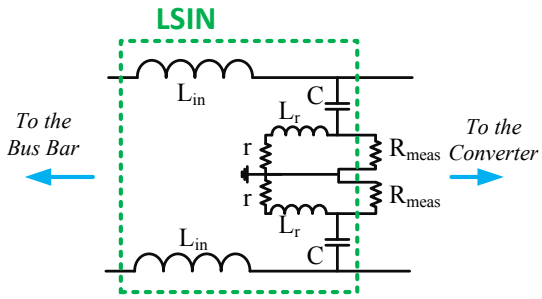
$$\omega_{n_\omega} = \frac{\omega_{n_i}}{10} = \frac{2\pi f_{sw}}{100} \tag{4-21}$$

In the optimization loop, only the first and seconds HVDC standard tests are taken into account with the frequency solver. The transient test requires a time-domain simulation and it cannot be considered in the optimization step as it requires a much higher computation time. Instead, using the final optimized result, a time-domain simulation using SABER^{TM} software is launched and the compliance of the transient test is verified.

4.4.2 Common mode

All electrical systems are normally connected to the mass plane to ensure protection function or to have a common reference for all the magnitudes. The mass plane is a common point for all the electric systems and circulating currents through it must be avoided. Common mode interference is a major and critical issue in the design of power converters. Different propagation mechanisms take place for these currents and each mechanism is dominant in a different frequency range. In the present work, only conducted common mode currents are considered. The conducted common mode currents are mainly created by fast voltage variations (Particularly at the output of the switching cells, were high voltage variations, *dv/dt*, appear) associated with the parasitic capacitances of the system.

The DO160 standard [94] specifies a test to ensure equipment compliance to common mode emissions. In the test, common mode conducted current harmonics must be below a certain limit envelope. In addition, as the DC bus impedance varies depending on the connected equipment, a Line Impedance Stabilizer Network (LISN) is inserted between the equipment under test (the inverter in this case) and the bus bar. The LISN isolates the impact of the bus. The LISN circuit used in the present work is shown in Figure 4.7. The input impedance of the LISN respects the DO160 standard limits [75].



Parameter	Value
L_{in}	250 µF
C	220 nF
L_r	50 µH
r	5 Ω
R_{meas}	50 Ω

Figure 4.7 : LISN circuit representation and values

The R_{meas} resistor corresponds to the probe resistance value, which is 50 Ω (the standard is normalized for that value). The currents are measured using both terminals, as shown in Figure 4.8. Additional resistors of 50 Ω are placed at the measure terminals of the LISN even if the probe is not situated at those terminals.

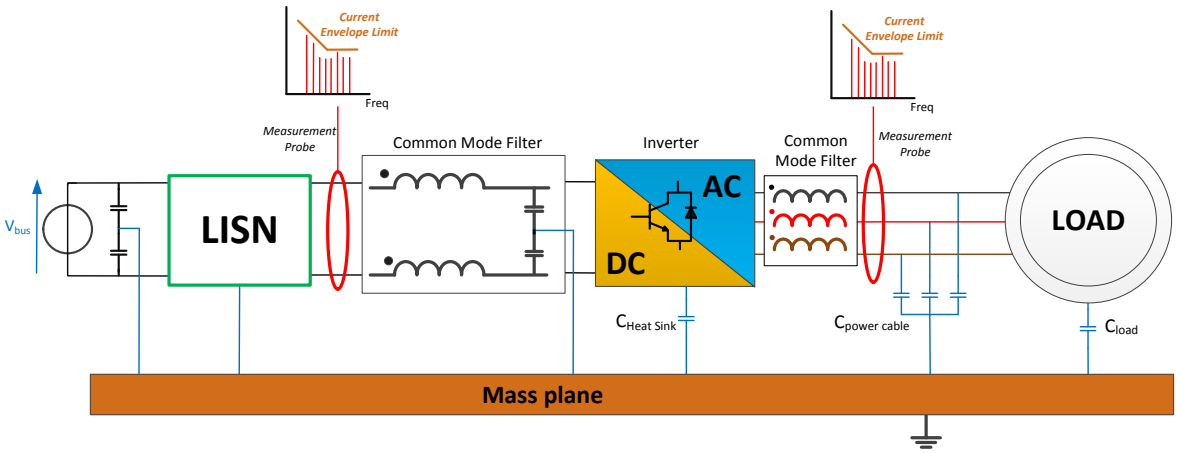


Figure 4.8 : DO160 common mode current measurement setup

The DO160 standard also specifies an Interference Band Width (BWI) for the interference measure. The bandwidth is so narrow (1kHz for frequencies up to 30 MHz) that the measure is supposed to be the amplitude at the specific frequencies and no special post processing function needs to be applied to the simulated values. The specification is treated as a constraint in the optimization problem as follows:

$$\max\left[I_{common}(f) - I_{DO160NORM}(f)\right] \leq 0 \tag{4-22}$$

With I_{common} the evaluated (in our case, the values are extracted from a simulation with a frequency solver) conducted common mode current and $I_{DO160NORM}$ the specifications limits of the standard. In our study, only the DC common mode filter is considered. AC Common mode filter design should be considered in future works. For the common mode impedances, the reference values from [37] are used. That is, for the common mode capacitor of each power module a 300pF parasitic capacitor is considered and for the power load the same values of the same document are taken (see Figure 4.9 : Common mode impedance of the

load). For the power cable, the reference value of a shielded power cable of 5m that was presented in section 3.5.1 is used. For the rise and fall times of the switching cell a reference value of 30ns is taken from the *CAS120M12BM2* power *SiC* module reference (Validity of the common mode simulation up to F_{val}=30 MHz)

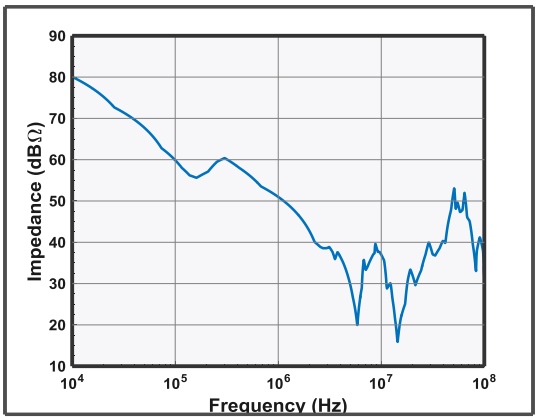


Figure 4.9 : Common mode impedance of the load used in the present work (Hypothesis)

4.4.3 Stability specifications

When a closed-control loop is applied to regulate the output of a power converter, it presents a constant power load behavior. The dynamic impedance of a constant power load is locally a negative resistance (as presented in Figure 4.10, the local slope of the (*V, I*) characteristic of a constant power load is negative).

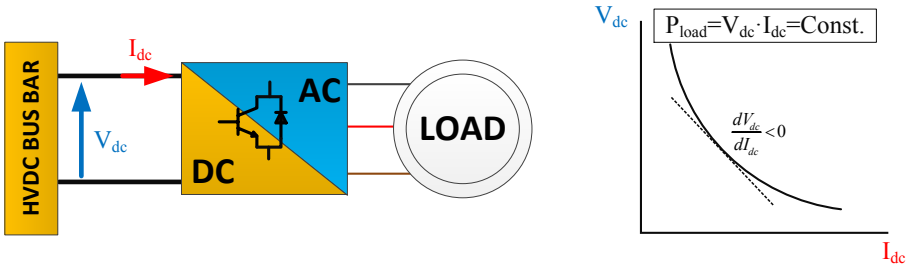


Figure 4.10 : Constant power load characteristic curve representation

As a result, an increment of the network voltage causes a decrement of the network current and vice-versa. The negative resistance can lead to instability if the filter is not sufficiently damped [19][20] Filter design must consider possible instabilities created by the interaction of both systems (filter and inverter).

To consider stability constraints, the basic condition of stability is applied [95]. All poles of the transfer function need to be in the region of convergence. That is, in the left side of the imaginary axis (negative real part) in a pole-zero plot.

$$real(p_i) < 0;\ \forall i = 1...n \tag{4-23}$$

with p_i the poles of the system. To calculate the poles, the transfer function of the whole system needs to be determined. The inverter is a non-linear system and therefore a linear

continuous transfer function cannot be representative for all the operating points. However, at frequencies below the switching function, the transfer function can be approximated by performing a linearization for a given operation point. In [19], a full approach is presented and validated to calculate the transfer function of an inverter connected to a PMSM. The transfer function of the input admittance Y_{PMSM} is approximated by a fourth order transfer function.

$$Y_{PMSM}(s) = \frac{\delta I_{DC}}{\delta V_{DC}} = \frac{\alpha_0 + \alpha_1 s + \alpha_2 s^2 + \alpha_3 s^3 + \alpha_4 s^4}{\beta_0 + \beta_1 s + \beta_2 s^2 + \beta_3 s^3 + \beta_4 s^4} \tag{4-24}$$

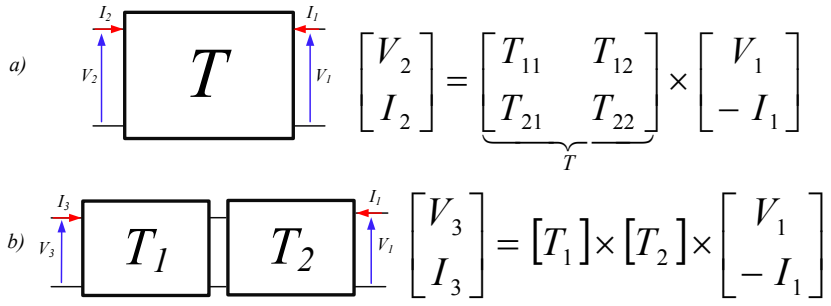
The approach is valid for a maximal torque regulation strategy as the one used in the present work (see Figure 4.6). The derivate terms are obtained from the derivation around a certain voltage-current operating point (V_{DC_0}, I_{DC_0}).

$$V_{DC} \cdot I_{DC} = V_d \cdot I_d + V_q \cdot I_q + V_h \cdot I_h \tag{4-25}$$

$$\delta V_{DC} \cdot I_{DC_0} + V_{DC_0} \cdot \delta I_{DC} = \delta V_d \cdot I_{d_0} + V_{d_0} \cdot \delta I_d + \delta V_q \cdot I_{q_0} + V_{q_0} \cdot \delta I_q \tag{4-26}$$

with (V_d, V_q, I_d, I_q) the voltages and currents in the *dq* reference frame using a power conservative transformation (appendix D). The whole description of the transfer function coefficients (α, β) calculation is explained in Appendix E.

The filters are represented using the ABCD quadripole formalism as shown in Figure 4.11. This representation helps to cascade filters by direct multiplication of the matrices.



$$\begin{bmatrix} V_2 \\ I_2 \end{bmatrix} = \underbrace{\begin{bmatrix} T_{11} & T_{12} \\ T_{21} & T_{22} \end{bmatrix}}_{T} \times \begin{bmatrix} V_1 \\ -I_1 \end{bmatrix}$$

$$\begin{bmatrix} V_3 \\ I_3 \end{bmatrix} = [T_1] \times [T_2] \times \begin{bmatrix} V_1 \\ -I_1 \end{bmatrix}$$

Figure 4.11 : a) Quadrupole representation b) Cascading quadrupoles association

Multiplying successively the filter matrices, the busbar voltages and currents (V_{bus}, I_{bus}) are expressed as a function of the DC inverter+PMSM load voltage and current (V_{DC}, I_{DC}). The admittance seen by the bus bar Y_{TOT} is calculated with the expression (4-27) where the admittance of the inverter+PMSM (Y_{PMSM}) is replaced by the fourth order expression calculated with equation (4-27).

$$Y_{TOT}(s) = \frac{I_{bus}}{V_{bus}} = \frac{T_{21} V_{DC} - T_{22} I_{DC}}{T_{11} V_{DC} - T_{12} I_{DC}} = \frac{T_{21} + T_{22} Y_{PMSM}}{T_{11} + T_{12} Y_{PMSM}} \tag{4-27}$$

Using the roots of the admittance transfer function, the stability specification is expressed as an optimization constraint.

$$max(real(p_i)) + k_{margin} \leq 0; \forall i = 1...n \;\; k_{margin} > 0 \tag{4-28}$$

With: k_{margin} a margin to avoid oscillatory systems (p_i = 0). In our case it is fixed at 10^{-6}. Calculating the transfer function has other advantages. In [97], the filters are designed using the natural frequencies (calculated from the poles of the transfer function). This approach reduces the computation time while obtaining the same results. The same approach is used in the present approach. For the impedance envelope constraint (4-11) the natural frequencies of the input admittance and the abrupt variations of the norm are calculated (corners in the norm). By performing this simplification, the number of calculated frequencies to determine the frequency envelope compliance decreases from 6000 to a few tens.

4.4.4 Filter design

Only passive filter topologies are considered due to their high robustness. Moreover, the envelope specification imposes a damping resistance to limit resonance effects. A differential filter is placed as close as possible to the switching cells to absorb the high frequency harmonics generated by the cells and a common mode filter is inserted to control the common mode current harmonics. As presented in Chapter III, leakage inductance of the common mode filter and common mode capacitors will modify the input admittance seen by the DC bus bar. When adding a filter to a determined input admittance Y_0, the resulting modified Y_0' admittance is expressed as follows:

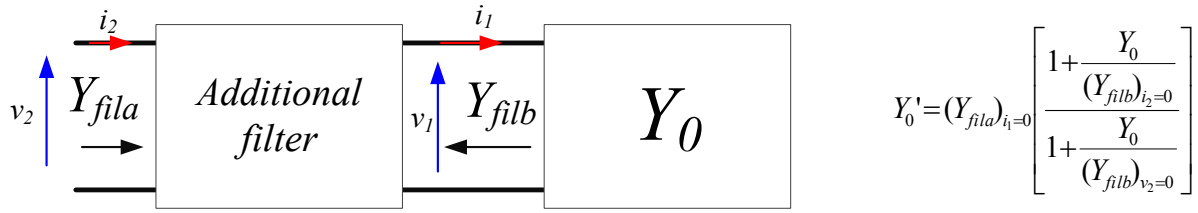


Figure 4.12 : Modified input admittance by insertion of filter

Let us simply demonstrate the previous equation, using the ABCD quadripole notation in Figure 4.11, the modified input admittance Y_0' is expressed as follows:

$$Y_0' = \frac{i_2}{v_2} = \frac{T_{21} \cdot v_1 + T_{22} \cdot i_1}{T_{11} \cdot v_1 + T_{12} \cdot i_1} = \frac{T_{21} + T_{22} \cdot Y_0}{T_{11} + T_{12} \cdot Y_0} \tag{4-29}$$

Extracting the common mode factors of numerator and denominator, the following equation is obtained.

$$Y_0' = \frac{T_{21}}{T_{11}} \frac{1+\dfrac{Y_0}{T_{21}/T_{22}}}{1+\dfrac{Y_0}{T_{11}/T_{12}}} = (Y_{fila})_{i_1=0} \left[\frac{1+\dfrac{Y_0}{(Y_{filb})_{i_2=0}}}{1+\dfrac{Y_0}{(Y_{filb})_{v_2=0}}} \right] \tag{4-30}$$

The poles of the first stage input open filter admittance $(Y_{fila})_{i_1=0}$ are as well poles of the modified admittance.

As a result, if the common mode filter is present in the first input stage (from the bus bar side) the high resonant differential frequency of the common mode filter is present as well in the admittance seen by the bus bar. In addition, the differential filter (close to the cell) and the inverter + PMSM admittance magnitude are relatively low at high frequencies. As a consequence, the input admittance seen by the bus bar ($Y_0 << (Y_{filb})_{i_2=0}$ & $Y_0 << (Y_{filb})_{v_2=0}$) will be the open filter admittance of the first stage. If the first stage is a common mode filter, the input admittance is the input admittance of the common mode filter at high frequencies.

To solve this situation an additional differential filter is inserted between the common mode filter and the dc bus bar. The Figure 4.13 describes an example of what has been previously said. Three filters stages with different differential cut-off frequencies are used ($f_{c1} = f_{sw}/10$; $f_{c2}=100f_{sw}$ for the differential mode cut-off frequency of the common mode filter, $f_{c3} = f_{sw}/sqrt(100)$). In the first one, the common mode filter is present in the first stage while on the second it is inserted in the second stage. As shown, the second architecture respects the input admittance constraint while the other one does not. The second topology is therefore the one used for our design problem.

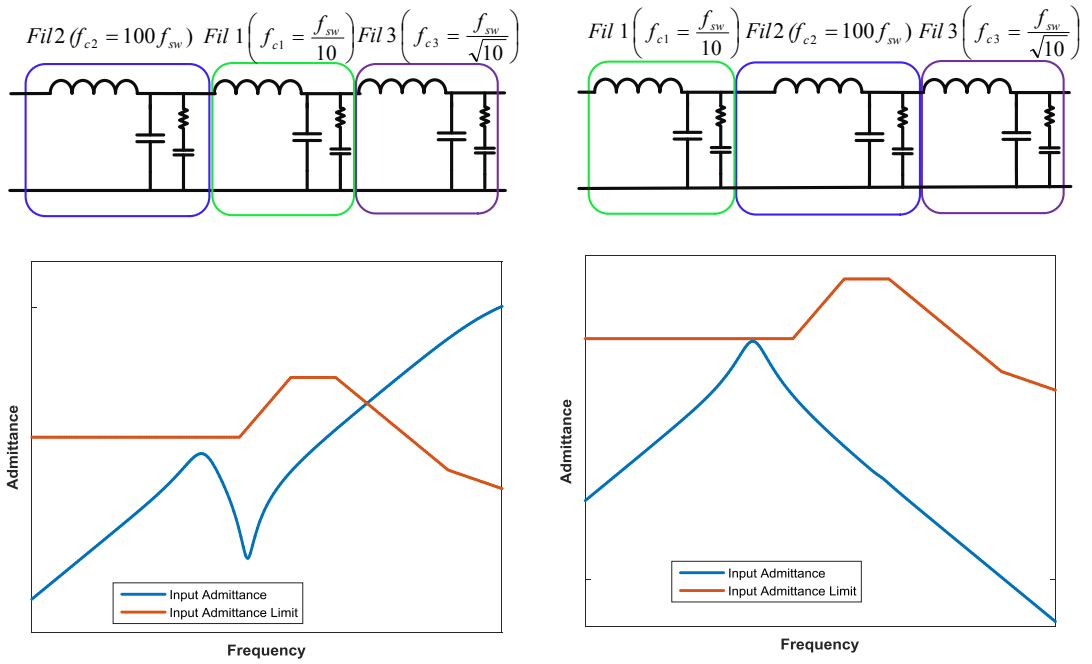


Figure 4.13 : Solution with common mode filter at beginning of the load (left) and chosen solution (right)

4.4.4.1 Material selection

The dimensions of the components are the optimization variables of all the problems as was presented in Chapter II. However, material choice remains an important input for the design of capacitors and magnetic elements.

4.4.4.1.a Dielectric material

For the capacitors, as presented in Chapter III, the main criterion to choose the film or ceramic technology is the specific energy density depending on the rated voltage. Film capacitors give a better energy density at voltages above 500 V and ceramic should be preferred at lower voltages.

4.4.4.1.b Magnetic material

In the case of magnetic components, there is no "best" material for all cases and as a consequence designers must select the different materials according to certain criteria. For example, they can choose the best material according to the performance factor $f \cdot B_{ac}$ (in Hz·T) [98]. Other approaches consider a hypothetical metamaterial, gathering the properties of the best material for each operation point [25]. The last approach however, is limited to a certain family of materials that share similar properties (families of ferrites for example).

In the present work, the main criterion taken into account for the design of the different inductors is the maximal allowed magnetic field. For a given inductance value L, operating current I and magnetic field B, the product of the number of turns N by section of the core A_c is expressed as follows:

$$N \cdot A_c = \frac{L \cdot I}{B} \tag{4-31}$$

The $N \cdot A_c$ product is directly related to the volume of the inductor; higher magnetic fields will lead to compact inductors. The maximal magnetic field is limited by two different phenomena: the saturation field B_{sat} and the maximal temperature. Indeed, depending on the thermal environment (natural convection, forced convection…) the maximal loss density of the core is limited. If the core is expected to operate at a certain frequency, the maximal allowed magnetic field is calculated using the loss equations presented in section 3.3.1.2. As a result, the maximal magnetic field is calculated with the following equation.

$$B = min(B_{sat}, f(Freq, Loss\ Density)) \tag{4-32}$$

If the previous equation is represented versus the operating for different materials and core losses density, we get the following curves:

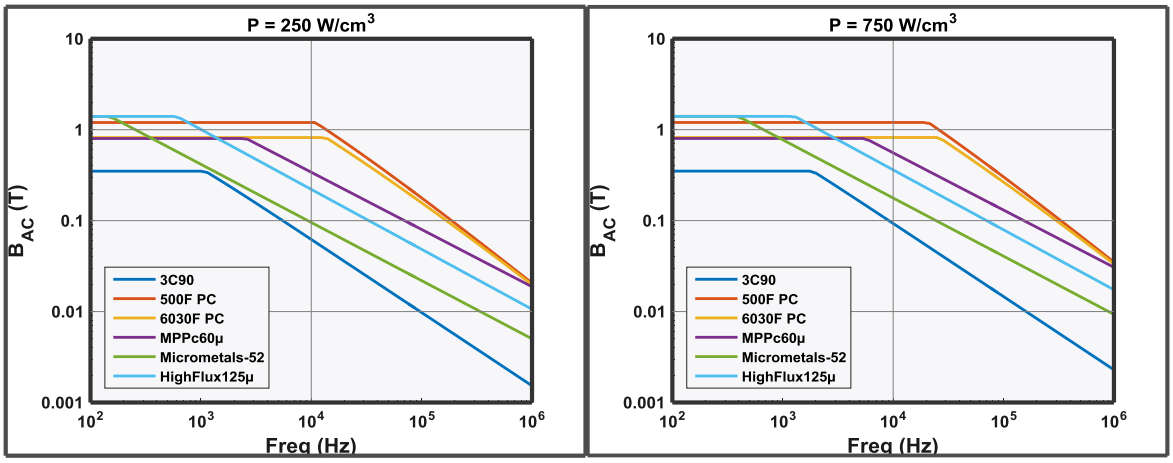


Figure 4.14 : Maximal allowed magnetic field vs frequency for different losses densities left) 250 W/m^3, right) 750W/m^3

As shown, magnetic saturation field determines the maximal allowed magnetic field up to a certain frequency, where the thermal constraints limit the maximal allowed magnetic field. Higher loss densities (improved cooling conditions) lead to higher maximal allowed magnetic field and more compact inductors. Best core materials are those allowing higher saturation fields and having lower core densities as for example the Nanocristallyne 500F.

4.4.4.1.c Conductors material

For the conductor material of magnetic elements, the key factor, determining the final weight is the maximal loss density which is limited by cooling conditions. The loss density of a conductor is directly related to the current density in the conductor. As a result, the conductor section must satisfy the following inequality:

$$A_w \geq \frac{I_{rms}}{J_{rms}} \tag{4-33}$$

with J_{rms} the maximal allowed current density of the winding, I_{rms} the RMS current and A_w the winding section.

It has been presented how to calculate the best magnetic and conductor material to reduce the volume. However, we are looking for the optimal combination of conductor and magnetic material. In addition, it is not the volume that is important but the weight, so the density of the materials must be taken into account. In [64], the material combinations with higher ratio of densities $\rho_{core} / \rho_{winding}$ led to lighter inductors.

In the present work, the same approach as in [64] is used to determine the optimal combination of materials. Knowing the operating conditions (peak current $\hat{I}$, RMS current I_{rms}), the inductance value and the winding filling factor k_w (set at 0.9 in our case) the area product of core section A_c and winding section A_w is determined for each combination of conductor-core material.

$$A_c \cdot A_w = \frac{L \cdot \hat{I} \cdot I_{rms}}{k_w \cdot J_{rms} \cdot B} \tag{4-34}$$

J_{rms} and B depend on the material and the cooling environment. The area product is directly related to the final volume of the inductor. Using the area product, the dimensions of the inductor are calculated using the affinity model presented in section 3.3.1.10. For the number of turns the following equation is used.

$$A_w = 0.83\sqrt{A_w A_c}\left(\frac{\rho_{mag}}{k_w \cdot \rho_{cond}}\right)^{0.46} \tag{4-35}$$

$$N = \frac{J_{rms} \cdot k_w \cdot A_w}{I_{rms}} \tag{4-36}$$

The air-gap is determined to achieve the necessary inductor value.

$$airgap = \mu_0 A_c\left(\frac{N^2}{L} - \sum R_{core}\right) \tag{4-37}$$

with $\sum R_{core}$ the different reluctances of the core sections and μ_0 the air permeability. From this "preliminary" design, the optimal combination of conductor and core material is chosen. In our case the correction factor for the skin and effect was just calculated for the copper and therefore it is the only conductor material proposed in the process.

4.4.4.2 Optimization results (filter design)

The DC filter (common and differential mode) is optimized considering different nominal operating points for the load.

- 16 different nominal phase currents ranging from 20% to 100% of a reference nominal phase current,
- 3 different switching frequencies *{0.6f; f; 1.4f}*.

To choose the starting point, the cut-off frequencies of each section of the filters (See Figure 4.13) must be chosen. In [99], a mathematical demonstration shows how to choose the value of the damping resistor to minimize the peak filter output impedance in an *LC* filter with an *R*-C_d damping circuit. The "optimal" resistor depends on the *n* (see eq. (4-38)) ratio between the damping circuit capacitor C_d and the LC-filter capacitor *C*.

$$n = \frac{C_d}{C} \tag{4-38}$$

The value that leads to optimum damping is:

$$R = \sqrt{\frac{L(2+n)(4+3n)}{2Cn^2(4+n)}} \tag{4-39}$$

the maximum peak filter output impedance occurs at the frequency :

$$f' = \frac{1}{2\pi\sqrt{LC}}\sqrt{\frac{2}{2+n}} \tag{4-40}$$

and the absolute maximal value of the output filter impedance Z_{max} is:

$$Z_{max} = \sqrt{\frac{L}{C}}\frac{\sqrt{4+2n}}{n} \tag{4-41}$$

Each section of the filter is chosen according to the previous equation, by selecting the cut-off frequency *f'* and the maximal output filter impedance Z_{max} (The system of equations (4-40) and (4-41) determines the L,C values of the filter). For the common mode filter section, L represents the leakage inductance of the common mode inductor. For our calculations the value of *n* is fixed at 2.

Once the different values (*L*,*C*, *R*, C_d) of the filter have been determined, the dimensions of the component need to be determined. For the capacitor the value is directly extracted from the regression surface of the model. The resistor model has not been developed in the present work. To avoid resistors of high values and therefore high losses, the electric losses of the resistor are treated as a penalty for the objective function:

$$Penalty_{resisotr} = 0.01RI_{rms}^2 \tag{4-42}$$

For the inductor the area product described in section 4.4.4.1 is used and the material choice is also performed. In any case, for the optimization requiring a starting point, the dimensions are chosen to respect the different constraints.

Apart from the aforementioned aeronautic constraints, some other constraints, inherent to the physics of the components, are chosen. For magnetic components, the temperatures and magnetic fields must remain below a certain limit.

$$T_{ind_{max}} - 125 \le 0 \tag{4-43}$$

$$B_{max} - 0.95 \cdot B_{sat} \le 0 \tag{4-44}$$

with $T_{ind_{\max}}$ the maximal inductor temperature (in °C), B_{max} the maximum of the magnetic field (in T) and B_{sat} the magnetic saturation of the material (in T). A *5%* margin is used for the magnetic constraint to avoid reaching the non-linearity of the B-H curve. The capacitor maximal temperature $T_{cap_{max}}$ (in °C) must be as well below a certain limit.

$$T_{cap_{max}} - 90 \le 0 \tag{4-45}$$

The optimization problem for the design of the inverter DC filter is launched using the *fmincon* interior point algorithm and the affinity model of the inductor. The design problem involves the three stages of the filter; this means the 3 inductors, 7 capacitors and the 3 resistors. The problem involves 21 optimization variables which are the dimensions of the different components and 40 constraints. The results where the optimization converged for the

cases of the switching frequency 1*f* are shown in Figure 4.15 right (blue points). As presented in the aforementioned figure, the optimization only converged in 3 cases out of 17, which means that the optimization method is really poor and not robust. An example of an optimization failure is shown in Figure 4.15 left. In this example, although the initial point for each satisfies the constraints (See max constraint not respected in the red line), the optimization goes into a region where the constraints are not respected to find a possible minimum and the optimization algorithm is not able to return into a region where the constraints are satisfied.

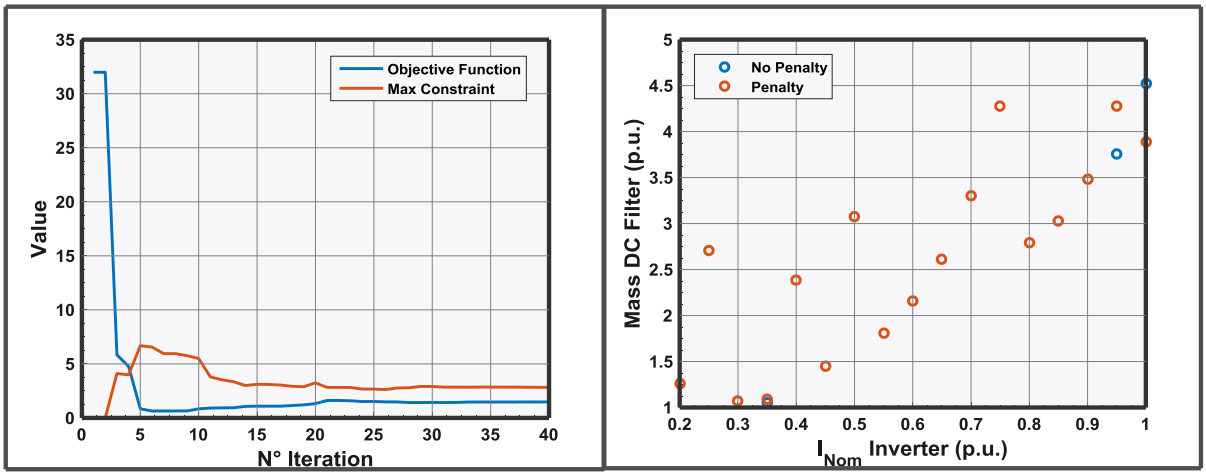


Figure 4.15 : Filter optimization. left) Evolution of the objective function and the maximal value of the constrain vector for 45% of the nominal current & switching frequency equal to 1f right) comparison of results between the optimization results with and without a penalty function

To solve this problem, a consequent penalty factor is set into the objective function. The objective function is represented as follows.

$$min \quad \sum weight_i + M \cdot \sum (g(x) > 0); \ \forall i = 1,..., N_{components} \tag{4-46}$$

with M a penalty factor much bigger than the estimated weight of the system in order to penalize solutions not respecting the constraints. The formulation of this objective has the disadvantage of being discontinuous at the constraints limits but it proved to give good results in this particular problem. Future works, should reconsider the way this penalty function is described.

The comparison between optimization results, with and without the penalty function, for the switching frequency *f*, is presented in Figure 4.15 right. As shown, the use of the penalty function helps reaching a feasible solution. However, a lot of points are out of the general trend and they correspond clearly to local minima. For example, looking at the results at 0.45 and 0.55 p.u. (see Figure 4.15), we can guess that the solution found at 0.5 p.u. can be improved.

As a result, for the points were the final solution objective function is above the objective function of the next point in nominal current, the optimization is re-launched using as initial point the optimal solution of the point above in nominal current. Indeed, normally solutions

for high nominal currents should be compliant at lower nominal currents. Depending on the final results, the new solution is accepted or discarded. The algorithm for this new phase is described in Figure 4.16.

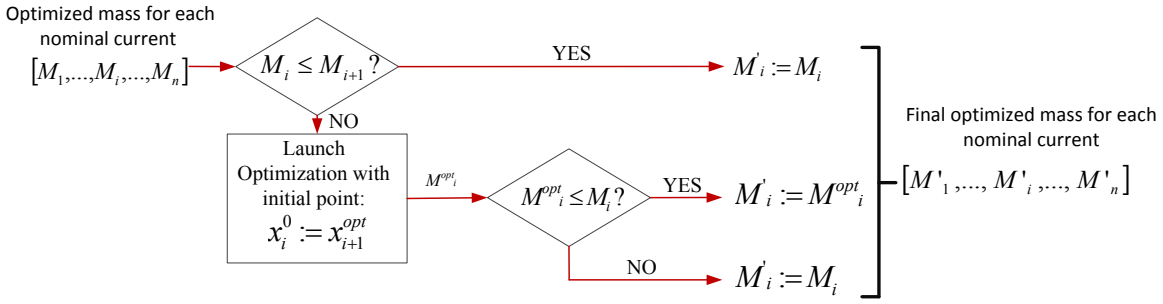


Figure 4.16 : Algorithm to eliminate undesired local minima

The comparison of results is shown in Figure 4.17.

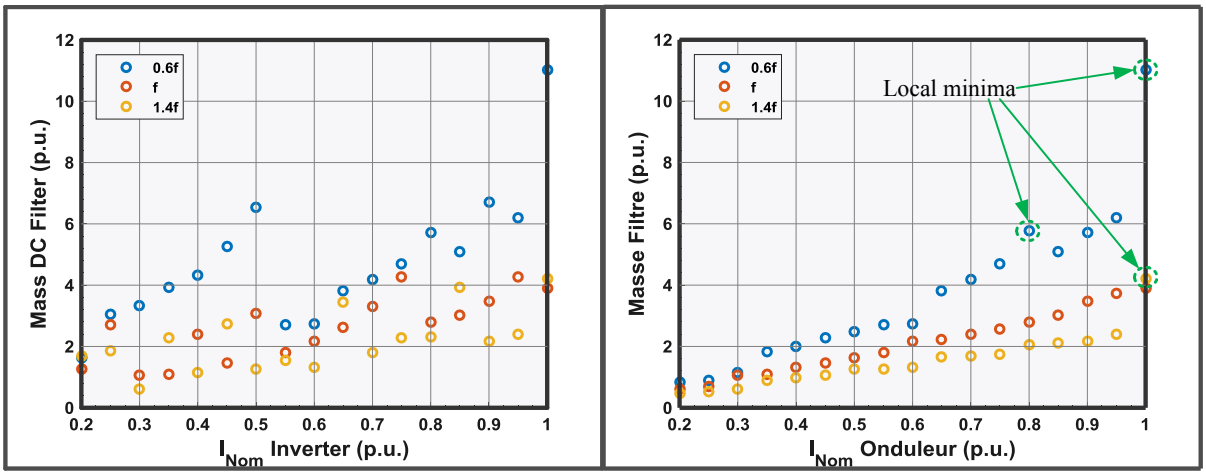


Figure 4.17 : Filter results vs nominal inverter current for different power: (left) optimized results using the penalty function & (right) re-optimization using the methodology described in Figure 4.16

As shown, the results fall more into a tendency and local minima are reduced except in some cases. Indeed, the algorithm did not work or there was no higher power nominal current (1 p.u.) to re-launch the optimization. As a result, for these specific cases, interpolation was used as way of "estimating" if there is a potential solution in that area. In case the final calculation gives these points as best results, we will try to find of way of arriving to a feasible solution corresponding to that value.

This solution is clearly a hint for future works: optimization could begin from higher nominal currents and after the solution has converged use the optimal point for lower nominal currents. In all cases, the solution is calculated with the affinity models of the inductor (See section 3.3.1.10). No further work was developed using the free models of the magnetics components as the robustness of our optimization solution is not very high and it remains a point to be improved. However, this could be a key element to further reduce the mass of the filters.

4.5 Thermal specifications

4.5.1 Cabin air flow recycling

In the present work, the electric power cabinet is situated in the pressurized area of the aircraft. This is an advantage for the design as cooling conditions : temperature and pressure are quite stable for all flight phases (around 18% variation). The majority of the power converter components will be cooled by natural convection to avoid auxiliary systems installation and increase robustness. In some cases however, forced convection might be necessary. For example, in power semiconductors where the loss density is very high.

In these special cases, the cabin air flow is re-used; the pressurized blown air of the cabin provided by the Environmental Control System (ECS) is extracted and blown into the power electronic cabinet. The air is equally distributed within the different power electronics converters as shown in Figure 4.18.

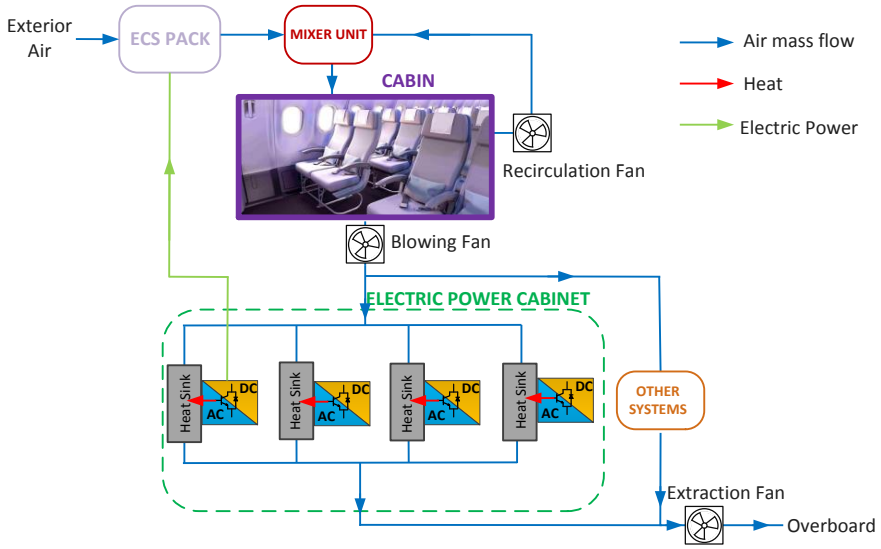


Figure 4.18 : Cooling architecture of the power cabinet

As a consequence, the air flow depends on the number of inverters. The temperature of the blown air varies slightly depending on the altitude of the aircraft as shown in Figure 4.19. A 18% difference exists between the temperature on ground and during flight.

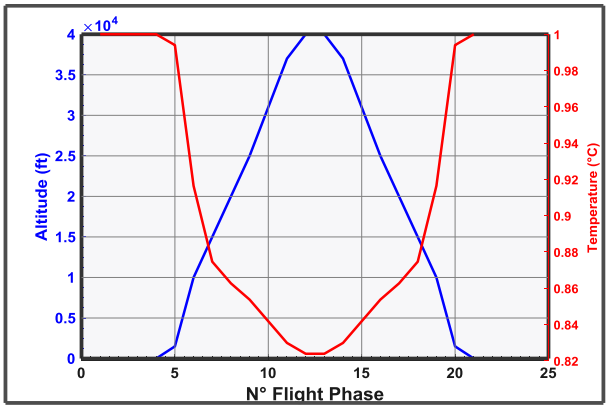


Figure 4.19 : Input temperature variation depending on the altitude and flight phase (See Figure 1.6)

A certain maximal amount of air is available for the cooling of the power electronics cabinet. Otherwise, the design will require to oversize the ECS system. One objective of the present study is to determine the minimal necessary airflow and the power cabinet mass sensibility to the airflow.

Other specifications are as well applied to the design of the cooling systems. Aeronautic standards define a certain sonic limit for the forced air $v_{air_{sonic}}$. The following constraint must be verified for the air speed v_{air}.

$$v_{air} - v_{air_{sonic}} \leq 0 \tag{4-47}$$

In addition, ΔP the pressure drop when air is flowing through the heat sink, is limited below a certain threshold ΔP_{limit}

$$\Delta P - \Delta P_{limit} \leq 0 \tag{4-48}$$

4.5.2 Power module and heat sink

The first step is to estimate the number of inverters in the cabinet which depends on the inverter nominal current. The design algorithm involves four steps:

1. determination of the necessary number of inverters,
2. calculation of the losses on each power inverter for all the flight phases,
3. determination of the worst case,
4. optimization of the heat sink,
5. validation of the design for the four different cases.

A schematic of the steps and the different involved variables is presented in Figure 4.20.

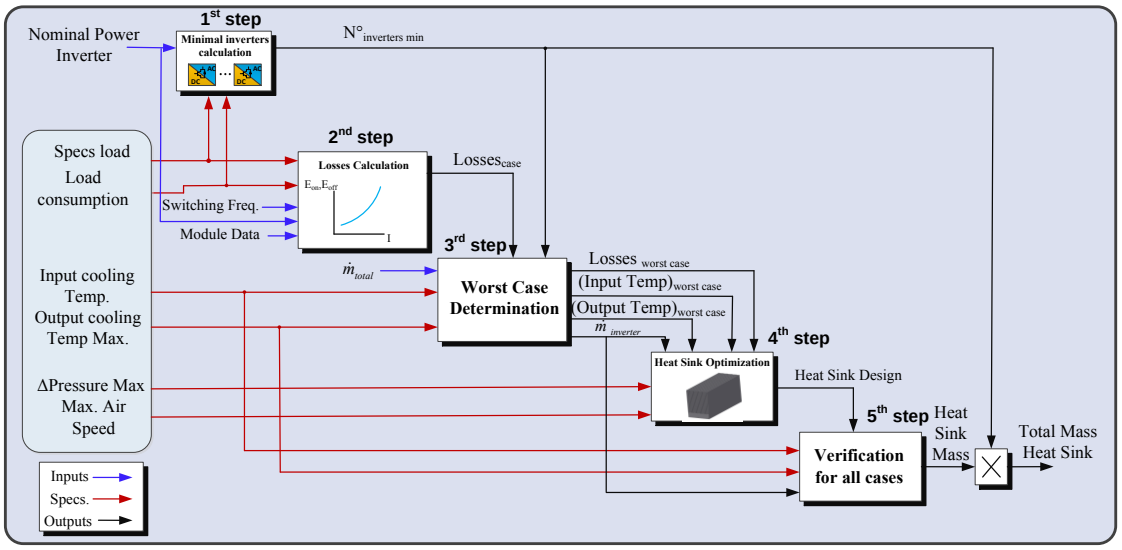


Figure 4.20 : Heat Sink design algorithm graphical description

As presented in Figure 4.18, the air mass flow is distributed equally among the different inverters. The number of inverters will be higher if the unitary nominal current is low. As a result, less forced air is available for each inverter but, at the same time, the losses of one inverter will be lower. The determination of the minimal number of inverter is simple: a further discussion is detailed in Chapter V. Let us consider N loads and M flight phases. For each flight phase k the minimal number of inverters of nominal current $I_{nom_inverter}$ to supply one load j is:

$$N°inverters_{j,k} = ceil\left(\frac{I_{j,k}}{I_{nom_inverter}}\right); \forall j = 1...N, \forall k = 1...M \tag{4-49}$$

With *ceil(x)* a function that gives the upper integer of the ratio x. (Ex, ceil(1.45) = 2) and $I_{j,k}$ the consumed current of the load j for the case k. The power electronic cabinet must consider as well the failure of the inverters for each case ($N°fail_k$). At the end, the number of necessary inverters per flight phase is:

$$N°inverters_k = \sum_{j=1}^{N} N°inverters_{j,k} + N°fail_k, \forall k = 1...M \tag{4-50}$$

The minimal number of necessary inverters ($N°inverters_{min}$) is the maximum number of required modules:

$$N°inverters_{min} = \max\left(\sum_{j=1}^{N} N°inverters_{j,k} + N°fail_k\right), \forall k = 1...M \tag{4-51}$$

Given the load specifications defined for the six loads of our problem and the power consumptions of a reference case for a More Electrical Aircraft, the following number of required inverters is a function of the nominal current of each inverter.

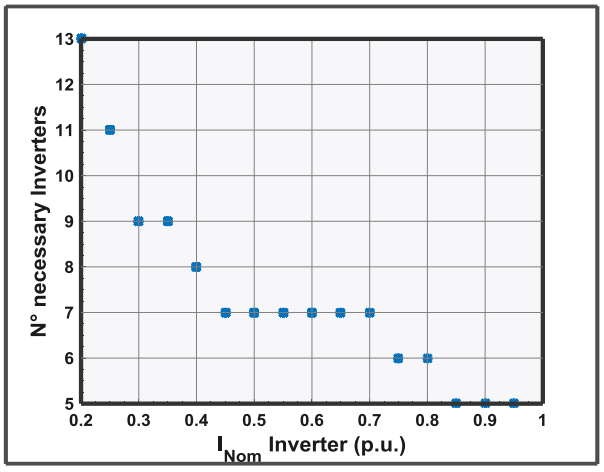


Figure 4.21 : N° of necessary inverters vs the nominal current of each inverter

The mass flow per inverter ($\dot{m}_{inverter}$) is determined from the total blown air to the cabinet ($\dot{m}_{total}$). Solutions including inverters with higher nominal current will have as a consequence more available air flow per inverter:

$$\dot{m}_{inverter} = \frac{\dot{m}_{total}}{N°inverters_{\min}} \tag{4-52}$$

The second step is to calculate the power losses of each power inverter for every case. In section 4.3 and in Appendix D, the calculation of the operating point of the load and the inverters is described. From the operation point, the switching frequency and the number of power inverters supplying the load at each case a steady-state simulation is performed. From this simulation the voltage/current waveforms of each semiconductor are extracted. The waveforms are used to estimate the losses using the procedure presented in section 3.2 and the datasheets of the manufacturer.

The third step is to determine the most critical point to serve as basis to the optimization of the heat sink. The maximal possible extracted power for each inverter is determined by the cabinet thermal constraints.

$$P_{cooled_{max}} = \dot{m}_{module} \cdot C_p \cdot \left(T_{out_{max}} - T_{in}\right) \tag{4-53}$$

In this expression, T_{in} is the input temperature of the air flow in the heat sink, which varies with altitude (Figure 4.19); $T_{out_{max}}$ is the maximal allowed output temperature and C_p is the specific heat of the air. The cooled power is directly related to the thermal resistance of the heat sink and the power module.

$$P_{cooled} = P_{losses} = R_{th} \cdot \left(T_j - \overline{T}_{HS} \right) \tag{4-54}$$

with R_{th} the sum of the thermal resistances of the power module and the heat sink, T_j the junction temperature of the power module and $\overline{T}_{HS}$ the average air temperature between the heat sink fins.

The most critical case will have the maximal output temperature T_{out_max} and the maximal junction temperature $T_{j_{\max}}$. As a result, the average air temperature $\overline{T}_{HS}$ is obtained from these two temperature limit values. For all flight cases, the total thermal resistance (power modules + heat sink) must fulfill the following inequality.

$$R_{th} \leq \frac{T_{j_{max}} - \overline{T}_{HS}}{P_{losses,i,k}} = \frac{T_{j_{max}} - \dfrac{T_{out_max} + T_{in}}{2}}{P_{losses,i,k}}; \forall i = 1...N° inverters\ min; \forall k = 1...M \tag{4-55}$$

The minimal required thermal resistance will correspond to the most critical and dimensioning point.

The fourth step is the heat sink optimization. Using all the thermal specifications (Section 4.5), the critical point and the heat sink model (section 3.4.1), the optimization process is performed. The optimization variables are the physical dimensions of the heat sink and the *fmincon* interior point optimization algorithm is used. In this case, no penalty function is used. The fifth step checks the optimized solution for all the rest of cases and loads.

Using the aforementioned algorithm, the heat sink & power module are designed for the same nominal currents and switching frequencies as in the DC filter problem. However, there are two more parameters to determine: the power module reference and the total necessary air flow for the power cabinet.

For the power modules, wide-band gap technologies are chosen due to their lower switching losses and their higher operation temperature. Taking as reference the switched voltage level (over 540 V), full MOSFET SiC power modules is the chosen technology. Three references from Wolfspeed™ (*CAS120M12BM2-Ref 1*, *CAS300M12BM2-Ref 2*, *CAS325M12HM2-Ref 3*) are compared. These modules are chosen because their nominal values fit the operation points of the inverter. However, the study could be performed for any other power module reference.

For the total mass flow, 7 different mass flows are chosen for the sensitivity analysis (20% to 100% of a reference mass flow). In Figure 4.22 left, the obtained results of power modules & heat sink mass (concerning a single inverter) and the maximal air mass flow are shown. Missing points indicate no feasible solution was found at those points.

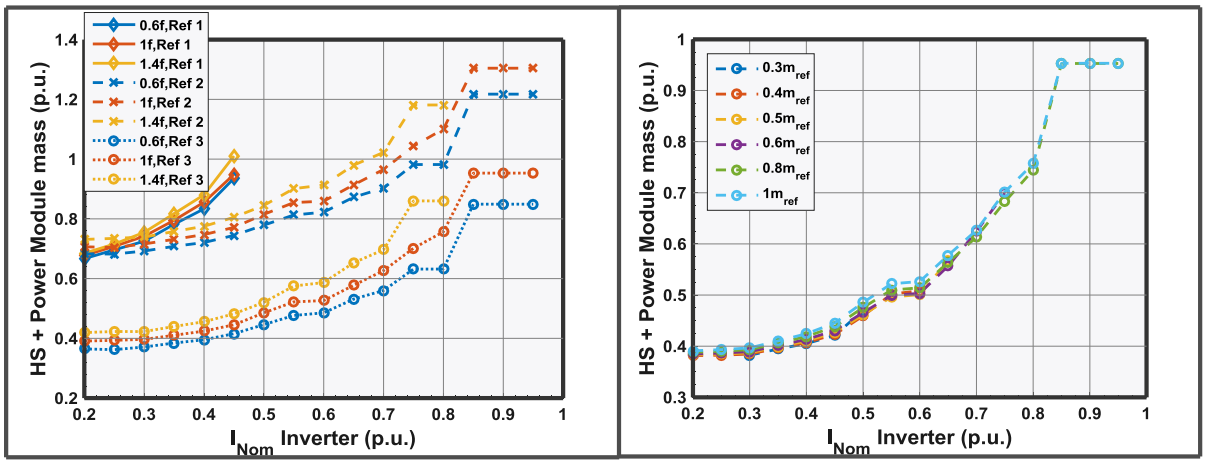


Figure 4.22 : Heat Sink & Power module per inverter mass vs I_{Nom} : (left) for different power modules references and switching frequencies and fixed $m=m_{ref}$ (right) Heat Sink & Power module per inverter mass vs I_{Nom} for different mass flow and fixed switching frequency f_2 and Ref. 3.

Power module with *Ref 3* remains the best solution for all the unitary inverter nominal currents. As expected, weight increases with nominal current and switching frequency (losses increase with current and switching frequency). Another important conclusion is related to flat zones in the solution (Ex. high nominal currents of the inverter in Figure 4.22 left). In these cases, the critical design point is the same and it is not the nominal current of the inverter.

In Figure 4.22 right, for the chosen power module reference (*Ref 3*) and switching frequency f_2 the weight results are shown for different total mass flow. The mass sensitivity to forced air mass flow is low and it even slightly increases when mass flow increases. The reason for this low sensibility is that sonic constraint limits the transversal area between fins and when mass flow increases, the minimum transversal area needs must also be increased. As a result, the fin height or the spacing between fins needs to increase which means higher weight :

$$v_{sonic_{max}} = \frac{\dot{m}_{air}}{\rho_{air}(N-1)A_{spacing}} = \frac{\dot{m}_{air}}{\rho_{air}(N-1)bh_{fin}} \rightarrow\uparrow \dot{m}_{air} \rightarrow\uparrow A_{spacing} \tag{4-56}$$

with $\dot{m}_{air}$ the mass flow cooling the inverter, ρ_{air} the air density, N the number of fins, b the distance between fins and h_{fin} the fin height. However, a minimum air flow is required for every solution. As shown in Figure 4.22, the solutions having a higher nominal current are only feasible with a high total air mass flow.

In Figure 4.23 left, the minimum total air flow is calculated as a function of the nominal inverter current. The optimal values from a cooling system point of view are values between 0.3-0.55 p.u., as they require less total air flow and therefore a smaller fan. In Figure 4.23 right, the total mass in the power cabinet concerning the power modules and heat sinks is presented. A nominal power of 0.5 p.u. is the lightest solution. Indeed, a trade-off exists between nominal power and number of power modules which is responsible of the valley

shape. The total mass results are presented at $0.8m_{ref}$ which is the reference total air flow value for all the heat sink design in the rest of the results. To compare all the different solutions, the same external cooling system must be considered and 0.8 m_{ref} is the minimal necessary total air flow giving feasible heat sinks. However, an important fact to remember is that solutions between 0.3-0.55 require less mass flow which means less weight for the cooling system. As consequence, an important perspective to perform a good trade-off will be to determine the cooling system weight added by gr/s of airflow. However, all the impact at aircraft level should be considered which can easily increase the complexity of the problem.

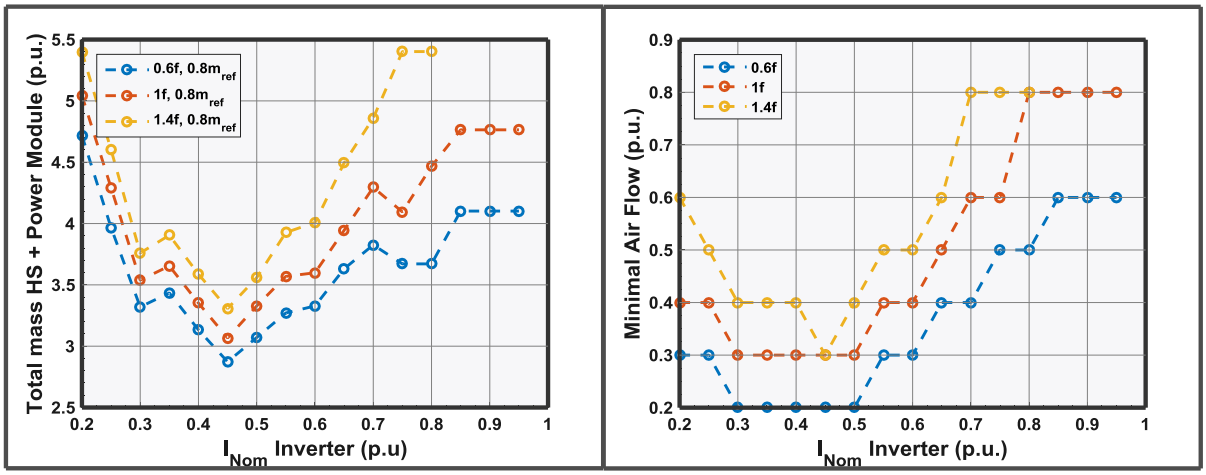


Figure 4.23 : (left) Minimal required total mass flow versuss nominal current for power module Ref. 3 and different switching frequencies & (right) Total mass of the power modules + heat sinks for $0.8m_{ref}$ and power module Ref. 3

4.6 Parallel inverter operation

Inverter parallelizing is a freedom degree of the study to determine the optimal solution in terms of mass.

4.6.1 Paralleling cells problematic

In power conversion, to deal with current limitations of semiconductors, switching cells are set in parallel. When connecting two cells in parallel, the waveforms of the output voltages must be rigorously the same to avoid short circuits between them. As a result, all properties of the components, and all parameters of the regulation loops must be perfectly equal. From an industrial point of view, this is difficult to achieve as manufactured devices always present dispersion in their properties. Figure 4.24 shows how the dispersion of the propagation time of the components involved in the transition of the semiconductors will cause short circuits between cells.

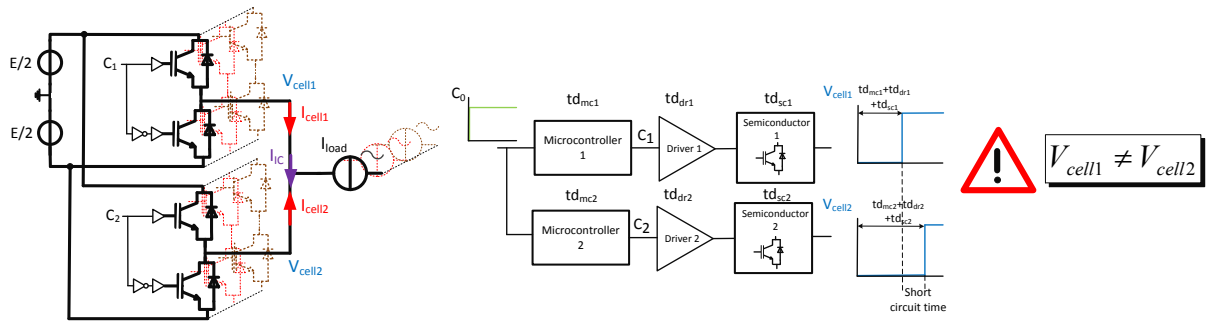


Figure 4.24 : Propagation time dispersion problem example

To limit short-circuits currents, inductors are inserted at the output of the switching cell. When a voltage difference appears between cells, the slope of the circulating current is determined by the voltage difference and the inductor value.

$$\frac{dI_{ic}}{dt} = \frac{V_{cell1} - V_{cell2}}{2L} \tag{4-57}$$

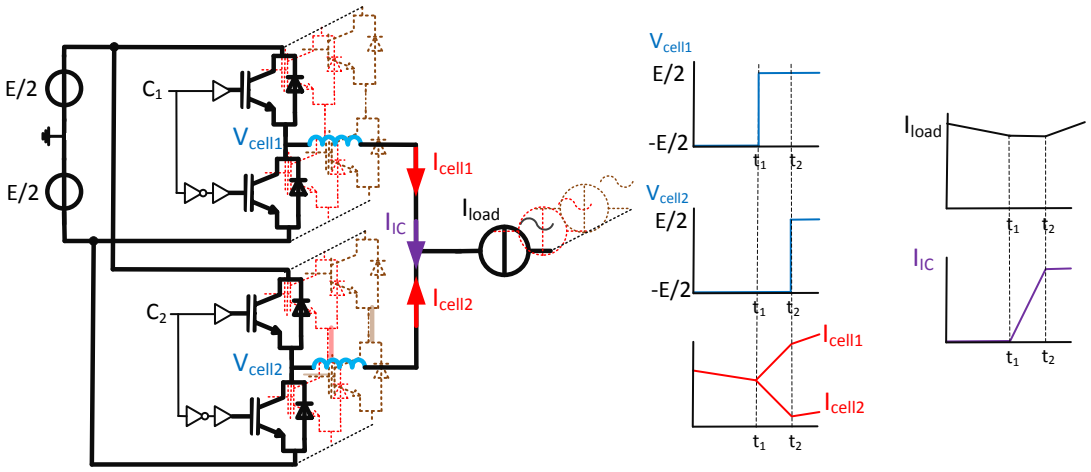


Figure 4.25 : Insertion of the coupling inductors and the chronogram of the different waveforms

The extra inter-cell currents caused by the output voltage cell difference have two main consequences:

- *Increase of power losses*: the current ripple increases the winding and core losses of the inductor. Moreover, one of the cells will switch higher currents resulting in higher conduction and switching losses.
- *Regulation impact*: the current increment is seen by the current probes which may impact the regulation loop performances.

Nevertheless, voltage difference between cells can be turned into an advantage. Interleaving techniques are applied to increase the apparent frequency of the input and common outputs waveforms [100]. Interleaving techniques shift the carrier waveforms of the *N* parallel cells

by $2\pi/N$ radians. As a result, the input current and output voltages have higher apparent frequency (N times the switching frequency of each cell). Higher frequencies allow reducing the size of the differential mode filters, the transient response time, the current load current ripple and the dc bus voltage ripple.

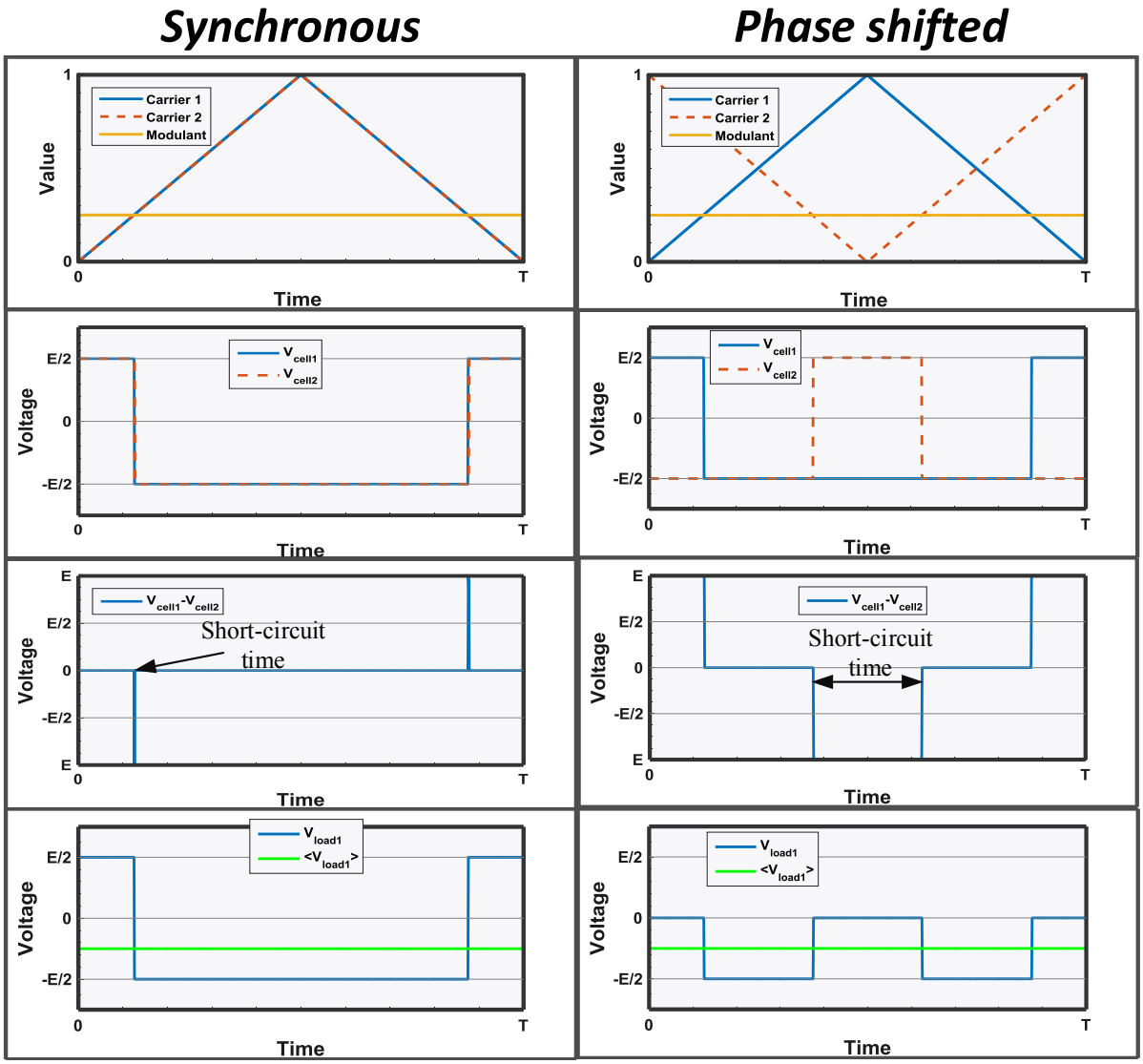


Figure 4.26 : Synchronous (left) and Phase-Shifted (right) command waveforms

In Figure 4.26, the different cell output voltage waveforms for the two command strategies are presented. Interleaving techniques result in longer durations of the voltage difference between cells and as consequence, higher output cell inductors are required to limit short-circuits. High inductor values may cause re-design of high speed machines. Indeed, when adding an inductor between the inverter and the load, an impedance of ($Z=j\omega L/N$) is being inserted. The voltage of the inverter is divided between the load and the inductor, which means the available voltage for the load is reduced.

In the present work, the value of the inductor limits the inter-cell phase current to 10% of the cell nominal current. For the short-circuit time a value of $T_{switching}/2$ (worst-case) is taken for the phase-shifted control mode. In the case of the synchronous control, the value is

considered as the sum of the driver semiconductor propagations times and rise time of the semiconductors. The power module chosen in section 4.5.2 was the CAS325M12HM2, and the driver CGD15HB62LP is selected, based on the recommendation of the manufacturer. The typical driver propagation time value is 75 ns. Unfortunately, no information is given for the switching times of the CAS325M12HM2. Instead the values of the CAS120M12BM2 are used as reference (best switching performances from the other two references), knowing that probably CAS325M12HM2 has better switching performances (lower switching losses, lower stray inductance). A worst case propagation time of 70 ns and fall time of 22 ns is given. The worst-case for the short-circuit time is estimated at 167 ns (one cell commutes instantaneously and the other after the typical delay). The value is considered a conservative hypothesis. Future works should address the determination of the dispersion times.

The dispersion times are considered equal for the ON-OFF and OFF-ON transitions. This is a strong hypothesis since in reality dispersion times for both transients are different. By applying this hypothesis the inter-cell current becomes an isosceles trapezoid.

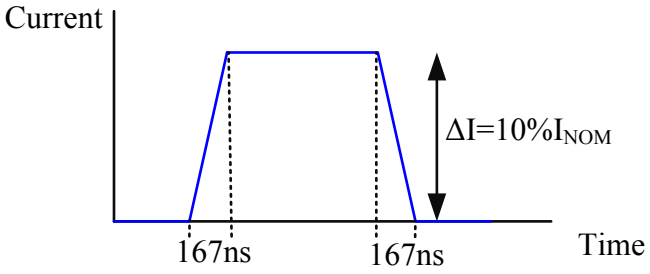


Figure 4.27 : Trapezoidal waveform for the inter-cell current

The hypothesis is helpful for our design approach since otherwise the differences in dispersion times will generate a low frequency inter-cell current that will be compensated by the current regulation; for the simulation study of this situation, a time domain solver will be needed. The difference in transition times also imposes a current regulation on the inter-cell current (with null reference), as otherwise the current does not stop increasing/decreasing.

For the high speed machines as in our case, the phase shifted mode is feasible but not realistic for the application. Even in the best case (I_{nom} = *1 p.u.*, $f_{sw} = f_3$), the necessary inter-cell inductors are 13 times the cyclic inductance of the machine and the re-design will completely change the performances of the machine. As a result, only the synchronous mode is considered in this work.

For the synchronous mode, another parameter to be determined is the cooling solution. Indeed, thermal constraint is the key parameter that determines the mass of the inductors. Both natural and forced convection are compared. For the forced convection, the same cooling conditions as in heat sink design problem are used: input temperature, maximal output temperature and maximal air speed. However, no calculation is performed for the total pressure losses (which can be a limitation) in this work. The constraint for the maximal output temperature is expressed as follows:

$$T_{out} - T_{out_{max}} = T_{in} + \frac{P_{losses}}{\dot{m} C_p} - T_{out_{max}} \leq 0 \tag{4-58}$$

with T_{out} the air temperature after cooling the inductors, $\dot{m}$ the available air mass flow per group of three inductors, C_p the specific heat of the air, P_{losses} the losses of the three inductors and T_{in} and $T_{out_{max}}$ the same cooling conditions as for the heat sink (section 4.5). The available air mass flow per group of three phase inductors is set at $0.008 m_{ref}$ and the maximal allowed temperature is 125°C. The calculations are performed for the affinity and the free models (See section 3.3.1.10). The optimization algorithm is *fmincon* and the area product equations are used to find the initial point.

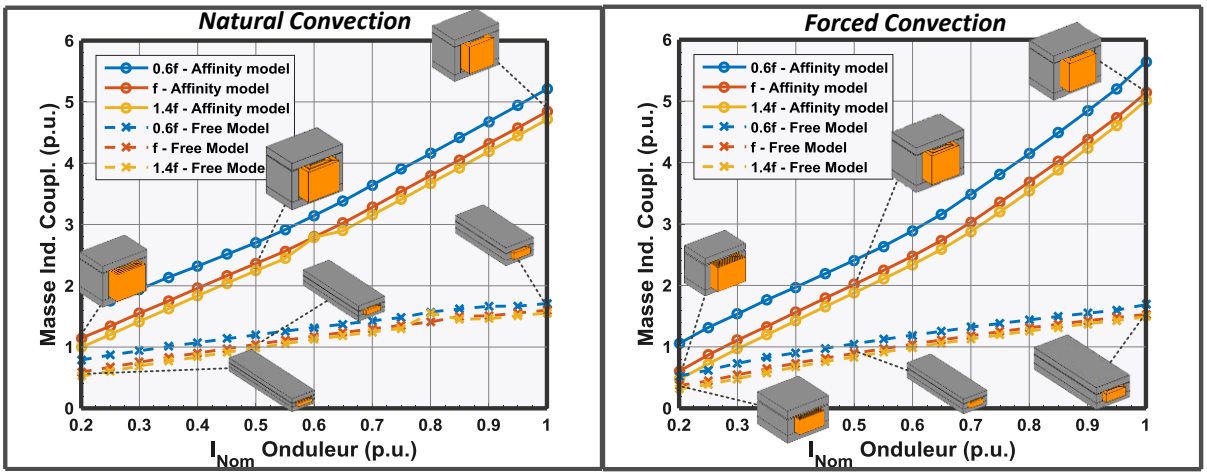


Figure 4.28 : Coupling mass results for: (left) natural convection and (right) forced convection. (Note: Components are not on the same scale)

The results show clearly the advantages of a "direct modelling" approach. By arranging the dimensions of the components the cooling conditions can be improved, thus reducing the mass. Moreover, mass sensibility towards nominal current is reduced. Feasibility of the optimized solutions with off-the-shelf components should be evaluated more in detail, but in our present work all the inductors are considered feasible.

Using forced cooling reduces slightly the mass of the coupling inductors in most of the cases. However, forced convection does not involve a significant step to reduce the mass of the inductors and at the same time requires auxiliary systems (pipes …). As a result only natural convection is used for the cooling of the coupling inductors.

4.7 Final inverter results

The results for the inverter (heat sink, power module and filter), group of three coupling inductors and three-phase contactors are presented and compared in the following figure.

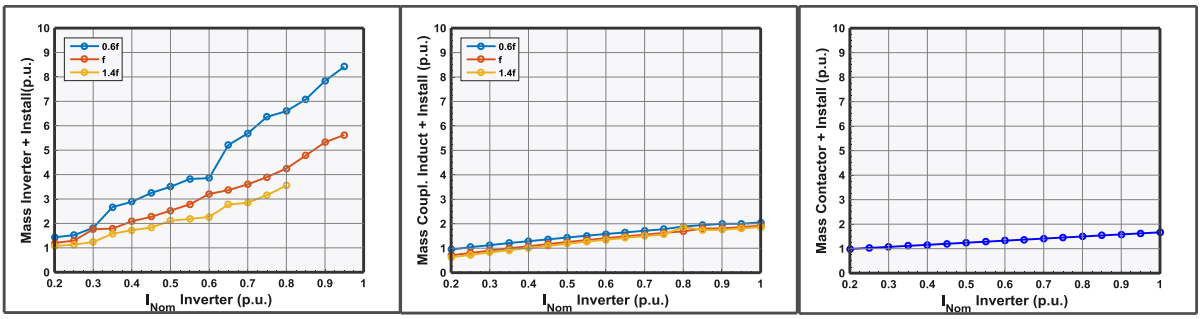


Figure 4.29 : Mass of the different elements as function of the switching frequency and nominal current for: (left) Inverter + installation, (center) coupling inductor + installation & (right) contactor + installation

As expected, the heaviest part is the power module and increasing the switching frequency always decreases the mass of the inverter (only the heat sink mass increases with switching frequency). The mass of the group of three coupling inductors + installation is similar to the one of the contactors. Indeed, the contactor matrix requires additional connections, power cables…

4.8 Conclusions

In this chapter, the different specifications for the design of the power inverter have been presented. The specifications were used to design three different sub-problems: the DC filter, the power module & heat sink and the coupling inductors.

For the DC filter a three stage cascaded topology (differential mode filter + common mode filter + differential mode filter) has been chosen to respect the different standards (HVDC standard and DO160). An approach has been presented to take into account the stability of the whole system (filter + inverter + machine), using a transfer function around a certain operation point. A method to estimate the best materials has been also presented. Once the topology and the materials determined, the optimization has been launched for differential nominal current of the inverters and switching frequency. Interior-point *fmincon* optimization has proved a low robustness for this particular optimization problem and therefore a modification of the objective function has proven to give better results.

For the power module a global optimization from a cabinet point of view has been determined. This optimization allows us to estimate what is the minimal necessary air flow to be blown in the power cabinet which is an important design variable at aircraft-level. The best solution was found at 0.45 p.u. nominal current and 0.6*f*. In addition, some points were unfeasible for the defined operation conditions.

In the end, the coupling inductor has been designed. Synchronous carriers are chosen to command parallel cells because their lower inductance value. The optimization results have shown clearly the advantages of using a “direct modelling” approach to reduce the mass of an inductor (about 66% of mass reduction for our case). Indeed, direct modelling changes the form factor of the inductor to improve the cooling performances thus reducing the total mass.

Chapter 5 : Cabinet design

5.1 Introduction

In Chapter I, the electrical power cabinet concept and the advantages were described. The cabinet consists of a set of power inverters connected to a matrix of contactors managing the connections between the inverters and loads for all the different flight cases. Chapters II, III and IV have been dedicated to describe the different steps for the design of the power inverters. At the end of Chapter IV, the mass of the different elements of the inverter and the coupling inductor as a function of the nominal power and the switching frequency was obtained.

So far, the design has been focused on the power inverter. However, the trade-off between the number of power inverters and nominal current of each inverter needs to be assessed. In this design, the contactor matrix plays a key role. It must be ensured that every load is supplied with the necessary power for every flight phase. Solutions with a high number of power inverters require for example a higher number of contactors to manage all the different reconfigurations between inverters and loads.

In the first part of this chapter, the functional requirements of the power electronic cabinet are described. The functional requirements describe all the power load needs for every flight case. From these inputs, and considering a certain nominal power for the inverter, the minimal number of power inverters, coupling inductors and contactors are calculated. The design does not end here, a compliant solution must be found. The different contactors and coupling inductors must be allocated to specific loads and power inverters to ensure the load demands are met for all flight missions. A methodology to design the contactor matrix based work of [11] constitutes the starting point for our design problem. In the present document, only a brief explanation of the algorithm is given; for more precise details please refer to [4].

In the last part, another design problematic for the power cabinet is solved. So far, it has been assumed that the inductors were located between the inverters and the contactors; another approach would be to insert the inductors between the contactor matrix and the load. This new solution also allows using coupled inductors. An approximate comparison between both solutions is made in this document.

5.2 Functional requirements

Section 1.4.1 stated all the different flight cases for the power load demands that are our specifications for the electric power cabinet. Moreover, the power cabinet must consider as

well failure of the power inverters during the flight mission. The six different loads the power cabinet of our work must supply have been described in section 1.4.2. The load demand depends on the following conditions:

- *mission phases of the aircraft operation:* the load demand depends on the altitude, and speed of the aircraft. In our design approach, 11 flight mission phases are considered. (See Figure 1.6),
- *network state*: to take into account the loss of one power source (generators and bus bars). In the present work, *nominal operation* and *loss of one generator case* are studied,
- *load availability*: considers the loss of the different loads found in both electrical power cabinets. *Nominal operation*, *loss of one AC load bar* and *loss of one ECS pack* are studied,
- *external conditions*: refers to the impact on load consumption depending on the external air conditions of the aircraft. The external conditions are always those defined by the International Standard Atmosphere (ISA). In the present study, *ISA+8* and *ISA+23* external conditions are used,
- *inverter availability*: during flight mission, failure may occur in some power inverters. When a failure occurs in an inverter feeding a critical load for operation, another non-critical load will be disconnected and the attached inverter will supply the critical load. Only the failure of *one* or simultaneously *two* power inverters are considered (3 or more simultaneous inverter failures are considered a statistically unlikely situation). In addition, all possible combinations of inverter failures must be considered, case by case. For example in Figure 5.1, the loss of one inverter in the power cabinet means considering three additional cases (as there are three inverters). This specification increases enormously the number of cases to be considered.

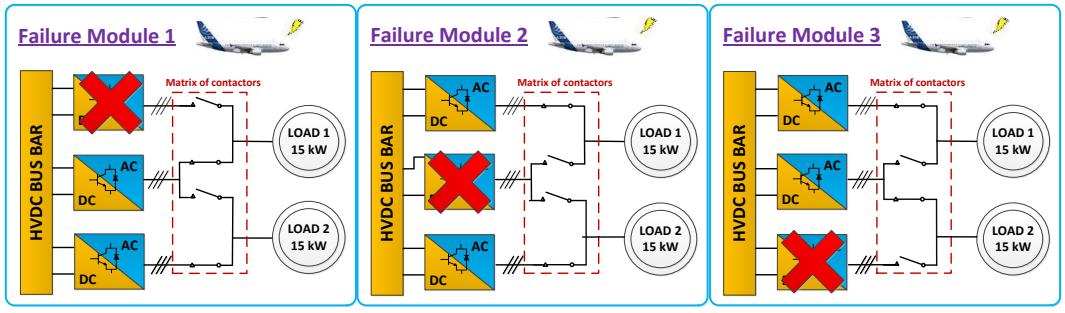


Figure 5.1 : Failure example of one module

Apart from the power demands requirements, other specifications are considered for the power cabinet: all the elements (inverters & contactors) are exactly the same (part number reduction) and one power inverter supplies only one load at the same time.

5.3 Determination of minimal theoretical elements

Knowing the nominal power of each inverter, the number of necessary power modules for each load and case is determined with the equations presented in Chapter IV (See eq. (4-49), (4-50), (4-51)). The total mass contribution of the cabinet power inverters ($M_{T_{inverters}}$) is calculated using the previous response surface and the minimal number of inverters calculated with equation (4-51).

$$M_{T_{inverters}} = N°inverters_{min} \cdot M_{inverter}(P_{nom}, f_{sw}) \tag{5-1}$$

The minimal number of coupling inductors ($N°inductors_{min}$) is calculated in an analogous way, only considering the cases where the load must be supplied with more than 2 inverters.

$$N°inductors_{min} = max\left(\left(\sum_{i=1}^{N_{loads}} N°inverter_{load_i} + N°inverter_{fail}\right)_k\right); \forall\left(\frac{I_{load_i}}{I_{nom}}\right)_k \geq 2 \; ; \quad \forall k = 1...N°cases \tag{5-2}$$

with $N°inverter_{load_i}$ the number of necessary inverters to operate the load *i*, $N°inverter_{fail}$ the number of inverters that were supplying the load and have failed, I_{nom} the nominal current of the inverter and I_{load_i} the absorbed load current. To estimate the overall minimal number of contactors ($N°contactors_{min}$), the numbers of contactors needed for each load *i* are summed.

$$N°contactors_{load_i} = max\left(\left(N°inverter_{load_i} + N°inverter_{fail}\right)_k\right); \forall k = 1...N°cases \tag{5-3}$$

$$N°contactors_{min} = \sum_{i=1}^{N_{loads}} N°contactors_{load_i} \tag{5-4}$$

5.4 Contactor matrix design

5.4.1 Problem description

Finding the connections between loads and inverters using the minimal number of inductors and contactors is a difficult combinatory problem. In [4], for a certain flight case with 5 loads and 9 inverters and with maximum 3 power inverters in parallel, the number of possible configurations between loads and inverters is 2497320. It is easily understood that if this quantity is multiplied by the number of cases (up to 3074) the number of combinations to consider becomes unmanageable. In [4] a heuristic was presented to solve this particular problem.

5.4.2 Minimal contactor matrix

The first step of the design algorithm involves finding a contactor matrix using the minimal theoretical number of contactors. To choose this matrix, the same formalism as in [4] is used. A matrix term *M(j,i)* states if a contactor connects the inverter *j* to the load *i* (*M(j,i) =1*), or not (*M(j,i)=0*).

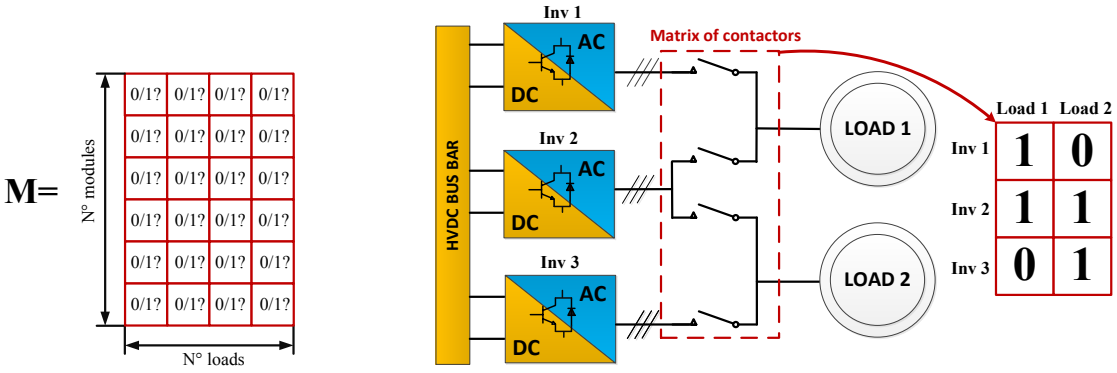


Figure 5.2 : Problem description (left) & example of matrix for a given architecture (right)

The minimal contactor matrix must satisfy the following constraints:

- the number of contactors in the matrix must be equal to the minimal number of contactors,

$$N°contactors_{min} = \sum_{j=1}^{N_{inv}} \sum_{i=1}^{N_{loads}} M(j,i) \tag{5-5}$$

- the number of contactors of each column *i* must be equal to the required minimal contactors for load *i*,

$$N°contactors_{load_i} = \sum_{j=1}^{N_{inv}} M(j,i); \forall i = 1...N_{loads} \tag{5-6}$$

- each of the inverters must be connected to at least one load,

$$N°contactors_{inverter_j} = \sum_{j=1}^{N_{loads}} M(j,i) \geq 1; \forall j = 1...N_{inv} \tag{5-7}$$

- for every case, there is a possible configuration between loads and modules that satisfies the load power needs. This step is performed using a *backtracking algorithm* [11], thus increasing the computation time.

5.4.3 Reconfiguration of the contactor matrix

Once the minimal number of contactors is set, the connection configuration between inverters and loads needs to be defined. For each case we must decide which contactors are closed to connect the inverters and the loads. For example, in Figure 5.3, one configuration is compliant while the other is not.

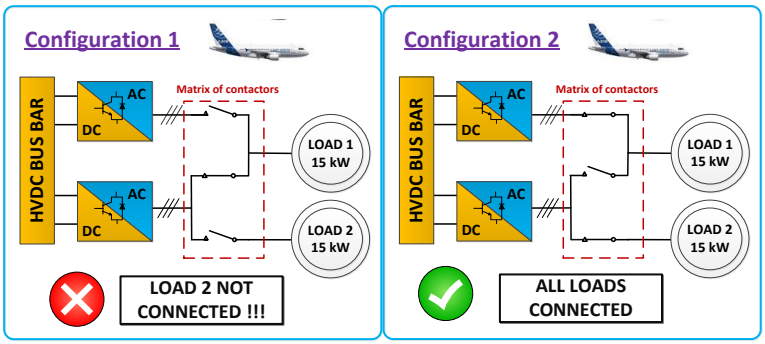


Figure 5.3 : Example of compliant and not compliant configuration for the same case

The choice of the closed contactors has a direct impact on the introduction of coupling inductors. When two inverters are connected in parallel, we need to insert coupling inductors at the output of the inverter. Determining the modules having a coupling inductor such that the number of inductors is minimal can be troublesome or impossible given the chosen contactor matrix. The approach is to use a *greedy algorithm* [4] to determine the inverters having a coupling inductor. An example of a single step decision is presented in Figure 5.4. From a reference architecture, in case *k* (See Figure 5.4) two possible connections exists (configuration 1 & 2), however configuration 2 needs an additional inductor and therefore is discarded. The next case is treated with the chosen solution (configuration 1).

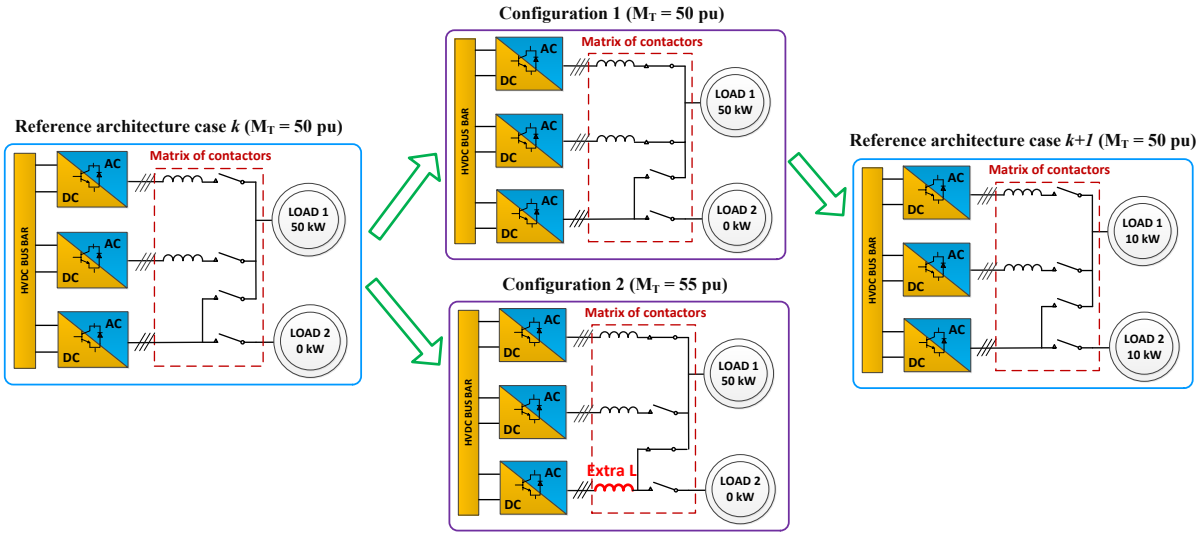


Figure 5.4 : Step example of " Greedy Algorithm" for the case k

Once a configuration is chosen, it is not questioned for the next steps. In the previous example, after choosing configuration 1, the question of what is the best configuration (1 or 2) for case *k* is no further asked. As a result, the degrees of freedom are reduced from one step to another. The impact of the case order treatment is studied in [4], using random sequences. For 90% of the sequences, the mass reduction compared to the deterministic approach is less than 1%. The maximal difference between deterministic and stochastic approach is found to be 2%. The impact of case sequence treatment is therefore neglected.

5.4.4 Inductance suppression

At this moment, the solution has the minimal number of contactors but not necessarily the minimal number of inductors: indeed, the *greedy algorithm* has included inductors whenever it was found necessary. The next design step tries to delete some of the "extra" coupling inductors. However, if an inductor is suppressed, some additional contactors must be added. The trade-off between suppressed inductor mass and added contactor mass will determine the best choice. In the example shown in Figure 5.5, after the *greedy algorithm* step, the solution is formed by 4 contactors and 3 inductors. The calculated minimal theoretical necessary inductors are 2 (we have one extra inductor). As a consequence, the deletion of each single inductor is looked into detail. Inductor 1 is deleted because the resulting solution has reduced the inductance number and has not required to add extra contactors. Inductor deletion can find worst solutions than the initial. For example deletion of inductor 3 carries a heavier architecture than the initial one.

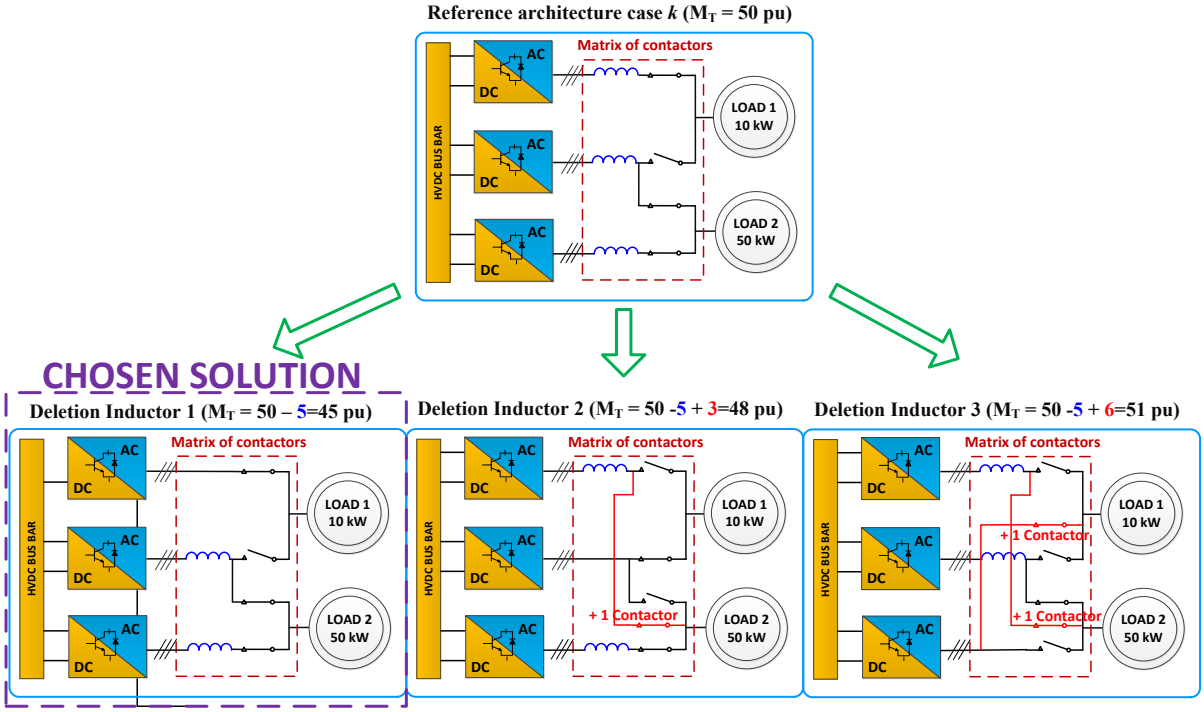


Figure 5.5 : Example of inductor deletion algorithm

After the inductor suppression step, a feasible and compliant contactor matrix is determined.

The contactor matrix design algorithm is summarized in Figure 5.6.

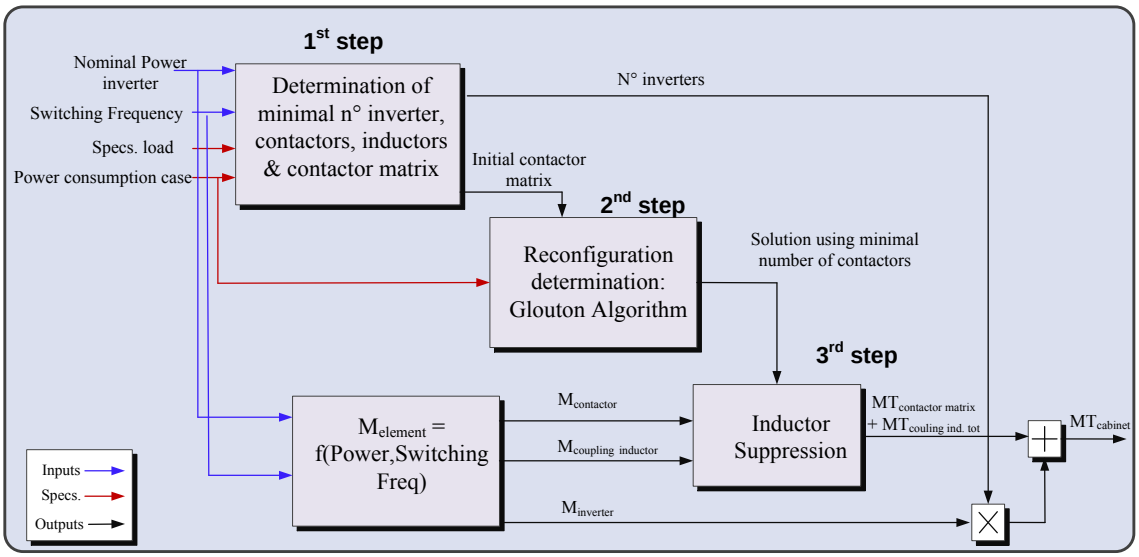


Figure 5.6 : Architectural cabinet design algorithm

5.5 Results

Using the previous design algorithm and the response surface for the power inverters, the electric power cabinet is designed for different nominal currents of the inverter and different switching frequencies. The results are shown in Figure 5.7.

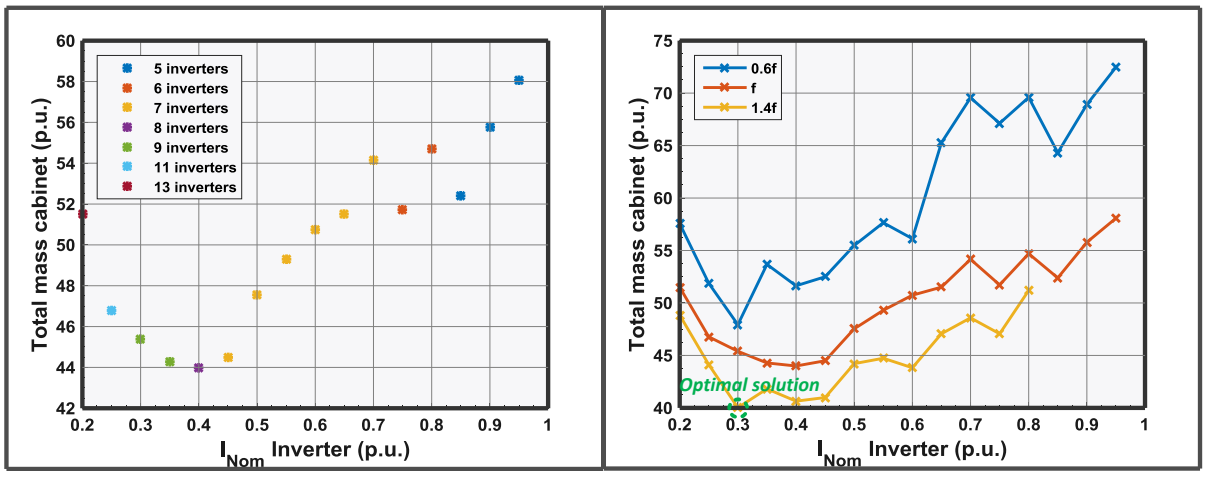


Figure 5.7 : total mass results for the electrical cabinet vs nominal current of the inverter: (left) for f switching frequency & right) for all the different switching frequencies

There is an optimal trade-off between the number of power modules and the nominal current of the inverter. The optimal solution is found at 0.3 p.u. and the highest switching frequency (1.4*f*). Looking for solutions with higher switching frequencies is certainly a perspective for future works but we may encounter limitations due to thermal constraints. In the left figure it is shown how the solutions can be grouped depending on the number of inverters. For each group, the minimal mass corresponds to the minimal current. (for the case

of 9 inverters, the difference is due to the filter non-smoothing curve of the mass; see Figure 4.17).

Optimal solution validation

The optimal solution at a system level is found using inverters of 0.3 p.u. nominal current and switching frequency of 1.4f. The next steps require performing more precise calculations using the calculated optimal dimensions. This step is performed by numerical calculations (FEMM™ and COMSOL™) which offer the highest precision. These calculations require a lot of computations resources and time making them unacceptable for an optimization process. The simulations calculate as well the error of the analytic models at the optimal point. In the present work the numerical simulation is performed just for magnetic components: indeed, these components have currently fully developed numerical simulation models. In the future, more numerical calculations models will be added to the design framework.

DC Filter

For the magnetic components in the DC filter, the Joule losses are compared to a 2D numerical simulation and the conduction thermal model used in Chapter III to validate the thermal model. For the thermal model, the error presented in the table does not consider the error in the calculation of the Joule losses.

	Joule Losses			*Temperature*		
Inductor	*Analytic(W)*	*Finite-element (W)*	*Rel. Error (%)*	*Analytic (°C)*	*Finite-element(°C)*	*Rel. Error (%)*
DM Bus Inductor	2.5626	2.5618	0.034	100.97	98.5	2.5
CM Inductor	2.015	2.043	-1.39	82.175	83.8	-1.94
DM Inverter Inductor	1.5679	1.5728	-0.314	114.26	114	0.23

Table 5-1 : Validation of optimal inductors in the DC filter

For this particular solution, the analytical calculations correlate the numerical simulation with an exceptional precision (worst case below 2%). The next step would be to compare with experimental measurements.

In addition, the compliance of the filter with the different HVDC standards (steady-state, common-mode, stability and transient) is presented.

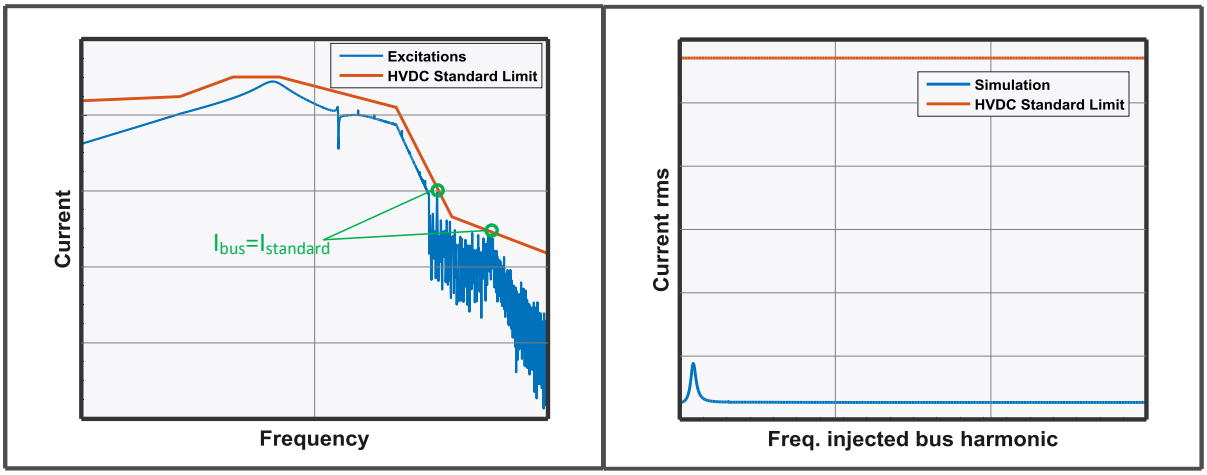


Figure 5.8 : comparison of simulation data with differential HVDC standard: (left) current envelope test & (right) RMS current test

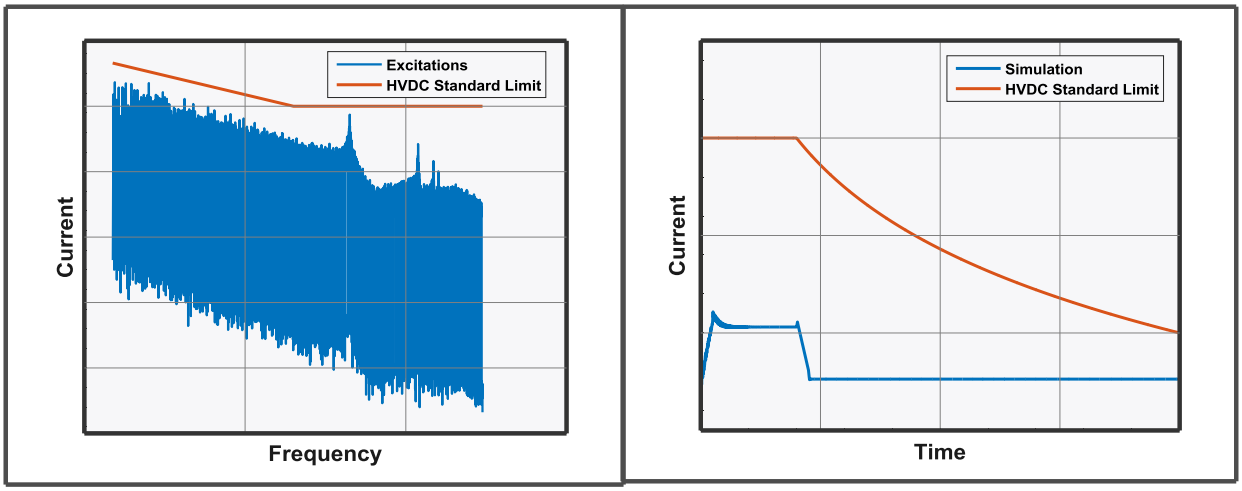


Figure 5.9 : comparison of simulation data with HVDC standard: (left) common mode current envelope test & (right) differential current transient test

The simulation results show that the designed filter is compliant with all the different standards. Moreover, these results also show how the differential current envelope test (Figure 5.9 left) is the element determining the filter values. As can be seen, the dc current envelope "touches" the limits at two different points meaning a reduction of the capacitors or inductors values will not allow satisfying the standard.

Coupling Inductor

For the coupling inductor the analytic expressions are validated again using the numerical analysis.

	Joule Losses			Temperature		
	Analytic(W)	Finite-element (W)	Rel. Error (%)	Analytic (°C)	Finite-element(°C)	Rel. Error (%)
Separate Inductor	9.31	8.05	15.63	125	120	4.167

Table 5-2 : Validation of coupling inductor

Here, the relative error is more significant but still within an acceptable range (below 16%) and as a consequence the solution is accepted. Again, future works should address experimental validation.

5.6 Coupling inductor technology

Two main solutions were presented in Chapter III as possible candidates to parallelize power inverter cells: separate inductors and coupled inductors. So far, separate inductors have been considered between the contactor matrix and the inverters. If coupled inductors are inserted to associate the cells of the inverters, this configuration is incompatible. If a coupled inductor is inserted between two inverters then at some flight phases the legs of the coupled inductors are attached to different power loads phase. As a consequence, there will be an undesired interaction between both inverters which is not desired. As a consequence, the coupled inductors are inserted between the contactor matrix and the loads as shown in Figure 5.10. Of course the second case is also compatible with separate inductors but it has not been investigated in this work.

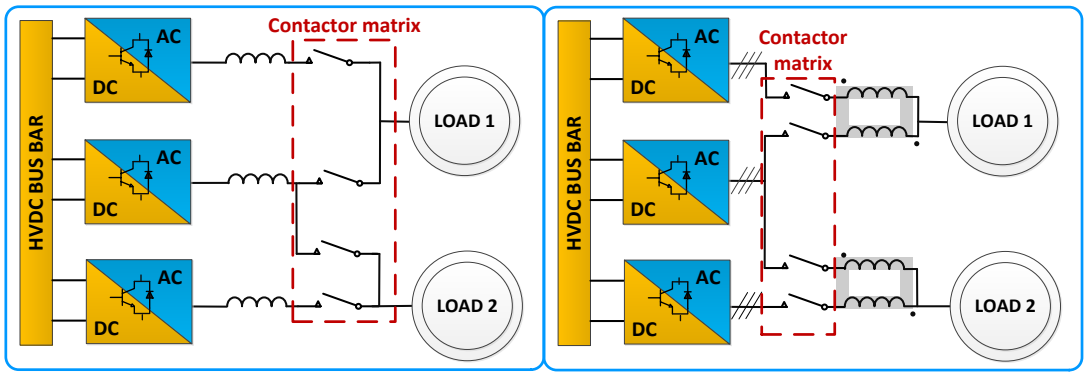


Figure 5.10 : left) Separate inductor structure & right) Coupled Inductor structure

Two main families of coupling inductor technology are available: *monolithic* and *cyclic cascade*.

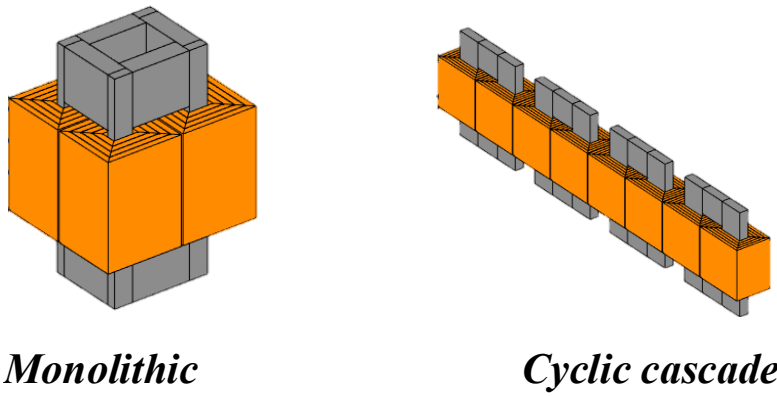


Figure 5.11 : Coupled inductors technology: (left) monolithic and (right) cyclic cascade

Monolithic technology uses a single core to connect all the cells. This solution is discarded in our work for two reasons. First, each load requires a specific design since the number of coupled cells varies from one load to another, meaning a higher part number (higher cost). Second, as the number of inverters connected to the load varies depending on the power consumption, special care must be taken to avoid saturation in the inductor. This means adding additional air-gap thus reducing the interest of coupled inductors.

As a result, cyclic cascade is the chosen technology for its advantages in terms of part number and simplicity. To estimate the number of necessary coupled inductors we first determine the maximal number of necessary cyclic cascaded inductors in parallel with equation (5-2). Indeed, because the inverters are connected and disconnected depending on the flight phase, we must ensure that any possible configuration between loads and inverters has the necessary magnetic coupling inductors. Every combination of 2 inverters for the same load (the ones with a contactor between the load and the inverter obviously) must be considered:

$$N°coupl_{load_i} = \begin{pmatrix} N°inverters_{load_i} \\ 2 \end{pmatrix} = \frac{N°inverters_{load_i}!}{2!\,(N°inverters_{load_i} - 2)!} \tag{5-8}$$

Summing all the necessary inductors for each load, we get the total number of necessary cyclic cascaded inductors. Figure 5.12 represents the comparison of numbers of elements between the solutions using coupled inductors and the previous calculations with separate inductors.

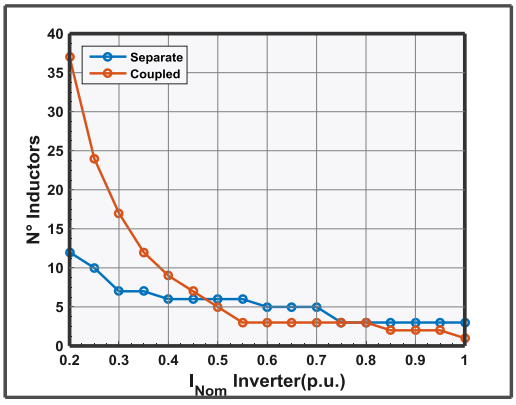


Figure 5.12 : Number of coupling elements versus nominal power of the inverters

As presented, the coupled solution is clearly interesting for solutions with nominal currents above 0.5 p.u., where the number of coupling elements is reduced. In addition, as coupled inductors should be lighter than separate inductors the solutions above 0.4 p.u. are studied.

To design the coupled inductors, the optimization algorithm used is the interior-point *fmincon* algorithm from MATLAB™. The optimization variables are the dimensions of the coupling inductor presented in section 3.3.1.11. When the two phases of the coupled inductors are connected, the constraints are:

$$T_{max} - 125 \leq 0 \tag{5-9}$$

$$B - 0.95B_{sat} \leq 0 \tag{5-10}$$

$$L_{min} - L_{IC}^{CI} \leq 0 \tag{5-11}$$

with T_{max} the maximal temperature of the component (in °C), B the magnetic field (in T), L_{min} the minimal value of inter-cell inductance and L_{IC}^{CI} the value of inter-cell inductance. In addition we must consider the operation when only one phase is connected. In these cases, the inductor will perform the whole hysteresis cycle at the frequency of the load. From an operation point of view inductor saturation is not critical because the inductor value is smaller than the machine inductance value (at least 8 times smaller). However, core losses at this point are critical and must be taken into account. As a result, the temperature constraint (5-9) is also considered when one phase is supplied and the magnetic field waveform presented in Figure 5.13.

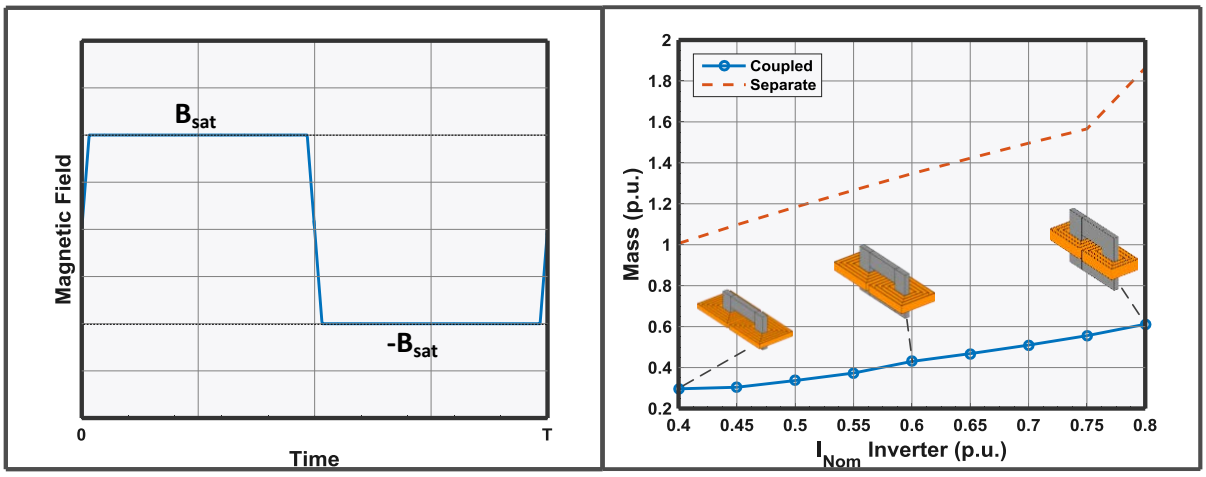


Figure 5.13 : (left) Magnetic field in the core when only one phase of the inductor is connected & (right) mass results of the group of 3 coupled inductors + installation versus nominal current of the inverter and compared to the results of separate inductors

The results for the case of 1.4*f* are shown in Figure 5.13. Using coupled inductors instead of separate inductors reduces the inductance mass about one third so is clearly an interesting solution to reduce the mass of the power cabinet. However, if coupled inductors are used, the way the contactor matrix is designed needs to be reviewed. Indeed in this case the contactors are inserted between the inverters and the legs of each coupled inverter. Addition of extra contactors must be required. For example, let us consider we want to create a solution tolerant to the failure of one power inverter. As it is shown, depending on the elements (separate or coupled) the solution requires a different number of contactors.

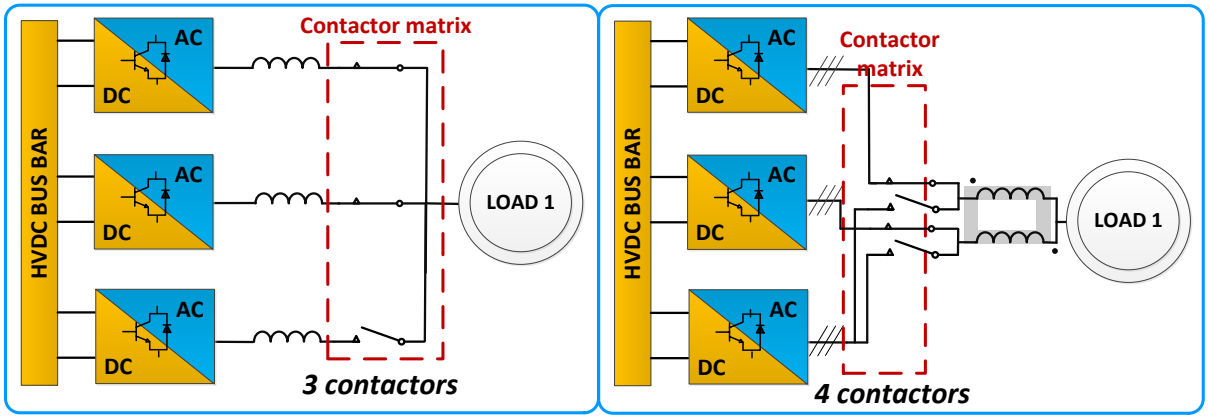


Figure 5.14 : redundant solution using : (left) separate inductors & (right) coupled inductors

The design algorithm for this new case has not been developed in this work and is certainly a perspective for future works. In our case, we estimate the margin in number of contactors if the coupled inductor solution is used. Our objective is to have a first-order estimation whether this solution is promising or not;

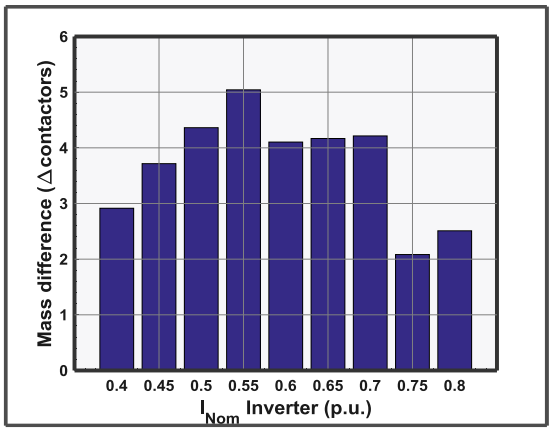


Figure 5.15 : Magnetic coupling elements mass difference between the solution using coupled inductors and the solution using separate inductors in terms of contactor number

As shown in Figure 5.15, there is not a high number of extra contactors margin for this particular case (best case is 5 contactors) and as a result the potential mass reduction of the coupled inductor solution is not very interesting with the current state-of-the-art solution. However, if a significant step is made to reduce the mass of the contactors (for example, using electronic contactors) this solution could be advantageous.

5.7 Conclusion

In this chapter, the power inverter results extracted from the optimization framework (chapters 2-4) are used to design the electrical power cabinet. The heuristic algorithm from [4] has been used to determine the optimal trade-off between nominal power of the inverter and number of inverters. The algorithm also designs a compliant contactor matrix with the defined power demands. Results show that the solution of a 0.3 p.u. nominal current along with a switching frequency of 1.4*f* is the optimal solution. The magnetic elements analytic model calculations have been compared to numerical simulations showing a good correlation. Filter compliance to HVDC standards has been presented as well.

In the last part, the potential of solution using coupled inductors instead of separate inductors has been treated. Solutions show a mass reduction of magnetic elements of 66%. However this solution requires additional contactors and the margin of extra contactors is not very high meaning final solution will be heavier. This solution will be certainly more interesting with another technology of contactors or with reduced installation requirements.

Conclusions & Perspectives

The main objective of this manuscript has been to define and test a new framework to aid the design of the new electrical power cabinet, for future aircrafts implementing a HVDC electrical energy distribution network.

When defining new electric architectures, system designers need a good estimation of all the possibilities and design margins they can obtain using innovative power converters. In addition, they must anticipate the impact of new specifications at system level with a high precision. Classically, these estimations take into account a reduced number of solutions and are highly dependent on the designer experience.

In this work, a tool for the automatic design of power converters has been presented. In this tool, all the components are represented using an "object-oriented" approach where the components are described by their physical dimensions, materials and shape. From these inputs, a series of properties are calculated (mass, volume, cost…) and the equivalent simulation models are extracted. These models are coupled to a fast steady-state frequency solver that simulates the interactions between all components (electric, magnetic, thermal…). The waveforms from the simulation are then used to calculate some extra data relevant to the design of the components (losses, magnetic field, temperatures…). The component models and the solver are inserted in an optimization loop which aims to find out the best performances of the power converters in terms of mass, efficiency, volume and reliability.

In our work, the bases of this design environment have been presented and used for the design of integrated and modular electrical power distribution cabinet featuring shared inverters. Indeed, in the context of the "More Electrical Aircraft" a solution using a set of generic power inverters to supply the different electrical loads of the aircraft seems promising in terms of mass, cost and reliability. The proposed solution includes as well a contactor matrix to connect the different inverters to the loads, depending on the loads power needs. In [4], a methodology was presented to find the optimal trade-off between the number of power inverters and the nominal power of each generic inverter, including the design of the contactor matrix. This methodology is the starting-point for our design, but it requires the estimation of the mass of the power inverter as a function of the nominal power. The automatic design environment provides this information.

In chapter III, the different analytic equations of the components used in our work are presented. In some components, because of manufacturing limitations, the data are directly extracted from manufacturers' datasheet (power semiconductors) or a response surface is obtained from the datasheets (capacitors). In some others (heatsinks and magnetic elements), the analytic equations come from the literature. The main contribution of this work is the calculation of the conductor losses where linear interpolation is applied to pre-calculate 2D numerical simulation data. All the analytic models have been validated using experimental

data or numerical simulations, showing a good correlation with the analytic calculation. As a result, these models provide a first library of the environment that can potentially assess a large variety of problems.

In chapter IV, the automatic design environment is employed to assess the design of several sub-parts of the power inverter (heat sink and power module, DC filter) and the magnetic coupling element to connect several power inverters in parallel. The optimizations have been performed for several nominal current values and switching frequency. The results have shown the sensibility of the power inverter mass to these two design variables. In the case of the heat sink, we were able to determine the minimal total airflow required for the power cabinet, which is an important design parameter for the cooling system at aircraft level. For the DC filter, the differential filter and common mode filter were designed at the same time and the optimization took advantage of the frequency solver, thus calculating only some specific frequencies and reducing the computation time. At the end, the design of the magnetic coupling element has shown the interests of the "direct modeling" approach, where the mass was reduced to a third of the mass calculated using the classical approach of the area product.

Finally, these results were used to feed the cabinet design algorithm, showing the best result in terms of nominal current and switching frequency. For the magnetic components, the optimal solution was compared to numerical simulations showing good accuracy. Finally, in this chapter a pre-estimation of the mass gain when using cyclic cascaded inductors to use the power inverters in parallel was shown. The magnetic elements mass was divided by three but this gain was not sufficient, as this solution requires a higher number of contactors.

In this work, the bases of a new automatic design tool have been described to assess the design of power converters. The tool has been used specifically for the design of the power electronic cabinet in the "More Electrical Aircraft". However, due to time limitations a lot of points remain to be treated or improved in future works:

- for the automatic design environment, the only optimization algorithms used in this work have been gradient-descent type. The environment has been designed to include a large variety of algorithms such as evolutionary algorithms…. Future works should try to determine the best algorithm in terms of convergence time and robustness.

- in terms of analytic models, the component library needs to include more models to asses other topologies (transformer…) or technological solutions (cold-plates, non shielded cable). As for the models presented in this work a lot of points will need to be treated in the future:

- ✓ *magnetic devices*:
  - for the core losses, other methods that take into account relaxation effects (i^2GSE) or DC bias should be included. In addition, the temperature effects should be better taken into account. For the copper losses, the gridded interpolation method has shown its limitations, when using a large number of input variables (for example in the proximity effect). Other interpolation methods requiring an irregular grid (kriging…) should be considered in the future.
  - For the thermal models, the number of necessary nodes to reach a fair precision should be calculated. Moreover, the semi-empirical convection exchange coefficients should be validated as well using numerical simulation or experimentation. A reconsideration of the radiation thermal resistance that takes into account the environment needs to be performed as well,
- ✓ *heat-sink*: a heat-sink numerical simulation model needs to be created to validate the thermal resistance and pressure drop calculations of the optimal solutions,
- ✓ *power module*:
  - future modeling should take into account the impact of modifying the driver circuit (gate resistance, supply voltage) regarding the losses and EMC (dv/dt…),
  - the common mode equivalent model of the switching cell should be reconsidered to take into account the interaction between differential and common mode in a single simulation,
- ✓ *power cable*: other cable constructions need to be modeled (no shielding) that can potentially impact the conducted and emitted EMC.

- for the specific design of the power inverter, several points need to be addressed as well:
  - ✓ the design of the EMC filter on the AC side needs to be considered,
  - ✓ the parasitic common impedances (machine, heatsink…) should be reconsidered either by using experimental data from applications or by creating analytic models to anticipate the common mode impedances of the designs,
  - ✓ the trade-off between air-cooling and water-cooling for the power modules and the rest of the inverter components should be investigated,
  - ✓ other DC filters topologies should be compared in future works. The choice in this work was based on preliminary studies but these topologies could be

reconsidered. In addition, the optimization method should be improved. Other regulations strategies for the supplied electric drives should be considered to treat the stability and quality constraints. In addition, an assessment on the mass impact of the different specifications should be performed,

- ✓ the mass impact for different PWM strategies should be assessed,
- ✓ for the coupling inductor design, the short-circuit time needs to be validated with experimental data.

- for the design of the electrical power cabinet:
  - ✓ the results have shown that increasing the switching frequency reduced the mass of the electrical power cabinet. The calculation should be performed as well at even higher switching frequencies,
  - ✓ The models for the installation components (connectors, casing…) should be improved to increase the accuracy of the solution,
  - ✓ the optimal results should be validated (heat sink, capacitors) or examined more into details (Ex. in magnetic elements, 3D validations for the copper losses, validation of heat exchange coefficients),
  - ✓ the case using monolithic coupled inductors to use the inverters in parallel should be looked.

Certainly, these are only some of the perspectives for the present work; however, the bases for a new way of designing power converters have been settled and the number of problems and new possibilities opened by this new environment is enormous.

Appendix

Appendix A: Magnetic validation results

Inductor

Parameter	Case 1	Case 2	Case 3	Case 4
leg_{width}(cm)	4	3.5	2	1
$leg_{thickness}$(cm)	4	5	1	1
$t_{dielectric}$(mm)	1	0.5	1	2
air gap (mm)	0	2	0	1
h_{wind}(cm)	4	1	10	2
t_{wind}(cm)	0.2	1	0.1	0.7
N_{turns}	10	5	3	2
Q_{core}(mW/cm^3)	29.38	0.27	118.72	4.421
Q_{wind}(mW/cm^3)	44.92	75	6.427	122.45
T_{max} model(°C)	80.24	55.35	74.1	90.965
T_{max} COMSOL(°C)	79.9	57.2	81.9	90.7

Coupled Inductor

Parameter	Case 1	Case 2	Case 3	Case 4
$legV_{width}$(cm)	3	3.5	3	2
$legH_{width}$(cm)	3	3.5	3	2
$leg_{thickness}$(cm)	4	5	2	1
$d_{interturn}$(mm)	1	0.5	0.5	2
air gap (mm)	0	2	0	1
h_{wind}(cm)	4	1.7	10	2
$t_{winding}$(cm)	0.2	1	0.1	0.7
N_{turns}	4	5	15	2
Q_{core}(mW/cm^3)	27.21	3.3497	11.38	28.28
Q_{wind}(mW/cm^3)	53.48	82.6833	1.47	26.54
T_{max} model(°C)	85.54	90.01	40.01	89.22
T_{max} COMSOL(°C)	77.9	87.9	38.3	90.7

Common Mode Inductor

Parameter	Case 1	Case 2	Case 3
leg_{width}(cm)	4	3.5	2
$leg_{thickness}$(cm)	4	5	1
$d_{interturn}$(mm)	1	0.5	1
$t_{dielectric}$ (mm)	0.1	0.5	1
$diameter_{wind}$(mm)	7	5	4
N_{turns} (Per Phase)	10	5	3
Q_{core}(mW/cm^3)	0.1	3.6e-5	33.76
Q_{wind}(mW/cm^3)	74.3	285.54	88.77
T_{max} model(°C)	34.42	46.186	37.3124
T_{max} COMSOL(°C)	38.4	47.7	38.4

Appendix B: Heat Sink Thermal Model

The thermal resistance of the heat sink base plate is calculated with the following expression:

$$R_{base} = \frac{h_{BP}}{k_{BP} \cdot W \cdot L} \tag{0-1}$$

where h_{BP}, W, L are the dimensions of the base plate and k_{BP} is the thermal conductivity(Figure 3.36).

To model the thermal resistance from heat sink to air, the convection with the air and the conduction effect on each fin is taken into account. The fin and the air in-between are divided into a series of N thermal resistances as shown in the Figure 0.1.

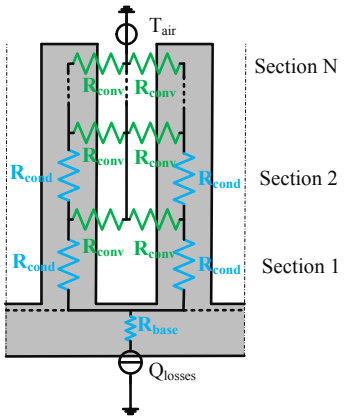


Figure 0.1 : Network representation of two fins

Formulas to calculate each resistance are:

$$R_{cond} = \frac{h_{fin}}{N \cdot k_{fin} \cdot t_{fin} \cdot L} \tag{0-2}$$

$$R_{conv} = \frac{1}{N \cdot h_{conv} \cdot A_{fin} \cdot \eta_{fin}} \tag{0-3}$$

where h_{fin}, t_{fin}, and L represent the dimensions of the heat sink as shown on Figure 3.36, A_{fin} the external area of one fin, k_{fin} the thermal conductivity and the term η_{fin} is obtained from the equation (0-4). In addition, h_{conv} is the heat exchange coefficient calculated with the Nusselt adimensional number, Nu.

$$\eta_{fin} = \frac{\tanh\left(\sqrt{\frac{2 \cdot h_{conv} \cdot h_{fin}}{k_{fin} \cdot t_{fin}}}\right)\sqrt{k_{fin} \cdot t_{fin}}}{h_{fin} \cdot \sqrt{2 \cdot h_{conv}}} \tag{0-4}$$

$$h_{conv} = \frac{Nu \cdot k_{air}}{b} \tag{0-5}$$

In this last expression, k_{air} is the thermal conductivity of the air evaluated at the mean temperature between the input and output temperature and b is the distance between consecutive fins. The Nusselt calculation needs as previous steps, the calculation of two adimensional numbers: the modified Reynolds number Re^* and the Prandtl Pr number.

$$Re^* = \frac{\rho_{air} \cdot V_{air} \cdot b}{\mu_{air}} \cdot \frac{b}{L} \tag{0-6}$$

$$Pr = \frac{\mu_{air} \cdot C_p}{k_{air}} \tag{0-7}$$

with ρ_{air}, μ_{air}, C_p the density, dynamic viscosity and specific heat of the air respectively. The air speed (V_{air}) is extracted from the pressure loss model in Appendix B. The semi-empirical expression to calculate the Nusselt number comes from [78] and is valid for a range of $0.1<Re^*<100$.

$$Nu = \left(\frac{1}{\left(\frac{\mathrm{Re}^* \cdot \mathrm{Pr}}{2}\right)^3} + \frac{1}{\left(0.664 \cdot \sqrt[3]{\mathrm{Pr}} \cdot \sqrt{\mathrm{Re}^* + 3.65 \cdot \sqrt{\mathrm{Re}^*}}\right)^3} \right)^{-1/3} \tag{0-8}$$

Using equations (0-2), (0-3) the overall thermal resistance of the fin is:

$$R_{fin} = -\frac{1}{2} \frac{A \cdot (-B)^N - R_{cond} \cdot (-B)^N + A \cdot C^N + R_{cond}}{(-B)^N - C^N} \tag{0-9}$$

$$A = \sqrt{R_{cond} \cdot (R_{cond} + 4 \cdot R_{conv})} \tag{0-10}$$

$$B = \frac{\sqrt{-2 \cdot R_{conv} - R_{cond} + A}}{R_{conv}} \tag{0-11}$$

$$C = \frac{2 \cdot R_{conv} + R_{cond} + A}{R_{conv}} \tag{0-12}$$

The total thermal resistance of the heat sink is calculated adding all thermal resistances. The parameter N_{fin} represents the number of fins on the heat sink.

$$R_{heatsink} = R_{base} + \frac{R_{fin}}{N_{fin}} \tag{0-13}$$

Appendix C: Heat-sink aeraulic model

As shown in Figure 0.2. The fan works at a certain operating point ($\Delta P, \dot{m}$) which is determined by the intersection of the pressure drop curves of fan and heat sink.

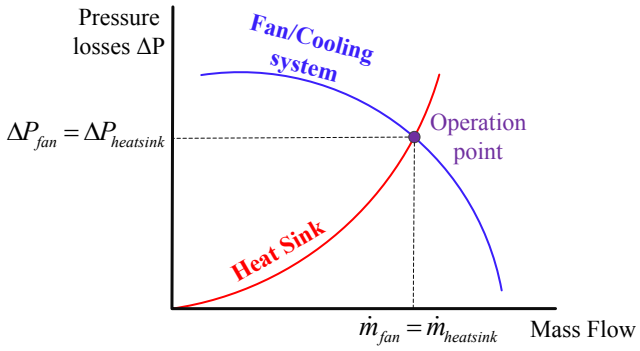


Figure 0.2 : Pressure drop- mass flow chart for operating point of the system

The pressure drop of a heat sink is a function of the air speed in the channel:

$$\Delta P = \left(\frac{f_{app} \cdot N_{fin} \cdot (2 \cdot h_{fin} \cdot L + b \cdot L)}{h_{fin} \cdot W} + K_c + K_e \right) \left(\frac{1}{2} \rho_{air} V_{air}^2 \right) \tag{0-14}$$

$$V_{air} = \frac{\dot{m}}{\rho_{air} \cdot h_{fin} \cdot b} \tag{0-15}$$

with L, b, h_{fin}, W and N_{fin} the dimensions and the number of fins as shown in Figure 3.36, ρ_{air} is the air density and V_{air} is the air speed on the fin channels. The terms f_{app} take into account the friction losses and the terms K_c, K_e take into account singular losses at the input and output of the heat sink.

$$f_{app} = \frac{1}{\mathrm{Re}_{ch}} \left[\frac{11.83 \cdot D_h \cdot \mathrm{Re}_{ch}}{L} + \left(f \cdot \mathrm{Re}_{ch} \right)^2 \right]^{1/2} \tag{0-16}$$

$$K_c = 0.42 \cdot (1 - \alpha^2) \tag{0-17}$$

$$K_e = (1 - \alpha^2)^2 \tag{0-18}$$

The Reynolds number on the channel Re_{ch}, the hydraulic diameter D_h and the auxiliary parameters α, f are extracted from the following expressions.

$$Re_{ch} = \frac{V_{air} \cdot D_h \cdot \rho_{air}}{\mu_{air}} \tag{0-19}$$

$$D_h = \frac{4 \cdot b \cdot h_{fin}}{\left(2b + 2h_{fin}\right)} \tag{0-20}$$

$$\alpha = \frac{b}{h_{fin}} \tag{0-21}$$

$$f = \frac{1}{\mathrm{Re}_{ch}}\left(24 - 32.53\beta + 46.72\beta^2 - 40.83\beta^3 + 22.96\beta^4 - 6.09\beta^5\right) ; \quad \beta = \frac{b}{h_{fin}} \tag{0-22}$$

Appendix D: DQ model of the machine

The magnitudes in the a,b,c reference frame are transformed into a the dq0 rotating reference frame [92] as shown on Figure 0.3.

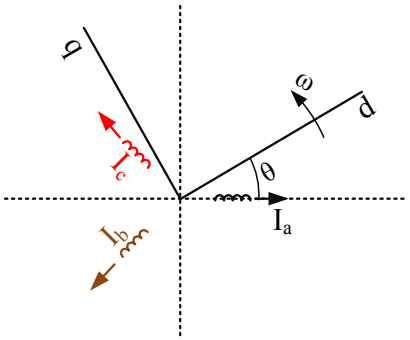


Figure 0.3 : dq reference frame representation

The meaning of the different machine variables used on the present appendix are found in the following tables (They were mentioned in section 4.3).

Symbol	Meaning
$R_{d,q}$	Stator phase resistance of the machine in the *dq* frame
$L_{d,q}$	Cyclic phase inductance of the machine in the *dq* frame
N_p	Number of poles pairs of the machine
Φ_{rd}	Magnet flux of the machine in the *dq* frame
J	Moment of Inertia of the machine
f	Friction coefficient of the machine
Kem	Motor torque constant
V_{DC}	Bus bar voltage
I_{DC}	Bus bar current
$I_{d,q}$	Machine phase current in the *dq* frame
$I_{a,b,c}$	Machine phase current in the *abc* frame
$V_{d,q}$	Machine phase voltage in the *dq* frame
$V_{a,b,c}$	Machine phase voltage in the *abc* frame
ω	Mechanical speed of the machine
C_{res}	Resistive torque of the machine
K_p	Proportional coefficient for the Proportional-Integral corrector
τ_i	Time constant for the Proportional-Integral corrector
G	Ratio of the modulator (Assumed $1/V_{DC}$ at the nominal operation point)

Subscript	Meaning
0	Initial value of the magnitude at a certain operation point of the machine
ref	Reference value of the magnitude desired in the control loop
i	Variable associated to the current control loop
ω	Variable associated to the speed control loop

The mathematical transformation of the magnitudes from *a,b,c* frame to the *d,q* frame is performed according to the following transformation ('power transformation'):

$$\begin{bmatrix} x_d \\ x_q \\ x_0 \end{bmatrix} = \sqrt{\frac{2}{3}} \begin{bmatrix} \cos\theta & \cos(\theta - 2\pi/3) & \cos(\theta + 2\pi/3) \\ -\sin\theta & -\sin(\theta - 2\pi/3) & -\sin(\theta + 2\pi/3) \\ 1/\sqrt{2} & 1/\sqrt{2} & 1/\sqrt{2} \end{bmatrix} \times \begin{bmatrix} x_a \\ x_b \\ x_c \end{bmatrix} \tag{0-23}$$

And the inverse transformation is:

$$\begin{bmatrix} x_a \\ x_b \\ x_c \end{bmatrix} = \sqrt{\frac{2}{3}} \begin{bmatrix} \cos\theta & -\sin & 1/\sqrt{2} \\ \cos(\theta - 2\pi/3) & -\sin(\theta - 2\pi/3) & 1/\sqrt{2} \\ \cos(\theta + 2\pi/3) & \sin(\theta - 2\pi/3) & 1/\sqrt{2} \end{bmatrix} \times \begin{bmatrix} x_d \\ x_q \\ x_0 \end{bmatrix} \tag{0-24}$$

The 'power transformation' means that the product of the current/voltages magnitudes in the *d,q* domain also gives the power consumed by the machine

$$P_{load} = V_a \cdot I_a + V_b \cdot I_b + V_c \cdot I_c = V_d \cdot I_d + V_q \cdot I_q \tag{0-25}$$

The electrical equations of the machine expressed in the *dq* reference frame are:

$$V_d = R_d \cdot I_d + \frac{d\Psi_d}{dt} - \omega \cdot \Psi_q \tag{0-26}$$

$$V_q = R_q \cdot I_q + \frac{d\Psi_q}{dt} + \omega \cdot \Psi_d \tag{0-27}$$

The symbol Ψ_d represents the magnetic flux on each axis. As shown on Figure 0.3, the *dq* frame has been set-up so as its *d* axis always is aligned with the magnetic flux of the rotor:

$$\Psi_d = L_d \cdot I_d + \Phi_{rd} \tag{0-28}$$

$$\Psi_q = L_q \cdot I_q \tag{0-29}$$

The torque of the machine is expressed as follows:

$$T = n_p \cdot (\Psi_d \cdot I_q - \Psi_q \cdot I_d) \tag{0-30}$$

In smooth pair poles machines the inductances and the resistances on the two axes have equal values.

$$R_d = R_q \tag{0-31}$$

$$L_d = L_q \tag{0-32}$$

As a consequence, the torque equation is simplified to the following expression:

$$T = Kem \cdot I_q = n_p \cdot \Phi_{rd} \cdot I_q \tag{0-33}$$

In section 4.3, the different torque/speed operation points of the loads were calculated. Using the operation points and the dq frame, the reference currents $I_{q_{ref}}$, $I_{d_{ref}}$ are estimated. For low speeds, a "maximal torque" control is performed. The $I_{d_{ref}}$ is set to 0 and the equation (0-34) calculates directly the necessary $I_{q_{ref}}$.

$$I_{q_{ref}} = \frac{T}{n_p \cdot \Phi_{rd}} \tag{0-34}$$

$$I_{d_{ref}} = 0 \tag{0-35}$$

However, the amplitude of the voltage delivered by the inverter is limited. In the present case, third harmonic injection is used (sinus injection), which is the case of study the maximal allowed phase voltage is:

$$V_{dq_\max} = \frac{V_{DC}}{\sqrt{2}} \tag{0-36}$$

The maximal voltage limits the operation zone of the "maximal torque" control, which is defined by the following equation.

$$(-\omega \cdot L_q \cdot I_q)^2 + (R_q \cdot I_q + \omega \cdot \Phi_{rd})^2 \le V_{dq_{max}}^2 \tag{0-37}$$

As shown in chapter IV, for some loads it is not desired to operate at "maximal torque" but at high speeds. In these cases, a I_d current is inserted to de-flux the machine. The calculation of the $I_{d_{ref}}$ current depends on the operating point. The current limits of I_d are solved from the following equation:

$$V_d^2 + V_q^2 = (R_d \cdot I_{d_{ref}} - \omega \cdot L_q \cdot I_{q_{ref}})^2 + (R_q \cdot I_{q_{ref}} + \omega \cdot (\Phi_{rd} + L_d \cdot I_{d_{ref}})^2) = V_{dq_{max}}^2 \quad (0\text{-}38)$$

The previous equation has two different solutions for I_d. The smaller one is used as it reduces the machine losses. In fact, a thermal limitation imposed by the nominal current exists for any operation point.

$$I_q^2 + I_d^2 \leq I_{dq_{max}}^2 \quad (0\text{-}39)$$

From the *dq* references currents and using the equation (0-24), the reference voltages that the power converter must supply are calculated.

Appendix E: Equivalent linearized transfer function of the inverter + PMSM machine

In this part, the equivalent transfer function of the inverter+PMSM for a certain operation point is presented. The equations are directly extracted from the following document [19] where the validation of this expression is presented. In the present appendix, only the equations used for our transfer function are presented. The admittance of the inverter and the machine is associated to a fourth-order transfer function.

$$Y(s) = \frac{\delta I_{DC}}{\delta V_{DC}} = \frac{\alpha_0 + \alpha_1 s + \alpha_2 s^2 + \alpha_3 s^3 + \alpha_4 s^4}{\beta_0 + \beta_1 s + \beta_2 s^2 + \beta_3 s^3 + \beta_4 s^4} \tag{0-40}$$

The coefficients of the denominator are extracted from the following formulas using the different parameters of the machine.

$$\beta_0 = GK_{p_\omega} K_{p_i} V_{DC_0}^2 N_p \Phi_{rd} \tag{0-41}$$

$$\beta_1 = GK_{p_i} V_{DC_0}^2 \left[K_{p_\omega} N_p \Phi_{rd} \left(\tau_{i_\omega} + \tau_{i_i} \right) + \tau_{i_v} f \right] \tag{0-42}$$

$$\beta_2 = \tau_{i_\omega} V_{DC_0} \left(GK_{p_i} V_{DC0} \left(\tau_{i_i} \left(K_{p_\omega} N_p \Phi_{rd} + f \right) + J \right) + \tau_{i_i} Rf \right) \tag{0-43}$$

$$\beta_3 = \tau_{i_\omega} \tau_{i_i} V_{DC_0} \left(RJ + Lf + GK_{p_i} V_{DC_0} J \right) \tag{0-44}$$

$$\beta_4 = \tau_{i_\omega} \tau_{i_i} LJV_{DC_0} \tag{0-45}$$

And the coefficients of the denominator are extracted from the following formulas

$$\alpha_0 = -GK_{p_\omega}K_{p_i}V_{DC_0}I_{DC_0}N_p\Phi_{rd} \tag{0-46}$$

$$\alpha_1 = -GK_{p_i}V_{DC_0}I_{DC_0}\left(K_{p_\omega}N_p\Phi_{rd}\left(\tau_{i_\omega}+\tau_{i_i}\right)+\tau_{i_v}f\right) \tag{0-47}$$

$$\begin{aligned}\alpha_2 &= \tau_{i_\omega}\tau_{i_i}G^2V_{DC_0}f(R^2I_{q_0}^2+(N_p\omega_{ref}\Phi_{rd})^2)+\\ &+\tau_{i_\omega}\tau_{i_i}GI_{q_0}Rf(RI_{q_0}+N_p\omega_{ref}\Phi_{rd})-\tau_{i_\omega}\tau_{i_i}GK_{p_\omega}K_{p_i}V_{DC_0}I_{DC_0}N_p\Phi_{rd}\\ &+\tau_{i_\omega}\tau_{i_i}G^2V_{DC_0}I_{q_0}N_p\Phi_{rd}(N_p\Phi_{rd}(RI_{q_0}+N_p\omega_{ref}\Phi_{rd})+2Rf\omega_{ref})\\ &-\tau_{i_\omega}\tau_{i_i}RfI_{DC_0}-\tau_{i_\omega}K_{p_i}V_{DC_0}I_{DC_0}(J+\tau_{i_i}f)\end{aligned} \tag{0-48}$$

$$\begin{aligned}\alpha_3 &= \tau_{i_\omega}\tau_{i_i}G^2V_{DC_0}JN_p\omega_{ref}\Phi_{rd}(2RI_{q_0}+N_p\omega_{ref}\Phi_{rd})\\ &+\tau_{i_\omega}\tau_{i_i}(RJ+Lf)(GI_{q_0}(RI_{q_0}+N_p\omega_{ref}\Phi_{rd})-I_{DC_0})\\ &+\tau_{i_\omega}\tau_{i_i}GV_{DC_0}J(G^2R^2I_{q_0}^2-K_{p_i}I_{DC_0})\end{aligned} \tag{0-49}$$

$$\alpha_4 = \tau_{i_\omega}\tau_{i_i}LJ\left(GI_{q_0}\left(RI_{q_0}+N_p\omega_{ref}\Phi_{rd}\right)-I_{DC_0}\right) \tag{0-50}$$

References

[1] ACARE (Advisory Council for Aeronautics Research in Europe "Beyond Vision 2020", 2010

[2] Airbus " Flying by Numbers", Airbus Global Market Forecast, 2015

[3] http://kids.britannica.com/comptons/art-167707/Air-enters-the-turbofan-jet-engine-propulsion-system-from-the

[4] X. Giraud, "Méthodes et outils pour la conception optimale des réseaux de distribution d'électricité dans les aéronefs," *Diss. INSA de Toulouse*, 2014.

[5] S. Liscouet-Hanke, "A model-based methodology for integrated preliminary sizing and analysis of aircraft power system architectures," *Diss.* INSA de Toulouse , 2008.

[6] Airbus website, web : http://www.airbus.com/aircraftfamilies/passengeraircraft/a380family/innovation/

[7] D. Van Den Bossche, "The A380 flight control electrohydrostatic actuators, achievements and lessons learnt," in 25TH International congress of the aeronautical sciences, 2006, pp. 1–8.

[8] Todeschi, "Airbus – EMAs for Flight Controls Actuation System – An Important Step Achieved in 2011," SAE Technical Paper 2011-01-2732, 2011. doi : 10.4271/2011-01-2732

[9] B. Sarlioglu and C. T. Morris, "More Electric Aircraft: Review, Challenges, and Opportunities for Commercial Transport Aircraft," IEEE Transactions on Transportation Electrification, vol. 1, no. 1, pp. 54–64, Jun. 2015. doi: 10.1109/TTE.2015.2426499

[10] CleanSky project, web:http://www.cleansky.eu/content/interview/towards-all-electric-aircraft-focus-environmental-control-and-ice-protection.

[11] X. Giraud, M. Budinger, X. Roboam, H. Piquet, M. Sartor, and J. Faucher, "Optimal design of the Integrated Modular Power Electronics Cabinet," Aerospace Science and Technology, vol. 48, pp. 37–52, Jan. 2016.

[12] O. Langlois, "Conception d'un réseau de secours électrique pour l'aéronautique," *Diss. Institut National Polytechnique de Toulouse-INPT,* 2006.

[13] X. Roboam, "New trends and challenges of electrical networks embedded in 'more electrical aircraft,'" in Industrial Electronics (ISIE), 2011 IEEE International Symposium on, 2011, pp. 26–31. doi: 10.1109/MIE.2012.2221355

[14] T. Meynard, B. Cougo, and J. Brandelero, "Design of differential mode filters for two-level and multicell converters," in Electronics, Control, Measurement, Signals and their application to Mechatronics (ECMSM), 2013 IEEE 11th International Workshop of, 2013, pp. 1–6. doi: 10.1109/ECMSM.2013.6648963

[15] C. Baumann, "Architecture et gestion d'un réseau continu maillé haute-tension pour l'aéronautique," *Diss. Institut National Polytechnique de Toulouse-INPT*, 2009.

[16] M. Sinnett, "787 No-Bleed Systems: Saving Fuel and Enhancing Operational efficiencies", Boeing, Aero Magazine QTR_4.07

[17] J. Brombach, A. Lücken, B. Nya, M. Johannsen, and D. Schulz, "Comparison of different electrical HVDC-architectures for aircraft application," in Electrical Systems for Aircraft, Railway and Ship Propulsion (ESARS), 2012, 2012, pp. 1–6. doi: 10.1109/ESARS.2012.6387380

[18] J. Brombach , T. Schroeter , A. Luecken, & D. Schulz, "Optimizing the weight of an aircraft power supply system through a+/-270 VDC main voltage". Gen, 2012 vol. 360, p. 800.

[19] S. Girinon, "Etude de la stabilité et de la qualité des réseaux distribués de puissance", *Diss. Institut National Polytechnique de Toulouse-INPT*, 2010.

[20] M. Charrada, "Etude de qualité et de stabilité des réseaux aéronautiques embarqués HVDC," *Diss. Institut National Polytechnique de Toulouse-INPT*, 2013.

[21] L. Prisse, D. Ferer, H. Foch, and A. Lacoste, "New power centre and power electronics sharing in aircraft," in Power Electronics and Applications, 2009. EPE'09. 13th European Conference on, 2009, pp. 1–9.

[22] R. Ramaker, W. Krug, and W. Phebus, "Application of a civil integrated modular architecture to military transport aircraft," in Digital Avionics Systems Conference, 2007. DASC'07. IEEE/AIAA 26th, 2007, p. 2–A. doi: 10.1109/DASC.2007.4391845

[23] J.W. Kolar, "What are the "Big CHALLENGES" in Power Electronics?," in *CIPS*, 2014.

[24] J. Biela, U. Badstuebner, and J. W. Kolar, "Impact of Power Density Maximization on Efficiency of DC-DC Converter Systems," *IEEE Transactions on Power Electronics*, vol. 24, no. 1, pp. 288–300, Jan. 2009.

[25] J. C. Brandelero, "Conception et réalisation d'un convertisseur multicellulaire DC/DC isolé pour application aéronautique," *Diss. Institut National Polytechnique de Toulouse-INPT*, 2015.

[26] A. Andrade, A. Lesage, B. Sareni, T. Meynard, X. Roboam, R. Ruelland, M. Couderc, "Integrated optimal design for power systems of more electrical aircraft", in *International conference on More Electric Aircraft*, Nov. 2012.

[27] B. Delinchant D. Duret L. Estrabaut L. Gerbaud H. Nguyen Huu B. Du Peloux H.L. Rakotoarison F. Verdiere F. Wurtz, (2007), "An optimizer using the software component paradigm for the optimization of engineering systems", *COMPEL - The international journal for computation and mathematics in electrical and electronic engineering*, Vol. 26 Iss 2 pp. 368 - 379

[28] F. Forest, J. Brunello, J. Bourdon, T. Meynard, E. Labouré, and J. J. Huselstein, "Modèles analytiques simplifiés des composants de puissance passifs et actifs pour la conception optimale de convertisseurs," in *Symposium de Génie Électrique 2014*, 2014.

[29] L. Xing, M. Shen, M. Li and W. Said, "Common mode choke optimization for three-phase motor drive systems," *2012 IEEE Energy Conversion Congress and Exposition (ECCE)*, Raleigh, NC, 2012, pp. 1399-1405.
doi: 10.1109/ECCE.2012.6342651

[30] Dépôt à l'Agence de Protections des Programmes : IDDN.FR.001.360033.000.S.P.205.000.20600.

[31] E. Kreyszig,"Advanced engineering mathematics," *John Wiley & Sons*, 2010

[32] M. L. Heldwein, "EMC filtering of three-phase PWM converters". *Diss. ETH* ,2008.

[33] B. B. Toure. "Modélisation haute-fréquence des variateurs de vitesse pour aéronefs : contribution au dimensionnement et à l'optimisation de filtres CEM", *Diss. Université Grenoble Alpes*, 2012

[34] C. Vermaelen. "Contribution à la modélisation et à la réduction des perturbations conduites dans les systèmes d'entraînement à vitesse variable", *Diss. École normale supérieure de Cachan – ENS Cachan*, 2003

[35] B. Revol, "Modélisation et optimisation des performances CEM d'une association variateur de vitesse – machine asynchrone," *Diss. Université Joseph-Fourier – Grenoble I*, 2003.

[36] C. Marlier, "Modélisation des perturbations électromagnétiques dans les convertisseurs statiques pour des aplications aéronautiques", *Université de Lille* 1, 2013

[37] M. Beltramini, "Contribution à l'optimisation de l'ensemble convertisseur / filtres de sortie vis-à-vis des contraintes CEM avion", *PhD Institut National Polytechnique de Toulouse-INPT*, 2011

[38] B. Sareni, L. Krähenbühl, and A. Nicolas, "Niching genetic algorithms for optimization in electromagnetics. I. Fundamentals." *IEEE Transactions on Magnetics*, 1998, vol. 34 (n° 5). pp. 2984-2987. ISSN 0018-9464

[39] B. Sareni, J Régnier and X. Roboam, "Recombination and Self-Adaptation in Multi-objective Genetic Algorithms." *Lecture Notes in Computer Sciences*, 2004, vol. 2936. pp. 115-126. ISSN 0302-9743

[40] R. Hooke and T. A. Jeeves. "Direct Search Solution of Numerical and Statistical Problems," *J. ACM 8*, 2 (April 1961), 212-229.

[41] J. Faucher, "Les plans d'expériences pour le réglage de commandes à base de logique floue," *PhD Institut National Polytechnique de Toulouse-INPT*, 2006

[42] N. Videau. "Convertisseurs continu-continu non isolés à haut rapport de conversion pour Piles à Combustible et Electrolyseurs – Apport des composants GaN," *Phd Institut National Polytechnique de Toulouse-INPT*, 2014

[43] S. V. Araújo. "On the Perspectives of Wide-Band Gap Power Devices in Electronic-Based Power Conversion for Renewable Systems" *Diss. Kassel university*, 2013

[44] A. F. Moreira, T. A. Lipo, G. Venkataramanan and S. Bernet, "High-frequency modelling for cable and induction motor overvoltage studies in long cable drives," in *IEEE Transactions on Industry Applications*, vol. 38, no. 5, pp. 1297-1306, Sep/Oct 2002. doi: 10.1109/TIA.2002.802920

[45] Drofenik, Uwe, Gerold Laimer, and Johann W. Kolar. "Theoretical converter power density limits for forced convection cooling." *Proceedings of the International PCIM Europe 2005 Conference*. 2005.

[46] N. Videau *et al*., "5-phase interleaved buck converter with gallium nitride transistors," *Wide Bandgap Power Devices and Applications (WiPDA), 2013 IEEE Workshop on*, Columbus, OH, 2013, pp. 190-193.
doi: 10.1109/WiPDA.2013.6695594

[47] Mühlethaler, Jonas, "Modelling and multi-objective optimization of inductive power components," *Diss*. *ETH / Power Electronic Systems Laboratory*, 2012

[48] C. P. Steinmetz. "On the Law of Hysteresis". *American Institute of Electrical Engineers, Transactions of the,* vol. IX, n° 11, pp. 1,64, Jan. 1892.

[49] F. Forest, E. Labouré, T. Meynard et M. Arab ,"Analytic Design Method Based on Homothetic Shape of Magnetic Cores for High-Frequency Transformers", *Power Electronics, IEEE Transactions on,* vol. 22, n° 15, pp. 2070,2080, Sept. 2007.
Doi: 10.1109/TPEL.2007.904251

[50] K. Venkatachalam, C. R. Sullivan, T. Abdallah and H. Tacca, "Accurate prediction of ferrite core loss with nonsinusoidal waveforms using only Steinmetz parameters," *Computers in Power Electronics, 2002. Proceedings. 2002 IEEE Workshop on,* 2002*,* pp.36-41. doi: 10.1109/CIPE.2002.1196712

[51] J. Muhlethaler, J. Biela, J. W. Kolar and A. Ecklebe, "Improved Core-Loss Calculation for Magnetic Components Employed in Power Electronic Systems," in *IEEE Transactions on Power Electronics*, vol. 27, no. 2, pp. 964-973, Feb. 2012. doi: 10.1109/TPEL.2011.2162252

[52] K. Terashima, K. Wada, T. Shimizu, T. Nakazawa, K. Ishii and Y. Hayashi, "Evaluation of the iron loss of an inductor based on dynamic minor characteristics," *Power Electronics and Applications, 2007 European Conference on*, Aalborg, 2007, pp.1-8. doi: 10.1109/EPE.2007.4417555

[53] M. S. Rylko. "Magnetic materials and soft-switched topologies for high-current DC-DC converters". *PhD Thesis, University College Cork*. 2011

[54] V. Costan, "Convertisseurs parallèles entrelacés : étude des pertes fer dans les transformateurs inter-cellules", *Institut National Polytechnique de Toulouse-INPT* 2007

[55] J. Lammeraner, & M. Štafl, "Eddy currents", *CRC Press*,1966

[56] P. Dowell, "Effects of eddy currents in transformer windings", *Electrical Engineers, Proceedings of the Institution of ,* vol. 8, n° 1113, pp. 1387,1394, Aug 1966. doi: 10.1049/piee.1966.0236

[57] R. M. Burkart, H. Uemura and J. W. Kolar, "Optimal inductor design for 3-phase voltage-source PWM converters considering different magnetic materials and a wide switching frequency range," *2014 International Power Electronics Conference (IPEC-Hiroshima 2014 – ECCE ASIA)*, Hiroshima, 2014, pp. 891-898. doi: 10.1109/IPEC.2014.6869693

[58] MATLAB Documentation

[59] B. Cougo, "Design and optimization of intercell transformers for parallel multicell converters", *Phd Institut National Polytechnique de Toulouse-INPT*, 2010.

[60] J. A. Ferreira, "Improved analytical modelling of conductive losses in magnetic components," in *IEEE Transactions on Power Electronics*, vol. 9, no. 1, pp. 127-131, Jan 1994. doi: 10.1109/63.285503

[61] D. Hamill, "Lumped equivalent circuits of magnetic components: the gyrator-capacitor approach", *Power Electronics, IEEE Transactions on,* vol. 8, n° 12, pp. 97,103, Apr 1993. doi**:** 10.1109/63.223957

[62] E. C. Cherry, "The Duality between Interlinked Electric and Magnetic Circuits and the Formation of Transformer Equivalent Circuits", *Proceedings of the Physical Society. Section B,* vol. 62, n° 12, pp. 101-111, 1949.

[63] A. Hilal, "Magnetic components modelling including thermal effects for DC-DC converters virtual prototyping", *Diss. Université Claude Bernard-Lyon I*, 2014.

[64] T. Meynard. "Analysis and Design of Multicell DCDC Converters Using Vectorized Models". *John Wiley & Sons*, 2015.

[65] A. Van den Bossche, V. Valchev and J. Melkebeek, "Thermal modelling of E-type magnetic components," *IECON 02 Industrial Electronics Society, IEEE 2002 28th Annual Conference of the*, 2002, pp. 1312-1317 vol.2.
doi: 10.1109/IECON.2002.1185465

[66] T. L. Bergman, F. P. Incropera, D. P. DeWitt, & A. S. Lavine, "Fundamentals of heat and mass transfer", *John Wiley & Sons* , 2011

[67] A. Van den Bossche, , V. Valchev, "Thermal Design of Transformers and Inductors in Power Electronics", In *4ième Conférence internationale sur le Génie Electrique (CIGE 2010)* (No. 2, pp. 10-13). Université de Bechar Algérie.

[68] S. Sanchez, "Contribution à la conception de coupleurs magnétiques robustes pour convertisseurs multicellulaires parallèles", *Diss. Institut National Polytechnique de Toulouse-INPT,* 2015

[69] F. Forest, E. Labouré, T. A. Meynard and V. Smet, "Design and Comparison of Inductors and Intercell Transformers for Filtering of PWM Inverter Output," in *IEEE Transactions on Power Electronics*, vol. 24, no. 3, pp. 812-821, March 2009. doi: 10.1109/TPEL.2008.2007900

[70] K. Guepratte. "Onduleur triphasé à structure innovante pour application aéronautique". *Diss. Université Grenoble Alpes*, 2011

[71] M. L. Heldwein, L. Dalessandro and J. W. Kolar, "The Three-Phase Common-Mode Inductor: Modelling and Design Issues," in *IEEE Transactions on Industrial Electronics*, vol. 58, no. 8, pp. 3264-3274, Aug. 2011. doi: 10.1109/TIE.2010.2089949

[72] Chansung Catalog v12 " Magnetic powder cores"

[73] M. J. Nave, "On modelling the common mode inductor", *Electromagnetic Compatibility, 1991. Symposium Record., IEEE 1991 International Symposium on*, Cherry Hill, NJ, 1991, pp. 452-457. doi: 10.1109/ISEMC.1991.148275

[74] A.J. Chapman, "Heat transfer", *New York, NY, The Macmiiian Co., cl960*, 1984.

[75] J. Bourdon, "Optimal design methodology for static converters - application to the aeronautical context", *Diss. Institut National Polytechnique de Toulouse-INPT*, 2016.

[76] J. Biela and J. W. Kolar, "Cooling Concepts for High Power Density Magnetic Devices," *Power Conversion Conference – Nagoya, 2007. PCC '07*, Nagoya, 2007, pp. 1-8. doi : 10.1109/PCCON.2007.372915

[77] S. S. Kang, "Advanced Cooling for Power Electronics," *2012 7th International Conference on Integrated Power Electronics Systems (CIPS)*, Nuremberg, 2012, pp. 1-8.

[78] P. Teertstra, , M. Yovanovich, & J. R. Culham, "Analytical forced convection modelling of plate fin heat sinks," *Journal of Electronics Manufacturing*, *10*(04), 253-261, 2000

[79] A. Castelan, B. Cougo, J. Brandelero, D. Flumian and T. Meynard, "Optimization of forced-air cooling system for accurate design of power converters," *2015 IEEE 24th International Symposium on Industrial Electronics (ISIE)*, Buzios, 2015, pp. 367-372. doi: 10.1109/ISIE.2015.7281496

[80] C. K. Loh and D. J. Chou, "Comparative analysis of heat sink pressure drop using different methodologies," *Semiconductor Thermal Measurement and Management Symposium, 2004. Twentieth Annual IEEE*, 2004, pp. 148-153. doi : 10.1109/STHERM.2004.1291317

[81] S., Seaho, V. Au, and K. P. Moran. "Constriction/spreading resistance model for electronics packaging", *Proceedings of the 4th ASME/JSME thermal engineering joint conference*, Vol. 4, 1995.

[82] Yovanovich, M. M., Y. S. Muzychka, and J. R. Culham. "Spreading resistance of isoflux rectangles and strips on compound flux channels." *Journal of Thermophysics and Heat Transfer* 13.4, 495-500, 1999

[83] Y. S. Muzychka, J. R. Culham, and M. M. Yovanovich. "Thermal spreading resistance of eccentric heat sources on rectangular flux channels", *Journal of Electronic packaging* 125.2 178-185, 2003, doi: 10.1115/1.1568125

[84] Nexans Product Catalog " Aircraft Wires and Cables"

[85] Y. Weens, "Modélisation des câbles d'énergie soumis aux contraintes générées par les convertisseurs électroniques de puissance". *Diss. Université des Sciences et Technologies de Lille*, 2006.

[86] M. Kane, "Modeles analytiques originaux pour la détermination des parametres linéiques des lignes et câbles multifilaires parcourus par des signaux large bande". *Diss. Ecole Centrale de Lyon*, 1994.

[87] L. Havez, "Contribution au prototypage virtuel 3D par éléments finis de composants magnétiques utilisés en électronique de puissance," *Diss. Institut National Polytechnique de Toulouse-INPT*, 2016.

[88] D. Izquierdo, A. Barrado, C. Raga, M. Sanz and A. Lazaro, "Protection Devices for Aircraft Electrical Power Distribution Systems: State of the Art", in *IEEE Transactions on Aerospace and Electronic Systems*, vol. 47, no. 3, pp. 1538-1550, July 2011. doi: 10.1109/TAES.2011.5937248

[89] G. Buja and G. Indri, "Improvement of pulse width modulation techniques," *Archiv fur Elektrotechnik*, 57, pp. 281-289, 1975.

[90] J. W. Kolar, H. Ertl and F. C. Zach, "Minimization of the harmonic RMS content of the mains current of a PWM converter system based on the solution of an extreme value problem," *ICHPC Conf. Records*, pp. 234-243, Budapest, Hungary, 1990.

[91] K. Taniguchi, Y. Ogino and H. Irie, "PWM technique for power MOSFET inverter," *IEEE Trans. on Power Electronics*, pp. 328-334, July 1988.

[92] P.M. Anderson and A.A. Fouad, "Power System Control and Stability", *IEEE Press*, 2003

[93] Airbus, "Electrical characteristics of HVDC load equipment"

[94] EUROCAE ED-14D/ RTCA DO-160D, "Environmental conditions and test procedures for airbone equipment"

[95] K. Ogata, & Y. Yang, "Modern control engineering", 1970

[96] R. D. Middlebrook, "Input Filter Considerations in Design and Application of Switching Regulators," IEEE Industry Applications Society Annual Meeting, 1976 Record, pp. 366-382.

[97] Hadbi, Djamel. "Formulations de problèmes d'optimisation multiniveaux pour la conception de réseaux de bord électriques en aéronautique" *Diss. Université Grenoble Alpes*, 2015.

[98] Sakr, Nadim. "Fast on-board integrated chargers for electric vehicles". *Diss. Paris Saclay*, 2016.

[99] R. W. Erickson, "Optimal single resistors damping of input filters," *Applied Power Electronics Conference and Exposition, 1999. APEC '99. Fourteenth Annual*, Dallas, TX, 1999, pp. 1073-1079 vol.2. doi: 10.1109/APEC.1999.750502

[100] B. Cougo, G. Gateau, T. Meynard, M. Bobrowska-Rafal and M. Cousineau, "PD Modulation Scheme for Three-Phase Parallel Multilevel Inverters," in *IEEE Transactions on Industrial Electronics*, vol. 59, no. 2, pp. 690-700, Feb. 2012. doi: 10.1109/TIE.2011.2158773